Dissertation

submitted to the
Combined Faculties for the Natural Sciences and for Mathematics
of the Ruperto-Carola University of Heidelberg, Germany
for the degree of
Doctor of Natural Sciences

Put forward by
Felix Friedrich Florian Frey
born in Kirchheim unter Teck
Oral examination: 05.06.2019

Physical models for uptake processes at the cell membrane

Referees: Prof. Dr. Ulrich Schwarz

Prof. Dr. Heinz Horner

Physical models for uptake processes at the cell membrane

All biological cells are enclosed by a fluid membrane and have to continuously transport information and material across this interface. Cells have developed multiple strategies by which they take up small particles. In this thesis, I use theoretical models from statistical physics and computer simulations to investigate two of these strategies, namely receptor-mediated endocytosis driven by adhesion energy and clathrin-mediated endocytosis driven by the polymerisation energy of supramolecular assembly. For receptor-mediated uptake, I focus on systems with sizes in the order of $10-300\,\mathrm{nm}$, few tens of cell surface receptors and address stochastic effects. We show how the stochastic dynamics of uptake is influenced by particle geometry and compare theoretically predicted adhesion energies to experimental data. For clathrin-mediated endocytosis we demonstrate by combining different experimental data sets with physical models how clathrin triskelia assemble and rearrange during endocytosis. Using computer simulations we show that flat clathrin lattices grow sparsely and that an increasing clathrin density could drive a flat-to-curved transition of clathrin lattices. Together, these results demonstrate how physical models can help to understand the complex biological process of cellular uptake.

Physikalische Modelle für Aufnahmeprozesse an der Zellmembran

Alle biologischen Zellen sind von einer Plasmamembran umgeben über welche sie kontinuierlich Informationen und Stoffe transportieren. Zellen haben verschiedene Strategien entwickelt mit Hilfe derer sie kleine Partikel aufnehmen. In dieser Arbeit benutze ich theoretische Modell aus der Statistischen Physik sowie Computersimulationen, um zwei dieser Strategien, nämlich Rezeptor-vermittelte Endozytose, getrieben durch Anhaftungsenergie, und Clathrin-vermittelte Endozytose, getrieben durch Polymerisationsenergie, zu untersuchen. Für die Rezeptor-vermittelte Endozytose konzentriere ich mich auf Systeme mit einer Größe von $10-300\,\mathrm{nm}$, einigen Dutzend Membranrezeptoren und adressiere stochastische Effekte. Wir zeigen wie die stochastische Dynamik der Partikelaufnahme durch die Teilchengeometrie beeinflusst ist und vergleichen theoretische Vorhersagen der Anhaftungsenergien mit experimentellen Daten. Für die Clathrin-vermittelte Endozytose zeigen wir, indem wir verschiedene experimentelle Datensätze mit physikalischen Modellen kombinieren, wie Clathrin Triskelia assemblieren und sich während der Endozytose umorganisieren. Anhand von Computersimulationen zeigen wir wie flache Clathringitter spärlich besetzt wachsen und dass eine ansteigende Clathringitterdichte den Übergang von flachen zu gekrümmten Clathringittern antreiben könnte. Zusammenfassend demonstrieren die Ergebnisse wie physikalische Modelle dabei helfen können, den komplexen biologischen Prozess der zellulären Aufnahme zu verstehen.

Contents

1 Introduction

The biological cell is the functional unit of life. Cells contain proteins and organelles that provide all relevant functions, accommodate the genetic material and are enclosed by a plasma membrane. One of the most important conditions for cellular life is the ability to create order and structure from molecular chaos, using energy provided by their metabolism. From a physical point of view this implies a constant energy flux into the cell in order to reduce entropy locally, which is typically achieved by an entropy flux out of the cell [1]. Besides the import of energy, cells also have to take up information to respond to changing environmental conditions. The human body is a multicellular organism that consists of roughly 10^{13} cells. Such a complex system can only function properly if spatial and temporal coordination between cells among themselves and between cells and the surroundings is precise [2]. Thus, the ability of cells to communicate with their environment is essential. Both aspects demonstrate the significance of the cellular ability to constantly relay material and information in the form of small particles, such as nutrient and signalling molecules, across their membrane, serving as both communication interface and physical barrier [3].

Mostly, cellular uptake (or endocytosis) occurs on purpose, but it can also happen unintentionally, being accompanied by negative consequences. The uptake of microplastics ($< 1\,\mathrm{mm}$) is an example where uptake occurs although it is undesirable, as the cellular uptake system is triggered by physical processes [4]. In this case, indigestion can induce dangerous chemicals to cells as recently shown [5]. The consequences of undesirable uptake might even be more dramatic when it comes to uptake and entry of pathogens. A prominent example is the uptake of virus particles such as Influenza, human immunodeficiency virus (HIV), or Ebola, where viruses hijack cellular uptake pathways in order to infect host cells, replicate and spread [6]. Another example where pathogens are interacting with the cell membrane is the cellular entry of malaria parasites, followed by severe implications for health [3]. Particle uptake can also be beneficial for medical applications, for example when delivering drugs to cells [7]. The therapeutical application of nano-sized containers to deliver drugs and nano-machines to cells seems to be in reach. In particular, we have recently seen huge advances in the field of nano science, where self-assembled structures can now be fabricated in a templated way [8]. Such applications bear enormous potential as they could allow examination or manipulation at the nanoscale within cells. One of the key challenges, not only in biophysics but across the natural sciences is to explain the origin of life. A

significant part of a minimal living system is the module that provides material and information exchange. Following the approach of synthetic biology, one strategy to understand the cell (as minimal unit of life) is to reengineer and construct it bottom up [9]. Thus, the study of cellular uptake is necessary to explore the origin of life.

Cells have developed multiple strategies to take up particles. Such strategies always involve mechanisms to overcome the cell membrane, separating the cellular interior from its environment. In addition, they have to fulfil several criteria: First, they have to work robustly and independent from special environmental conditions and function preferably error-free. Secondly, cells have developed multiple uptake strategies in order to ensure redundancy. Thirdly, the underlying machinery should be recyclable such that the same mechanism can be used over and over again. Fourthly, the mechanisms have to be efficient without consuming too much energy. To conclude, the discussed facets show the importance of investigating cellular uptake. Although lots of experimental findings have been gathered over the last decades, many aspects of cellular uptake are still elusive. Traditionally, physics contributes to systematise and organise our understanding into a more abstract and general form [10]. There is also a long tradition of theoretical models for uptake processes, motivated in particular by the physical nature of this essential part of the life of cells. Thus, in this thesis we develop theoretical models for several uptake processes at the plasma membrane in order to gain understanding of the physical principles of endocytosis.

In the first part we investigate adhesion-mediated uptake, driven by the energetic gain of binding cell surface receptors. From a physical point of view, several aspects of this process are interesting. First, the cell membrane, presenting a barrier, has to be overcome. Second, during uptake one has to consider shape changes and mechanical deformations of the membrane, which is a two-dimensional surface embedded in three-dimensional space with elastic properties. In addition, cargo particles can assume different shapes with important consequences for the dynamics of the uptake process. Finally, the uptake is driven by ligand-receptor binding. As the system size is small, fluctuations in the ligand-receptor binding kinetics are relevant. Hence, in the first part we are dealing with membrane mechanics, geometry and stochastic dynamics.

In the second part we investigate assembly-mediated uptake at the example of clathrin-mediated endocytosis (CME). CME is one of the major cellular uptake pathways, driven by the supramolecular protein assembly of a clathrin lattice onto the membrane. From a physical point of view, the assembly of clathrin lattices represents a complex system that is much more plastic than previously thought. Recent studies have shown that the flat hexagonal clathrin lattice can develop curvature by lattice rearrangements even relatively late in the uptake process. Thus, in the second part we are studying the self-assembly of clathrin lattices that leads to a topology transition of the plasma membrane.

Outline

This thesis uses theoretical physical concepts to investigate cellular uptake processes at the cell membrane. Our work is divided into two coherent parts. We investigate receptor-mediated particle uptake in chapter 3-5, whereas we study CME in chapter 6-8.

In **chapter 2** we discuss the biological background and important physical concepts relevant for cellular uptake. First, we introduce different mechanisms for cellular uptake. In particular, we explain receptor-mediated (virus) uptake and CME. Secondly, we summarise the experimental methods that are used to study cellular uptake. We introduce the physical concepts, which are at the basis of membrane biophysics, stochastic dynamics, self-assembly and aggregation. Because cellular uptake is a complex problem with many degrees of freedom, it is typically studied with computer simulations. Therefore, we also review the most prominent computational methods, which are used to study cellular uptake of small particles at the end of this chapter.

In **chapter 3** we investigate the stochastic dynamics of nanoparticle and virus uptake while considering cylindrical, spherical and spherocylindrical particles. We start by developing a deterministic model for the dynamics of particle uptake. We use the model to compute uptake times and to compare the different shapes quantitatively. In the second part we address stochastic effects, which are expected to be relevant, as ligand-receptor interactions are discrete and the particles that are taken up are small. For this purpose, we develop a stochastic model that is based on our deterministic description. We study the uptake of various shaped particles by calculating the mean uptake times both analytically and computationally.

In **chapter 4** we study the dynamics of particle uptake once again. However, in contrast to chapter 3, where we neglected the free parts of the membrane that do not adhere to the particle, we now take these contributions explicitly into account. By studying the different energy contributions, we develop a dynamical model in which we represent the contribution of the free membrane parts either by a line tension or an extended line tension. Again, using this dynamical model we investigate the uptake dynamics of cylindrical and spherical particles both qualitatively and quantitatively. In the second part we analyse a stochastic version of this model. Last but not least we explore how the particle's position relative to the cell membrane is affected by fluctuations during uptake.

In **chapter 5** we investigate the dynamics of substrate-attached virus and nanoparticle uptake motivated by recent experiments. We first discuss these experiments, in which

tension probes are used to quantify uptake forces, before we apply our deterministic model of chapter 3 to describe the data. In particular, we investigate forces and adhesion energies. Based on these experiments we then extend our model to study the stochastic dynamics of substrate-attached particle uptake. We model substrate-attachment by either a linear spring or a polymer that behaves like a worm-like chain.

In **chapter 6** we investigate the flat-to-curved-transition during CME. We combine correlative electron and light microscopy and mathematical growth laws to calculate the size and morphology distributions of clathrin-coated structures during endocytosis. In this way, we test whether clathrin lattices grow with constant curvature, i.e. by assembling directly in the form of a coated pit or if they first grow flat before they start to bend, while keeping their surface area constant. In the second part of this chapter, we analyse the assembly kinetics of adaptor proteins to which clathrin triskelia bind to during coat formation. Finally, we investigate CME under an osmotic shock that changes membrane tension and thus affects clathrin coat assembly.

In **chapter 7** we investigate the growth of flat clathrin lattices on plasma membranes by combining correlative light and electron microscopy data with computer simulations. We aim to test our hypothesis that flat clathrin lattices grow with many structural gaps. Such spatial heterogeneity could explain the known fast exchange kinetics of clathrin triskelia and should lower the energetic and topological barriers for the flat-to-curved transition. For this purpose we first develop a model that includes different variants of how clathrin molecules can interact with each other and then simulate the growth of flat lattices. We analyse the simulated clathrin lattices and study their structural composition, integrity and focus on structural gaps within the lattice.

In **chapter 8** we model the flat-to-curved transition during clathrin coat assembly. We first investigate the possibility that the flat-to-curved transition is driven by an increasing density of clathrin triskelia within the clathrin coat. Based on a consideration of the involved energies of the plasma membrane and the clathrin coat, we study the shape and size of clathrin coats. Importantly, we implement the assumption of an increasing clathrin density within the lattice by either an increasing coat rigidity or an increasing line tension. From the energetic model we then deduce phenomenological equations to investigate the growth and assembly dynamics of clathrin coated structures. These dynamic equations are then used to fit experimental data.

In **chapter 9** we summarise and discuss our results and give a short outlook on future studies.

2 Cellular uptake

2.1 Biological background

All biological cells have to transport material and information across their cell membranes, acting as both physical barrier, that separates the cellular interior from its environment, and as a barrier to the free flow of information [3]. Transport across the plasma membrane can be either intentional when nutrients and signalling molecules are endocytosed or undesirable, thinking of uptake of microplastics [4] or pathogen entry [3]. The central platform on which each and every uptake process starts is the cell or plasma membrane, which has very special physical properties.

2.1.1 The cell membrane

Membranes are a basic structural element of all kinds of cells. In eukaryotic cells different types of membranes occur. First, there is the cell or plasma membrane which surrounds the cell and secondly, there are membranes that enclose entire organelles. In the following we summarise the main purposes which membranes serve [11]:

- Membranes are a **physical barrier** that either enclose the cell as a total or subcellular regions, thereby defining cell organelles. They define spatial boundaries, that separate the interior from the exterior and spatial compartments, in which biochemical reactions can run robustly.
- Membranes act as an **interface** in order to relay material an information.
- Membranes **sort and select** molecules by either being permeable for some of them or repellent (thinking of e.g. ion channels).
- Membranes provide a **platform** that enables the proper functioning of proteins (e.g. enzymes or receptors).

The basic structure of a membrane is that of a **lipid bilayer**, which is mostly built up from phospholipids. In Fig. 2.1 (a) the basic structure is illustrated. A eukaryotic cell (nucleus in yellow) with a typical size of $\sim 10\,\mu$m is surrounded by a lipid bilayer (red). The lipid bilayer of thickness of $\sim 4\,$nm is made up from phospholipids with a hydrophilic head and typically two hydrophobic tails [14]. Fig. 2.1 (b) shows a more detailed schematics of the cell membrane. Here, also proteins are asymmetrically

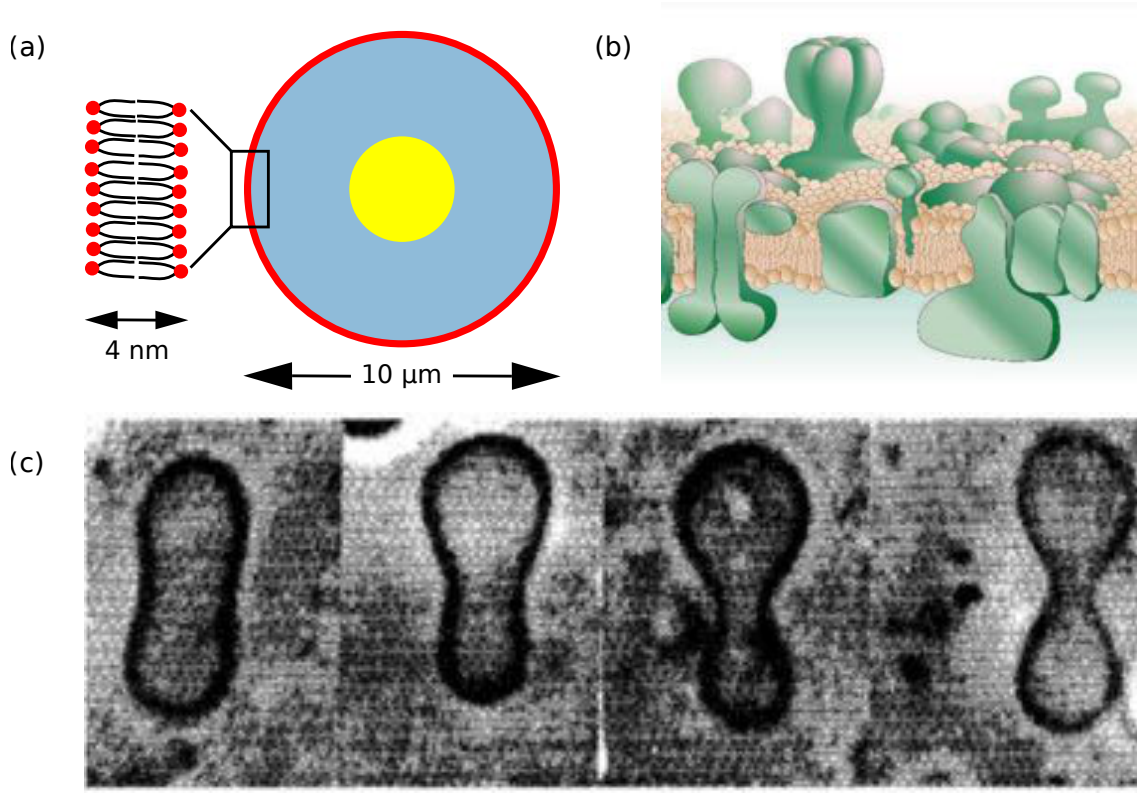

Figure 2.1 | Structure and shape of the cell membrane. **(a)** A eukaryotic cell (nucleus in yellow), surrounded by a lipid bilayer (red), which is built up from phospholipids with a hydrophilic head and two hydrophobic tails. **(b)** Schematics representing a snapshot of the highly dynamic cell membrane in which many proteins are embedded. **(c)** Membranes adopting minimal energy shapes. Figure **(b)** and **(c)** are taken and adapted from [12, 13].

embedded in the lipid bilayer either facing or adverting the cytoplasm, dependent on their function. Importantly, both lipids and proteins are not static but dynamic within the context of the cell membrane. In principle, three different types of motion could exist: Translational, rotational and transbilayer motion, although the energy barrier for the last one is very high. This basic model of the cell membrane is the so-called **fluid mosaic model**, proposed in 1972 by Singer and Nicolson [15]. Today, we know that membranes are highly dynamic and crowded by many different proteins, that can be partially exchanged between the cytosol and the membrane [16]. Diffusion of proteins within the membrane can be decreased due to protein crowding, leading to sub-diffusive behaviour [17]. The interplay of hydrophilic and hydrophobic motifs of the phospholipids gives rise to differently shaped lipid bilayers that can spontaneously self-assemble in water. The polar heads orient toward the surrounding water and hence shield the non-polar tails. In general, the shape of a membrane adopts the minimal energy configuration, with respect to internal interactions and external forces. In addition, the shape is subject to passive thermal [13] and active fluctuations [18]. In Fig. 2.1 (c) examples of differently shaped membranes are shown.

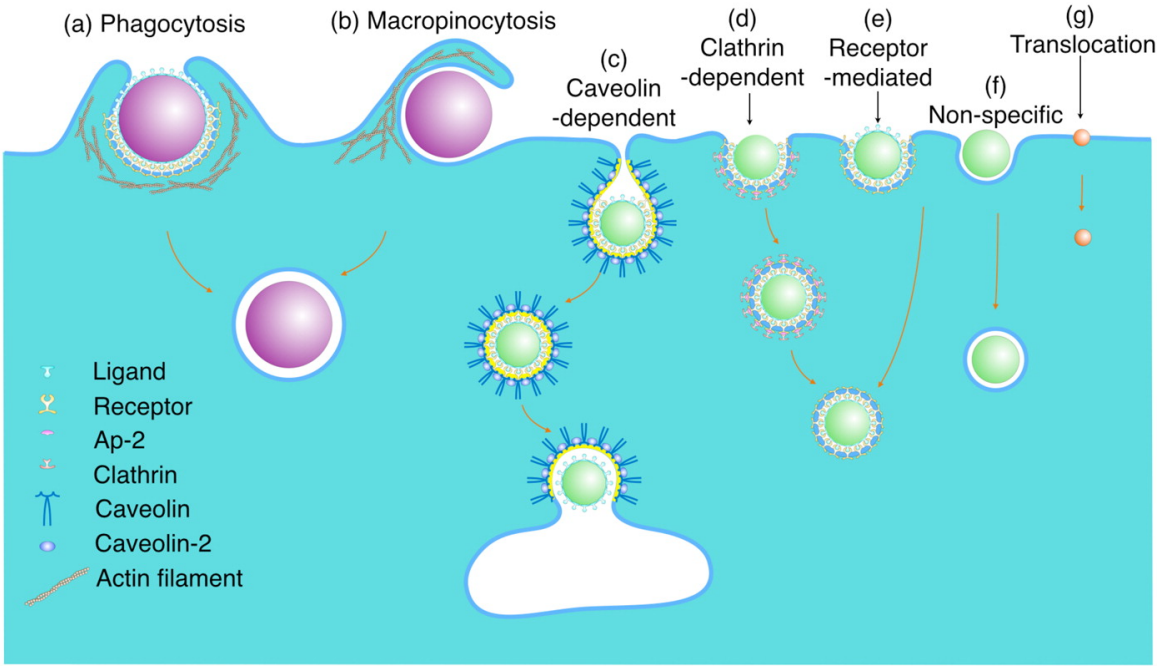

Figure 2.2 | Mechanisms of cellular uptake. **(a)** Phagocytosis. **(b)** Macropinocytosis. **(c)** Caveolin-dependent endocytosis. **(d)** Clathrin-mediated endocytosis. **(e)** Receptor-mediated endocytosis. **(f)** Non-specific uptake. **(g)** Translocation. **(a)-(d)** Represent examples of assembly-mediated uptake, either driven by actin polymerisation or assembly of caveolin or clathrin. **(e)-(f)** Represent examples of adhesion-mediated uptake, driven by the direct interaction of the cargo particle and the cell membrane. Figure taken and adapted from [20].

In order to prevent non-specific adhesion, the membrane is covered by the glycocalyx (formed from sugar molecules), inducing electrostatic repulsion. The cell membrane is anchored to the interior of the cell by the cytoskeleton (CSK), which is a network of filamentous proteins that provides stability and organises the cell. Actin filaments are part of the CSK and form together with myosin molecular motors the actomyosin cortex [19]. The cortex changes the material properties of the membrane.

A major task of the membrane is to serve as a communication interface. Small molecules like ions are transported through the membrane via channels or pumps. This is of special importance in the brain where information is processed by transmitting voltage potentials so-called action potentials along neurones, which are amplified and repeated at a certain distance, induced by the transport of ions into and out of neurones [14]. For particles with a typical size of tens of nanometers multiple other import strategies exist, which are discussed in the following.

2.1.2 Mechanisms of cellular uptake

Cells have to import nutrients and signalling molecules to maintain their metabolism and communicate with their surroundings, respectively. Thus, several uptake strategies

have developed, which have been reviewed, for instance, in [20]. An overview is shown in Fig. 2.2. In general, the particle size and surface composition determine the way of how particles enter the cell. One can distinguish between two main strategies. First, in adhesion-energy mediated uptake the particle is endocytosed by direct interaction with the cell membrane, e.g. by ligand-receptor binding. Secondly, in assembly-mediated uptake the process is driven by the assembly of additional proteins e.g. actin, caveolin or clathrin triskelia, which favour the engulfment of the particle. Along the same lines one could classify adhesion-energy-mediated and assembly-mediated uptake as passive or active uptake, respectively. Large particles ($\sim \mu$m) can get endocytosed either by **Phagocytosis** (a) or **Macropinocytosis** (b). Importantly, both processes are dependent on the active polymerisation of actin. In Phagocytosis membrane protrusions are pushed by actin along the particle, a dead cell or pathogen, leading to gradual uptake. Macropinocytosis is less specific and takes up a huge amount of extracellular fluid including the particle by membrane ruffling. **Caveolin-dependent endocytosis** is driven by the molecular assembly of caveolin forming flask-shaped coats at the cytosolic side of the cell membrane (c). In **Clathrin-mediated endocytosis (CME)** a coat of clathrin triskelia assembles at the cytosolic side of the cell membrane (d). These clathrin lattices then bend the plasma membrane. Importantly, both CME and caveolin-dependent endocytosis heavily rely on biochemical signalling and receptor-ligand binding. Endocytosis can be also mediated by **receptor-ligand binding** alone (e) or even by **non-specific interactions** (f). For both pathways the interaction between cell membrane and particle must be sufficiently large to drive endocytosis. Finally, sub-nanometer sized particles can enter the cell by **translocation**, mediated through diffusion across the plasma membrane (g).

Uptake mediated by a gain of adhesion-energy

Perhaps the most basic mechanism for cellular uptake is adhesion-energy driven. The target particle bears ligands that bind to cell membrane receptors or the particle binds non-specifically to the membrane. In principle, electrostatic, van der Waals and hydrophobic interactions can be summarised as adhesion-interactions. Uptake is possible if the adhesion energy is larger than the bending and tension energy of the membrane, both counteracting endocytosis. Importantly, specific and non-specific binding interactions between target particle and cell membrane differ by three key aspects [20]: First, since receptor-ligand binding is a discrete event, it comes with typical time scales that receptors need to diffuse toward the uptake site and bind to ligands on the particle surface. Secondly, due to its discrete nature it introduces an energy barrier that need needs to be overcome to bind the next receptor. Thirdly, redistribution of receptors within the cell membrane involves a change in entropy that could in addition counteract uptake.

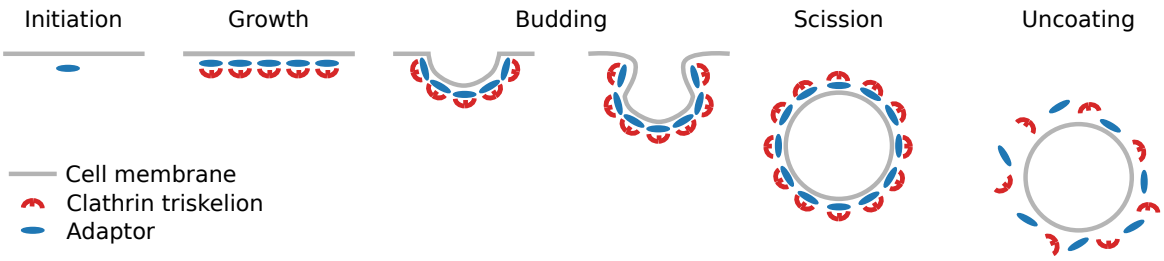

Figure 2.3 | Standard sequence and checkpoints of clathrin-mediated endocytosis. Initiation. Growth. Budding. Scission. Uncoating.

Uptake mediated by protein assembly

In assembly-mediated uptake the process is driven by the assembly of additional proteins e.g. actin, caveolin or clathrin triskelia. These supramolecular protein assemblies then provide the necessary force that is needed to act against membrane bending and tension. In Phagocytosis and Macropinocytosis the assembly of actin protrusions pushes the cell membrane around the target particle such that it becomes successively endocytosed. In caveolin-mediated endocytosis the assembly of caveolin forms invaginations at the cell membrane by which cargo can be internalised. Last but not least in CME clathrin-triskelia assemble at the cell membrane in order to invaginate a membrane patch and form a clathrin-coated vesicle (CCV).

2.1.3 Clathrin-mediated endocytosis

Clathrin-mediated endocytosis (CME) is one of the major pathways for cellular trafficking and internalising signalling or nutrient molecules [14]. Because clathrin molecules form cages during assembly they are called clathrin, coming from the latin word clatratus meaning latticed or barred. The **standard sequence** of how CME proceeds in the cell is illustrated in Fig. 2.3. CME is initiated by the binding of extracellular cargo particles to receptor proteins on the plasma membrane. Next, accessory and adaptor proteins, such as AP2, bind to surface receptors from the cytosolic side. The process is rather complex as many different proteins are involved. It is followed by the assembly of clathrin triskelia onto adaptors, that leads to membrane bending and invagination of a membrane patch of several tens of nanometer radius. Next, the fully formed clathrin-coated vesicle (CCV) pinches off the cell membrane mediated by dynamin proteins [21]. Last but not least the CCV gets uncoated and all involving proteins are recycled in another round of CME and the created vesicle is transported to its destination. In summary, CME is a prominent example of a complex biological system where the constituent molecules can self-assemble.

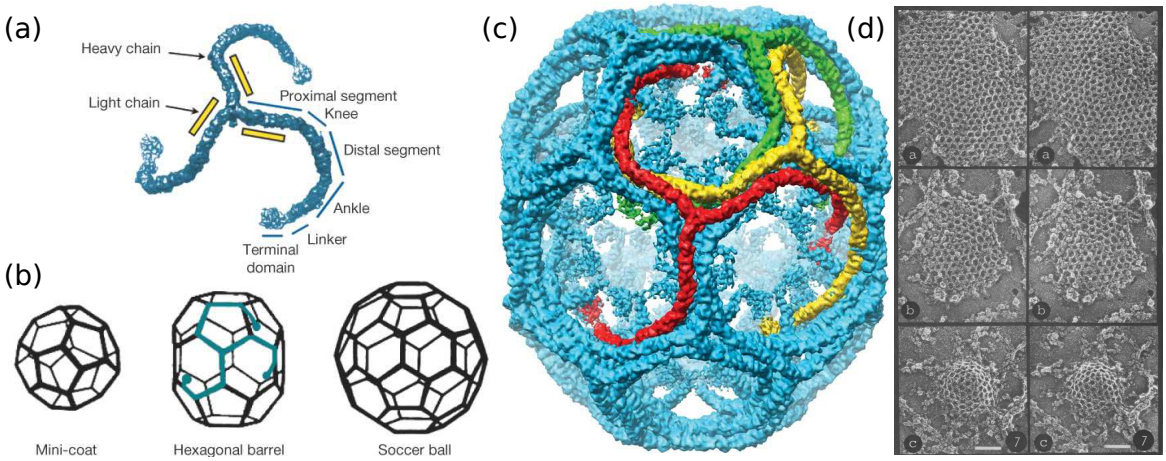

Figure 2.4 | A single clathrin triskelion and an assembled structure of many clathrin triskelia. **(a)** The clathrin triskelion is built from three dimers, where each dimer consists of a light and a heavy chain. **(b)** Different assembled clathrin structures. **(c)** Averaged image reconstruction from reconstituted clathrin structures in vitro. **(d)** Flat and spherical clathrin structures, registered in EM. Figures taken and adapted from **(a)**-**(c)** [22] and **(d)** [23].

Structure of the clathrin triskelion and clathrin coats

The functional unit of clathrin lattices is the clathrin triskelion, whose molecular structure is shown in Fig. 2.4 (a). Each triskelion has a tripod structure and consists of three dimers, where each dimer is built up of a light and a heavy chain of proximal, distal and terminal domain that are linked by the knee and ankle [22]. In the test tube clathrin triskelia assemble into well defined geometries which are shown as schematics in Fig. 2.4 (b) and as an average structure of an image reconstruction from electron microscopy (EM) from in vitro reconstituted clathrin triskelia in (c). Clathrin triskelia can also assemble as cubes or tetrahedra dependent on ionic strength and acidity [24, 25]. **Euler's polyhedron formula** states that the number of vertices (V) minus the edges (E) plus the facets (F) has to equal two for closed polyhedra [26]

$$V - E + F = 2\,. \tag{2.1}$$

Therefore, CCV as well as empty clathrin cages in vitro, can contain an arbitrary number of hexagons but have to contain precisely twelve pentagons. For example, the mini-coat consists of four, the hexagonal barrel of eight and the truncated icosahedron or soccer ball of 20 hexagons but all structures have twelve pentagons (compare Fig. 2.4 (b)). In the cell the situation of clathrin assembly is even more involved. Here, besides coated spherical vesicles also flat, hexagonal structures have been observed by means of EM [23] (Fig. 2.4 (d)). In addition, clathrin triskelia can also form huge hexagonal arrays, so-called clathrin plaques, of the size of several μm [27]. Recently, it has been suggested that plaques assist in cell adhesion [28], are platforms for signalling [29] that are mechanosensitive and a consequence of frustrated endocytosis [30].

Table 2.1 | Clathrin-mediated endocytosis by the numbers.

Quantity	Value	Reference
Clathrin coat bending rigidity	$\kappa_c = 300\,k_bT$	[31, 32]
Membrane bending rigidity	$\kappa_m = 10 - 25\,k_bT$	[33]
Binding energy per triskelion	$\kappa_{mon} = 5 - 30\,k_bT$	[31, 33, 34]
Triskelia in a closed coat	$N = 60 - 140$	[33]
Radius of CCV	$R = 30 - 350\,nm$	[31, 34]
Mean lifetime of CCV	$t_{life} = 30 - 120\,s$	[33]
Mean area of a triskelion	$A_{trisk} = 800\,nm^2$	[31]

Assembly of clathrin coats

Euler's theorem and its implications are also at the centre of the debate, addressing the question of how the assembly process of clathrin triskelia proceeds exactly. Two models have been proposed for clathrin coat assembly [35]. In the first one, the so-called **constant curvature model (CCM)**, the clathrin coat assembles with constant curvature, implying that pentagons, which are associated with curvature are incorporated from the beginning within the clathrin coat. In the second model, the so-called **constant area model (CAM)**, the clathrin coat first assembles flat to finite size before the clathrin coat starts to bend. Because of energetic arguments [32], as a well as for topological reasons [36] and computer simulations [37], the remodelling of the CAM was considered to be unlikely. However, a recent electron microscopy study found that the CAM likely describes the assembly pathway of CCV, by using the invagination angle as a surrogate of time [38]. In addition, the assembled clathrin structures are dynamic and exhibit turnover, which has been shown by fluorescence recovery after photobleaching (FRAP) experiments [39, 40, 38, 41].

In eukaryotic cells, actin is only involved in CME under enhanced membrane tension [42], whereas the force production by actin is required in yeast cells [43]. Here, the budding process has to work against the cell's turgor pressure such that an additional budding force has to be generated by the polymerisation of actin [44]. To sum up, the most important numbers concerning CME that are used later are shown in Table 2.1.

2.1.4 Viruses

Viruses are taken up by cells as they hijack cellular uptake pathways to infect host cells, replicate and spread viral infections. Viruses occur with a large variety in shape, which can affect the way of how they are taken up by cells. In this thesis we study the interplay between particle shape and uptake dynamics in chapter 3 and 4. Therefore, we discuss the structure, shape and life cycle of viruses in the following.

Structure and shape

Viruses are the biological entity that probably occurs most often in nature [45] with an estimated **number** of 10^{31} individuals, which are most abundantly phages, i.e. viruses that infect bacteria [46]. In total three main hypotheses have been suggested to explain the **origin of viruses**. In the primordial hypothesis viruses are agents of the precellular world that represent evolutionary intermediates. In the regression hypothesis viruses represent degenerated cells. Finally, in the escape hypothesis viruses developed from cellular genes and became an independent biological entity. To what extent these hypotheses explain the origin of viruses is still under debate and also hybrid hypotheses are discussed [47].

Surprisingly, viruses are entities that travel continuously between the realm of life and death, as they do not show any metabolism but are dependent on the infrastructure of host cells in order to replicate. Hence, they also rely on the endocytic mechanisms of cells in order to enter their hosts [48]. Virus particles either come with a single or double stranded, RNA or DNA genome that is surrounded by a protein shell - the capsid - composed of capsid proteins (capsomeres). The **typical sizes** of virus particles range from 20 nm - 1 μm. Examples are the Parvovirus (20 nm), the Poxvirus (300 nm) and giant viruses like the Pandoravirus or the Tupanvirus (1 μm) [45, 49].

Although Crick and Watson argued that viruses are typically spheres or rod-like particles, because their capsids are built from identical building blocks [50], they can also occur in many other shapes [45, 51]. In general there are three types of **virus shapes**. Around 50 % of all viruses (and most animal viruses) are of icosahedral (i.e. spherical) shape, 10 % are of helical shape and 40% are neither icosahedral nor helical and thus of complex shape [52]. Fig. 2.5 shows examples of various virus shapes. (a) Shows filamentous Ebola virus and (b) and (c) and show human papillomavirus (HPV) and Reovirus, both of icosahedral shape. (d) And (e) show tobacco mosaic virus (TMV) and vesicular stomatitis indiana virus (VSV), both having helical shape. (f) Shows human immunodeficiency virus (HIV) of conical shape, (g) shows Influenza of elliptical shape and (h) shows enterobacteria phage T4 of complex shape.

The viral life cycle: entry, transport, replication, assembly and spread

To replicate and spread, viruses have to cross several barriers in order to **enter** their future host [6]. First, viruses make contact with surface receptors distributed along the host's plasma membrane. The membrane consist of lipids, proteins and carbohydrates [61] and occur with an enormous variety and very specific functions [62]. Then several pathways exist for virus entry: First, viruses can trigger the endocytotic machinery of the cell, that is activated by the binding of surface receptors. The internalisation process is then driven by assembly-mediated uptake like CME, Macropinocytosis or

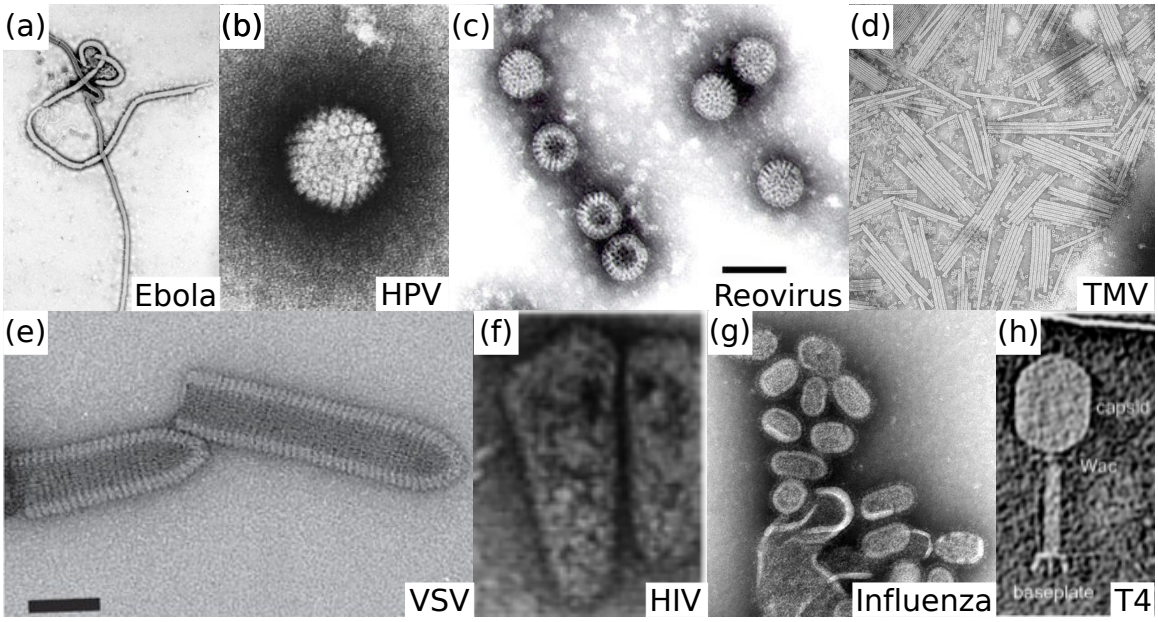

Figure 2.5 | Diversity of virus shapes. **(a)** Filamentous Ebola virus. **(b)** Icosahedral human papillomavirus (HPV). **(c)** Icosahedral Reovirus. **(d)** Rod-like tobacco mosaic virus (TMV). **(e)** Bullet-like vesicular stomatitis Indiana virus (VSV). **(f)** Cone-like human immunodeficiency virus (HIV). **(g)** Elliptical Influenza. **(h)** Complex enterobacteria phage T4. Figures taken and adapted in listed order [53, 54, 55, 56, 57, 58, 59, 60].

caveolae [63]. Secondly, viruses can use adhesion-mediated uptake either by successive receptor-ligand binding or membrane fusion of enveloped virus particles [64]. After crossing the plasma membrane the actin cortex represents another barrier that has to be crossed. Next, viruses can benefit from the cell's own **transport system** in order to get transported by molecular motors along cytoskeletal filaments (as microtubules) toward the nucleus or perinuclear region [65], as the cytoplasm is too crowded to be traversed simply by diffusion. The transport process is influenced by stochasticity, as the copy number of molecular motors is limited, the organisation of cytoskeletal filaments is irregular and molecular motors are affected by thermal noise. Thus, in the language of stochastic dynamics the transport toward the cell nucleus is a first-passage process or narrow-escape problem. Therefore, one typically considers the mean first arrival time of a particle to reach a small domain in a large boundary [66, 67].

In the **replication step** new genetic material as well as capsomeres are produced by the hijacked cell. In the assembly step those capsomeres assemble and form the new virus capsid to protect and enclose the genetic material. From a physical point of view this step is of special interest as the formation of the capsid is a paradigm for a **self-assembly** process in biology [68]. Interestingly, the process also runs autonomously in the test tube given favourable environmental conditions, which was first shown for TMV [69]. In the final step, viruses have to exit their host to **spread** the viral infection either by triggering exocytosis, budding from the membrane or by lysis [6].

2.2 Experimental methods

In this section, we discuss important experimental methods to study cellular uptake.

Electron microscopy (EM) is a structural imaging technique that provides ultrastructural resolution by illuminating samples with fast electrons and operates either in scanning or transmission mode. Before samples are examined they have to be fixated either by chemical treatment or in cryoEM by rapid cooling. In replica EM the sample is stained with heavy metals. After removal of the sample the produced metal replica is illuminated by electrons. EM can visualise membranes, clathrin assemblies during CME and also viruses or nanoparticles. However, EM only provides snapshots of often highly dynamic processes and thus lacks information in the time domain [70].

Atomic force microscopy (AFM) is a structural imaging technique that visualises by scanning the topology of a sample with a thin probe at the end of a cantilever [71]. Using high-speed AFM (HS-AFM) it is not only possible to probe the structure of clathrin lattices [72] but also to study their assembly kinetics [73]. AFM can also provide insight into the mechanical properties of cargo particles as e.g. viruses [71].

X-ray crystallography is another structural imaging technique that illuminates crystalline samples with X-rays to provide ultrastructural resolution. From the diffracted X-rays the image can be reconstructed [74]. Besides synchrotron radiation also X-ray free electron lasers can be used as X-ray sources [75]. X-ray crystallography is an important tool to get structural insight of clathrin molecules or virus shapes.

Fluorescnece microscopy (FM) techniques provide molecular specificity and temporal resolution [70]. In FM target molecules are fluorescently labeled, illuminated and the emitted light is detected. Thus, the resolution is limited by diffraction. **Spinning disc confocal microscopy** uses a set of pinholes, lenses and a rotating disc to illuminate the sample while decreasing phototoxicity [76]. **Total internal reflection fluorescence** (TIRF) microscopy uses the evanescent wave of a total internal reflection at an interface to illuminate the sample. As the evanescent wave decays exponentially, only molecules close to the interface can be illuminated, which is desirable to observe CME at the plasma membrane [76]. **Super-resolution** techniques are used to resolve structures beyond the diffraction limit by switching fluorescent labels on and off [70].

Correlative light and electron microscopy (CLEM) combines overlaid FM and EM imaging [77]. In CLEM samples are imaged by FM, fixated, stained and later imaged by EM. Thus, CLEM combines the spatial and temporal resolution of EM and FM.

Fluorescence recovery after photobleaching (FRAP) is a technique in which fluorescently labeled molecules are photo-bleached in a target domain using a focused laser beam. The fluorescence intensity gradually recovers, as fluorescently labeled molecules diffuse from the not-bleached environment into the target domain [78]. In the context of CME, FRAP experiments show that the assembly of clathrin lattices is a highly dynamic process [38].

Manipulating membrane tension is a convenient approach to change cellular uptake behaviour for which several methods have been developed. First, one can stretch the surface of the cell by micropipette aspiration [79]. Secondly, one can stretch the substrate on which the cell is cultured [80]. Thirdly, one can push onto the cell by a micro-manipulator [79] or fourthly, apply an osmotic shock in which the concentration of the cell surrounding solute is abruptly changed. As a consequence the cell either swells or shrinks, depending on the solute [42]. In addition, optical tweezers can be used to investigate the elastic properties of membranes. The basic principle is that small particles (adhered to the membrane) are trapped and manipulated by light induced forces [19].

Nanoparticles (NPs) are an adequate model system to probe cellular uptake, as they can be fabricated from different material (elastic, non-elastic), with diverse shapes (spherical, cube-like, rod-like) and sizes. The size of the NP plays an important role during uptake, as indicated by many studies [81]. Various experimental methods like EM, fluorescence correlation spectroscopy dynamics light scattering or AFM are applied to determine the NP size distribution [81]. NPs can acquire a protein corona of biomolecules (lipids, sugars or proteins), either intentionally by surface treatment or unintentionally, that coats the NP surface and changes the uptake behaviour [81].

2.3 Theoretical concepts

In the following we introduce to the basics of membrane biophysics, stochastic dynamics, self-assembly and growth, representing the most important concepts for cellular uptake.

2.3.1 Membrane biophysics

From the view point of physics the plasma membrane is a hyper-surface, i.e. a two-dimensional manifold in three-dimensional space [11]. It can be parametrised in every point by two vectors tangential to the surface and a normal vector that is oriented orthogonally to the tangential vectors. Next, one can define the two **principal**

curvatures [82]. Therefore, one defines planes for each particular direction that contain the normal vector. A circle to the plane that contacts the surface then defines the curvature for every direction. The minimum and maximum curvature correspond to the principal curvatures κ_1 and κ_2. The sum and product of the principal curvatures define the **mean curvature** $H = (\kappa_1 + \kappa_2)/2$ and the **Gaussian curvature** $K = \kappa_1 \cdot \kappa_2$. As an illustration, the mean and Gaussian curvature for a cylinder with Radius R are $H = 1/2R$, $K = 0$, for a sphere $H = 1/R$, $K = 1/R^2$ and for a saddle $H = 0$, $K = -1/R^2$. An important theorem in this context is the **Gauss-Bonnet theorem** that states that the Gaussian curvature K, integrated over a closed surface gives a topological invariant

$$\oint K \, \mathrm{d}A = 2\pi\chi \,. \tag{2.2}$$

The Euler characteristic χ can be either calculated by the number of handles G with $\chi = 2(1-G)$ or by means of **Euler's polyhedron formula** for topological equivalent polyhedra

$$\chi = V - E + F \,, \tag{2.3}$$

where V are the vertices, E the edges and F the facets. As an example, for a sphere $G = 0$, i.e. $\chi = 2$, which one also gets for the topological equivalent cube.

In order to model the shape of the plasma membrane during particle uptake, one usually balances the adhesion energy of the particle and the bending energy and tension energy of the membrane [83, 84, 85]. Then, the total energy can be written by the **Helfrich Hamiltonian** [86]

$$E = -\int_{A_{\mathrm{ad}}} W \mathrm{d}A + \int_{A_{\mathrm{mem}}} \left(2\kappa \left(H - C_0\right)^2 + \sigma + \bar{\kappa} K\right) \mathrm{d}A \,. \tag{2.4}$$

The first term represents the adhesion energy gain, where W is the adhesion energy. The second term is the membrane bending energy, where κ is the bending rigidity and C_0 a possible spontaneous curvature of the membrane and the third term is the energetic cost of increasing the membrane area, where σ is the membrane tension. The last term represents the membrane's tendency to undergo topological changes where $\bar{\kappa}$ is the Gaussian saddle-spay modulus. Considering particle uptake (Fig. 2.6), the first term has to be integrated only along the adhered part of the membrane A_{ad}, whereas the other terms have to be integrated over the adhered and the free parts of the membrane A_{mem}. Importantly, we here neglect the contribution of the Gaussian curvature, as it is constant as long as topological changes do not occur, according to the Gauss-Bonet theorem. Hence, this energy constant will not contribute in the following [3]. In addition, we mostly consider membranes with vanishing C_0, i.e. without asymmetric lipid or protein composition. Then the total energy reads

$$E = -\int_{A_{\mathrm{ad}}} W \mathrm{d}A + \int_{A_{\mathrm{mem}}} \left(2\kappa H^2 + \sigma\right) \mathrm{d}A \,. \tag{2.5}$$

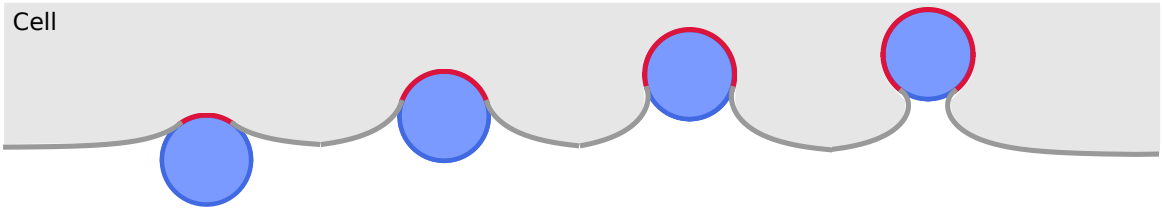

Figure 2.6 | Particle uptake ($\lambda/R = 1$). During uptake, the particle (blue) adheres to the membrane (red) whereas the free parts of the membrane (grey) get deformed.

The two membrane parameters, bending rigidity and membrane tension κ and σ, define a typical **length scale for uptake** $\lambda = \sqrt{\kappa/\sigma}$. Typical parameter values in the context of cellular uptake are $\kappa = 25\,\mathrm{k_B}T$ and $\sigma = 10^{-5} - 10^{-3}\,\mathrm{N/m}$ [87, 34], i.e. the uptake length scale is $\lambda = 10 - 100\,\mathrm{nm}$. By comparing the particle size R to the uptake length λ one can define several limits. In the limit of a loose membrane ($\lambda/R \gg 1$) it is energetically cheap to pull against membrane tension. Hence, the membrane adopts the shape of a saddle-shaped neck with vanishing mean curvature, i.e. zero bending energy. In the tense ($\lambda/R \ll 1$) regime it is very costly to pull against membrane tension, therefore the energy is dominated by far from the contribution of the membrane adhered to the particle that is taken up [87]. However, considering typical parameter values ($\lambda/R \approx 1$, compare Fig. 2.6), neither contribution dominates and the membrane shape is also determined by the contribution of the free parts. In this case one typically determines the shape that minimises the energy functional by solving the **Euler-Lagrange equations** (also referred to as shape equations) [83, 84, 88] and chapter 4.

2.3.2 Stochastic dynamics

Complex biological processes tend to be prone to fluctuations, as typically only few tens of small components constitute the system and the involved energy scales are comparable to thermal energy. A paradigm is self-assembly, where the copy number of constituents is small, the assembly process is discrete and thus, sensitive to fluctuations [89]. Fluctuations and noise, however, can change the dynamics of a system in a fundamental manner, which is why many biological problems have to be formulated in the language of stochastic dynamics. From this viewpoint, also receptor-mediated cellular uptake is a stochastic process, as the system size is small and ligand-receptor binding is a discrete process. In particular, it can be interpreted as a first passage time problem, i.e. the time when complete uptake is reached is a stochastic variable. In the following section, we briefly review some basics of stochastic dynamics. Mostly we follow the notation of Gardiner [90] and Iyer-Biswas and Zilman [91]. For more details also see the books of van Kampen [92], Honerkamp [93] and Risken [94] and the review articles of Bressloff and Newby [66].

Stochastic processes

We start by considering a time dependent stochastic process of a random variable X_t. A sequence of realisations of X_t is called **trajectory** $\{x_{t_1}, x_{t_2}, ...\}$ for the discrete times $\{t_1, t_2, ...\}$. A **probability distribution function** (PDF) assigns at each time t a probability $p(x)\mathrm{d}x$ to the realisation between x and $x + \mathrm{d}x$. Importantly, the PDF is normalised $\int p(x)\,\mathrm{d}x = 1$ and non-negative $p(x) \geq 0$. The joint PDF of n points $p_n(x_1, t_1; x_2, t_2; ...)$ describes the probability of a specific trajectory of the stochastic process. A **Markov process** is a stochastic process which is defined by the property that the future state is completely given by the present state. The past states are irrelevant. Then, the conditional probability for realisation x_n at time t_n is only determined by the realisation x_{n-1} at t_{n-1}

$$p_n(x_n, t_n|x_{n-1}, t_{n-1}; ...; x_1, t_1) = p_2(x_n, t_n|x_{n-1}, t_{n-1}). \tag{2.6}$$

Master equation

The last property of the Markov process implies that each n-point joint PDF can be written as a product of two-point joint PDFs. The contained first order behaviour in time gives rise to the Master equation (ME) (for a derivation see e.g. [93]). The ME describes jump processes, therefore, it is typically formulated as a discrete equation, in which the state variable x is called n, such that the PDF is denoted by $p_n(t)$. As a balance equation it states that the change of probability $\dot{p}_n(t)$ of state n equals all transitions from other states n' to that particular state n and vice versa. The transitions are given by the transition rates, denoted by $\omega_{nn'}$ from n' to n ($\omega_{n'n}$ from n to n') times the probability for being in state n', $p_{n'}(t)$ or in state n, $p_n(t)$, respectively

$$\dot{p}_n(t) = \sum_{n'} \left(\omega_{nn'}(t)p_{n'}(t) - \omega_{n'n}(t)p_n(t)\right) . \tag{2.7}$$

Given that there are only two transition rates between single states, i.e. one in forward $g_n = w_{nn-1}$ and one in backward direction $r_n = w_{nn+1}$, the ME simplifies to a **one-step Master equation**

$$\dot{p}_n(t) = g_{n-1}p_{n-1}(t) + r_{n+1}p_{n+1}(t) - (g_n + r_n)p_n(t)\,. \tag{2.8}$$

The Fokker-Planck equation

The Fokker-Planck equation (FPE) is a partial differential equation (PDE) describing via drift and diffusion processes the time evolution of a PDF. It can be deduced from a ME by means of a Kramers-Moyal-expansion in general. As it is a continuous equation we replace the state variable n again by a continuous variable x. For a one-step ME

with constant rates $g_n = \alpha$ and $r_n = \beta$, one can deduce the corresponding FPE by a simple Taylor expansion around x up to second order in space

$$\dot{p}(x,t) = \left(-\nu\partial_x + \frac{1}{2}D\partial_x^2\right) p(x,t)\,, \tag{2.9}$$

where $\nu = \alpha - \beta$ is the drift coefficient and $D = \alpha + \beta$ is the diffusion coefficient. The general form of a FPE for the two-point correlation $p_2(x,t|x',t')$ is given by

$$\partial_t p_2(x,t|x',t') = -\partial_x\left(\nu(x,t)p_2(x,t|x',t')\right) + \frac{1}{2}\partial_x^2\left(D(x,t)p_2(x,t|x',t')\right)\,, \tag{2.10}$$

where both the drift and the diffusion coefficient can depend on space x and time t.

First passage time problems

Cellular uptake can be interpreted as a first passage time problem. Therefore, a suitable approach is to consider the **backward Fokker-Planck equation** (BFPE) [90] that is equivalent to the FPE and given by

$$\partial_{t'} p_2(x,t|x',t') = -\nu(x',t')\partial_{x'}p_2(x,t|x',t') - \frac{1}{2}D(x',t')\partial_{x'}^2 p_2(x,t|x',t')\,. \tag{2.11}$$

We are interested in the first passage time that a stochastic process, subject to drift and diffusion that starts initially within $[a,b]$, leaves the interval (we here assume that at least one of the boundaries is absorbing). The probability that the process, initiated at $t = 0$, is still contained within the interval at time t is given by

$$G(t|x') = \int_a^b p_2(x,t|x',0)\mathrm{d}x\,. \tag{2.12}$$

Thus, $1 - G(t|x')$ is the probability that the process is not contained in the interval anymore, i.e. the probability per time with which the process reaches a boundary reads

$$f(t|x') = \frac{\partial}{\partial t}\left(1 - G(t|x')\right) = -\frac{\partial G(t|x')}{\partial t}\,. \tag{2.13}$$

The **mean first passage time** (MFPT) can then be calculated by

$$T(x') = \int_0^\infty f(t|x')\,t\,\mathrm{d}t = -\int_0^\infty \frac{\partial G(t|x')}{\partial t}\,t\,\mathrm{d}t = \int_0^\infty G(t|x')\mathrm{d}t\,, \tag{2.14}$$

using integration by parts and the boundary (initial) condition $G(\infty) = 0$ ($G(0) = 1$). Rewriting Eq. (2.11) as a function of t and integrating it over x, we find a PDE for G

$$\partial_t G(t|x') = \left(\nu(x')\partial_{x'} + \frac{1}{2}D(x')\partial_{x'}^2\right) G(t|x')\,. \tag{2.15}$$

By integrating Eq. (2.15) over t we can transform the PDE into an ordinary differential equation (ODE) of second order for the MFPT

$$-1 = \left(\nu(x')\partial_{x'} + \frac{1}{2}D(x')\partial_{x'}^2\right) T(x')\,. \tag{2.16}$$

Eq. (2.16) can be often solved analytically by integration.

Langevin equation

ME and FPE are descriptions of stochastic processes on the level of differential equations for PDFs. The Langevin equation (LE) uses the complementary approach and introduces stochasticity on the level of a single trajectory. Consider x as the position of a particle (or some generalised coordinate). Then, the time evolution reads

$$\dot{x} = A(x) + \sqrt{B(x)}\xi(t) \tag{2.17}$$

where $A(x)$ represents the determinist dynamics and $\xi(t)$ represents Gaussian white noise with $B(x)$ the noise amplitude. The noise is Gaussian and white, i.e. $\langle \xi(t) \rangle = 0$ and $\langle \xi(t)\xi(t') \rangle = \delta(t - t')$. One distinguishes the case where the noise amplitude is constant giving rise to **additive noise** and the case where it is a function of the state x, giving rise to **multiplicative noise**. Importantly, the LE approach (describing stochasticity on the level of single trajectories) and the FPE approach (describing stochasticity on the level of distributions) are equivalent. Hence, Eq. (2.17) can be related to a FPE. In the case of additive noise via $\nu = A$ and $D = B^2$. In the case of multiplicative noise Eq. (2.17) is not unambiguously defined. The two main interpretations are Itô, in which calculus follows special rules and the correspondence to the FPE is similar to the additive noise case and Stratonovich, in which calculus follows the usual rules but the correspondence to the FPE changes [90].

2.3.3 Assembly and aggregation

Self-assembly and structure formation occurs on all scales, bridging from the largest natural structures to the smallest, thinking of the formation of galaxies to the formation of molecules or proteins. At the heart of every self-assembling system lies the ability to create (spontaneously) order and structure from chaos. Life itself can be considered as a self-assembly process. Especially human life, encompassing a lifespan of around 10^9 s, in which a total of 10^{16} cells are formed [100], constantly relies on self-assembly. In the realm of biology there are many prominent examples on the nano- and micrometer scale where we find self-assembly of filaments, tubes, networks, rings and closed shells [101, 26, 89]. To name a few, the self-assembly of shell-like virus capsids from capsomeres that enclose the genetic material of viruses (see Fig. 2.7 (a)), the formation of cytoskeletal filaments, as e.g. microtubules from globular α- and β-tubulin dimers, providing a structural scaffold that organises the cell and enables cellular transport (see Fig. 2.7 (b)) or the self-assembly of clathrin cages from single triskelia (see Fig. 2.7 (c)). In addition, artificial assemblies of complex DNA structures by DNA folding [8] or the assembly of carbon nanotubes [102] shows that self-assembly can work in a hierarchical and templated manner, with enormous potential for applications. Especially the formation of clathrin coats on the plasma membrane is a fascinating example of

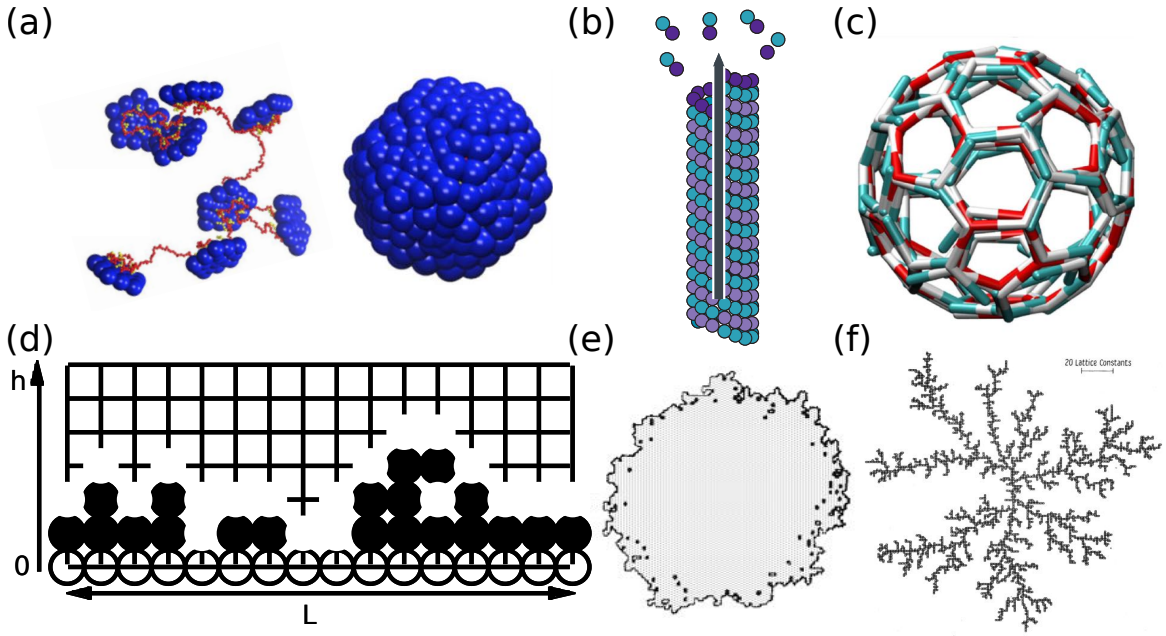

Figure 2.7 | Examples of self-assembly and physical models for aggregation. **(a)** Self-assembly of a shell-like virus capsid from capsomeres. **(b)** Self-assembly of a filamentous microtubule from α-tubulin (cyan) and β-tubulin (purple) dimers. **(c)** Self-assembly of a clathrin cage from single triskelia. **(d)** Eden model in one dimension. Each site of the lattice (of length L) with height $h(x)$ at position x, neighbouring an occupied site (filled black circle) can get occupied (open circle). **(e)** Eden cluster in two dimensions. **(f)** Cluster formed by diffusion-limited aggregation. Figures taken and adapted in listed order from [95, 96, 97, 98, 98, 99].

self-assembly. On the one hand, clathrin coats are rigid enough to bend the membrane and on the other hand, they are highly dynamic and can adapt their shape quickly.

Physical principles of self assembly

Despite the diversity in shape, size and structure of self-assembled systems, several common physical principles govern self-assembly:

- Self-assembly involves **many (typically identical) constituents**, representing a complex system with many degrees of freedom.
- Self-assembly requires that constituents **interact** with each other. In the realm of biological systems the interactions are mostly electrostatic (including van der Waals interactions and hydrogen bonds) or entropic. Importantly, interactions have to be intermediate both in range and strength, in order to ensure that the constituents find each other on a reasonable time scale and to give the system the chance to explore phase space and avoid kinetic trapping, i.e. malformed configurations and constituent depletion. Thus, reactions in self-assembly processes are reversible.

- Self-assembly involves **thermal fluctuations** that help the system to explore the accessible phase space.

- Self-assembly is an **energetic downhill process** that approaches equilibrium. However, one still has to prepare the right initial state in order to ensure assembly.

- Self-assembly can be driven by **entropy gain**. For example colloidal particles can self-assemble into crystal structures driven by a gain in entropy [103]. The reason is that by crystallisation each colloidal particle gains on average more space to roam compared to a random configuration.

Physical models of self assembly

As we are mostly interested in the self-assembly of clathrin lattices we consider self-assembly from the viewpoint of domain growth or aggregation, similar to growth of bacterial colonies or crystals. The first step during cluster growth is nucleation. **Classical nucleation theory** explains for example how fast a cluster is nucleated [104]. As an example we consider the nucleation of a circular cluster of radius R, area $A = \pi R^2$ and edge length $L = 2\pi R$ from single particles. We assume that the process is driven by the aggregation energy μ of the aggregating particles, covering A and counteracted by open binding sites at the edge L, giving rise to a line tension λ. The total energy reads $E = -\mu\pi R^2 + \lambda 2\pi R$, and the nucleation barrier is given by $\Delta E = \pi\lambda^2/\mu$. To traverse this energy barrier, thermal fluctuations are required. Assuming a Boltzmann distribution, the nucleation rate is supposed to be proportional to $\sim \exp(\Delta E/(k_{\mathrm{B}}T))$. Once the nucleus has formed, growth or aggregation begins. Aggregation is frequently studied by means of simple models [98]. For illustration we consider a substrate represented as a line in one dimension (see Fig. 2.7 (d)). Probably the simplest growth model is **random deposition** in which particles fall at random positions normal to the substrate and pile up if they hit either another particle or the substrate. An extension is **random deposition with diffusion** where particles can diffuse horizontally after hitting another particle. In **ballistic deposition** particles that fall from above stick to other particles as soon as they share one common edge. Finally, in the **Eden model** one considers the line and the space above as a two dimensional grid. Each site that is neighboured to a particle can get occupied by another particle with equal probability [105]. A sketch of the Eden model in one and two dimensions is shown in Fig. 2.7 (d) and (e). Interestingly, these different models can be described by the **Kadar-Parisi-Zhang equation** (KPZ), which is the simplest non-linear and most general equation of growth [106, 107]. It is a non-linear stochastic differential equation that describes an interface by a height function $h(x,t)$ at position x and time t. In one spatial dimension it can be formulated as

$$\frac{\partial h}{\partial t} = \nu \frac{\partial^2 h}{\partial x^2} + \frac{\lambda}{2}\left(\frac{\partial h}{\partial x}\right)^2 + \sqrt{D}\xi(x,t)\,, \tag{2.18}$$

where the first term describes the diffusivity of the surface with strength ν. The second term describes the interface growth with strength λ, dependent on the slope of the interface and the third term is the noise term of strength D and Gaussian white noise with $\langle \xi(x,t)\xi(x',t')\rangle = \delta(x-x')\delta(t-t)$. As already said, all four models are contained within this equation. $\nu = 0$, $\lambda = 0$, $D \neq 0$ describes random deposition, $\nu \neq 0$, $\lambda = 0$, $D \neq 0$ describes random deposition with diffusion and $\nu \neq 0$, $\lambda \neq 0$, $D \neq 0$ describes both ballistic deposition and the Eden model. Thus, based on the analysis of the KPZ equation the scaling behaviour of these models can be deduced. We apply the Eden model in chapter 7 to describe the growth of flat clathrin lattices.

So far we considered examples of **reaction-limited aggregation**, in which clusters typically grow limited by the reaction velocity and form compact clusters. The second limiting case is **diffusion-limited aggregation** (DLA) [99]. Here, clusters typically grow limited by the transport of new material by diffusion. In DLA one considers a particle that diffuses toward an already developed cluster. As soon as the particle touches a particle from the cluster it stays attached. Importantly, DLA clusters have fractal structure, see Fig. 2.7 (f). Examples for DLA clusters include the aggregation of smoke particles or electrolytic deposition [98]. One can introduce a sticking probability p in the DLA model with which particles in the proximity of the cluster attach to it. Interestingly, in the limit of $p \ll 1$ one recovers the Eden model.

A very general approach, based on the law of chemical mass action, is to formulate aggregation by a set of ODEs that describes all possible reactions how clusters can grow, merge and split. The **Smoluchowski coagulation-fragmentation equation** is an important equation in this context [108]. Here, one considers reversible reactions of clusters C consisting of r and s monomers of the form $C_r + C_s \rightleftharpoons C_{r+s}$. Then, the concentration c of C_r at time t is given by

$$\dot{c}_r(t) = \frac{1}{2}\sum_{s=1}^{r-1} W_{s,r-s} - \sum_{s=1}^{\infty} W_{r,s}\,, \tag{2.19}$$

with $W_{r,s} = a_{r,s}c_r c_s - b_{r,s}c_{r+s}$, where a (b) denotes the aggregation (fragmentation) rate. The rate for the monomer concentration is given by ignoring the first term in the equation above. If only monomer steps are possible one gets the **Becker-Döring equation** [108]. By neglecting the fragmentation rates and choosing appropriate aggregation rates it is possible to recover both reaction and diffusion-limited aggregation [109]. Besides ODE and PDE approaches also Monte Carlo techniques and particle based simulations are used to study self-assembly and growth as discussed in the next section.

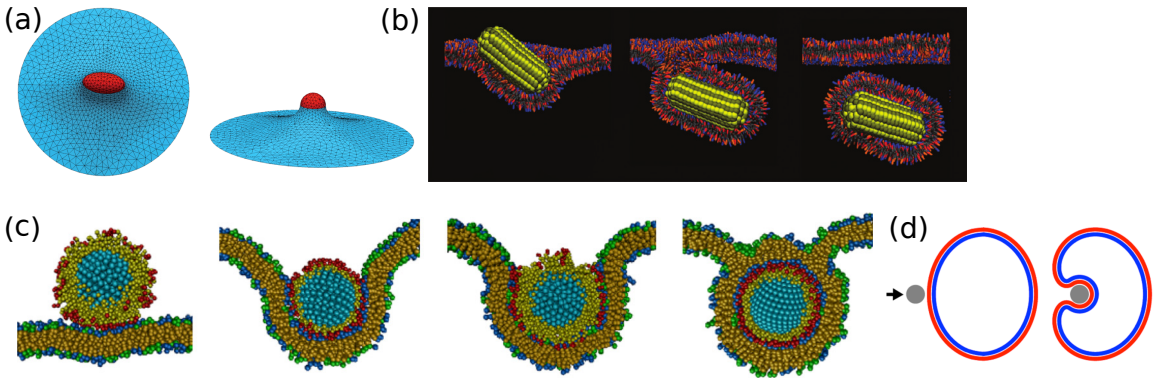

Figure 2.8 | Models for receptor-ligand-mediated uptake. **(a)** Continuous numerical calculation of the minimal energy shapes using triangulated surfaces (Surface Evolver [112]). **(b)** MD simulation of cellular uptake. **(c)** DPD simulations of cellular uptake. **(d)** Calculation of the minimal energy shape by solving the shape equations numerically. Figures taken and adapted in listed order from [113, 114, 115, 85].

2.4 Models for cellular uptake

In order to investigate cellular particle uptake driven either by receptor-ligand interactions or clathrin-mediated endocytosis (CME) different methods and modelling approaches are applied. Fig. 2.8 shows examples of various methods to study uptake mediated by receptor-ligand interactions, whereas Fig. 2.9 demonstrates examples of different methods to study uptake by CME. In the following, we give a short overview and list the most important methods, where we partially follow the review by Angioletti-Uberti [110]. For a review on mesoscale modelling methods see [111].

Analytical methods

Energetic considerations: The starting point of most models on cellular uptake is the energetic description of the membrane by the Helfrich Hamiltonian (cf. Eq. (2.4)) and either the receptor-ligand contacts or the aggregation energy due to the assembly of clathrin. By assuming that the membrane adopts the shape of a spherical cap, it is possible to calculate the phase digram for uptake analytically and infer the role of the single parameters. An impression of the used membrane shapes gives Fig. 2.9 (e) which shows a model of CME [31].

Numerical methods

Deterministic approaches: If one does not want to restrict to simple membrane shapes one can also calculate the shape of the membrane by numerically minimising the Helfrich Hamiltonian. One technique is to **triangulate the membrane** and then calculate the interaction energies between neighbouring triangles. Minimising the summed energy then gives the minimal energy shape. Fig. 2.8 (a) shows a triangulated

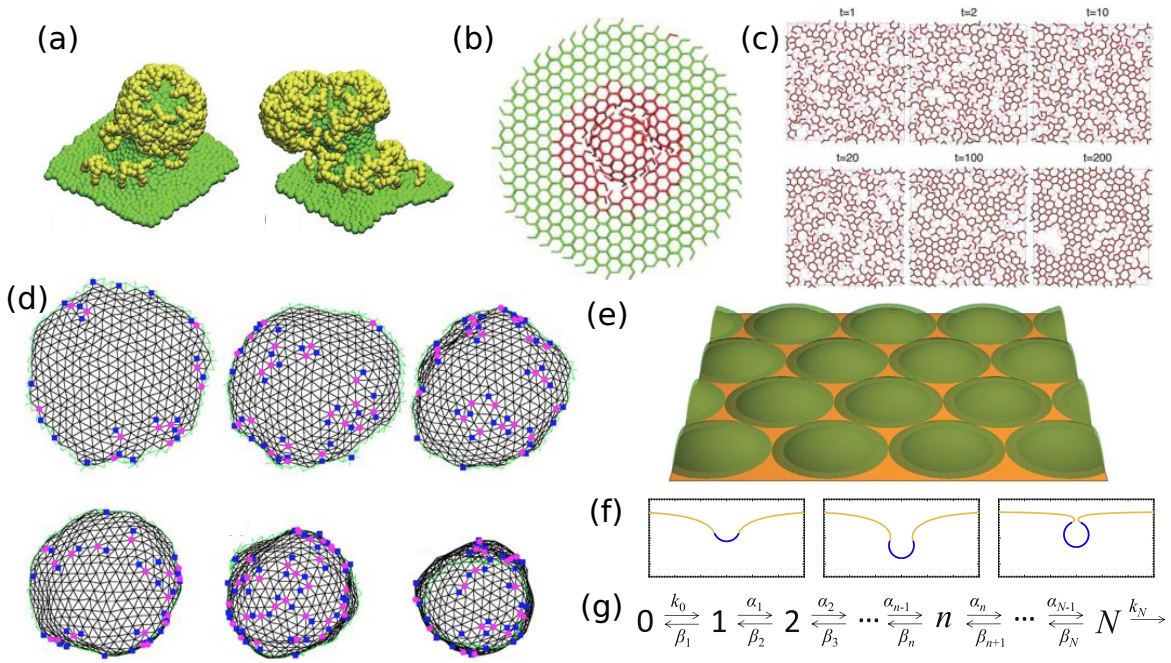

Figure 2.9 | Models for clathrin-mediated uptake. **(a)** Self-assembly of clathrin triskelia onto a fluctuating membrane. **(b)** MC simulation of a budding clathrin pit from a flat clathrin lattice. **(c)** BD simulation of assembling clathrin lattices. **(d)** MC simulation of a budding clathrin pit, embedded in a membrane (not shown). **(e)** Analytical calculation of the phase diagram of clathrin coats. **(f)** Numerical calculation of the minimal energy membrane shapes with clathrin coats. **(g)** KMC model of assembling clathrin coats. Figures taken and adapted in listed order from [116, 37, 117, 118, 31, 119, 120].

membrane during particle uptake [113] and Fig. 2.9 (d) shows a similar situation with clathrin coat [118]. Another method is to study cellular uptake for particles with rotational symmetry. In this case, it is possible to minimise the Helfrich Hamiltonian and to find an **ordinary differential equation** (ODE) of fourth order. Fig. 2.8 (d) shows particle uptake by a vesicle studied with this method [85] and Fig. 2.9 (f) shows minimal energy membrane shapes with clathrin coats [119].

Stochastic approaches: In **Monte Carlo** (MC) simulations, the typical procedure is to evolve the system by first randomly choosing a site of action. Then a simulation step of that site is either accepted or rejected according to the probability of the corresponding Boltzmann factor for that particular move. As an example, see the work of budding clathrin lattices in Fig. 2.9 (b) [37].
In **kinetic Monte Carlo** (KMC) simulations, the dynamics of the system is formulated by means of a ME, i.e. the system's phase space is discretised into states and the rates between these states are fixed. Therefore, KMC is a stochastic approach to cellular uptake. The ME is then solved by simulating single trajectories whose probability distribution function at given times solves the ME. The Gillespie algorithm

simulates the system on an event-based manner [121, 122], i.e. the rates with which the system jumps to the next state define both the probability with which this jump occurs as well as the time when the jump happens. For an example of how the assembly of clathrin pits at the cell membrane is studied by KMC simulations, see the work by Banerjee et al. [120] and a schematics of the underlying ME in Fig. 2.9 (g). We apply the Gillespie algorithm in chapter 3-5 to simulate particle uptake and explain the algorithm in Appendix A.2.

Particle based methods

In **molecular dynamics** (MD) simulations one either represents all atoms by particles or one summarises constituent atoms to a coarse-grained particle, to access longer time scales. The structure of the involved molecules can be deduced from either EM, X-ray crystallography or nuclear magnetic resonance spectroscopy of proteins and is accessible e.g. via the protein database [123]. Then Newton's equations of motions are formulated including all relevant molecular interactions (ionic bridges, hydrogen bonds, van der Waals interactions, etc.), integrated and the simulation temperature is controlled by a thermostat. The advantage of MD simulations is the detailed implementation of protein-protein interactions, but they come at high computational cost. Therefore, uptake processes can only be studied in a coarse-grained manner, on short timescales, see e.g. particle uptake studied with MD in Fig. 2.8 (b) [114].
In **multi-particle collision dynamics** (MPCD) simulations one represents the system by colloidal particles that represent e.g. proteins that are embedded in solvent particles, representing a coarse-grained version of the solvent. The system is evolved in time by subsequent application of streaming and collision steps in which interactions between particles, solvent and randomness are taken into account. MPCD correctly incorporates hydrodynamic interactions and thermal fluctuations, however, still coming at relatively high computational cost. As an example, see the work of assembling clathrin lattices at the cell membrane in Fig. 2.9 (a) [116].
In **dissipative particle dynamics** (DPD) simulations one represents the system by coarse-grained particles that represent the system's molecules. Then, a force balance is formulated for particle pairs including conservative, dissipative and random forces. Importantly, the random forces of the system are not independent. By integrating the force balance equation the system is evolved in time, see Fig. 2.8 (c) [115].
Finally, in **Brownian dynamics** (BD) simulations one represents the coarse-grained system by particles. Then, Newton's equations of motion are formulated for the system with effective interactions. By adding thermal noise to the equation one gets a Langevin equation that is then integrated in the over-damped limit to arrive at BD. As an example, see assembling clathrin lattices at the cell membrane in Fig. 2.9 (c) [117].

3 Stochastic dynamics of nanoparticle and virus uptake

Some of the results presented here have already been published in Physical Review Letters [124].

3.1 Introduction

Biological cells constantly communicate with their environment by relaying signals and material across their plasma membranes. In particular, cells routinely take up small particles with sizes in the order of $10 - 300\,\mathrm{nm}$. This process is usually driven by receptor-ligand interactions [14], such that the adhesion energy can overcome the energy required for membrane bending. It is also exploited by viruses that have to enter host cells for replication [61]. Due to the physical nature of this process, cells also take up artificial nanoparticles of various shapes [20], whose uptake may be either intentional or undesired, as in drug delivery [7] or in case of microplastics [4], respectively. Viruses come in many different shapes [45], but the most paradigmatic and most frequently occuring ones are spherical and cylindrical [50, 68].

In this chapter, we thus focus our discussion on spheres, cylinders and a combination of both, as shown in Fig. 3.1. It is generally believed that the spherical shape is optimal because it maximises the volume to surface ratio and confers high mechanical stability [125]. However, it is less clear which shapes are optimal in regard to interactions with the membrane [20]. Here we show that stochasticity might play an important role in this context.

Due to their small size, viruses are typically covered with only few tens of ligands for cell surface receptors [6, 126] and thus stochastic effects are expected to be relevant. For example, the icosahedral and medium-sized ($60 - 100\,\mathrm{nm}$) members of the family of Reoviruses have only 12 primary JAM-A-σ1 ligands on their surfaces [127]. While stochastic effects have been argued to be essential for the stability of small adhesion clusters [128, 129], particle uptake is usually studied analytically only with deterministic approaches. Stochastic effects are automatically included in computer simulations with thermostats [114, 130], but such approaches do not allow for a systematic study of the role of noise. Thus, we here analytically calculate the first passage times for particle uptake of various shapes and study the interplay between stochastic uptake dynamics and particle geometry.

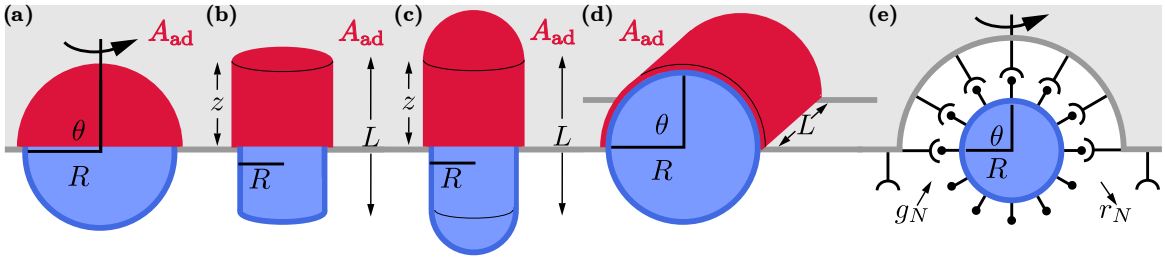

Figure 3.1 | Uptake of a particle of **(a)** spherical, **(b)** normal cylindrical (*rocket mode*), **(c)** spherocylindrical and **(d)** parallel cylindrical shape (*submarine mode*). In a deterministic model, the virus is homogeneously covered with ligands, adhering to the cell membrane along the adhesive area A_{ad}. **(e)** Stochastic uptake of a virus, whose surface presents discrete ligands. The virus particle binds (unbinds) with forward rate g_N (backward rate r_N) to receptors on the cell membrane.

3.2 Deterministic model

3.2.1 Energy balance of particle uptake

Deterministic approaches usually start by balancing the contributions from adhesion and bending. Because adhesion energy scales with the radius squared, while bending energy is independent of radius, a minimal size exists for particle uptake [83]. The most investigated aspect of receptor-mediated uptake is the role of particle shape [130, 131, 132]. More detailed approaches include the variational problem for finding minimal energy shapes [84, 85], the role of receptor diffusion towards the nanoparticle [133, 134], particle deformability [135, 136], the physics of the scission step [137] and the role of the cytoskeleton [126]. In order to develop a stochastic description, here we start with a minimal deterministic model, which we then extended to the stochastic case.

We assume that ligands to the cellular adhesive receptors are homogeneously distributed on the viral surface. The total free energy can be written as [86]

$$E_{\text{total}} = -\int_{A_{\text{ad}}} W \mathrm{d}A + \int_{A_{\text{mem}}} 2\kappa H^2 \mathrm{d}A + \sigma \Delta A \tag{3.1}$$

where W is the adhesion energy per area, κ is the bending rigidity, H is the mean curvature, σ is the membrane tension and ΔA the excess area due to the deformation (compared to the flat case). Typical parameter values are $W = 10^{-1}\,\mathrm{mJ/m^2}$, $\kappa = 25\,\mathrm{k_B T}$ and $\sigma = 10^{-4}\,\mathrm{N/m}$ [87, 34]. For example, a Reovirus has potentially 12 major and 60 minor ligands. With a binding energy of around $15\,\mathrm{k_B T}$ each, one estimates $W = 4.4 \cdot 10^{-2}\,\mathrm{mJ/m^2}$ for a homogeneous adhesion model.

The two membrane parameters define a typical length scale $\lambda = \sqrt{\kappa/\sigma} \approx 32\,\mathrm{nm}$. As shown schematically in Fig. 3.1, we consider a spherical or cylindrical particle of radius R adhering to the membrane. Then the bending energy in Eq. (3.1) has contributions

both from the adhering (A_{ad}) and free part ($A_{\mathrm{mem}} - A_{\mathrm{ad}}$) of the membrane. It has been previously shown [87, 34, 131, 138] that the contributions from the free part can be neglected in two special regimes. In the loose regime ($R \ll \lambda$), the free membrane can adopt the shape of a minimal surface and thus its bending contribution vanishes. In the tense regime ($R \gg \lambda$), the free part is essentially flat and the contribution from the adhered membrane is much larger than the one from the free membrane. To arrive at an analytical model, here we neglect the contributions from the free membrane also for the intermediate case.

Eq. (3.1) can now easily be analysed for the geometries sketched in Fig. 3.1, namely (a) for a sphere ($\circ$), (b) for a cylinder oriented normally to the membrane ($\perp$), (c) for a spherocylinder ($\cap$) and (d) for a cylinder oriented parallel to the membrane ($\parallel$). Although it has been shown in coarse-grained molecular dynamics simulations that spherocylinders might undergo a dynamical sequence of first lying down and then standing up [130], the two cylindrical modes considered here are the paradigmatic configurations encountered during wrapping [131]. In case of the normal cylinder, the top and bottom surfaces are neglected as they do not contribute to the uptake force. To keep our calculations as transparent as possible, we neglect them also for the parallel cylinder. In both cases, we neglect the bending energies at the kinked edges.

3.2.2 Uptake dynamics for various particle shapes

Spherical particle

First, we consider the case of a spherical particle. Thus, we model the virus particle as a sphere with radius R that adheres to the membrane with area $A_{\mathrm{ad}} = 2\pi R^2(1-\cos(\theta))$ and describe the progress of wrapping by the uptake angle θ (compare Fig. 3.1 (a)). The uptake is driven by the energetic gain of binding to membrane surface receptors and counteracted by the energetic cost for bending the membrane and increasing the membrane area. In this case the total free energy evaluates to

$$E^{\circ}_{\mathrm{total}}(\theta) = \Big(4\pi\kappa - W2\pi R^2 + \sigma\pi R^2(1-\cos(\theta))\Big)\,(1-\cos(\theta))\ . \tag{3.2}$$

As the virus particle adheres to the cell membrane, it experiences a force at the rim. This uptake force can be calculated by taking the variation of the total energy with respect to the position of the rim $s = R\theta$

$$\begin{aligned} F^{\circ}_{\mathrm{up}}(\theta) &= -\frac{\mathrm{d}E_{\mathrm{total}}(\theta)}{\mathrm{d}s} = -\frac{1}{R}\frac{\mathrm{d}E_{\mathrm{total}}(\theta)}{\mathrm{d}\theta} \\ &= \left(2\pi WR - \frac{4\pi\kappa}{R} - 2\sigma\pi R(1-\cos(\theta))\right)\sin(\theta), \end{aligned} \tag{3.3}$$

so we expect the highest force as half of the virus particle is enveloped (the same result is found for the normal force, which one obtains by varying the height of the particle

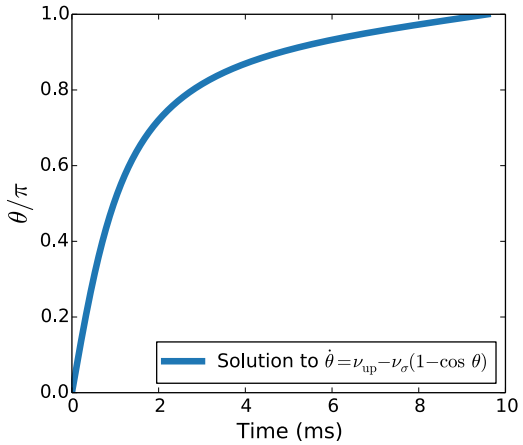

Figure 3.2 | The uptake angle as a function of time where the parameter values are $R = 90\,\mathrm{nm}$, $W = 4.4 \cdot 10^{-2}\,\mathrm{mJ/m^2}$, $\kappa = 25\,k_B T$ and $\sigma = 0.9 \cdot 10^{-5}\,\mathrm{N/m}$.

and which can be measured in AFM-experiments). We compute the deterministic uptake time T°_{det} by equating the force balance [85]

$$F^{\circ}_{\mathrm{up}} = F^{\circ}_{\mathrm{friction}}\,, \tag{3.4}$$

where the friction force $F^{\circ}_{\mathrm{friction}}$ depends on an effective membrane microviscosity of order $\eta = 1\,\mathrm{Pa\,s}$ times the change of the membrane-covered particle surface $L_{\mathrm{edge}}\dot{s}$

$$F^{\circ}_{\mathrm{friction}} = \eta L_{\mathrm{edge}}\dot{s} = \eta 2\pi R \sin(\theta) R\dot{\theta}. \tag{3.5}$$

The velocity $\dot{s} = R\dot{\theta}$ is the speed with which the edge (between the part of the membrane adhering to the virus particle and the free part) shifts and $L_{\mathrm{edge}} = 2\pi R\sin(\theta)$ is the length of this edge. From the force balance we get

$$\dot{\theta} = \nu_{\mathrm{w}} - \nu_{\kappa} - \nu_{\sigma}(1-\cos(\theta)) = \nu_{\mathrm{up}} - \nu_{\sigma}(1-\cos(\theta)), \tag{3.6}$$

where $\nu_{\mathrm{w}} = W/(R\eta)$ is the adhesion energy contribution, $\nu_{\kappa} = 2\kappa/(R^3\eta)$ the bending contribution, $\nu_{\sigma} = \sigma/(R\eta)$ the tension contribution and $\nu_{\mathrm{up}} = \nu_{\mathrm{w}} - \nu_{\kappa}$. Integrating Eq. (3.6) we find the uptake angle θ as a function of time

$$\theta(t) = 2\arctan\left(\frac{\sqrt{\nu_{\mathrm{up}}}\tan\left(\frac{1}{2}t\sqrt{\nu_{\mathrm{up}}^2 - 2\nu_{\mathrm{up}}\nu_{\sigma}}\right)}{\sqrt{\nu_{\mathrm{up}} - 2\nu_{\sigma}}}\right), \tag{3.7}$$

which is shown in Fig. 3.2. Using Eq. (3.7) we can calculate the deterministic uptake time by $\theta(T^{\circ}_{\mathrm{det}}) = \pi$, i.e.

$$T^{\circ}_{\mathrm{det}} = \frac{2\arctan\left(\sqrt{1-\frac{2\nu_{\sigma}}{\nu_{\mathrm{up}}}}\tan\left(\frac{\pi}{2}\right)\right)}{\nu_{\mathrm{up}}\sqrt{1-\frac{2\nu_{\sigma}}{\nu_{\mathrm{up}}}}} \approx \frac{\pi}{\nu_{\mathrm{up}}\sqrt{1-\frac{2\nu_{\sigma}}{\nu_{\mathrm{up}}}}}. \tag{3.8}$$

Note that it diverges for $\nu_{\mathrm{up}} = 2\nu_\sigma$, defining a critical radius

$$R_{\mathrm{crit}} = \sqrt{\frac{2\kappa}{W - 2\sigma}}\,, \tag{3.9}$$

below which uptake is not possible. In the limit of vanishing membrane tension ($\sigma = 0$), we recover the classical result $R_{\mathrm{crit}} = \sqrt{2\kappa/W}$ [83]. We note that our theory predicts normal uptake forces of around 10 pN, which agrees well with results from recent atomic force microscopy experiments [139, 140]. By differentiating T°_{det} with respect to R we find the radius, where the uptake time is minimal to be

$$R_* = \sqrt{\frac{4\kappa(W - \sigma) + 2\kappa\sqrt{W^2 - 2\sigma W + 4\sigma^2}}{W(W - 2\sigma)}}. \tag{3.10}$$

Cylindrical particle

The same calculations can be done for a normal ($\perp$) or parallel cylinder ($\parallel$). For the normal cylinder we get the total energy as a function of the height z

$$E^{\perp}_{\mathrm{total}}(z) = -W2\pi Rz + 2\kappa\frac{1}{4R^2}2\pi Rz + \sigma 2\pi Rz\,, \tag{3.11}$$

and by again balancing the uptake force by a friction force we find the dynamical equation

$$\dot{z}^{\perp}(\theta) = \nu^{\perp}_{\mathrm{up}}, \tag{3.12}$$

where $\nu^{\perp}_{\mathrm{up}} = \nu^{\perp}_{\mathrm{w}} - \nu^{\perp}_{\kappa} - \nu^{\perp}_{\sigma} = W/\eta - \kappa/(2R^2\eta) - \sigma/\eta$ for which the uptake time is given by $T^{\perp}_{\mathrm{det}} = L/\nu^{\perp}_{\mathrm{up}}$. Hence, the optimal radius (for which the uptake time is minimal), at the volume that is equal to the volume of a sphere with the same radius, is

$$R_* = \sqrt{\frac{3\kappa}{2(W - \sigma)}}. \tag{3.13}$$

The critical radius is given by

$$R^{\perp}_{\mathrm{crit}} = \sqrt{\frac{\kappa}{2(W - \sigma)}}. \tag{3.14}$$

For the parallel cylinder with length L we get the energy

$$E^{\parallel}_{\mathrm{total}}(\theta) = -W2\theta RL + 2\kappa\frac{1}{4R^2}2\theta RL + 2(\theta - \sin(\theta))RL\sigma, \tag{3.15}$$

and the dynamical equation

$$\dot{\theta}^{\parallel}(\theta) = \nu^{\parallel}_{\mathrm{up}} - \nu^{\parallel}_{\sigma}(1 - \cos(\theta)), \tag{3.16}$$

where $\nu_{\mathrm{up}}^{\parallel} = \nu_{\mathrm{w}}^{\parallel} - \nu_{\kappa}^{\parallel} = W/(\eta R) - \kappa/(2R^3\eta)$ and $\nu_{\sigma}^{\parallel} = \sigma/(R\eta)$, which has basically the same structure as for the sphere. Consequently, the uptake time is given by

$$T_{\mathrm{det}}^{\parallel} \approx \frac{\pi}{\nu_{\mathrm{up}}^{\parallel}\sqrt{1 - \frac{2\nu_{\sigma}^{\parallel}}{\nu_{\mathrm{up}}^{\parallel}}}}\,, \tag{3.17}$$

and the critical radius reads

$$R_{\mathrm{crit}}^{\parallel} = \sqrt{\frac{\kappa}{2W - 4\sigma}}\,. \tag{3.18}$$

Spherocylindrical particle

The spherocylindrical particle is considered to be oriented orthogonally to the cell membrane. The uptake time is then given by the sum of the uptake times for a sphere and a normal cylinder $T_{\mathrm{det}}^{\cap} = T_{\mathrm{det}}^{\circ} + T_{\mathrm{det}}^{\perp}$. However, to compare at equal volume, the radius and aspect ratio have to be adjusted. For the spherocylinder, a cylindrical part is inserted into a sphere and thus the radius of half-spheres and cylindrical part has to be reduced to maintain equal volume. We choose equal aspect ratio (3/2) as for the cylinders and thus have to reduce the radius to around 79% of the value of the sphere. Because of the modest value for the aspect ratio, the spherocylinder considered here is close to the spherical case.

3.2.3 Comparison of the different particle shapes

Fig. 3.3 (a) compares the resulting uptake times. For the normal and parallel cylinders, we take the same radius like for the sphere and adjust the aspect ratio. For the spherocylinder, we take the same aspect ratio like for the cylinders and adjust the radius. All four geometries show similar behaviour: a critical radius R_{crit} exists, below which uptake is not possible. The parallel cylinder has half the critical radius of the sphere because its mean curvature is half as large at equal radius. Moreover an optimal radius R_* exists, at which the uptake time is minimal. Interestingly, the critical and optimal values are very close to each other, and the cylindrical particles are taken up faster than the spherical ones. The spherocylinder is the slowest case, because at equal volumes, the aspect ratio is modest and the spherical part dominates. Fig. 3.3 (b) and (c) display the uptake time for a spherical particle as a function of W and R or σ, respectively, showing that a smaller adhesion energy has to be compensated by either larger radius or smaller membrane tension. Importantly, in the deterministic case certain parameter values do not lead to any uptake.

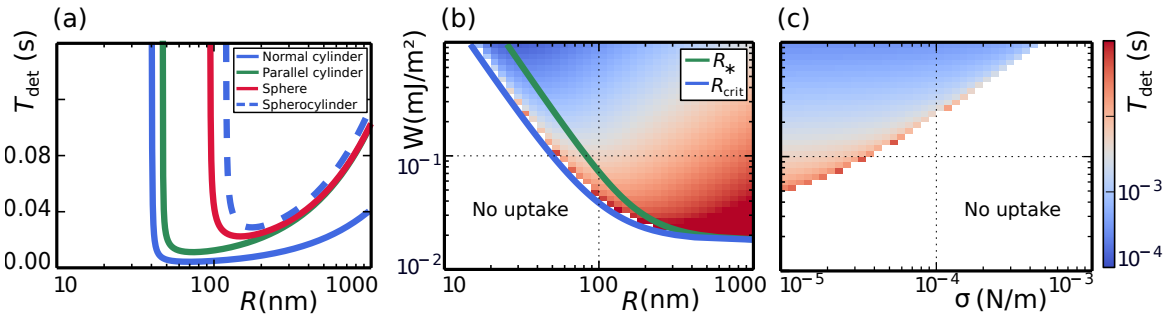

Figure 3.3 | Deterministic uptake dynamics. **(a)** Uptake times for sphere (red), normal cylinder (blue), spherocylinder (dashed blue) and parallel cylinder (green) as function of radius R at equal particle volume. **(b)**, **(c)** Uptake times for a sphere as a function of adhesion energy W and radius R or membrane tension σ, respectively. In **(b)** the critical (optimal) radius for spherical uptake is shown in blue (green). Parameter values (if not varied) are $R = 90\,\mathrm{nm}$, $W = 4.4 \cdot 10^{-2}\,\mathrm{mJ/m^2}$ and $\sigma = 0.9 \cdot 10^{-5}\,\mathrm{N/m}$.

3.3 Stochastic model

3.3.1 One-step master equation

We now turn to the stochastic variant of our uptake model (compare Fig. 3.1 (e)), i.e. we now explicitly model the stochastic dynamics of receptor-ligand binding since the system size is small and binding-unbinding is a discrete process. First, we consider a spherical particle (compare Fig. 3.1 (e)). We map the membrane covered area $A_{\mathrm{ad}} = A(\theta)$ onto the number of bound receptors $N(\theta)$ by $A(\theta)/A_{\mathrm{max}} = (N(\theta) - 1)/(N_{\mathrm{max}} - 1)$, yielding $N(\theta) = (N_{\mathrm{max}} - 1)(1 - \cos\theta)/2 + 1$, assuming axial symmetry. Here $A(\theta = 0)$ corresponds to the binding of a single receptor ($N = 1$) and $A(\theta = \pi)$ to the binding of $N = N_{\mathrm{max}}$ receptors. Using Eq. (3.6) we find the dynamical equation for $N(\theta)$

$$\dot{N} = \frac{\mathrm{d}N}{\mathrm{d}\theta}\frac{\mathrm{d}\theta}{\mathrm{d}t} = \left(\nu_{\mathrm{w}} - \nu_\kappa - \frac{2\nu_\sigma(N-1)}{N_{\mathrm{max}} - 1}\right) N_{\mathcal{E}}(N)\,, \tag{3.19}$$

where $N_{\mathcal{E}}(N) = \sqrt{(N-1)\left((N_{\mathrm{max}} - 1) - (N-1)\right)} = (N_{\mathrm{max}} - 1)\sin(\theta)/2$, is the number of ligands at the moving edge between the membrane covered and the uncovered part of the particle. The general form of the one-step master equation (ME) [92] for the number of receptor-ligand bonds is given by

$$\frac{\mathrm{d}p_N}{\mathrm{d}\tau} = g_{N-1}p_{N-1} + r_{N+1}p_{N+1} - (g_N + r_N)p_N, \tag{3.20}$$

where p_N is the probability of finding a virus particle bound by N ligands to the membrane, g_N is the forward and r_N the backward rate. From Eq. (3.19) we deduce g_N to be proportional to a kinetic parameter ν_{w} and the number of available receptor-ligand bonds $N_{\mathcal{E}}(N)$ located at the edge between membrane coated and uncoated virus

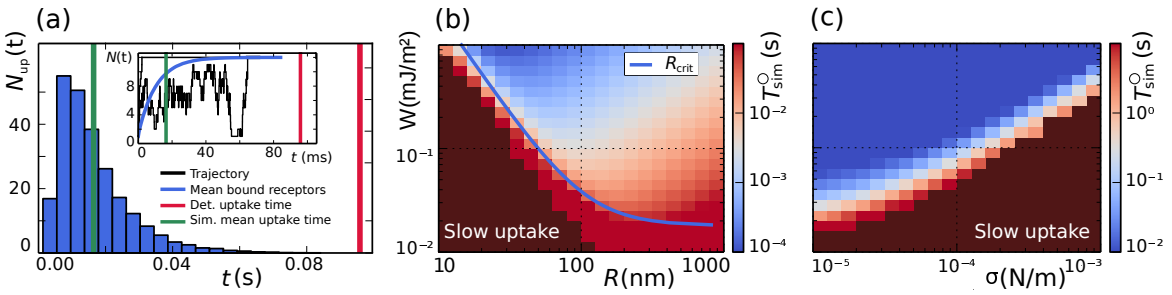

Figure 3.4 | Stochastic uptake dynamics for a spherical particle (Reovirus with $N_{\max} = 12$). **(a)** Histogram of uptake times with obtained mean $T^{\circ}_{\text{sim}} \approx 16\,\text{ms}$ (green line; standard deviation $\approx 11\,\text{ms}$) compared to the deterministic value $T^{\circ}_{\text{det}} \approx 96\,\text{ms}$ (red line). (Inset) Two example trajectories (black) of the number of bound receptors as a function of time and the mean number $\langle N^{\text{sim}} \rangle$ obtained from simulating the master equation (blue). **(b)**, **(c)** Mean uptake time T°_{sim} as a function of W and either R or σ. In the dark coloured region, uptake may still occur beyond the used simulation time. In **(b)** the blue line is the critical radius R_{crit} of the deterministic model. Parameter values as in Fig. 3.3.

particle. The backward rate follows in the same spirit and we obtain

$$g_N = \nu_{\text{w}} N_{\mathcal{E}}(N) \qquad r_N = \nu_{\kappa} N_{\mathcal{E}}(N) + 2\nu_{\sigma} N_{\mathcal{E}}(N) \frac{N-1}{N_{\max}-1}. \tag{3.21}$$

To complete the description we set $g_1 = \nu_{\text{w}} \sqrt{N_{\max}}$ as the first rate should be proportional to ν_{w} and the transition time from state $N = 1$ to state $N = 2$ should vanish for $N_{\max} \to \infty$. Thus, we obtain an artificial reflecting pure boundary at $N = 1$ (virus particles stay attached to the membrane) as $r_1 = 0$ and a natural absorbing boundary at $N = N_{\max}$ (uptake stops for full uptake) as $N_{\mathcal{E}}(N_{\max}) = 0$, i.e. $r_{N_{\max}} = 0$.

3.3.2 Simulation results

We first solved the ME numerically using the Gillespie algorithm [121] (compare Appendix A.2) and averaging over 10^4 trajectories. Fig. 3.4 (a) shows the resulting distribution of uptake times and the results for the number of bound receptors as a function of time (inset). Clearly, the mean uptake time is substantially smaller than the uptake time from the deterministic approach. Fig. 3.4 (b) and (c) display the simulated mean uptake times as a function of W and R or σ, respectively. Comparing to the deterministic approach (Fig. 3.3 (b) and (c)), we see that now uptake is possible for any parameter value, although it can be rather long in regions where the deterministic model does not allow for uptake. However, the parameter region with uptake in experimentally accessible uptake times is strongly increased and now also extends below the blue line indicating the critical radius R_{crit} of the deterministic model. This expansion of the parameter regime that allows the process to complete is also known from the stochastic dynamics of small adhesion clusters [128, 129].

3.4 Analytical treatment of the stochastic model

3.4.1 Various analytical approximations

In contrast to the previous section, where we solved the ME for the sphere numerically to get the mean uptake time we here study some special cases in which we can solve the ME by analytical approximations. In general, we cannot get analytical solutions because the one-step master equation incorporates non-linear rates [92].

Uptake time for vanishing backward rates

First, we consider a spherical particle in the case of vanishing backward rates ($r_N = 0\ \forall N$), corresponding to zero bending and tension energy. Then, we can analytically calculate the mean uptake time, which is given by the sum of the inverse rates

$$\begin{aligned} T &= \frac{1}{g_1} + \sum_{N=2}^{N_{\max}-1} \frac{1}{\nu_w} \frac{1}{\sqrt{(N-1)(N_{\max}-N)}} \\ &\to \frac{1}{\nu_{\mathrm{w}}} \int_0^1 \frac{\mathrm{d}x}{\sqrt{x(1-x)}} = \frac{\pi}{\nu_{\mathrm{w}}} = T^{\circ}_{\mathrm{det}}, \end{aligned} \tag{3.22}$$

where we used in the last step $N_{\max} \to \infty$, with $x = N/N_{\max}$. We see that the stochastic uptake time asymptotically approaches the deterministic uptake time for an increasing number of ligands $N_{\max}$. Importantly, for small systems with few ligands stochastic uptake is faster compared to deterministic uptake.

Probability distribution for vanishing backward rates

In the case of vanishing backward rates the probability distribution for all states P_N is known for non-repeating forward rates [141]

$$P_N(\tau) = \prod_{i=1}^{N-1} g_i \sum_{j=1}^{N} \left\{ \mathrm{e}^{-g_j \tau} \left(\prod_{\substack{k=1 \\ k \neq j}}^{N} \frac{1}{g_k - g_j} \right) \right\}. \tag{3.23}$$

However, for a spherical particle similar forward rates occur twice due to the spherical geometry, e.g. for $N_{\max} = 12$, $g_6 = g_7$. Therefore, we consider two terms of the sum in Eq. (3.23) in the limit where two rates become identical.

$$\lim_{g_b \to g_a} \left\{ \mathrm{e}^{-g_a \tau} \left(\prod_{\substack{k=1 \\ k \neq j}}^{N} \frac{1}{g_k - g_a} \right) + \mathrm{e}^{-g_b \tau} \left(\prod_{\substack{k=1 \\ k \neq j}}^{N} \frac{1}{g_k - g_b} \right) \right\} = \mathcal{A} \left\{ \tau - \left(\sum_{\substack{k=1 \\ k \neq j \\ g_a \neq g_b}}^{N} \frac{1}{g_k - g_b} \right) \right\},$$

with $\mathcal{A} = \mathrm{e}^{-g_a\tau}\left(\prod_{\substack{k=1\\k\neq j\\g_a\neq g_b}}^{N}\frac{1}{g_k-g_a}\right)$. For details see Appendix A.3. Using this result we find

$$P_N(\tau) = \prod_{i=1}^{N-1} g_i \sum_{j=1}^{N} \mathrm{e}^{-g_j\tau}\left(\prod_{\substack{k=1\\k\neq j\\g_k\neq g_j}}^{N}\frac{1}{g_k-g_j}\right)\left(\prod_{\substack{k=1\\k\neq j\\g_k=g_j}}^{N}\left(\frac{\tau}{2}-\sum_{\substack{l=1\\l\neq j\\g_l\neq g_j}}^{N}\frac{1}{2(g_l-g_j)}\right)\right), \tag{3.24}$$

where we divide by two in the inner brackets as we split the term among two addends of the sum. In Fig. 3.5 (a) $P_N(\tau)$ is plotted. We see how the system traverses the different binding states. Interestingly, not all states have once the highest occupation probability (cf. P_{10} and P_{11}).

Stochastic dynamics for vanishing membrane tension

To get analytical insight into the uptake dynamics we consider a spherical particle in the limit of vanishing tension ($\sigma = 0$) to simplify the description. As particle uptake relies on the binding and unbinding of a small number of ligand-receptor bonds, we are dealing with a stochastic process for which the mean uptake time is of large interest. Instead of treating the ME directly one can approximate the ME by a Fokker-Planck equation (FPE) to get analytical solutions. We begin by noting that the coefficients in the Kramers-Moyal-expansion are given by [92]

$$a^{(m)} = \sum_{N'=1}^{N_{\max}} (N'-N)^m W(N'|N), \tag{3.25}$$

where $W(N'|N)$ is the transition rate between state N' and state N. Therefore, the first two coefficients for a one-step ME read

$$\begin{aligned} a^{(1)} &= g_N - r_N = (\nu_\mathrm{w} - \nu_\kappa)N_\mathcal{E}(N) \\ a^{(2)} &= g_N + r_N = (\nu_\mathrm{w} + \nu_\kappa)N_\mathcal{E}(N). \end{aligned} \tag{3.26}$$

The corresponding Langevin equation with multiplicative noise reads

$$\dot{N} = (\nu_\mathrm{w} - \nu_\kappa)N_\mathcal{E}(N) + \sqrt{(\nu_\mathrm{w} + \nu_\kappa)N_\mathcal{E}(N)}\xi(t)\,, \tag{3.27}$$

where the noise $\xi(t)$ is assumed to be Gaussian with $\langle\xi(t)\rangle = 0$ and $\langle\xi(t)\xi(t')\rangle = \delta(t-t')$. The Langevin equation can be transformed into an equation for the growth angle θ using Itô's lemma [90]

$$\begin{aligned} \mathrm{d}\theta = &\left((\nu_\mathrm{w} - \nu_\kappa)N_\mathcal{E}(N)\frac{\mathrm{d}\theta}{\mathrm{d}N} + \frac{1}{2}(\nu_\mathrm{w} + \nu_\kappa)N_\mathcal{E}(N)\frac{\mathrm{d}^2\theta}{\mathrm{d}N^2}\right)\mathrm{d}t \\ &+ \sqrt{(\nu_\mathrm{w} + \nu_\kappa)N_\mathcal{E}(N)}\frac{\mathrm{d}\theta}{\mathrm{d}N}\mathrm{d}W(t). \end{aligned} \tag{3.28}$$

where $\mathrm{d}W$ is the infinitesimal increment of the Wiener process. Using

$$\theta = \arccos\left(1 - 2\frac{N-1}{N_{\max-1}}\right), \tag{3.29}$$

$$\frac{\mathrm{d}\theta}{\mathrm{d}N} = \frac{1}{\sqrt{(N-1)((N_{\max}-1)-(N-1))}} = \frac{1}{N_{\mathcal{E}}(N)} = \frac{2}{(N_{\max}-1)\sin(\theta)} \tag{3.30}$$

and

$$\frac{\mathrm{d}^2\theta}{\mathrm{d}N^2} = \frac{2N-1-N_{\max}}{2N_{\mathcal{E}}^3(N)} = -\frac{2\cos(\theta)}{(N_{\max}-1)\sin^2(\theta)} \tag{3.31}$$

we finally arrive at

$$\frac{\mathrm{d}\theta}{\mathrm{d}t} = \frac{\mathrm{d}\theta}{\mathrm{d}N}\frac{\mathrm{d}N}{\mathrm{d}t} = \nu_{\mathrm{up}} - D\frac{\cos(\theta)}{\sin(\theta)^2} + \sqrt{\frac{2D}{\sin(\theta)}}\xi(t), \tag{3.32}$$

where $\nu_{\mathrm{up}} = \nu_{\mathrm{w}} - \nu_{\kappa}$ and $D = (\nu_{\mathrm{w}} + \nu_{\kappa})/(N_{\max}-1)$. From Eq. (3.32) one can directly read the drift term (or the corresponding potential) of the corresponding FPE in angle space and its diffusion coefficient. Because for the spherical case this diffusion constant depends on the state variable θ, here we deal with multiplicative noise. We note that the same drift and diffusion terms can be obtained by directly transforming the FPE for $p(N,t)$ to a FPE for $p(\theta,t)$.

Uptake time distribution for additive noise

As Eq. (3.32) or the equivalent FPE include non-linear terms it cannot be treated analytically. Therefore, instead of treating the full Eq. (3.32), let us first consider the case with constant drift term and additive noise

$$\dot{\theta} = \nu_{\mathrm{up}} + \sqrt{2D}\xi(t). \tag{3.33}$$

The Langevin equation is equivalent to a FPE [91] describing the density $P(\theta,t|\theta_0,0) = P(\theta,t)$ to find the virus particle at a certain uptake angle θ at a specific time t given that it started with initial angle θ_0 at time 0

$$\partial_t P(\theta,t) = -\partial_\theta \nu_{\mathrm{up}} P(\theta,t) + \frac{1}{2}\partial_\theta^2 2DP(\theta,t)\,, \tag{3.34}$$

with the initial condition $P(\theta_0, t=0) = 0$, the absorbing boundary condition $P(\theta = \pi, t) = 0$ and the reflecting boundary condition, expressed by the flux j, $j(\theta=0,t) = \nu_{\mathrm{up}}P(\theta=0,t) - D\partial_\theta P(\theta=0,t) = \delta(t)$, which ensures that the particle stays attached to the membrane. In order to solve Eq. (3.34) we first perform a Laplace transformation, transforming the PDE to an ODE [142]

$$sP(\theta,s) = -\nu_{\mathrm{up}}\partial_\theta P(\theta,s) + D\partial_\theta^2 P(\theta,s)\,, \tag{3.35}$$

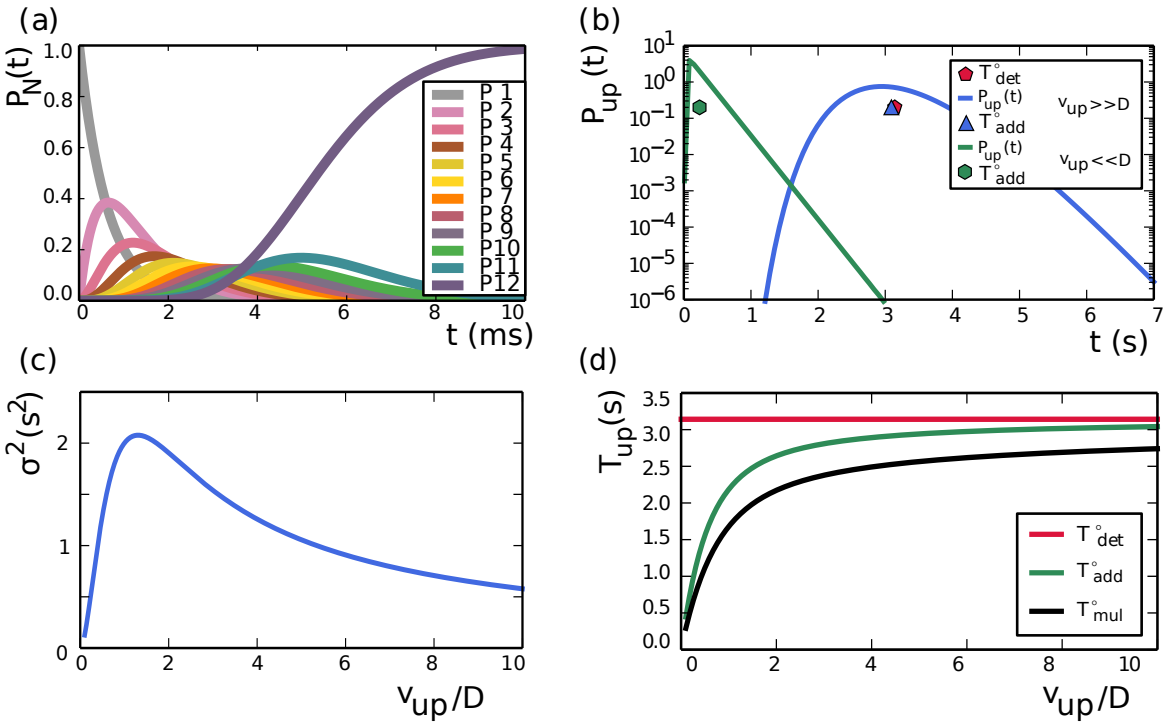

Figure 3.5 | Analytical and numerical solutions for limiting cases. **(a)** The probability distributions $P_N(\tau)$ as a function of time for vanishing backward rate. **(b)** Deterministic uptake time T°_{det} (red pentagon), numerically calculated uptake time distribution $P_{\text{up}}(t)$ and mean uptake time T°_{add} for $\nu_{\text{up}} \gg D$ (blue, triangle) and $\nu_{\text{up}} \ll D$ (green, hexagon) in the limit of vanishing membrane tension and additive noise. **(c)** $\sigma^{\circ\,2}_{\text{add}}$ as a function of ν_{up}/D (blue). **(d)** T°_{det} (red), T°_{add} (green) and T°_{mul} (black) as a function of ν_{up}/D.

which is solved by

$$P(\theta, s) = A \exp\left(\alpha_+(\theta - \pi)\right) + B \exp\left(\alpha_-(\theta - \pi)\right) , \tag{3.36}$$

with $\alpha_\pm = \nu_{\text{up}}/(2D) \pm 1/(2D)\sqrt{(\nu_{\text{up}})^2 + 4Ds}$. Using the reflecting boundary condition at $\theta = 0$ and the absorbing boundary condition at $\theta = \pi$ one can determine the constants A and B. The uptake time distribution P_{up} is then given by the flux through the boundary at $\theta = \pi$, i.e. by the derivative of the density $P(\theta, t)$ times D [142]

$$P_{\text{up}}(s) = -D\partial_\theta P(\theta = \pi, s) = \frac{\alpha_+ + \alpha_-}{\alpha_+ \mathrm{e}^{-\alpha_-\pi} - \alpha_- \mathrm{e}^{-\alpha_+\pi}}. \tag{3.37}$$

Next, the Laplace transformed uptake time distribution can be numerically back-transformed to find the uptake time distribution as a function of time [143]. The result is shown in Fig. 3.5 (b) and discussed in the following section.

Mean uptake time for additive noise

For Eq. (3.33) the mean uptake time can be obtained analytically by studying the mean first passage time problem using the backwards FPE [90, 142]. The mean uptake

time T°_{add} is then given by the following inhomogeneous differential equation [90]

$$\left(\nu_{\mathrm{up}}\partial_\theta + \frac{1}{2}2D\partial_\theta^2\right) T^{\circ}_{\mathrm{add}}(\theta) = -1, \tag{3.38}$$

which has to be solved under the absorbing boundary condition that the uptake process terminates as soon as the virus is completely taken up $T^{\circ}_{\mathrm{add}}(\theta = \pi) = 0$, and the reflecting boundary condition, implying that the particle stays attached to the membrane and cannot disappear, $\partial_\theta T^{\circ}_{\mathrm{add}}(\theta = 0) = 0$. The differential equation is solved by

$$T^{\circ}_{\mathrm{add}} = \frac{\pi}{\nu_{\mathrm{up}}} - \frac{D}{\nu_{\mathrm{up}}^2}\left(1 - \mathrm{e}^{-\frac{\pi\nu_{\mathrm{up}}}{D}}\right). \tag{3.39}$$

In the limit of weak fluctuations ($\nu_{\mathrm{up}} \gg D$) we get back the deterministic uptake time $\lim_{\nu_{\mathrm{up}}/D\to\infty} T^{\circ}_{\mathrm{add}} = \pi/\nu_{\mathrm{up}} = T_{\mathrm{det}}$. In the limit of strong fluctuations ($\nu_{\mathrm{up}} \ll D$) we find for complete uptake $\lim_{\nu_{\mathrm{up}}/D\to 0} T^{\circ}_{\mathrm{add}} = \pi^2/(2D)$. For intermediate fluctuations but negative uptake frequency ($-\nu_{\mathrm{up}} \gg D$) we find $\lim_{\nu_{\mathrm{up}}/D\to-\infty} T^{\circ}_{\mathrm{det}} = D/(\nu_{\mathrm{up}})^2 \mathrm{e}^{\frac{\pi|\nu_{\mathrm{up}}|}{D}}$. The ratio of the mean uptake time divided by the deterministic uptake time

$$\frac{T^{\circ}_{\mathrm{add}}}{T^{\circ}_{\mathrm{det}}} = 1 - \frac{1 - D\left(\mathrm{e}^{-\frac{\pi\nu_{\mathrm{up}}}{D}}\right)}{\nu_{\mathrm{up}}\pi}, \tag{3.40}$$

is always smaller than one. This behaviour is typical for a first passage time problem in a finite interval with these boundary conditions and also true for the a mean first passage time problem with linear drift see A.4.

In Fig. 3.5 (b) we show the numerically obtained inverse Laplace transform $P_{\mathrm{up}}(t)$ as a function of t and T°_{add} for different values of ν_{up}/D (blue and green) as well as T°_{det} (red). For weak fluctuations, the mean uptake time approaches the deterministic uptake time, which validates our approach. For strong fluctuations, the mean uptake time is decreased. Considering the distribution we observe that single trajectories can be slower compared to the deterministic uptake time although, on average, stochasticity decreases the uptake time. In addition, we observe that the uptake time distribution decreases exponentially fast (as it decreases linearly on the plotted logarithmic scale), implying that the mean of the distribution might be a good measure. We note that $\nu_{\mathrm{up}}/D = (1 - 2\nu_\kappa/(\nu_{\mathrm{w}} + \nu_\kappa)(N_{\mathrm{max}} - 1)$. Therefore, we expect large fluctuations ($\nu_{\mathrm{up}} \ll D$) for a small number of ligands and $\nu_{\mathrm{w}} \sim \nu_\kappa$.

Variance of the uptake time for additive noise

Next, we calculate the variance of the uptake time. For the second moment it holds [90]

$$-2T^{\circ}_{\mathrm{add}} = +\nu_{\mathrm{up}}\partial_\theta \left\langle t^2 \right\rangle(\theta) + \frac{1}{2}2D\partial_\theta^2 \left\langle t^2 \right\rangle(\theta) \tag{3.41}$$

which has to be solved under the same absorbing boundary condition $\langle t^2 \rangle (\theta = \pi) = 0$, and the reflecting boundary $\partial_\theta \langle t^2 \rangle (\theta = 0) = 0$ as before. The full solution for the second moment then reads for $\theta_0 = 0$

$$\left\langle t^2 \right\rangle = \left(D\mathrm{e}^{-\frac{2\pi\nu_{\mathrm{up}}}{D}} + \mathrm{e}^{-\frac{\pi\nu_{\mathrm{up}}}{D}}(D + 3\pi(\nu_{\mathrm{up}})^4) - 2D \right) \frac{2D}{(\nu_{\mathrm{up}})^4} + \frac{\pi^2}{(\nu_{\mathrm{up}})^2}. \tag{3.42}$$

The variance is then given by

$$\sigma^2 = \left\langle t^2 \right\rangle - (T^{\circ}_{\mathrm{add}})^2 =$$
$$\frac{D}{(\nu_{\mathrm{up}})^4}\left(D\mathrm{e}^{-\frac{2\pi\nu_{\mathrm{up}}}{D}} - 5D + 2\pi\nu_{\mathrm{up}} + 4\mathrm{e}^{-\frac{\pi\nu_{\mathrm{up}}}{D}}(D + \pi\nu_{\mathrm{up}}) \right). \tag{3.43}$$

In the limit of weak fluctuations compared to the uptake frequency ($\nu_{\mathrm{up}} \gg D$) we find a vanishing variance $\lim_{\nu_{\mathrm{up}}/D\to\infty} \sigma^2 = D/\nu_{\mathrm{up}}((2\pi)/(\nu_{\mathrm{up}})^2 - 5/(\nu_{\mathrm{up}})^3) \to 0$. In the limit of strong fluctuations compared to the uptake frequency ($\nu_{\mathrm{up}} \ll D$) we find also a vanishing variance $\lim_{\nu_{\mathrm{up}}/D\to 0} \sigma^2 = (2\pi^3)/(\nu_{\mathrm{up}})^2(D/\nu_{\mathrm{up}}) \to 0$, implying that for very strong fluctuations the combination of reflecting and absorbing boundary conditions drives the particle inwards. In Fig. 3.5 (c) we show σ^2 as a function of the ratio ν_{up}/D. Interestingly, the variance of uptake times has a maximum for intermediate fluctuations. As the variance of the distribution stays finite for all values of ν_{up}/D, we conclude that the mean uptake time represents the stochastic uptake dynamics well. In summary, these findings show that fluctuations accelerate the uptake process due to the fact that the uptake interval is limited.

Mean uptake time for multiplicative noise

Next, we consider Eq. (3.32) in the approximation of a constant drift term but multiplicative noise

$$\dot{\theta} = \nu_{\mathrm{up}} + \sqrt{\frac{2D}{\sin(\theta)}}\xi(t) \ . \tag{3.44}$$

Note that this equation corresponds to the case of a sphere, where we neglect the angle dependent drift term (as it is large only for the first and last step). Again, we compute the mean uptake time T°_{mul}, now with multiplicative noise, by the following inhomogeneous differential equation

$$\left(\nu_{\mathrm{up}}\partial_\theta + \frac{1}{2}\frac{2D}{\sin(\theta)}\partial_\theta^2 \right) T^{\circ}_{\mathrm{mul}}(\theta) = -1. \tag{3.45}$$

The equation can be solved with $A = \nu_{\mathrm{up}}$ and $B(\theta) = 2D/(\sin(\theta))$ by [90]

$$T^{\circ}_{\mathrm{mul}}(\theta_0 = 0) = 2\int_{\theta_0=0}^{\pi} \frac{\mathrm{d}y}{\Psi(y)} \int_0^y \mathrm{d}z \frac{\Psi(z)}{B},$$
$$\text{where } \ \Psi(x) = \exp\left\{ \int_0^x \mathrm{d}\theta \frac{2A(\theta)}{B(\theta)} \right\}, \tag{3.46}$$

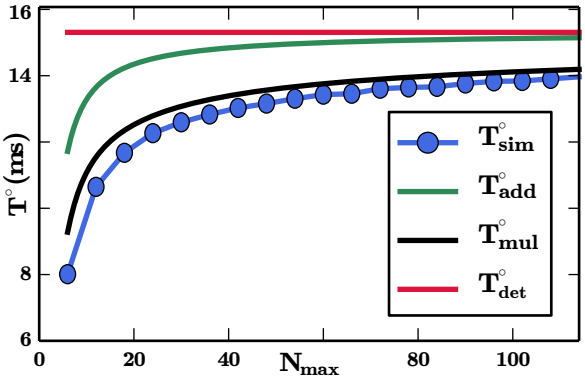

Figure 3.6 | Geometry-dependent fluctuation effects on the mean uptake time as a function of the maximum number of receptors. Shown are the analytical results for the deterministic case (red) for additive noise (green), for multiplicative noise (black) and the result from the direct simulation of the ME for the sphere, averaged over 10^4 trajectories (blue).

under the initial condition $\theta_0 = 0$, the absorbing boundary condition that the uptake process terminates as soon as the virus is completely taken up $T^{\circ}_{\mathrm{mul}}(\theta = \pi) = 0$, and the reflecting boundary condition that the virus particle stays attached to the membrane and cannot disappear $\partial_\theta T^{\circ}_{\mathrm{mul}}(\theta = 0) = 0$. We obtain

$$T^{\circ}_{\mathrm{mul}} = \frac{\pi}{\nu_{\mathrm{up}}} \left(1 - \mathrm{e}^{-\frac{\nu_{\mathrm{up}}}{D}} I_0\left(\frac{\nu_{\mathrm{up}}}{D}\right)\right), \tag{3.47}$$

where $I_0(z) = (1/\pi) \int_0^{\pi} \mathrm{d}\theta \mathrm{e}^{z\cos(\theta)}$ is the modified Bessel function of first kind. In the limit of weak fluctuations compared to the uptake frequency ($\nu_{\mathrm{up}} \gg D$) we get back the deterministic uptake time $\lim_{\nu_{\mathrm{up}}/D \to \infty} T^{\circ}_{\mathrm{mul}} = \pi/\nu_{\mathrm{up}} = T^{\circ}_{\mathrm{det}}$. In the limit of large fluctuations compared to the uptake frequency ($\nu_{\mathrm{up}} \ll D$) we find for complete uptake $\lim_{\nu_{\mathrm{up}}/D \to 0} T^{\circ}_{\mathrm{mul}} = \pi/D$, which is faster compared to the case of additive noise. The ratio of the stochastic uptake time divided by the deterministic uptake time

$$\frac{T^{\circ}_{\mathrm{mul}}}{T^{\circ}_{\mathrm{det}}} = 1 - \frac{\nu_{\mathrm{up}}}{\pi} \mathrm{e}^{-\frac{\nu_{\mathrm{up}}}{D}} I_0\left(\frac{\nu_{\mathrm{up}}}{D}\right), \tag{3.48}$$

is similar to the case with additive noise always smaller than one, implying that fluctuations accelerate the uptake process. Comparing Eq. (3.39) and Eq. (3.47) in Fig. 3.5 (d) as a function of ν_{up}/D we find that always $T^{\circ}_{\mathrm{mult}} < T^{\circ}_{\mathrm{add}} < T^{\circ}_{\mathrm{det}}$ holds, i.e. uptake in the case of multiplicative noise is faster than in the additive case, which in turn is faster than in the deterministic case. In addition, we compare Eq. (3.39) and Eq. (3.47) to our computer simulations of the ME as a function of the maximum number of receptors in Fig. 3.6. Although we neglected the additional drift term, our solution with multiplicative noise agrees well with the data.

Mean uptake times for cylindrical particles

Similar to the sphere, we here present the stochastic description for a normal and parallel cylindrical particle. For the normal cylinder we get

$$\dot{z}^{\perp}(\theta) = \nu_{\mathrm{up}}^{\perp} + \sqrt{2D^{\perp}}\xi(t), \tag{3.49}$$

where $D^{\perp} = (\nu_{\mathrm{w}}^{\perp} + \nu_{\kappa}^{\perp})L/(2(N_{\max}-1))$, and where we used that $N = (N_{\max}-1)z/L+1$. For the parallel cylinder we get qualitatively the same result

$$\dot{\theta}^{\parallel}(\theta) = \nu_{\mathrm{up}}^{\parallel} + \sqrt{2D^{\parallel}}\xi(t), \tag{3.50}$$

where $D^{\parallel} = (\nu_{\mathrm{w}}^{\parallel} + \nu_{\kappa}^{\parallel})\pi/(2(N_{\max}-1))$, and where we used that $N = (N_{\max}-1)\theta/\pi+1$. Consequently, we can interpret additive noise as the noise for the cylindrical system (compare Eq. (3.33)). As the structure of Eq. (3.50) is identical to Eq. (3.33) we find the mean uptake time for the parallel cylinder similar to Eq. (3.39)

$$T_{\mathrm{add}}^{\parallel} = \frac{\pi}{\nu_{\mathrm{up}}^{\parallel}} - \frac{D^{\parallel}}{{\nu_{\mathrm{up}}^{\parallel}}^2}\left(1 - \mathrm{e}^{-\frac{\pi\nu_{\mathrm{up}}^{\parallel}}{D^{\parallel}}}\right). \tag{3.51}$$

In the limit of weak fluctuations one again recovers the deterministic uptake time, while for large fluctuations one finds $T_{\mathrm{add}}^{\parallel} \approx \pi^2/(2D^{\parallel})$. We note that for the parallel cylinder it is also possible to compute the uptake time directly from the ME [90]

$$T_{\mathrm{ana}}^{\parallel} = \frac{1}{\nu_{\mathrm{w}}^{\parallel}} \sum_{y=1}^{N_{\max}} \left\{ \prod_{z=2}^{y} \frac{\nu_{\kappa}^{\parallel}}{\nu_{\mathrm{w}}^{\parallel}} \right\} \sum_{z=1}^{y} \left\{ \prod_{x=2}^{z} \frac{\nu_{\mathrm{w}}^{\parallel}}{\nu_{\kappa}^{\parallel}} \right\} \tag{3.52}$$

$$= \frac{\pi}{\nu_{\mathrm{up}}^{\parallel}} - \frac{\pi}{{\nu_{\mathrm{up}}^{\parallel}}^2} \frac{\nu_{\kappa}^{\parallel}}{N_{\max}} \left\{ 1 - \left(\frac{\nu_{\kappa}^{\parallel}}{\nu_{\mathrm{w}}^{\parallel}} \right)^{N_{\max}} \right\}. \tag{3.53}$$

Whereas Eq. (3.51) is an approximation to the mean uptake time and is supposed to hold only for large N Eq. (3.53) is exact.

3.4.2 Effective potentials

To characterise the uptake process one can also consider the forward (backward) rates, the effective potential $\mathcal{V}(\theta) = -\int_0^{\theta} (g_N(\theta) - r_N(\theta))$ and the diffusion coefficient $\mathcal{D}(\theta) = g_N + r_N$, which are shown in Fig. 3.7 (a) and (b) for vanishing membrane tension ($\sigma = 0$) and in (c) and (d) for non-vanishing membrane tension ($\sigma = 0.9 \cdot 10^{-5}\,\mathrm{N/m}$). For the parallel cylinder with rates $g_N = \nu_{\mathrm{w}}^{\parallel} N_{\max}/\pi$ and $g_N = (\nu_{\kappa}^{\parallel} + \nu_{\sigma}^{\parallel}(1-\cos\theta))N_{\max}/\pi$ we find

$$\mathcal{V}(\theta)^{\parallel} = -\int_0^{\theta} \left(\nu_{\mathrm{w}}^{\parallel} - \nu_{\kappa}^{\parallel} - \nu_{\sigma}^{\parallel}(1-\cos\theta') \right) \frac{N_{\max}}{\pi} \mathrm{d}\theta'$$

$$= -\left(\nu_{\mathrm{up}}^{\parallel} + \nu_{\sigma}^{\parallel}(\theta + \sin\theta) \right) \frac{N_{\max}}{\pi}\theta, \tag{3.54}$$

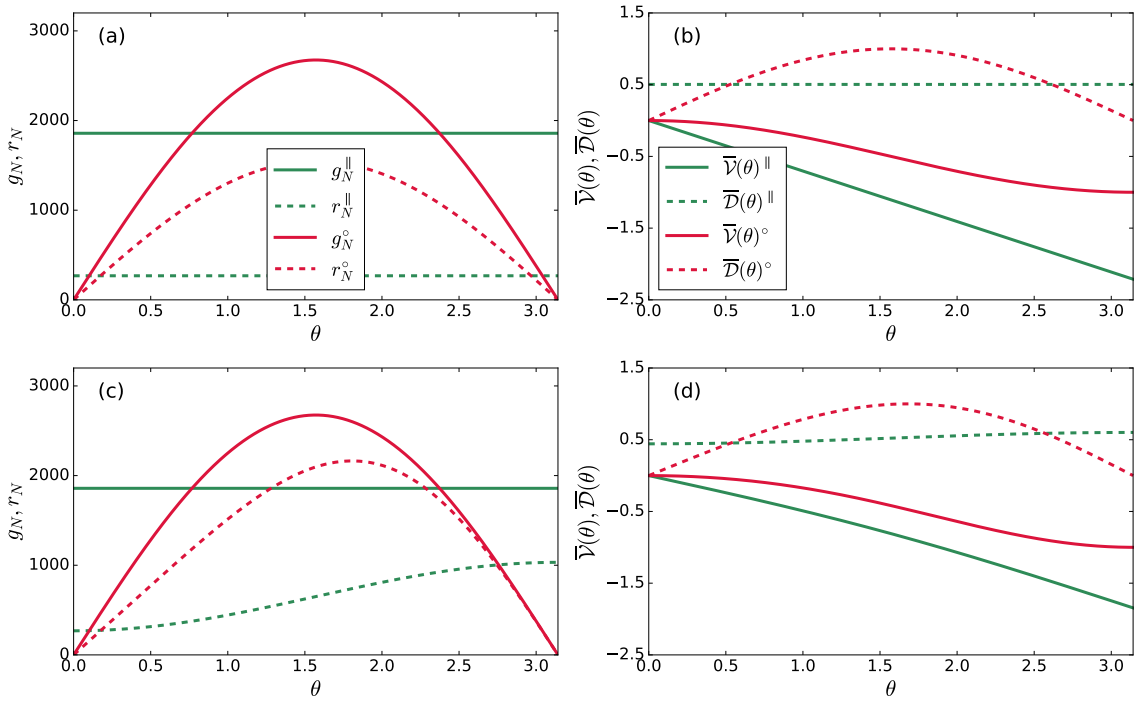

Figure 3.7 | (a) The forward (backward) rate g_N (r_N) plotted as a solid (dashed) line for the cylindrical geometry (green) and spherical geometry (red) for vanishing membrane tension ($\sigma = 0$). **(b)** The effective potential $\mathcal{V}(\theta)$ (diffusion constant $\mathcal{D}(\theta)$) plotted as a solid (dashed) line for the cylindrical geometry (green) and the spherical geometry (red) for vanishing membrane tension ($\sigma = 0$). The values are normalised to the minimal (maximal) value of the spherical effective potential (diffusion constant), which is marked by $\overline{\mathcal{V}}$ and $\overline{\mathcal{D}}$, respectively. **(c)** and **(d)** show the same as **(a)** and **(b)** but for non-vanishing membrane tension ($\sigma = 0.9 \cdot 10^{-5}\,\mathrm{N/m}$).

and for the sphere with rates $g_N = \nu_\mathrm{w}(N_\mathrm{max} - 1)\sin(\theta)/2$ and $r_N = (\nu_\kappa + \nu_\sigma(1 - \cos\theta))(N_\mathrm{max} - 1)\sin(\theta)/2$

$$\begin{aligned}\mathcal{V}^\circ &= -\int_0^\theta \left(\nu_\mathrm{w} - \nu_\kappa - \nu_\sigma(1-\cos\theta')\right)\frac{N_\mathrm{max}-1}{2}\sin(\theta')\mathrm{d}\theta' \\ &= \left(\nu_\mathrm{up} + \frac{\nu_\sigma}{2}(1-\cos\theta)\right)\left(\frac{N_\mathrm{max}-1}{2}\right)(\cos(\theta-1))\,. \end{aligned} \tag{3.55}$$

In the case of vanishing membrane tension the forward (backward) rate are changing with the angle for the sphere whereas these rates are constant for the parallel cylinder (cf. Fig.3.7 (a)). Fig.3.7 (b) shows that the effective potential for the sphere and the cylinder are monotonously decreasing; the diffusion coefficient for the sphere exhibits a maximum at $\theta = \pi/2$ while the one for the cylinder is constant. Adding membrane tension introduces an asymmetric (non-constant) backward rate (cf. Fig. 3.7 (c)) and an asymmetric (non-constant) diffusion coefficient for the sphere (cylinder), cf. Fig. 3.7 (d). We conclude that the differences between the cases without and with membrane tension is relatively small.

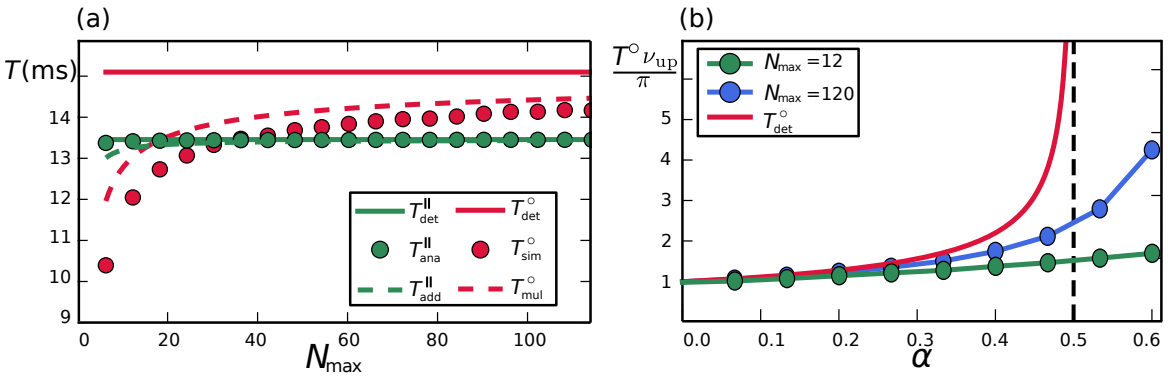

Figure 3.8 | (a) Geometry-dependent mean uptake times for spheres (red) and parallel cylinders (green) as a function of the maximum number of receptors. Shown are the analytical results for the deterministic case (solid) and for multiplicative (additive) noise corresponding to the spherical (cylindrical) geometry (dashed). The result from the simulations of the master equation is shown for sphere (cylinder) as symbols. **(b)** The case with membrane tension can be treated with computer simulations. Shown are the mean uptake times for a sphere as a function of the dimensionless parameter $\alpha = \nu_\sigma/\nu_{\mathrm{up}}$ (by varying σ) for two different numbers of receptors and the deterministic case (diverging at $\alpha = 1/2$).

3.5 Interplay between stochastic dynamics and particle geometry

We next discuss the interplay between shape and stochastic dynamics in detail and compare the two cylindrical cases to the spherical case. In the last section we have seen that for the parallel cylinder one obtains additive noise because the length of the moving contact line is constant, whereas for the sphere one obtains multiplicative noise because here the length of the moving contact line varies with angle. The different quality of the noise suggests that the uptake dynamics changes in a fundamental manner in the different geometries.

We now consider a particle with $R = 180\,\mathrm{nm}$, i.e. in the region of Fig. 3.3 (a) where the deterministic uptake times of sphere and parallel cylinder are similar. Fig. 3.8 (a) shows the mean uptake times for different geometries at equal volume as a function of the number of receptors. For the parallel cylinder we use Eq. (3.53) to calculate the mean uptake time $T^{\parallel}_{\mathrm{ana}}$ directly [90]. The agreement between simulations (symbols) and analytical results (lines) is very good for cylinders and rather good for spheres. For small number of receptors, i.e. strong fluctuations, the uptake of a sphere is faster than the one of a cylinder. Hence, for both geometries the mean uptake time is always smaller than the deterministic one. In general, fluctuations in small systems combined with a reflecting boundary should always decrease the mean first passage time, since the stochastic process profits from the presence of the boundary, while the deterministic process does not. We conclude that uptake of spherical particles dynamically benefits from the noise.

While membrane tension could not be treated analytically, it can be included in the simulations, and we get the same results, i.e. the uptake times are reduced by increasing stochasticity. Fig. 3.8 (b) shows the mean uptake times as a function of the dimensionless parameter $\alpha = \nu_\sigma/\nu_{\mathrm{up}}$ for different N_{max} and $R = 90\,\mathrm{nm}$. While stochasticity is most important for small numbers of receptors, nevertheless even for substantial numbers of order hundred receptors the stochastic effects survive.

3.6 Conclusion

Although the cellular uptake of viruses and nanoparticles, mediated by ligand-receptor binding, has been already studied by various methods [84, 133, 114, 131], we here addressed a relatively unexplored aspect, namely the stochastic dynamics during uptake and in particular the interplay between stochasticity and particle geometry. Rather than investigating a complicated model that is rich in detail but also comes with many parameters, here we chose a physical (i.e. reductionist) approach to carve out the intriguing interplay between particle shape and stochastic dynamics. Virus particles come with a huge variety in shape [45], and although the spherical shape has both maximal volume to surface ratio and provides high stability [125], it is not clear which shape is best when it comes to cellular uptake. By investigating the uptake dynamics our results suggest yet another advantage for viruses to be spherical.

We first considered a simple deterministic model in which particle uptake is described by the physical competition between particle adhesion and membrane elasticity. Here, the typical situation is that spherical particles are taken up slower compared to cylindrical particles, both in normal and parallel orientation relative to the cell membrane. We then included stochasticity in our model and find both by computer simulations and analytical calculations that the situation can reverse. Now spherical particles can get taken up faster compared to parallel cylindrical particles. This is due to the fact that the particle shape qualitatively influences the way of how the dynamics is affected by fluctuations. Cylindrical particles experience additive noise, whereas spherical particles are affected by multiplicative noise. In addition, our results show that stochasticity also decreases the uptake time and increases the parameter space where uptake is possible. We note that our results are dependent on the combination of reflecting and absorbing boundary conditions. However, by incorporating another rate in the model (e.g. to include that viruses or nanoparticles first have to make contact before the uptake begins), one should not change the fact that stochastic uptake is faster than deterministic uptake.

During the course of this chapter, we neglected several aspects that contribute to the dynamics of virus and nanoparticle uptake. In the following we discuss some of these aspects by considering the timescale of uptake. In our model this timescale is given

by the microviscosity of the cell membrane [85]. This implicitly assumes that either receptor concentration is high at the cell membrane or that receptors diffuse fast toward the site of endocytosis. However, in a more complete model this might contribute another timescale to the uptake dynamics, in particular when receptor diffusion is slow or when the receptor concentration is low [114]. Furthermore, we neglected the role of the actin cortex underlying the cell membrane and the formation of the membrane neck just before the endocytosed particle pinches off the cell membrane. Both steps represent additional barriers that might contribute additional timescales to the uptake time. In addition, we neglected the contributions of the bending and tension energies of the free membrane parts, as we argued that these contributions should be small compared to the bending and tension energies of the membrane adhered to the virus or nanoparticle. Hence, rather than calculating an exact biological uptake time, we here focussed on the interplay between particle geometry and stochastic dynamics during particle uptake. We note that we consider more complex variants of our model in chapter 4 and 5, where we study the effect of the free membrane and the effect of substrate-attachment on the uptake dynamics.

To conclude, we found that the uptake of spherical particles profits from the presence of noise, with obvious important implications for both viruses and drug delivery. Similar effects arising from the interplay between stochastic dynamics and geometry might also exist for other biologically relevant first passage problems, e.g. phagocytosis [144], the closure of transient pores on spherical vesicles [145] or the fusion of tissue over circular holes [146].

4 Dynamics of particle uptake at cell membranes

For the results presented in this chapter a preprint exists that will be submitted to Physical Review E [147].

4.1 Introduction

The plasma membrane presents a physical barrier and at the same time a communication interface that separates and connects the cell's interior with its environment [3]. Therefore, the ability of cells to exchange material and information across their plasma membrane is of major importance for cellular fate [20]. On the one hand it is vital for nutrient uptake and signal transduction [14], on the other hand pathogens like viruses usurp cellular uptake strategies to enter and hijack host cells in order to spread lethal infections [6]. In addition, particle uptake at cell membranes can be of practical interest in the context of drug-delivery [7] or come as a side effect in the context of microplastics [4].

In receptor-mediated endocytosis particles with sizes of around $10-300\,\mathrm{nm}$ are taken up because the energy gain upon particle binding to cell surface receptors overcomes the bending and tension energy of the membrane [133, 20], see Fig. 4.1. Although being small, cargo particles can come with a huge diversity in shape, especially when thinking of viruses. The most frequent virus shape is the spherical or icosahedral shape but also filamentous and even more complex shapes exist. For example Reovirus, causing respiratory or gastrointestinal illnesses has icosahedral shape [127], Marburg or Ebola virus have filamentous shape [148] and Rabies virus has bullet-like shape [149]. As uptake mediated by ligand-receptor binding is a discrete process and the involved cargo particles are small and typically covered by only few tens of ligands, stochastic effects during uptake should be relevant. The uptake of small particles has been previously studied both analytically and by computer simulations. Deterministic approaches usually focus on calculating minimal energy shapes of the plasma membrane to deduce phase diagrams [83, 84, 85], investigate uptake dynamics and the role of receptor diffusion within the plasma membrane [133, 134], study the consequences of elastic particles during uptake [135, 136], or interactions of the particle and the cytoskeleton [126]. Computer simulations complete these studies by considering the role of particle geometry during uptake [114, 130, 131, 132] or the scission step when the wrapped

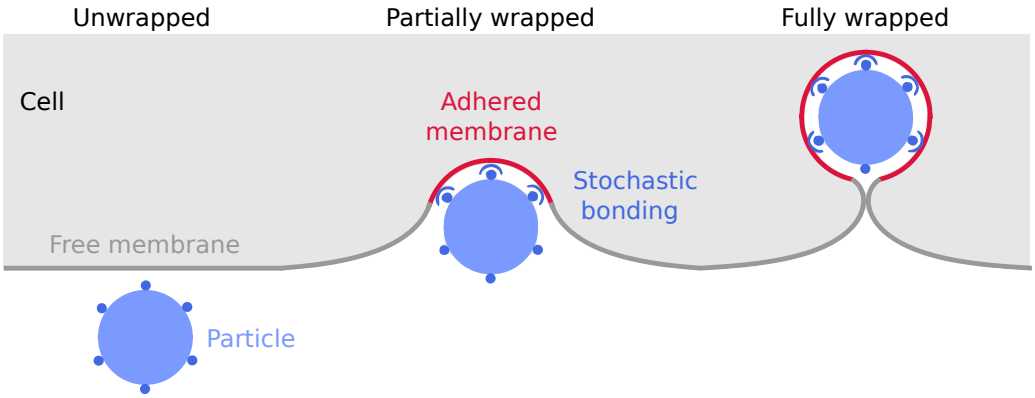

Figure 4.1 | States of particle uptake. In receptor-mediated endocytosis particles are taken up because the adhesion energy gain upon particle binding to cell surface receptors overcomes the bending and tension energy of the membrane.

particle is separated from the plasma membrane [137]. Stochastic approaches are rare and focus on the effect of ligand-receptor binding [150]. However, not much attention has been paid to the interplay between dynamics, stochasticity and particle shape. Considering uptake times we showed in chapter 3 that in a deterministic model spherical particles are taken up slower compared to cylindrical particles, whereas the situation can reverse in a stochastic description where spherical particles stronger profit from the presence of noise (see also [124]). The reason is that the quality of the noise changes induced by the particle geometry in a fundamental manner.

In this chapter we extend the work of chapter 3 on the interplay of dynamics, stochasticity and particle geometry. The most relevant energy contributions during uptake come from the part of the membrane to which the particle adheres during uptake (see Fig. 4.1). However, also the non-adhered or free membrane parts contribute to some extent [87]. While in chapter 3 the contributions of the free parts of the membrane have been neglected, we now critically discuss their influence on the dynamics. To incorporate these energy contributions within our framework, we first calculate the minimal energy shapes of the membrane by numerically solving the so-called shape equations for a spherical particle. From the membrane shapes the energies can then be determined. As we aim to get analytical insight and to later on allow for a consideration of the stochastic uptake dynamics, we will then propose a simpler phenomenological treatment that circumvents minimisation. Therefore, we approximate the free membrane parts and possibly involved curvature generating proteins by either a line tension or a phenomenologically extended line tension. We study the dynamical uptake behaviour of the system and extend our model to a stochastic description. Finally, we study the particle's positioning relative to the cell membrane during uptake, influenced by the stochastic ligand-receptor binding.

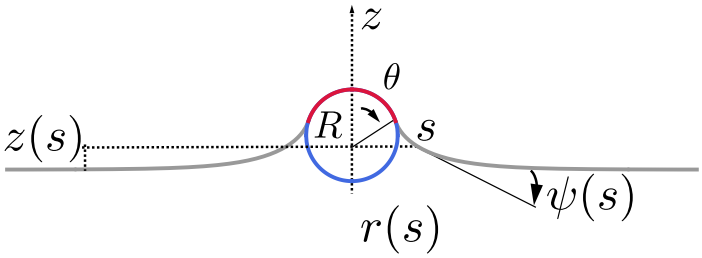

Figure 4.2 | Schematics and notation of particle uptake. The adhered part of the membrane (red), the free parts of the membrane (grey) and the particle (blue) are shown.

4.2 Membrane energies

To model deterministic particle uptake the usual approach is to balance the adhesion energy gain and the bending and tension energy cost [83, 84, 85, 3]. For the adhesion energy we assume that ligands to cell surface receptors are homogeneously distributed along the particle surface. Then, the total energy can be written by [86]

$$E = -\int_{A_{\mathrm{ad}}} W \mathrm{d}A + \int_{A_{\mathrm{mem}}} 2\kappa H^2 \mathrm{d}A + \sigma \Delta A \,, \tag{4.1}$$

where the first term is the gain in adhesion energy, with W the adhesion energy per area, the second term is the bending energy, with κ the bending rigidity and H the mean curvature of the membrane, and the third term is the tension energy, with σ the membrane tension and ΔA the excess area compared to the flat membrane state. Only the adhered part of the membrane A_{ad} contributes to the adhesion energy, whereas both the adhered and the free parts A_{mem} contribute to the bending and tension energy. While we neglected the contributions of the free parts in chapter 3 we now critically discuss their influence on the dynamics. To get analytical insight, we first study the importance of the different energy contributions for a spherical particle and then propose a simpler phenomenological treatment. Fig. 4.2 shows the used parametrisation (similar to [87]) where θ is the uptake angle, measured with respect to the symmetry axis (along the z-direction). The membrane contour is parameterised by its arc length s relative to the point where the adhered membrane is connected to the free part. Furthermore, $r(s)$ is the distance to the z-axis, $z(s)$ the height and $\psi(s)$ the angle between the radial axis normal to z-axis and the contour tangent. For a spherical particle with radius R the adhered area equals $A_{\mathrm{ad}} = 2\pi R^2(1-\cos(\theta))$. The different energy contributions are then given in non-dimensionalised form by [87, 88]

$$\begin{aligned} \frac{E_{\mathrm{ad}}^{\mathrm{adhe}}}{\kappa} + \frac{E_{\mathrm{ad}}^{\mathrm{bend}}}{\kappa} + \frac{E_{\mathrm{ad}}^{\mathrm{tens}}}{\kappa} &= 2\pi \frac{W}{\kappa} R^2 (1-\cos\theta) + 4\pi(1-\cos\theta) + \pi \frac{R^2}{\lambda^2}(1-\cos\theta)^2 \,, \\ \frac{E_{\mathrm{free}}^{\mathrm{bend}}}{\kappa} + \frac{E_{\mathrm{free}}^{\mathrm{tens}}}{\kappa} &= \pi \int_0^\infty \left(\dot{\psi} + \frac{\sin\psi}{r} \right)^2 r \,\mathrm{d}s + 2\pi \frac{1}{\lambda^2} \int_0^\infty (1-\cos\theta)\, r \,\mathrm{d}s \,. \end{aligned} \tag{4.2}$$

The two membrane parameters κ and σ define a typical length scale $\lambda = \sqrt{\kappa/\sigma}$ that together with R completely determine the bending and tension energies. The energies of the adhered part of the membrane are given by simple integration whereas the energy of the free parts has to be computed by minimising the energy functional with respect to the shape. Assuming equilibrium and axis-symmetry, this leads to the so called shape equations [151, 152, 83, 84]

$$\begin{aligned} \ddot{\psi} r^2 \cos\psi + \dot{\psi} r \cos^2\psi + \frac{1}{2}\dot{\psi}^2 r^2 \sin\psi - \frac{1}{2}(\cos^2\psi + 1)\sin\psi - \frac{r^2}{\lambda^2}\sin\psi = 0, \\ \dot{r} - \cos\psi = 0, \\ \dot{z} + \sin\psi = 0, \end{aligned} \tag{4.3}$$

with the boundary conditions

$$r(0) = R\sin\theta, \;\; \psi(0) = \theta, \;\; \psi(\infty) = 0, \;\; \dot{\psi}(\infty) = 0, \;\; z(\infty) = 0, \tag{4.4}$$

where the last condition is an arbitrary choice. To numerically solve the boundary value problem we rewrite Eq. (4.3) as a system of four first order ordinary differential equations. As three boundary conditions in Eq. (4.4) are given for $s \to \infty$ we use an asymptotic solution to shift the boundary conditions to a finite arc length $s_{\max}$. For weak membrane deformations ($\psi \ll 1$) one can linearise and solve the shape equations analytically [87]

$$r(s) = s\,, \quad \psi(s) = \beta K_1(s/\lambda)\,, \quad z(s) = \beta\lambda K_0(s/\lambda)\,, \tag{4.5}$$

where $\beta = \theta/K_1(R/\lambda\sin\theta)$ is a parameter and K_n are the modified Bessel functions of the second kind. Then the boundary conditions of the numerical solution can be adapted to

$$\begin{aligned} r(0) &= R\sin(\theta), \\ \psi(0) &= \theta, \\ \psi(s_{\max}) &= \beta K_1(R/\lambda\sin\theta), \\ \dot{\psi}(s_{\max}) &= -\frac{\beta}{2\lambda}\left(K_0(s_{\max}/\lambda) + K_2(s_{\max}/\lambda)\right), \\ z(s_{\max}) &= \beta\lambda K_0(s_{\max}/\lambda). \end{aligned} \tag{4.6}$$

We vary $s_{\max}$ such that the computed solution fulfils $\psi(s_{\max}) \ll 1$ and in this way match the numerical and asymptotic solution. In addition, the energy of the free membrane can be approximately calculated [87] in the limit of a tense ($\lambda/R \ll 1$)

$$\frac{E_{\text{free}}^{\text{Foret}}}{\kappa} = 4\pi\left\{\frac{4R}{\lambda}\sqrt{x(1-x)}(1-\sqrt{1-x}) - x - 2\ln\left(\frac{1+\sqrt{1-x}}{2}\right) - 2(1-\sqrt{1-x})^2\right\}, \tag{4.7}$$

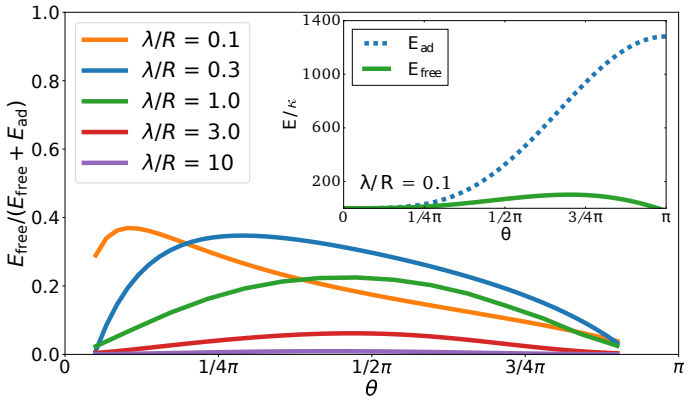

Figure 4.3 | The bending and tension energy of the free membrane relative to the total bending and tension energy, i.e. of the adhered and free parts of the membrane for different values of λ/R. To calculate the energy of the free parts we use Eq. (4.7) in the case of $\lambda/R < 1$ and Eq. (4.8) in the case of $\lambda/R > 1$ and the numerical solution for $\lambda/R = 1$. The inset shows the bending and tension energy of the adhered and free parts of the membrane for $\lambda/R = 0.1$.

and of a loose membrane ($\lambda/R \gg 1$)

$$\frac{E_{\text{free}}^{\text{Foret}}}{\kappa} = 4\pi\left(\frac{2R}{\lambda}x(1-x)\right)^2\left\{-\gamma + \frac{x}{2(1-x)} - \ln\left(\frac{R}{\lambda}\sqrt{x(1-x)}(1-x)\right)\right\}, \quad (4.8)$$

where $x = (1-\cos\theta)/2$. We solved Eqs. (4.3) using a 4th order collocation algorithm in Python with matched asymptotics [153]. We then evaluated the energy contributions from the free membrane. Fig. 4.3 shows the bending and tension energy of the free membrane relative to the total bending and tension energy of the membrane, i.e. of both the adhered and free parts for different values of λ/R. To calculate the energy of the free parts we use Eq. (4.7) in the case of $\lambda/R < 1$ and Eq. (4.8) in the case of $\lambda/R > 1$ and our numerical solution for $\lambda/R = 1$.

The analysis demonstrates that in the limit of a tense ($\lambda/R \ll 1$) and a loose membrane ($\lambda/R \gg 1$) the free parts of the membrane only contribute little to the total energy and hence can be neglected. However, considering typical parameter values occurring in the context of particle uptake at cell membranes $\kappa = 25\,\mathrm{k_B T}$ and $\sigma = 10^{-5} - 10^{-3}\,\mathrm{N/m}$ [87, 34] the uptake length scale is $\lambda = 10 - 100\,\mathrm{nm}$. For virus or nanoparticles with sizes ranging from $R = 10 - 100\,\mathrm{nm}$, $\lambda/R \sim 1$, and hence the free membrane contributes to some extent. The procedure of solving the shape equations is too involved to proceed with an analytical study of the uptake dynamics including later on also stochastic effects. It has been suggested earlier, that the effects of the free membrane may be seen as an effective line tension [83]. For a spherical particle, a line tension corresponds to an additional energy contribution

$$E_{\text{line}} = \zeta 2\pi R \sin\theta\,, \quad (4.9)$$

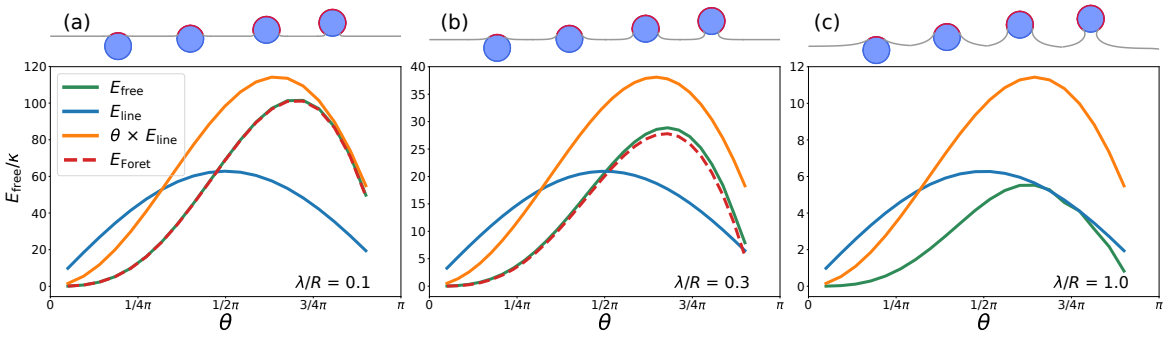

Figure 4.4 | Energies representing the free membrane for different combinations of λ/R. The numerically calculated total free energy of the membrane is shown in green, the line tension energy is shown in blue, the extended line tension energy is shown in orange and the analytically calculated energy of the free membrane according to Eq. 4.7 is shown in red for **(a)** $\lambda/R = 0.1$, **(b)** $\lambda/R = 0.3$ and **(c)** $\lambda/R = 1.0$. (Top) Numerically calculated shapes of the free membrane (grey) and adhered membrane (red) for increased wrapping and the corresponding values of λ/R.

with ζ the effective line tension. However, this simple form has been shown to be strictly true only in the double limit of high tension and large uptake angle, where indeed $E_{\text{free}}^{\text{tot}}$ scales like a line tension with $\zeta = \sqrt{\kappa\sigma}$ [84, 87]. We therefore compare in Fig. 4.4 the numerically computed total energy of the free membrane $E_{\text{free}}^{\text{tot}}$ (green) to a line tension E_{line} (blue) and an extended line tension $\theta E_{\text{line}} \propto \theta \sin\theta$ (orange) for different values of λ/R in the regime from tense to intermediate (a)-(c) as relevant for the uptake of $10-300\,\text{nm}$ particles and the corresponding membrane shapes (top). From Fig. 4.4, one can see the following: First, we can confirm our numerical calculations by comparing it to Eq. (4.7) (dashed red), which works excellent. Secondly, a line tension may be only a phenomenological description (compare blue curve). Thirdly, the extended line tension θE_{line} represents a rather good description of the qualitative behaviour, as the position of the asymmetric energy barrier and the scaling is represented quite well.

We tried other approximations. For instance, the asymptotic formula for the tense case, Eq. (4.7), in the limit of small uptake angles rather suggests $E_{\text{free}}^{\text{tot}}/\kappa \sim \pi(\lambda/R)\theta^2 \sin\theta$. However, using this form for all θ obviously improves the behaviour at small angles but leads to much worse agreement for larger angles. We hence judge the extended line tension to be a good compromise between the tense and the intermediate regime, which is the one of our interest. In the following, we study the deterministic and the stochastic uptake dynamics and include the free membrane effects only at the phenomenological level. For the deterministic dynamics we study both a line tension E_{line} and an extended line tension θE_{line}. For the stochastic dynamics we restrict ourselves to a line tension. From a more general point of view, we note that a 'true' line tension may even occur in case of membranes displaying lipid domains and/or curvature generating proteins, as e.g. clathrin triskelia [154].

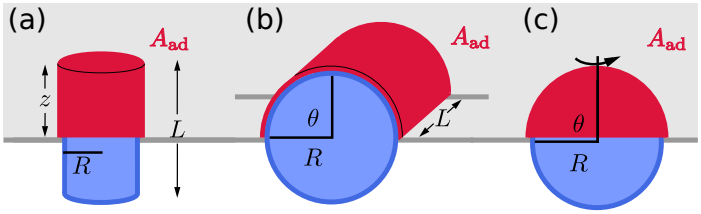

Figure 4.5 | Uptake of particles of **(a)** normal cylindrical (rocket mode), **(b)** parallel cylindrical (submarine mode), and **(c)** spherical shape. In a deterministic model, the particle is homogeneously covered with ligands (blue) and adhered to the membrane along A_{ad} (red).

4.3 Deterministic dynamics of particle uptake

4.3.1 General approach

Next, we develop a dynamical model for the uptake of particles of normal cylindrical, parallel cylindrical and spherical shape (compare Fig. 4.5). While a cylindrical particle may make contact to the cell membrane in any inclined orientation, a short (long) cylinder would position itself normal (parallel) to the membrane to maximise the initial adhered contact area. It is therefore reasonable to compare these two configurations to the spherical shape. In case of the normal cylinder, the top and bottom surfaces are neglected for simplicity as they do not contribute to the force. To keep calculations as transparent as possible we neglect them also for the parallel cylinder. We note that all shapes obey axial symmetry, useful in reducing the complexity of the problem. During uptake the particle adheres to the membrane along the adhered area A_{ad} and we describe the progress of uptake by the uptake height z for the normal cylinder (Fig. 4.5 (a)), or uptake angle θ for the parallel cylinder (Fig. 4.5 (b)) or sphere (Fig. 4.5 (c)). First, we incorporate the energy contribution of the free membrane (or curvature generating proteins) for all geometries by a line tension. In addition, we study the extended line tension for the sphere. The total energy for uptake including line tension hence reads

$$E = \int_{A_{ad}} (-W + 2\kappa H^2)\mathrm{d}A + \sigma \Delta A_{ad} + \zeta \mathcal{E}, \tag{4.10}$$

where ΔA_{ad} is the excess in adhered area compared to the flat reference state, $\mathcal{E}$ is the length of the edge between the membrane adhering to the particle and the free cell membrane and ζ is the effective line tension. While $\zeta = \sqrt{\kappa\sigma}$ if approximating the effects of the free membrane, we consider ζ as a free parameter here to study the dynamics in general. The typical scale is $\zeta = 1 - 10\,\mathrm{pN}$. Similar to chapter 3 we calculate a thermodynamic uptake force by taking the variation of the energy E with respect to the uptake height or angle, respectively $F_{up} = -\partial E/(\partial x)$, where $x = \{z, s = R\theta\}$. The uptake force is balanced by a friction force that the particle experiences, $F_{up} = F_{friction}$, that is proportional to an effective membrane microviscosity

of order $\eta = 1\,\mathrm{Pa\,s}$ [85], the length of the edge $\mathcal{E}$ and the velocity with which this edge moves $\dot{x}$, $F_{\mathrm{friction}} = \eta\mathcal{E}(x)\dot{x}$. By solving this equation for $\dot{x}$, we obtain the dynamics for particle uptake. In the next paragraphs we briefly summarise the relevant equations for the two cylinder orientations and the sphere.

4.3.2 Various particle shapes

Dynamics of cylindrical shaped particles in normal orientation ($\perp$)

For the normal cylinder with radius R, length L and adhered area $A_{\mathrm{ad}}^{\perp} = \mathcal{E}^{\perp}L$, where $\mathcal{E}^{\perp} = 2\pi R$ and $H^{\perp} = 1/(2R)$ we find

$$E^{\perp} = -W2\pi Rz + \frac{\kappa\pi}{R}z + \sigma 2\pi Rz + \zeta 2\pi R\,. \tag{4.11}$$

The differential equation for the uptake then reads

$$\dot{z}^{\perp} = \nu_{\mathrm{up}}^{\perp}\,, \tag{4.12}$$

where $\nu_{\mathrm{up}}^{\perp} = \nu_{\mathrm{w}}^{\perp} - \nu_{\kappa}^{\perp} - \nu_{\sigma}^{\perp} = W/\eta - \kappa/(2R^2\eta) - \sigma/\eta$. Importantly, the line tension does not affect the uptake dynamics. We also note that for the normal cylinder the energy of the free membrane would only give a constant term that would not contribute to the uptake force. As in chapter 3, the uptake time is given by integrating Eq. (4.12), $T_{\mathrm{det}}^{\perp} = L/\nu_{\mathrm{up}}^{\perp}$. The critical radius (at which the uptake time diverges) is given by $R_{\mathrm{crit}}^{\perp} = \sqrt{\kappa/(2(W-\sigma))}$. We can easily deduce the full dynamic behaviour, i.e. the normal cylinder either gets taken up ($\nu_{\mathrm{up}}^{\perp} > 0$) with constant speed or does not get taken up at all ($\nu_{\mathrm{up}}^{\perp} \leq 0$), however, partial uptake will never occur. Later on, we will compare all particle shapes at equal volume and equal radius. Taking the sphere as the reference shape, the normal cylinder has at equal radius the length $L = 4R/3$.

Dynamics of cylindrical shaped particles in parallel orientation ($\parallel$)

For the parallel cylinder with radius R and length L the energy is a function of the uptake angle instead of the uptake height. It reads

$$E^{\parallel} = -W2\theta RL + \kappa\frac{\theta L}{R} + 2(\theta - \sin\theta)RL\sigma + \zeta 2L, \tag{4.13}$$

such that the differential equation for uptake is given by

$$\dot{\theta}^{\parallel} = \nu_{\mathrm{up}}^{\parallel} - \nu_{\sigma}^{\parallel}(1 - \cos\theta), \tag{4.14}$$

where $\nu_{\mathrm{up}}^{\parallel} = \nu_{\mathrm{w}}^{\parallel} - \nu_{\kappa}^{\parallel} = W/(R\eta) - \kappa/(2R^3\eta)$ and $\nu_{\sigma}^{\parallel} = \sigma/(R\eta)$. Again, the line tension does not affect the uptake dynamics. The uptake time is given by integrating Eq. (4.14), $T_{\mathrm{det}}^{\parallel} \approx \pi/(\nu_{\mathrm{up}}^{\parallel}\sqrt{1-2\alpha^{\parallel}})$, (similar to chapter 3) with $\alpha^{\parallel} = \nu_{\sigma}^{\parallel}/\nu_{\mathrm{up}}^{\parallel}$. The critical radius

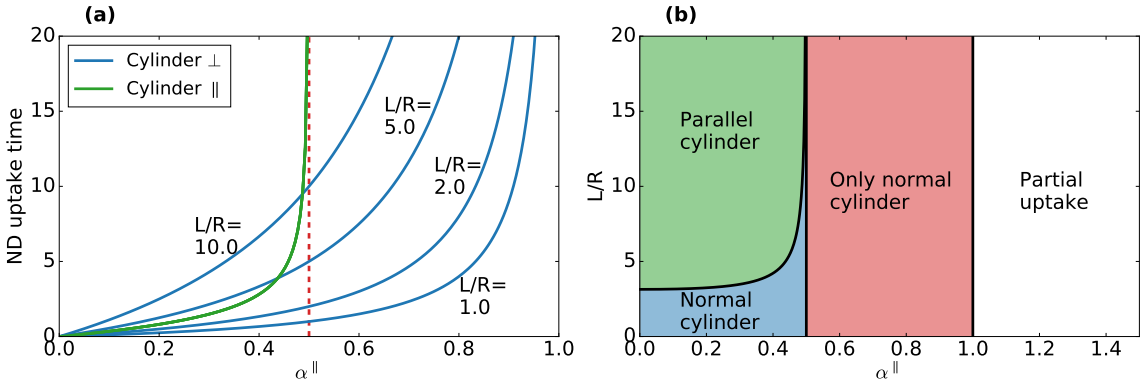

Figure 4.6 | Cylindrical uptake times in comparison. **(a)** Non-dimensionalised uptake times of normal (blue) and parallel cylinder (green) as a function of $\alpha^{\parallel}$ at equal radius but different aspect ratios (i.e. different volume). For the normal cylinder the uptake time varies with aspect ratio whereas it stays constant for the parallel cylinder. **(b)** Dynamic phase diagram of cylindrical uptake indicating the cylindrical mode which is fastest or which is the only possible mode in the corresponding parameter region.

is given by $R^{\parallel}_{\text{crit}} = \sqrt{\kappa/(2(W-2\sigma))}$. Comparing the uptake times of the normal and parallel cylinder we find that the normal cylinder is only faster as long as

$$\frac{L}{R} \leq \pi \frac{1-\alpha^{\parallel}}{\sqrt{1-2\alpha^{\parallel}}}. \tag{4.15}$$

Thus, the optimal uptake position depends on the aspect ratio. We non-dimensionalise Eq. (4.14) by introducing a characteristic time $t_{\text{c}}^{\parallel} = 1/\nu_{\text{up}}^{\parallel}$, $\tau = t/t_{\text{c}}$ and get

$$\frac{\mathrm{d}\theta}{\mathrm{d}\tau} = 1 - \alpha^{\parallel}(1-\cos\theta). \tag{4.16}$$

Now we can deduce the full dynamic behaviour for $\nu_{\text{up}}^{\parallel} > 0$. For $0 \leq \alpha^{\parallel} \leq 1/2$ one has a complete uptake (although the uptake time diverges at $\alpha^{\parallel} = 1/2$) and for $\alpha^{\parallel} > 1/2$ one has only partial uptake. Fig. 4.6 shows the uptake times for the normal (blue) and parallel cylinder (green) in comparison, as a dimensionless function of $\alpha^{\parallel}$, where

$$\frac{T_{\text{det}}^{\perp}}{\tau_\eta} = \frac{L}{R}\frac{\alpha^{\parallel}}{1-\alpha^{\parallel}}, \tag{4.17}$$

and

$$\frac{T_{\text{det}}^{\parallel}}{\tau_\eta} = \pi \frac{\alpha^{\parallel}}{\sqrt{1-2\alpha^{\parallel}}}, \tag{4.18}$$

with $\tau_\eta = R\eta/\sigma$. Fig. 4.6 (a) shows the uptake times at equal radius but different aspect ratios L/R (i.e. different volume). For the normal cylinder the uptake time varies with aspect ratio whereas it stays constant for the parallel cylinder. Importantly, the normal cylinder is faster only as long as the cylinder is rather short. Fig. 4.6 (b) shows the dynamic phase diagram of cylindrical uptake. In the blue region the uptake

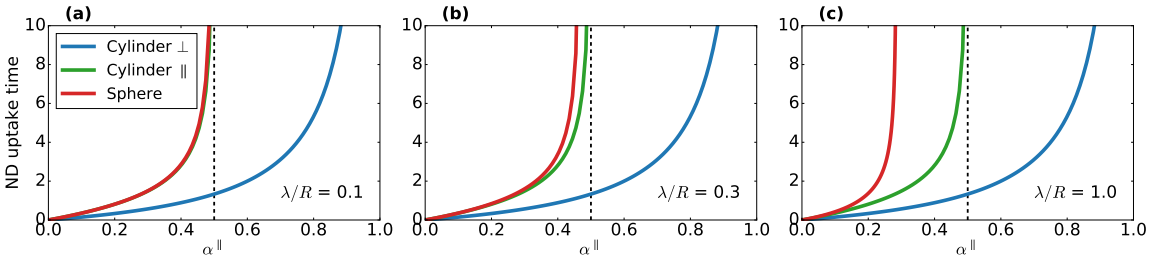

Figure 4.7 | Non-dimensional uptakes times for sphere (red), normal (blue) and parallel cylinder (green) for $\lambda/R = 0.1$ **(a)**, $\lambda/R = 0.3$ **(b)** and $\lambda/R = 1.0$ **(c)** as a function of $\alpha^{\parallel}$.

of normal cylinders is fastest and in the green region the uptake of parallel cylinders is fastest. Normal cylinders can get either taken up or not. In contrast, for parallel cylinders also partial uptake can occur. Therefore, the red region indicates where parallel cylinders are only taken up partially but normal cylinders completely. In the white region the normal cylinder cannot get taken up, whereas one still finds partial uptake for the parallel cylinder.

Dynamics of spherical shaped particles (○)

For the sphere with radius R and adhered area $A^{\circ}_{\mathrm{ad}} = 2\pi R^2(1-\cos\theta)$ the total energy reads

$$E^{\circ} = \left(-W2\pi R^2 + \kappa 4\pi + \sigma\pi R^2(1-\cos\theta)\right)(1-\cos\theta) + \zeta 2\pi R\sin\theta\,. \tag{4.19}$$

The differential equation for uptake reads

$$\dot{\theta}^{\circ} = \nu^{\circ}_{\mathrm{w}} - \nu^{\circ}_{\kappa} - \nu^{\circ}_{\sigma}(1-\cos\theta) - \nu^{\circ}_{\zeta}\cot\theta = \nu^{\circ}_{\mathrm{up}} - \nu^{\circ}_{\sigma}(1-\cos\theta) - \nu^{\circ}_{\zeta}\cot\theta, \tag{4.20}$$

where we have introduced $\nu^{\circ}_{\mathrm{up}} = \nu^{\circ}_{\mathrm{w}} - \nu^{\circ}_{\kappa} = W/(R\eta) - 2\kappa/(R^3\eta)$, $\nu^{\circ}_{\sigma} = \sigma/(R\eta)$ and $\nu^{\circ}_{\zeta} = \zeta/(R^2\eta)$. For vanishing line tension it is possible to calculate the deterministic uptake time by integrating Eq. (4.20), $T^{\circ}_{\mathrm{det}} \approx \pi/(\nu^{\circ}_{\mathrm{up}}\sqrt{1-2\alpha^{\circ}})$, where $\alpha^{\circ} = \nu^{\circ}_{\sigma}/\nu^{\circ}_{\mathrm{up}}$. It diverges for $\alpha^{\circ} = 1/2$ defining a critical radius $R^{\circ}_{\mathrm{crit}} = \sqrt{2\kappa/(W-2\sigma)}$. To compare the uptake dynamics to the uptake times of normal and parallel cylinder at equal volume and radius we formulate the uptake time as a function of $\alpha^{\parallel}$.

$$\frac{T^{\circ}_{\mathrm{det}}}{\tau} = \pi\frac{\alpha^{\circ}}{\sqrt{1-2\alpha^{\circ}}} \quad \text{with} \quad \alpha^{\circ} = \frac{1}{\frac{1}{\alpha^{\parallel}} - \frac{3\lambda^2}{2R^2}}\,. \tag{4.21}$$

The result of the comparison for vanishing line tension is shown in Fig. 4.7 using Eq. (4.17) for the normal cylinder, Eq. (4.18) for the parallel cylinder and Eq. (4.21) for the sphere. Comparing the different particles shapes at equal volume and radius, we find that the normal cylindrical particle is fastest followed by the parallel cylindrical particle. The spherical particle is always slowest. In the case, where the particle is

large compared to the characteristic length-scale of the membrane ($\lambda/R \ll 1$, i.e. a tense membrane), parallel cylinder and sphere have similar uptake times, compare (a). For smaller particles or a looser membrane the uptake times for parallel cylinder and sphere more and more diverge, compare (b) and (c).

To study the full dynamic behaviour including line tension, we can write Eq. (4.20) in a dimensionless form by choosing $t_\mathrm{c}^\circ = 1/\nu_\mathrm{up}^\circ$ as characteristic time and using an effective line tension $\beta = \nu_\zeta^\circ/\nu_\mathrm{up}^\circ$. Then, the equation reads

$$\frac{\mathrm{d}\theta}{\mathrm{d}\tau} = 1 - \alpha(1 - \cos\theta) - \beta\cot\theta\,, \tag{4.22}$$

from now on using $\alpha^\circ = \alpha$. Neglecting line tension for a moment ($\beta = 0$) deterministic uptake is only possible if $\dot\theta > 0$, i.e. $\nu_\mathrm{up}^\circ > 0$ and $0 \leq \alpha \leq 1/2$ (although the uptake time diverges for $\alpha = 1/2$), implying that the adhesion energy overcomes the bending energy and that the difference of both overcomes the tension energy. Hence, the we find partial uptake for $\alpha > 1/2$. Now we include line tension ($\beta > 0$). Then the analysis shows that the equation has at least one additional steady state, as $\lim\limits_{\theta\to\pi}^{\theta\to 0}\cot\theta = {}^{\infty}_{-\infty}$, related to uptake after crossing an initial energy barrier if the steady state is unstable and occurs for small uptake angles ($\theta < \pi/2$) or related to no uptake if the steady state occurs for large uptake angles ($\theta \geq \pi/2$).

In Fig. 4.8 we show the dynamical uptake behaviour for the sphere with line tension. In (a) the change of uptake angle as a function of uptake angle is shown for different values of α and β. The three graphs show the three cases of uptake (orange), partial uptake (blue) and no uptake (green). Importantly, we consider negative values for $\dot\theta$ for $\theta < \pi/2$ as initial energy barrier that will be overcome by thermal noise. Next, we discuss the structure of the steady states as a function of α and β. To get analytical insight we determine the number of steady states of Eq. (4.22). For a steady state it is necessary that the condition $\mathrm{d}\theta/\mathrm{d}\tau|_{\theta=\theta_\mathrm{ss}} = 0$ is fulfilled. We reformulate the problem to find the particular value of β where the number of steady states changes. In this case the two functions $f(\theta_\mathrm{ss}) = 1 - \alpha(1 - \cos\theta_\mathrm{ss})$ and $g(\theta_\mathrm{ss}) = \beta\cot\theta_\mathrm{ss}$ touch each other and fulfil $f(\theta_\mathrm{ss}) = g(\theta_\mathrm{ss})$ and $f'(\theta_\mathrm{ss}) = g'(\theta_\mathrm{ss})$. The second condition implies that $\sin^3\theta_\mathrm{ss} = \beta/\alpha$. Using this condition in the first equation we find

$$\beta(\alpha) = \alpha\left[1 - \left(\frac{1}{\alpha} - 1\right)^{\frac{2}{3}}\right]^{\frac{3}{2}}. \tag{4.23}$$

The result is shown as red curve in Fig. 4.8 (b) and defines regions with equal numbers of steady states. Below the curve we have partial uptake (blue region) and above we find either uptake (orange region) or no uptake (green region), dependent on the position of the steady state (compare the definition above). The steady states are shown as a function of α in Fig. 4.8 (c) and β (d) which we determine by numerically

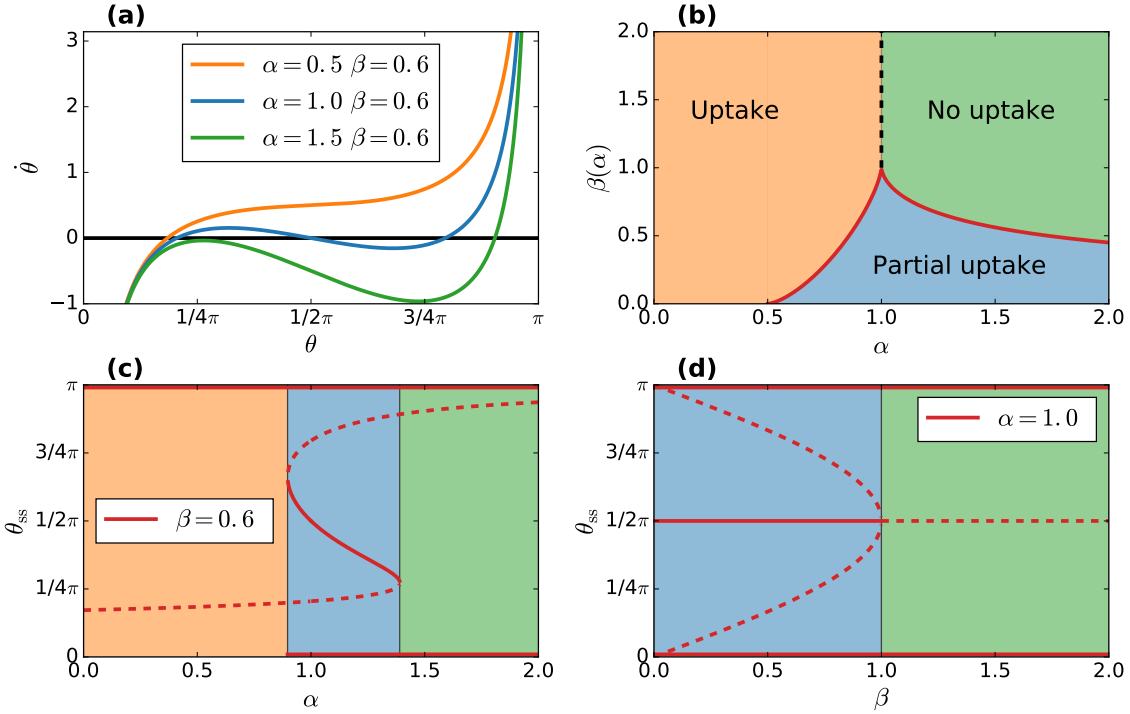

Figure 4.8 | Deterministic uptake dynamics of the spherical particle with line tension. **(a)** $\dot{\theta}$ as a function of θ for different parameter values α and β, showing graphs for uptake (orange), partial uptake (blue) and no uptake (green). **(b)** Structure of the steady states as a function of α and β. Below the curve we have partial uptake (blue region) and above we find either uptake (orange region) or no uptake (green region). **(c)** Steady states (stable: solid red line, unstable: dashed red line) for $\beta = 0.6$ as a function of α. Two saddle-node bifurcations occur as a function of α. The first corresponds to the appearance of partial uptake and the second one to the moment when no uptake at all occurs. According to the appearance/disappearance of these bifurcations we find uptake (orang region), partial uptake (blue region) and no uptake (green region). **(d)** Steady states for $\alpha = 1.0$ as a function of β. A subcritical pitchfork bifurcation occurs at $\beta = 1$, corresponding to the moment where the uptake behaviour changes from partial uptake (blue region) to no uptake (green region).

solving Eq. (4.22). We indicate stable steady states as a solid line and unstable steady states as a dashed line. Considering (c), where $\beta = 0.6$, we find that two saddle-node bifurcations occur as a function of α. The first one corresponds to the appearance of partial uptake and the second one to the moment when no uptake at all occurs. According to the appearance/disappearance of these bifurcations we find uptake (orange region), partial uptake (blue region) and no uptake (green region). Considering (d), where $\alpha = 1.0$, we find a subcritical pitchfork bifurcation, corresponding to the moment where the uptake behaviour changes from partial uptake (blue region) to no uptake (green region). Last but not least, we discuss the role of line tension. In general it has two effects. First, it introduces an unstable steady state (energy barrier) as long as the circumference of the edge increases, i.e. in the first half of uptake. Secondly, it drives the system if the circumference of the edge decreases, i.e. in the second half of

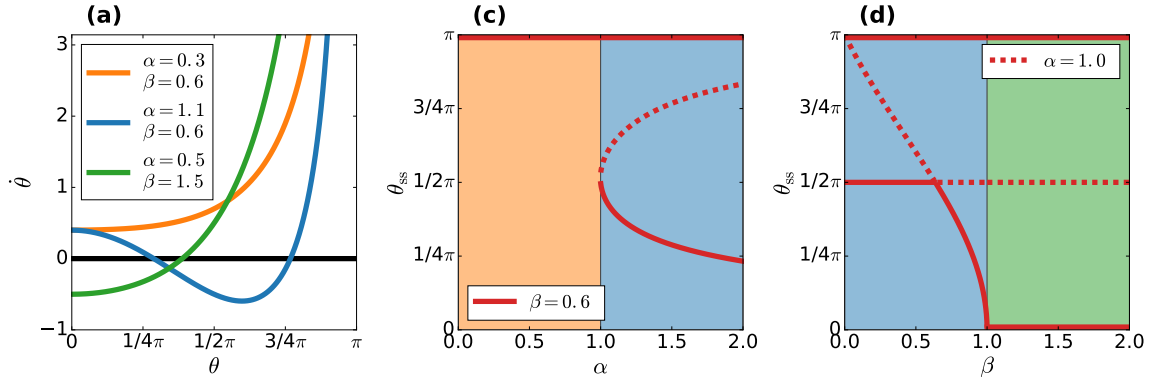

Figure 4.9 | Deterministic uptake dynamics of the spherical particle with extended line tension. **(a)** $\dot{\theta}$ as a function of θ for different parameter values α and β, showing graphs for uptake (orange), partial uptake (blue) and no uptake (green). **(b)** Steady states (stable: solid red line, unstable: dashed red line) for $\beta = 0.6$ as a function of α. A saddle-node bifurcation occurs for $\alpha = 1.0$, indicating the region where uptake (orange) and partial uptake (blue) occurs. **(c)** Steady states for $\alpha = 1.0$ as a function of β. A transcritical bifurcation occurs for $\beta = 0.64$, indicating the region where partial uptake (blue) and no uptake (green) occurs.

uptake. Considering thermal noise the system could be stochastically driven above this barrier. We introduce stochasticity in the next section to study this situation.

For the extended line tension we now study $\zeta 2\pi R\theta \sin\theta$ in the last term of Eq. (4.19) and therefore get as dimensionless dynamic equation

$$\frac{\mathrm{d}\theta}{\mathrm{d}\tau} = 1 - \alpha(1 - \cos\theta) - \beta\theta\cot\theta\,. \tag{4.24}$$

We note that in this case α and β are now differently defined compared to before. However, as α and β are considered as free parameters in Eq. (4.24) we use the same notation as before. Fig. 4.9 (a) shows the change of the uptake angle as a function of the uptake angle for different parameter values. The three curves show uptake (orange), partial uptake (blue) and no uptake (green). Compared to the line tension in Fig. 4.8 (a) the initial barrier, indicated by the negative values of $\dot{\theta}$ for small values of θ, has vanished. In Fig. 4.9 (b) the steady states are shown as a function of α where $\beta = 0.6$ is fixed. Importantly, we find a saddle-node bifurcation for $\alpha = 1.0$, indicating the region where uptake (orange) and partial uptake (blue) occurs. In Fig. 4.9 (c) the steady states are shown as a function of β where $\alpha = 1.0$ is fixed. Here, a transcritical bifurcation occurs for $\beta = 0.64$, indicating the region where partial uptake (blue) and no uptake (green) occurs.

To conclude, the dynamics with line tension in Fig. 4.8 and extended line tension in Fig. 4.9 are quite similar. Depending on the parameter region uptake, partial uptake or no uptake occurs. The main difference is that for the extended line tension no initial energy barrier exists. Next, we include stochasticity into the model. As we aim for a simple description we thus represent the free membrane as a line tension line.

4.4 Stochastic dynamics of particle uptake

Ligand-receptor binding is a stochastic process since it is discrete and involves typically only few tens of ligand-receptor pairs. Therefore, instead of treating the continuous deterministic system we now explicitly model the discrete stochastic dynamics of receptor-ligand binding (compare inset in Fig. (4.10)).

4.4.1 General approach

We map the adhered surface area onto the number of bound ligands N, in order to deduce a discrete differential equation $\mathrm{d}N/\mathrm{d}t = \mathrm{d}N/\mathrm{d}x\ \mathrm{d}x/\mathrm{d}t$, with $x = \{z, \theta\}$ and we use the dynamics of $\mathrm{d}x/\mathrm{d}t$ from the previous section. By this mapping, we make implicitly use of our previous assumption of axial symmetry. Next, we deduce the corresponding one-step Master equation (ME) [92] for the number of bound ligands

$$\frac{\mathrm{d}p_N}{\mathrm{d}\tau} = g_{N-1}p_{N-1} + r_{N+1}p_{N+1} - (g_N + r_N)p_N\,, \tag{4.25}$$

where p_N is the probability of finding a particle bound to the membrane by N receptors and g_N (r_N) is the forward (backward) rate by which ligands bind (unbind). In general we solve the ME numerically by means of the Gillespie algorithm [121] (compare Appendix A.2), as analytical solutions are available only for some special cases, which we treated in chapter 3. In the following, we briefly show the different equations for the particle shapes of Fig. 4.5.

4.4.2 Various particle shapes

Stochastic dynamics of cylindrical shaped particles in normal orientation ($\perp$)

We map the membrane covered area $A_{\mathrm{ad}}^{\perp} = A(z)$ onto the number of bound receptors $N^{\perp}(z)$ by $A(z)/A_{\mathrm{max}}^{\perp} = (N^{\perp}(z) - 1)/(N_{\mathrm{max}} - 1)$, where we assume that the particle is initially bound to the membrane by one ligand, yielding $N^{\perp}(z) = (N_{\mathrm{max}} - 1)z/L + 1$. Then the corresponding discrete equation reads

$$\frac{\mathrm{d}N^{\perp}}{\mathrm{d}t} = \frac{N_{\mathrm{max}} - 1}{L}\left(\nu_{\mathrm{w}}^{\perp} - \nu_{\kappa}^{\perp} - \nu_{\sigma}^{\perp}\right). \tag{4.26}$$

The corresponding rates of the master equation are given by $g_N = (N_{\mathrm{max}} - 1)\nu_{\mathrm{w}}^{\perp}/L$ and $r_N = (N_{\mathrm{max}} - 1)(\nu_{\kappa}^{\perp} + \nu_{\sigma}^{\perp})/L$.

Stochastic dynamics of cylindrical shaped particles in parallel orientation ($\parallel$)

We map the membrane covered area $A_{\mathrm{ad}}^{\parallel} = A(\theta)$ onto the number of bound receptors $N^{\parallel}(\theta)$ by $A(\theta)/A_{\mathrm{max}}^{\parallel} = (N^{\parallel}(\theta) - 1)/(N_{\mathrm{max}} - 1)$, yielding $N^{\parallel}(\theta) = (N_{\mathrm{max}} - 1)\theta/\pi + 1$.

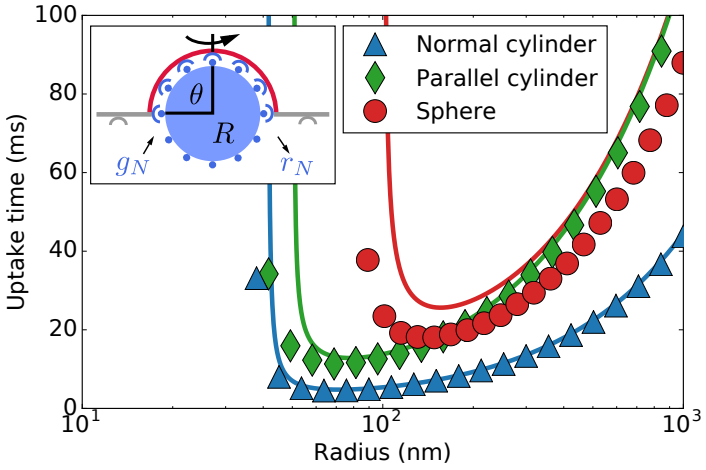

Figure 4.10 | Simulated mean uptake times for the normal cylinder (blue triangles), the parallel cylinder (green rhombs) and the sphere (red circles) as a function of particle radius at equal volume and radius for the parameter values in Table 4.1. For the normal cylinder, the parallel cylinder and the sphere the deterministic uptake times are plotted as solid lines for vanishing line tension. (Inset) Modelling discrete stochastic uptake. A spherical particle (blue), homogeneously covered with ligands that can bind (unbind) to cell surface receptors with rate g_N (r_N).

The corresponding discrete equation reads

$$\frac{\mathrm{d}N^{\parallel}}{\mathrm{d}t} = \frac{N_{\max}-1}{\pi}\left(\nu_{\mathrm{w}}^{\parallel} - \nu_{\kappa}^{\parallel} - \nu_{\sigma}^{\parallel}(1-\cos\theta)\right). \tag{4.27}$$

The corresponding rates of the master equation are given by $g_N = (N_{\max}-1)\nu_{\mathrm{w}}^{\parallel}/\pi$ and $r_N = (N_{\max}-1)(\nu_{\kappa}^{\parallel} + \nu_{\sigma}^{\parallel}(1-\cos\theta))/\pi$.

Stochastic dynamics of spherical shaped particles (○)

Finally, we map the membrane covered area $A_{\mathrm{ad}}^{\circ} = A(z)$ onto the number of bound receptors $N^{\circ}(\theta)$ by $A(\theta)/A_{\max}^{\circ} = (N^{\circ}(\theta)-1)/(N_{\max}-1)$ yielding $N^{\circ} = (N_{\max}-1)(1-\cos(\theta))/2+1$. The discrete equation reads

$$\frac{\mathrm{d}N^{\circ}}{\mathrm{d}t} = \left(\nu_{\mathrm{w}}^{\circ} - \nu_{\kappa}^{\circ} - \nu_{\sigma}^{\circ}(1-\cos\theta) - \nu_{\zeta}^{\circ}\cot\theta\right) N_{\mathcal{E}}(N), \tag{4.28}$$

where $N_{\mathcal{E}}(N) = \sqrt{(N-1)((N_{\max}-1)-(N-1))}$ or $N_{\mathcal{E}}(\theta) = (N_{\max}-1)\sin\theta/2$. The corresponding rates of the master equation are given by $g_N = \nu_{\mathrm{w}}^{\circ} N_{\mathcal{E}}(N)$ and $r_N = \left(\nu_{\kappa}^{\circ} + \nu_{\sigma}^{\circ}(1-\cos\theta) + \nu_{\zeta}^{\circ}\cot\theta\right) N_{\mathcal{E}}(N)$. In addition we define the first rate to equal $g_1 = \nu_w\sqrt{N_{\max}}$.

4.4.3 Stochastic simulations

After having deduced the discrete equations for all three particle shapes we here solve the corresponding ME numerically by means of the Gillespie algorithm [121] (compare

Appendix A.2). In addition, we compare our simulations to the deterministic analytical results in the limit of vanishing line tension. The parameter values of the simulation are summarised in Table 4.1.

Fig. 4.10 shows the simulated mean uptake time for the normal cylinder (blue triangles), the parallel cylinder (green rhombs) and the sphere (red circles) as a function of radius at equal volume and radius. The deterministic solutions for vanishing line tension are shown as solid lines in the corresponding colours. All particle shapes show similar behaviour. First, a critical radius exists beyond which uptake is not possible anymore, secondly an optimal radius exists for which the uptake time is minimal and thirdly, the uptake time increases with increasing radius. In the deterministic description parallel cylindrical particles are taken up faster or at least equally fast compared to spherical particles for all radii. In contrast, in the stochastic description parallel cylindrical particles are only faster compared to spherical particles in a specific range of radii. At around $R = 150\,\mathrm{nm}$ the situation reverses and spherical particles are taken up faster. This effect is caused for the reason that the different particle shapes are affected by a different quality of noise. As we have shown in chapter 3 and [124], cylindrical particles experience additive noise whereas spherical particles experience multiplicative noise. In addition, we see in Fig. 4.10 that stochastic uptake is always faster compared to deterministic uptake. This is to be expected for a system with noise and both a reflecting and an absorbing boundary condition.

An illustrative example is a biased one-dimensional random walk of a particle in the semi-infinite interval $(-\infty, a > 0]$ with constant drift v and constant noise. Initially, the particle is positioned at the origin. Then, the stochastic mean first passage time (MFPT) to reach a is given by $T_{\mathrm{MFPT}} = a/v$, i.e. the MFPT equals the deterministic passage time [142]. In the case where the reflecting boundary approaches the origin from $-\infty$, the MFPT will decrease and hence will be shorter compared to the deterministic passage time.

Table 4.1 | Used parameters for the stochastic simulations.

Parameter	Used value	Ref.
Bending rigidity	$\kappa = 25\,\mathrm{k_B}T$	[34]
Membrane tension	$\sigma = 1 \cdot 10^{-5}\,\mathrm{N/m}$	[87]
Energy density	$W = 0.04\,\mathrm{mJ/m^2}$	[85]
Membrane viscosity	$\eta = 1\,\mathrm{Pa\ s}$	[85]
Line tension	$\zeta = \sqrt{\kappa\sigma}$	
Particle radius	$R = 100\,\mathrm{nm}$	
Surface-ligands	$N_{\mathrm{max}} = 20$	
Simulation runs	$N_{\mathrm{sim}} = 10^4$	

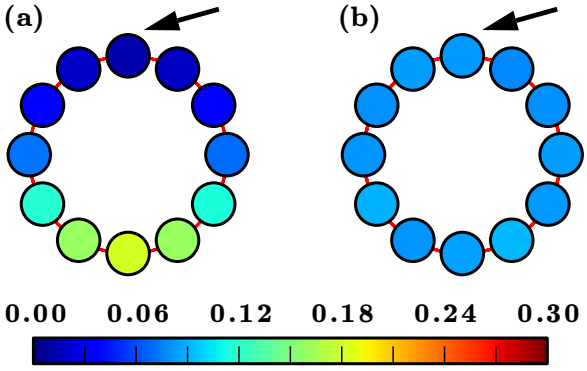

Figure 4.11 | Probability of being the last bound ligand during stochastic uptake of a parallel cylindrical particle. **(a)** For $W = 0.04\,\mathrm{mJ/m^2}$ uptake is favourable leading to the highest probability at the ligand opposed to the first bound ligand. **(b)** For $W = 0.01\,\mathrm{mJ/m^2}$ uptake is unfavourable leading to an equal probability at every ligand. The black arrows point to the first bound ligand. All results are averages over $N_{\mathrm{sim}} = 10^4$ simulation runs.

4.5 Stochastic ligand binding and particle positioning

4.5.1 Parallel cylindrical particle

Next, we analyse the effect of noise on the positioning of a particle during uptake relative to the membrane. First, we consider a parallel cylindrical particle in the case where uptake is either favourable or unfavourable, i.e. where uptake would also occur deterministically or only due to stochasticity. We assume that the particle symmetrises the position of bound ligands relative to the cell membrane due to membrane relaxation, which occurs on the same timescale as ligand-receptor binding (see Appendix A.5). This assumption also follows from the axis symmetry in the deterministic model and agrees with MD simulations for zero tension, which do not show any membrane overhangs [114], probably caused by the bending energy of the free membrane parts. Therefore, ligands are expected to bind and unbind with equal probability to receptors independent of their position relative to the particle. Fig. 4.11 (a) shows the probability for being the last bound ligand (in blue and red for low and high probability) for weak noise and favourable uptake ($W = 0.04\,\mathrm{mJ/m^2}$) and (b) for intermediate noise and unfavourable uptake ($W = 0.01\,\mathrm{mJ/m^2}$). Intriguingly, for weak noise the most likely last bound ligand is positioned opposed to the first bound ligand (indicated by the black arrow), whereas for intermediate noise every ligand has the same probability for being the last bound ligand.

4.5.2 Spherical particle

Next, we consider the uptake of a spherical particle. We slightly adapt the model and consider a truncated icosahedron with $N_{\mathrm{max}} = 60$ vertices. We assume that every

vertex of the truncated icosahedron represents a ligand that can bind to a receptor. For the dynamics we map the system onto the one-dimensional model for the spherical particle of the previous section to compute the forward and backward rates as

$$g_N = \nu_{\mathrm{w}} N_{\mathcal{E}}, \quad r_N = \nu_\kappa + \nu_\sigma x + \nu_\tau \frac{1-x}{\sqrt{1-(1-x)^2}} N_{\mathcal{E}}, \tag{4.29}$$

where $x = 2(N-1)/(N_{\max}-1)$. In contrast to before, $N_{\mathcal{E}}$ now equals the number of ligands at the edge, i.e. occupied sites that are adjacent to at least one free ligand. In Fig. 4.12 the distribution of uptake times T_{sim} (a) and (d), the number of edge sites $N_{\mathcal{E}}$ as a function of time (b) and (e) and the last bound ligand are shown (c) for weak noise and favourable uptake ($W = 0.4\,\mathrm{mJ/m^2}$) and (f) intermediate noise and unfavourable uptake ($W = 0.04\,\mathrm{mJ/m^2}$). As expected, for weak noise we find fast uptake and a large number of edge sites, whereas for intermediate noise and unfavourable uptake we find slower uptake and a smaller number of edge sites. For unfavourable uptake the particle is only weakly bound to cell surface receptors on average. Therefore, for an ensemble of many particles only few get taken up per time leading to a small number of edge sites. In addition, we find for weak noise in (c) that the last ligand is positioned opposed to the first bound ligand (indicated by the black arrow) and for intermediate noise in (f) that every ligand has equal probability to be the last ligand. The reason is that the for unfavourable uptake and intermediate noise the particle stays attached at the membrane for a long time and therefore the information of the first bound ligand is lost, similar to the result for the parallel cylinder.

4.5.3 Uptake vs. diffusive wandering of a parallel cylinder

This finding brings up the question if the particle might also wander at the cell membrane before it is finally taken up, given that the particle stays attached to the cell membrane. In the deterministic model partial uptake implies a stable state, independent of time, whereas in the stochastic model a partial uptake state can only exist for a limited time. Here fluctuations will keep the particle in motion, i.e. ligand-receptor bonds will continuously open and close, which will finally lead to uptake. Therefore, it is tempting to speculate that an extensive uptake time translates into an uptake length which the particle wanders at the cell membrane before it is taken up.

We start by considering a parallel cylindrical particle partially bound at the cell membrane. Due to fluctuations the number of bound ligands will fluctuate around the average. Following the same reasoning as before the particle will be symmetrically bound to the cell membrane without overhangs. Effectively, this implies that the particle performs a random walk at the cell membrane caused by the binding (unbinding) of cell surface receptors. To quantify the distance the particle would wander, we estimate the root mean square displacement (RMSD) for a symmetric random walk.

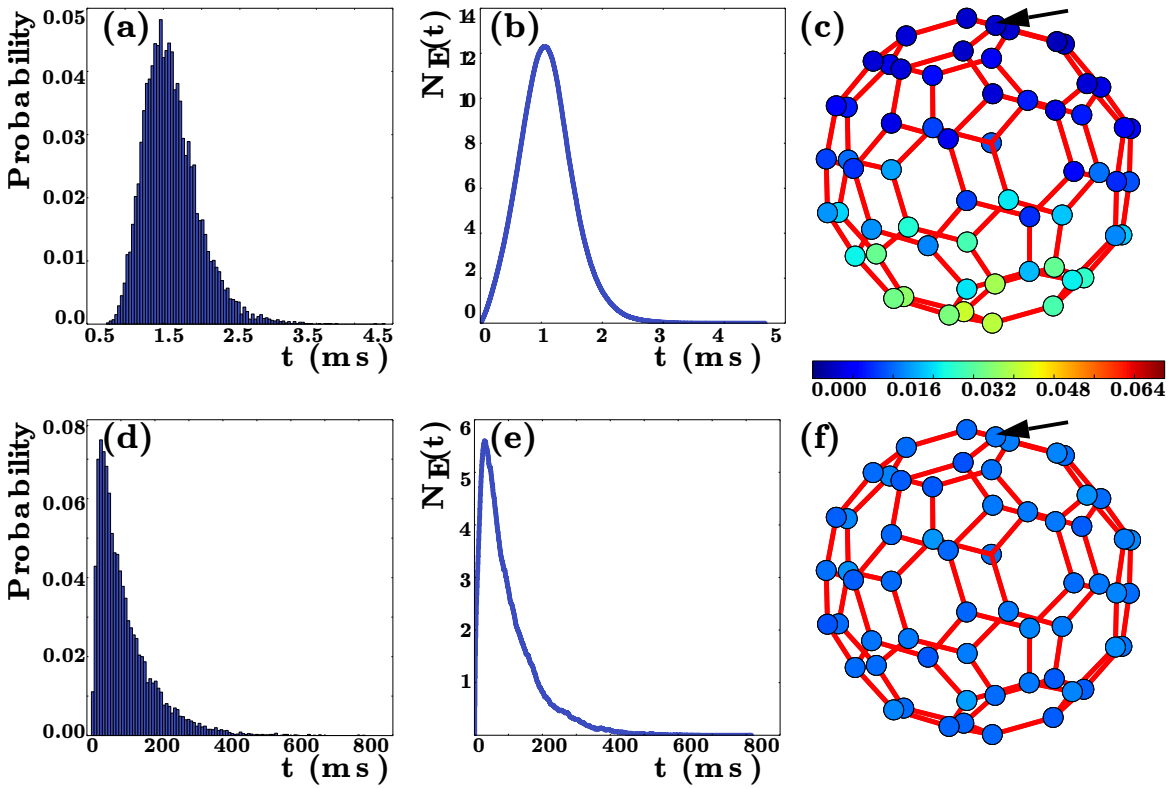

Figure 4.12 | Uptake of a spherical (icosahedral) particle with $N_{\max} = 60$ homogeneously distributed ligands for weak fluctuations ($W = 0.4\,\mathrm{mJ/m^2}$) **(a)**-**(c)** and intermediate fluctuations ($W = 0.04\,\mathrm{mJ/m^2}$) **(d)**-**(f)**. Distribution of mean uptake times **(a)** and **(d)**. Mean number of edge ligands $N_\epsilon(t)$ as a function of time **(b)** and **(e)**. Probability of being the last bound ligand during uptake **(c)** and **(f)**. The black arrows point to the first bound ligand. Results are averages over $N_{\mathrm{sim}} = 10^4$ simulation runs.

In the limit of vanishing membrane tension ($\sigma = 0$) we calculated the uptake time analytically in chapter 3 and [124]. When uptake is unfavourable and fluctuations are intermediate it increases exponentially as $T \sim D^{\parallel}/(\nu_{\mathrm{up}}^{\parallel})^2 \exp(\pi|\nu_{\mathrm{up}}^{\parallel}|/D\,\|)$. We can then calculate the RMSD for a one-dimensional random walk given by $\langle x^2\rangle = 2DT$, with $D = (\Delta x)^2/(2\Delta t)$, $\Delta x = 2\pi R/N_{\max}$ and $\Delta t = 1/(2(\nu_{\mathrm{w}}^{\parallel} + \nu_{\kappa}^{\parallel}))$. Using typical numbers we find $D = 0.01\,\mu\mathrm{m}^2/\mathrm{s}$, which is large compared to the diffusion constant of integrin clusters $D = 0.001\,\mu\mathrm{m}^2/\mathrm{s}$ in the cell membrane [155]. As a consequence, for huge uptake times, i.e. when uptake is unfavourable and fluctuations become important the RMSD can be of the order of $\sim \mu$m before uptake occurs.

4.6 Conclusion

Based on chapter 3 we here studied the contribution and effect of the free membrane on particle uptake mediated by ligand-receptor binding. First, we calculated the shapes of the membrane during particle uptake by solving the shape equations numerically.

From these shapes the energy of the free membrane was then determined and compared to two phenomenologically deduced energies, a line tension energy and an extended line tension. A line tension has been already earlier suggested to represent the energy of the free membrane [83] and it also may occur in case of membranes displaying lipid domains and/or curvature generating proteins, as e.g. clathrin triskelia [154]. The extended line tension represents a pure phenomenological representation of the free membrane. Our results show that the energy of the free membrane contributes up to $\sim 20\%$ relative to the energy of the adhered membrane. We found that qualitatively both representations of the energy of the free membrane are reasonable.

Next, we analysed the deterministic uptake dynamics of cylinders that are either oriented normal or parallel to the cell membrane and spheres. We calculated the corresponding phase diagrams for uptake as a function of aspect ratio and the dimensionless parameter $\alpha^{\parallel}$ that represents membrane tension. We found that short cylinders get taken up faster in normal orientation whereas long cylinders as taken up faster in parallel orientation. For increasing values of $\alpha^{\parallel}$ only normal cylinders get taken up completely. We speculate that cylinders that are initially oriented parallel to the membrane might reorient normal to the membrane to get taken up completely. We note that these results qualitatively agree with computer simulations that have previously shown that cylindrical particles might reorient from the parallel orientation to the normal orientation during uptake [131]. By calculating dynamic phase portraits for the sphere as a function of dimensionless parameters and including the free membrane by either a line tension or an extended line tension, we could show that either full, partial or no uptake can occur. Subsequently, we studied stochastic particle uptake dynamics by computer simulations for the two cylinders and the sphere, and in contrast to chapter 3 now with line tension. We found very similar behaviour compared to chapter 3. Due to stochasticity spherical particles can get taken up faster compared to parallel cylindrical particles.

Finally, we investigated the effect of ligand binding on the particle positioning by stochastic simulations. For weak noise and favourable uptake we found for both, cylindrical and spherical particles that the last bound ligand is located opposed to the first bound ligand. For intermediate noise and unfavourable uptake we found that every ligand has equal probability to be the last ligand. Thus, we concluded that particles could wander at the cell membrane. One could speculate that they wander to a distinct membrane region with enhanced receptor density enabling uptake. Within the cellular context we find very similar behaviour. For example, Reovirus was reported to wander at the cell membrane prior to internalisation. However, it is still unclear how the virus moves exactly [156]. Furthermore, experiments on supported lipid bilayers [157] and simulations [158] have shown the motion of virus particles.

5 Dynamics of substrate-attached virus and nanoparticle uptake

This chapter is based on a collaboration with experimentalists [159]. In section 5.2 we shortly present the experimental results of our collaboration partners which can be found in detail in [159], or in the PhD thesis of Tina Wiegand [160]. In section 5.3 and 5.4 we present our own results on modelling uptake of substrate-attached particles.

5.1 Introduction

In order to enter cells viruses and nanoparticles can adhere to the membrane and bind to cell surface receptors. By that they overcome membrane bending and tension energy. In chapter 3 and 4 we theoretically studied uptake, in particular considering the interplay between particle shape, stochasticity and dynamics. In this chapter we broaden or approach and compare and adapt our theoretical models to an experimental study. To measure forces that cells exert on virus particles during uptake one traditionally uses optical tweezers [161] or atomic force microscopy [139, 140]. These experimental techniques are restricted to the dorsal side of a cell. In the body, however, viruses could also come in contact and interact with cells from the ventral side. Hence, in the here presented experiments extracellular tension sensors are used to measure forces at the ventral side of cells as interactions with the surrounding extra-cellular matrix (ECM) might be important for the uptake of viruses. Thus, in order to investigate how cell-matrix interactions influence cellular uptake we study the experimentally measured uptake forces at the ventral side of adherent cells of substrate-attached viruses or nanoparticles and compare the results to our theoretical model.

5.2 Experimental setup and results

5.2.1 Cellular forces acting on substrate-attached virus particles

First, the forces in the initial step of virus uptake are studied, where the experimental setup is sketched in Fig. 5.1 (a). In the experiments cells are seeded onto a polyethylene glycol (PEG)-substrate on which cRGD ligands and tension sensors (to which Reovirus particles are tethered) are attached, to allow for cells to spread and adhere via integrins [162] and to measure uptake forces.

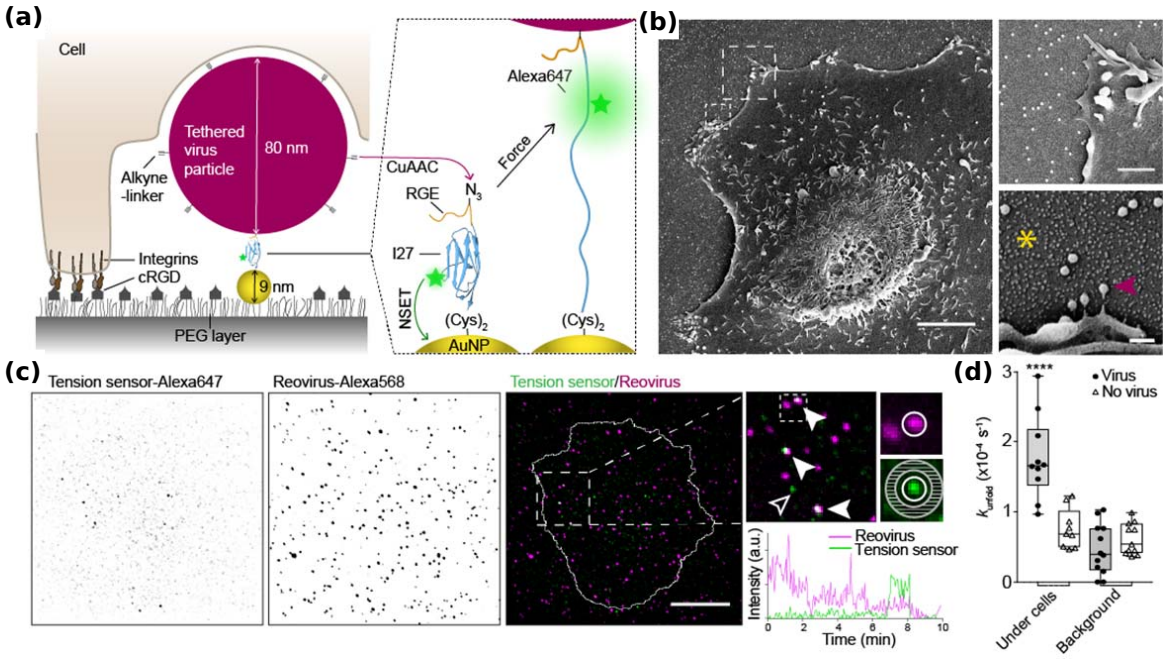

Figure 5.1 | Detection of forces by molecular tension sensors during the first step of cellular uptake of single virus particles at the ventral side of cells. **(a)** A cell adhering via integrins (brown) to cRGD peptides (grey) coated onto a PEG layered substrate pulls at a substrate-attached virus particle (magenta). The virus particle is attached onto the molecular tension sensor by alkyne linkers using click chemistry (CuAAC). The molecular tension sensor consists of a gold nanoparticles (AuNPs, 9 nm, gold) on which a titin I27 molecule (blue) is tethered. Upon acting a force on the virus particle the titin molecule unfolds and the fluorescence intensity of the quenched label (Alexa647) increases. **(b)** A BSC-1 cell is seeded onto a layer of AuNPs (left, scale bar 5 μm) and imaged using SEM. Magnifications (upper right, scale bar 1 μm, lower right, scale bar 200 nm) show the AuNPs (asterisk) and virus particles (arrowhead). **(c)** Image (using time-lapse TIRF microscopy) of molecular tension sensors (green), fluorescently labeled Reoviruses (magenta) and cell outline (white). Scale bar, 10 μm. Arrowheads indicate that unfolded tension sensors co-localise with Reoviruses whereas hollow arrowheads indicate a nonspecific signal from tension sensors (top right). Fluorescence intensity of a tension sensor (green) and Reovirus (magenta) as functions of time indicate the timepoint when the tension sensor unfolds (bottom right). **(d)** Rates with which the tension sensors unfold under cells (left) and in background (right) with and without viruses attached to tension sensors. Box-plots show median value ±95%, confidence interval, minimum and maximum value. Figure taken and adapted from Wiegand et al. [159].

The idea behind the tension sensor is that it unfolds under force, which leads to an increase in fluorescence intensity that can be detected. Hence, tension sensors consist of a gold-nanoparticle (AuNP) that is bound to the substrate and to a fluorescently labeled protein domain I27 of a titin molecule [163]. The fluorescence intensity of the label (Alexa647) is distance-dependently quenched by the AuNP via nano-metal surface energy transfer (NSET). Hence, upon unfolding the fluorescence intensity of the titin molecule increases and thus force is detected. The titin molecule is attached to a Reovirus particle. As the capsid of Reovirus contains $\lambda 2$ proteins it can bind to

integrins at the membrane [164]. Thus, forces transduced via integrins could mediate Reovirus uptake, leading to an fluorescence intensity increase. By using scanning EM (SEM) one observes that single virus particles are covalently bound to the substrate (see Fig. 5.1 (b)). In Fig. 5.1 (c) the fluorescence intensity of the tension sensor, of Reovirus and the merge of both with the cell outline is shown. The plot at the bottom right shows the fluorescence intensity of a tension sensor and Reovirus as functions of time. The increasing intensity of the tension sensor indicates the timepoint when the tension sensor unfolds, probably due to the interactions of the virus and the cell membrane. We note the stochastic character of such trajectories, motivating our modelling approach in section 5.4. One expects the operating forces to be around $\sim 40\,\mathrm{pN}$ as these are the necessary forces required to unfold the tension sensor [163]. Fig. 5.1 (d) shows the rates with which the tension sensors unfold under cells (left) and in background (right) with and without viruses attached to tension sensors. Clearly, the rate with which tethered tension sensors unfold in the presence of cells is larger compared to the background without cells and/or without viruses. To conclude, one finds that cells actively pull at virus particles with forces of at least 40 pN, in agreement with reported values for human enterovirus [140] or pseudo-typed rabies virus [139].

5.2.2 Forces and dynamics during virus particle uptake

To test whether the cellular forces, exerted on the virus particle, lead to uptake, the experimental setup is adapted as sketched in Fig. 5.2 (a). Now virus particles are non-covalently attached to the substrate by biotin-neutravidin bonds. Interestingly, one also observes virus uptake under these circumstances as one finds in Fig. 5.2 (b) virus factories, i.e. regions of viral replication (green) and virus particles (magenta) close to the cell nucleus (blue). The arrowheads (white) point towards subregions of the substrate where virus particles are removed due to interactions with the cell. In Fig. 5.2 (c) the dissociation rate of virus particles from biotin-neutravidin bonds under cells and in the background is shown. Clearly, virus particles at which cells exert forces dissociate faster compared to virus particles in the background. In order to quantify the kinetics of uptake, the number of virus particles that are removed from the substrate is analysed. Fig. 5.2 (d) shows snapshots of virus particles (magenta), the cell and the merged image at three timepoints. The first timepoint t_0 corresponds to 30 min after seeding the cell. Importantly, the number of virus particles decreases strongly under the cell. Fig. 5.2 (e) shows the number of surface bound virus particles $N(t)$, normalised to the number N_0 at t_0 as a function of time. The dissociation of virus particles can be fitted by an exponential of the form $N(t)/N(t_0) = \exp(k_{\mathrm{off}}t)$. From the fit one can calculate the dissociation rate for HeLa and U373 cells $k_{\mathrm{off}}^{\mathrm{HeLa}} = (0.9 \pm 0.5) \cdot 10^{-4}\,\mathrm{s}^{-1}$ and $k_{\mathrm{off}}^{\mathrm{U373}} = (1.0 \pm 0.8) \cdot 10^{-4}\,\mathrm{s}^{-1}$.

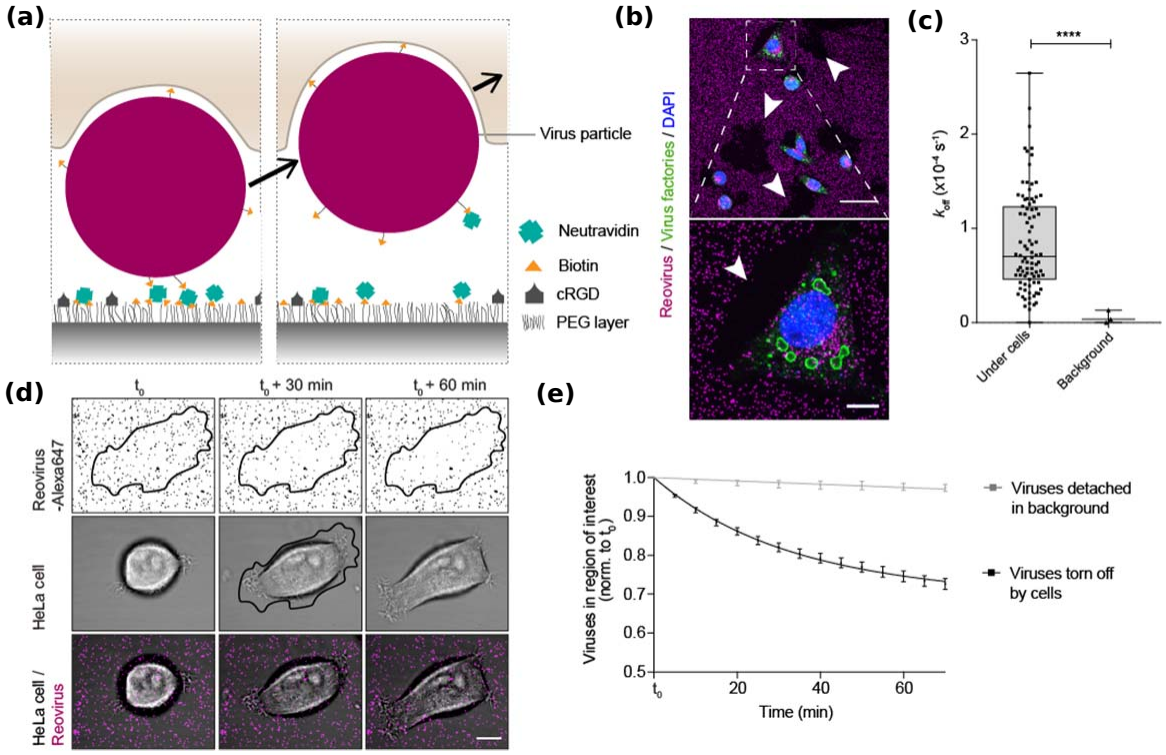

Figure 5.2 | Detection of forces during uptake of substrate-attached virus particles by biotin-neutravidin bonds at the ventral side of cells. **(a)** A cell (brown) adhering to cRGD peptides (grey) coated onto a PEG-layered substrate takes up a virus particle (magenta) that is substrate-attached by biotin-neutravidin bonds (orange-green). **(b)** Immunostaining of virus factories (green), virus particles (magenta) and the cell nucleus (blue). The arrowheads (white) point towards subregions of the substrate where virus particles are removed due to interactions with the cell. Scale bars 50 μm (top) and 10 μm (bottom). **(c)** Dissociation rate of virus particles from biotin-neutravidin bonds under cells and in the background. Box-plots as before. **(d)** Confocal images of three timepoints of virus particles (magenta), the cell and the merged image. The first time t_0 corresponds to 30 min after seeding the cells. **(e)** The number of surface bound virus particles $N(t)$, normalised to the number N_0 at t_0 as a function of time and exponential fit to the data. Figure taken and adapted from Wiegand et al. [159].

Without a cell that exerts force, i.e. in the background the dissociation rate is significantly smaller $k_{\text{off}}^0 = (7.2 \pm 1.0) \cdot 10^{-6}\,\text{s}^{-1}$, which is in agreement with values reported for streptavidin [165] and avidin [166]. In order to estimate the uptake force one can assume that the ensemble of virus particles is represented by the average particle on which a cell exerts a constant force. In this case the dissociation rate can be calculated using Bell's model [167], which describes how an external force F tilts the energy landscape and therefore increases the bond dissociation rate. Bell's model states $k_{\text{off}} = k_{\text{off}}^0 \exp(F\Delta x/k_{\text{B}}T)$, where one assumes that the biotin-neutravidin bond breaks for $\Delta x = 0.5\,\text{nm}$ [168]. Using the dissociation rates from before the corresponding forces equal $F^{\text{HeLa}} = 21 \pm 6\,\text{pN}$ and $F^{\text{U373}} = 22 \pm 7\,\text{pN}$.

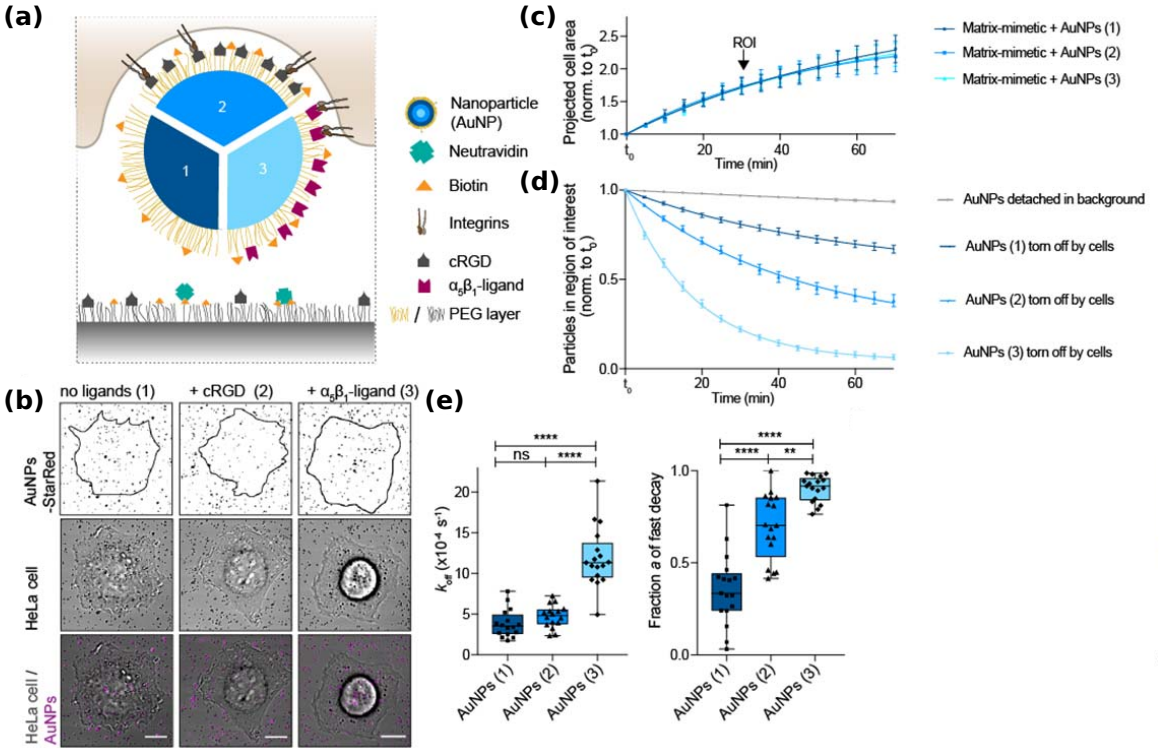

Figure 5.3 | Cellular uptake of nanoparticles at the ventral side of cells enhanced by receptor-ligand interactions. **(a)** A cell adhering via integrins (brown) to cRGD peptides (grey) coated onto a PEG layered substrate takes up a substrate-attached gold nanoparticle (AuNP) (blue). The nanoparticle is attached by biotin-neutravidin bonds (orange-green) and either binds non-specifically (1), by cRGD peptides (2) or $\alpha_5\beta_1$ ligands (3) to integrins. **(b)** Confocal images of the three nanoparticle preparations after $t = t_0 + 70\,\text{min}$, where t_0 corresponds to 30 min after seeding the cells. AuNPs (magenta), HeLa cell (grey) and merged image are shown. **(c)** Normalised projected area (to the cell area at t_0) of cells that spread on matrix-mimetic surfaces as a function of time for the three nanoparticle preparations. **(d)** Normalised number of nanoparticles (to the number at t_0) that are still substrate-attached as a function of time for the three nanoparticle preparations and fit of a two-phase exponential decay to the data. **(e)** Fast decay rate (k_{off}) and fraction of fast decay a for the three nanoparticle preparations. Box-plots as before. Figure taken and adapted from Wiegand et al. [159].

5.2.3 Forces and dynamics during nanoparticle uptake

To test the effect of receptor-ligand interactions during cellular uptake one can mimic virus particles by gold nanoparticles (AuNPs) of $\sim 100\,\text{nm}$ diameter with different nanoparticle surface preparations as a model system. Here, three different surface treatments are studied. (1) AuNPs are coated by a PEG layer such that the NPs bind non-specifically to the cell membrane. (2) AuNPs are coated by cRGD peptides and (3) AuNPs are coated by $\alpha_5\beta_1$ ligands to integrins at the cell membrane (see Fig. 5.3 (a)). Thus, the different surface preparations are supposed to change the adhesion energy

of the NPs. The uptake of substrate-attached NPs (by biotin-neutravidin bonds) is then monitored in confocal microscopy for the three NP preparations. Fig. 5.3 (b) shows images of AuNPs, HeLa cells and the merged image after $t = t_0 + 70\,\mathrm{min}$, where t_0 corresponds to 30 min after seeding the cells. As the cells are spreading on an ECM-mimetic surface it is possible to quantify their projected area. In Fig. 5.3 (c) the projected cell area normalised to the cell area at t_0 is shown as a function of time for the three nanoparticle preparations. Importantly, the spreading behaviour is similar in all three cases and does not dependent on the fact whether or not NPs present additional binding sites. In order to quantify the uptake dynamics the normalised number of NPs (to the number at t_0) that are still substrate-attached is shown as a function of time for the three nanoparticle preparations in Fig. 5.3 (d). Next, a two-phase exponential decay

$$N(t) = a \exp\Big(- k_{\mathrm{off}} t\Big) + (1 - a) \exp\Big(- k^0_{\mathrm{off}} t\Big)\,, \tag{5.1}$$

is fitted to the data, where a is the fraction of nanoparticles that are internalised during the spreading phase with fast decay rate k_{off} and $(1 - a)$ is the fraction of nanoparticles that dissociates with the background decay rate k^0_{off}. Interestingly, HeLa cells could take up NPs even without specific surface coating. In this case one finds the rate of $k^{(1)}_{\mathrm{off}} = (3.2 \pm 0.8) \cdot 10^{-4}\,\mathrm{s}^{-1}$. NPs with cRGD surface coating or $\alpha_5\beta_1$ ligands are taken up faster with rates $k^{(2)}_{\mathrm{off}} = (3.9 \pm 0.5) \cdot 10^{-4}\,\mathrm{s}^{-1}$ and $k^{(3)}_{\mathrm{off}} = (9.4 \pm 0.3) \cdot 10^{-4} s^{-1}$, respectively. The corresponding uptake forces can be calculated similar to before to $F^{(1)} = 28.0 \pm 2.0\,\mathrm{pN}$, $F^{(2)} = 29.7 \pm 1.1\,\mathrm{pN}$ and $F^{(3)} = 37.1 \pm 1.3\,\mathrm{pN}$. Importantly, also the fraction of internalised particles increases with the adhesion energy of the surface coating, see Fig. 5.3 (e). To conclude, one finds that an increased adhesion strength affects the uptake twofold. Both the probability of initial contact and the exerted force on the NP, increases.

5.3 Modelling nanoparticle uptake

5.3.1 Geometry and uptake energy

In order to study the adhesion energy density W and force F theoretically during particle uptake we model the uptake process similar to chapter 3 and 4. We consider the substrate-attached NP as a sphere with radius $R_{\mathrm{NP}} = 64\,\mathrm{nm}$ corresponding to the hydrodynamic radius of the functionalised AuNP. The particle can be covered with homogeneously distributed ligands and can adhere to membrane surface receptors along the area A_{ad}.

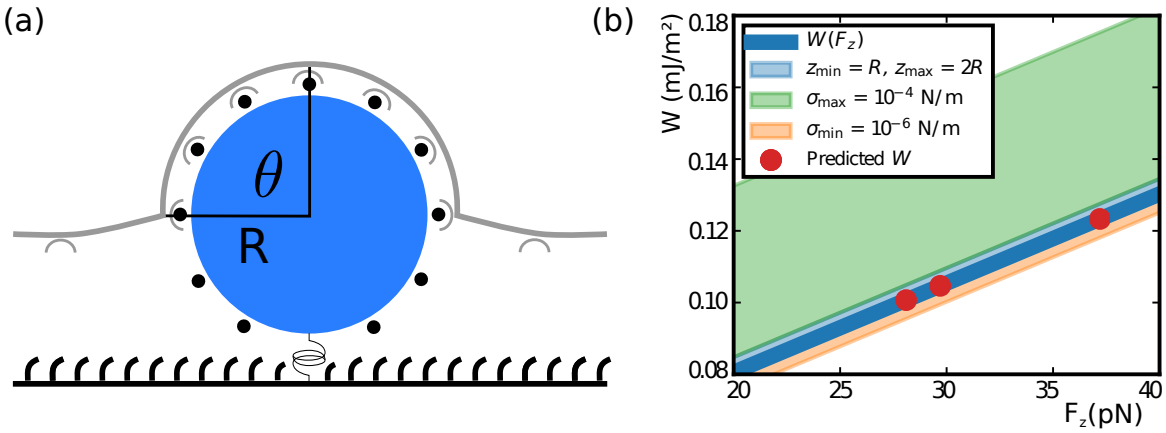

Figure 5.4 | Nanoparticle uptake. **(a)** In the model the particle (blue) with radius $R = 64\,\text{nm}$, immobilised by a tension sensor (spring) can be homogeneously covered with ligands (black dots) and adhere to cell surface receptors (grey). As the free membrane is 80 nm above the substrate and the PEG layer is around 15 nm thick we assume that initially the virus particle is already halfway wrapped. **(b)** Calculated adhesion energy as a function of uptake force (blue solid line) assuming typical parameter values as summarised in Table 5.1. The blue region shows the adhesion energy assuming that the tension sensor either breaks immediately or only if the particle is completely taken up. The green (orange) region shows the adhesion energy assuming a up to ten fold enhanced (reduced) membrane tension. The red points show the predicted adhesion energy for the measured uptake forces of the three differently coated nanoparticles.

We describe the progress of particle uptake by the uptake angle θ as sketched in Fig. 5.4 (a). We assume that the free membrane is 80 nm above the substrate, as measured recently [169] and that the PEG layer is around 15 nm thick. Hence, initially the NP is already halfway wrapped. In our model uptake is driven by the energetic gain of particle adhesion to the cell membrane, either specifically to cell membrane receptors or non-specifically. In contrast, uptake is counteracted by the energetic cost for bending the membrane, increasing the membrane area and also by the tension sensor as long as the uptake force is smaller than its rupture force. Following the same arguments as in chapter 3, we only consider the energy of the membrane that is adhered to the NP along the area $A_{\text{ad}} = 2\pi R^2(1-\cos(\theta))$, assuming the shape of a spherical cap. The total free energy of NP uptake then reads [86]

$$\begin{aligned} E_{\text{total}} &= -W A_{\text{ad}} + \frac{1}{2}\left(2\kappa H^2 A_{\text{ad}} + \sigma \Delta A_{\text{ad}}\right) \\ &= \left(2\pi\kappa + \frac{\sigma\pi R^2(1-\cos\theta)}{2} - W\right)(1-\cos\theta)\,, \end{aligned} \tag{5.2}$$

with the first term representing the adhesion energy gain, where W is the adhesion energy density times the adhering area A_{ad}. The second term is representing the membrane bending energy where κ is the bending rigidity and $H = 1/R$ the mean membrane curvature and the last term is representing the energetic cost for increasing

Table 5.1 | Used parameter values in the model.

Parameter	Value	Reference
Bending rigidity κ	$25\,\mathrm{k_B}T$	[120, 34]
Membrane tension σ	$10^{-5}\,\mathrm{N/m}$	[31]
NP radius R_{NP}	64 nm	Measured [159]
Rupture length z	10 nm	Estimated

the membrane area, where σ is the membrane tension and $\Delta A_{\mathrm{ad}} = A_{\mathrm{ad}}/2(1-\cos\theta)$ the area increase. As we assume that the particle is initially halfway wrapped, the energy contributions counteracting uptake are reduced by a factor of 2.

5.3.2 Uptake force

As the particle adheres to the cell membrane it experiences a force in z-direction [85]. This thermodynamic uptake force can be calculated by taking the derivative of the total energy with respect to z

$$F_z = -\frac{\mathrm{d}E_{\mathrm{total}}}{\mathrm{d}z} = 2\pi W R - \frac{2\pi\kappa}{R} - \pi\sigma z\,, \tag{5.3}$$

where we used $z = (1-\cos\theta)\,R$ and $\sin\theta(\partial\theta)/(\partial z) = 1/R$. Then, the adhesion energy can be calculated as a function of the uptake force

$$W(F_z) = c_0 + c_1 F_z\,, \tag{5.4}$$

with the constants $c_0 = \kappa/(R^2) + \sigma z/(2R)$ and $c_1 = 1/(2\pi R)$. Importantly, the adhesion energy density or force depends heavily on the rupture length z and membrane tension σ.

5.3.3 Adhesion energy as a function of uptake force

In Fig. 5.4 (b) the adhesion energy as a function of the uptake force (blue solid line) is shown, assuming the parameter values which are summarised in Table 5.1. As the membrane tension and rupture length have not been explicitly measured in the experiments we use typical values. The red points indicate the predicted adhesion energy for the uptake forces of the three differently coated nanoparticles which are also summarised in Table 5.2. In addition, the blue region shows the adhesion energy assuming that the tension sensor either breaks immediately $z = 0\,\mathrm{nm}$ or only if the particle is completely taken up $z = 64\,\mathrm{nm}$. The green (orange) region shows the adhesion energy assuming an up to ten fold enhanced (reduced) membrane tension. Comparing nanoparticle (1) and (2) as well as (1) and (3) we find an additional

Table 5.2 | Predicted adhesion energy density

Nanoparticle coating	Force F_z (pN)	Adhesion energy density W (mJ/m^2)
(1) Non-specific	28.1	0.101
(2) cRGD	29.7	0.105
(3) $\alpha_5\beta_1$	37.2	0.123

adhesion energy of $\Delta W_{12} = 0.004\,\mathrm{mJ/m^2}$ and $\Delta W_{13} = 0.022\,\mathrm{mJ/m^2}$. By using the additional adhesion energy $\Delta W \approx 0.02\,\mathrm{mJ/m^2}$, we can estimate the number of ligands onto the nanoparticle that bind to cell surface receptors on average. Assuming that a ligand-receptor bond typically contributes a binding energy of $\Delta\epsilon = 10\,\mathrm{k_B}T$ we find $N = \Delta W 4\pi R^2/\Delta\epsilon = 25$ additional ligands, which is comparable to the number of ligands onto the surface of Reovirus (compare chapter 3).

Importantly, we note that in our model the predicted adhesion energy strongly depends on the details of the tension sensor and the mechanical state of the cell. Thus, in order to study this effect, the uptake force is plotted as a function of membrane tension and rupture length in Fig. 5.5. Comparing the naked NP (which adheres non-specifically) and the NP coated with $\alpha_5\beta_1$ ligands in (a) and (b), we find that due to the surface coating the uptake force is strongly increased. In addition, we find that both a larger rupture length and membrane tension decrease the uptake force.

In conclusion, our model predicts the adhesion energy of coated NPs from experimentally measured uptake forces. The predicted values agree with typical adhesion energies [85].

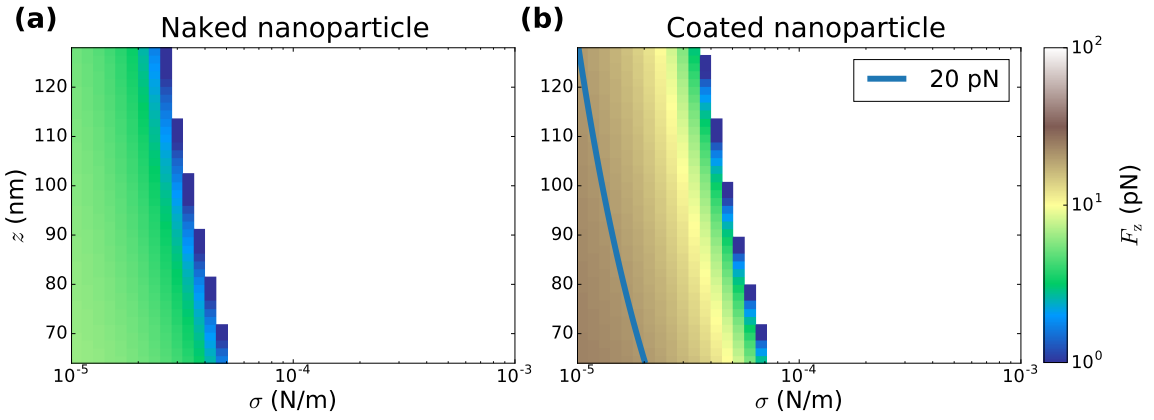

Figure 5.5 | Comparison of the uptake force F_z as a function of membrane tension σ and rupture length z generated by a naked **(a)** and coated **(b)** NP. In **(b)** also the contour on which the uptake force equals 20 pN is shown (blue line).

5.4 Modelling uptake of substrate-attached particles

5.4.1 Deterministic approach

In chapter 3 and 4 we have studied the stochastic dynamics of cellular uptake of free virus and nanoparticles. Now we study the dynamics of substrate-attached particles as sketched in Fig. 5.6 (a). Due to the stochastic ligand-receptor interactions of the particle and the cell membrane the substrate-attachment ruptures (sketched as a spring) and the particle is taken up. Importantly, and in contrast to chapter 3 and 4, here we only consider spherical particle geometries and neglect for simplicity any contribution of the free membrane parts or of a line tension. We study two models for the tension sensor. First, we model the tension sensor as a linear spring and secondly, as a polymer that behaves like a worm-like chain (WLC), corresponding to a more realistic scenario. In order to include the substrate-attachment in the deterministic model we rewrite the force balance equation from chapter 3, (see Eq. (3.4)) which now reads

$$F_{\text{friction}} = \begin{cases} F_{\text{up}} - F_z^s & \text{for} \quad F_z < F_{\text{r}} \\ F_{\text{up}} & \text{for} \quad F_z \geq F_{\text{r}}\,, \end{cases} \tag{5.5}$$

where F_z^s is the force that the tension sensor exerts (tangential to the particle as a projection of the force F_z in z-direction) as long as it is not ruptured (because the rupture force F_{r} is not reached yet). Importantly, F_z depends on the exact choice of our model, i.e. for the linear spring it holds $F_z = k_{\text{z}} z$, where z is the extension and k_{z} is the spring constant, and for the WLC $F_z = \mathrm{k_B}T/(l_{\text{p}})\left(z/L) + 1/4\,(1 - z/L)^2 - 1/4\right)$, where l_{p} is the persistence length of the tension sensor and L its total length [170].

Attachment by a linear spring: In the case of attachment by a linear spring the dynamic equation that can be deduced from the force balance reads (following the same approach as in chapter 3 and 4)

$$\dot{\theta} = \begin{cases} \nu_{\text{up}} - (\nu_\sigma + \nu_{\text{z}})\,(1 - \cos\theta) & \text{for} \quad F_z < F_{\text{r}} \\ \nu_{\text{up}} - \nu_\sigma\,(1 - \cos\theta) & \text{for} \quad F_z \geq F_{\text{r}}\,, \end{cases} \tag{5.6}$$

where $\nu_{\text{z}} = k_{\text{z}}/(2\pi\eta R)$, $\nu_\sigma = \sigma/(R\eta)$ and $\nu_{\text{up}} = \nu_{\text{w}} - \nu_\kappa$ with $\nu_{\text{w}} = W/(R\eta)$ and $\nu_\kappa = 2\kappa/(R^3\eta)$. Consequently, substrate-attachment modelled by a linear spring acts as tension stiffening with effective membrane tension $\sigma_{\text{eff}} = \sigma + k_{\text{z}}/(2\pi)$ until the spring ruptures upon reaching the rupture force F_{r} (or rupture angle θ_{r} equivalently). As soon as the spring is ruptured we get back the uptake dynamics without spring. Eq. (5.6) is solved by adding and subtracting the solution of Eq. (3.6), given by Eq. (3.8), for

the uptake times of substrate-attached and free uptake, respectively

$$T^{\circ}_{\text{det spring}} = \frac{2\arctan\left(\sqrt{1-\frac{2\nu_{\sigma\,\text{eff}}}{\nu_{\text{up}}}}\tan\frac{\theta_{\text{r}}}{2}\right)}{\nu_{\text{up}}\sqrt{1-\frac{2\nu_{\sigma\,\text{eff}}}{\nu_{\text{up}}}}} + \frac{2\arctan\left(\sqrt{1-\frac{2\nu_{\sigma}}{\nu_{\text{up}}}}\tan\frac{\pi}{2}\right)}{\nu_{\text{up}}\sqrt{1-\frac{2\nu_{\sigma}}{\nu_{\text{up}}}}} - \frac{2\arctan\left(\sqrt{1-\frac{2\nu_{\sigma}}{\nu_{\text{up}}}}\tan\frac{\theta_{\text{r}}}{2}\right)}{\nu_{\text{up}}\sqrt{1-\frac{2\nu_{\sigma}}{\nu_{\text{up}}}}}, \tag{5.7}$$

with $\nu_{\sigma\,\text{eff}} = \sigma_{\text{eff}}/(R\eta)$ and the rupture angle $\theta_{\text{r}} = \arccos(1 - F_{\text{r}}/(k_{\text{z}}R))$.

Attachment by a worm-like chain: In the case of attachment by a WLC the dynamic equation that can be deduced from the force balance reads

$$\dot{\theta} = \begin{cases} -\nu_{\text{l}}\left(\frac{R}{L}(1-\cos\theta) + \frac{1}{4(1-\frac{R}{L}(1-\cos\theta))^2} - \frac{1}{4}\right) + \nu_{\text{up}} - \nu_{\sigma}(1-\cos\theta) & \text{for} \quad F_z < F_{\text{r}} \\ \nu_{\text{up}} - \nu_{\sigma}\,(1-\cos\theta) & \text{for} \quad F_z \geq F_{\text{r}}\,, \end{cases} \tag{5.8}$$

where $\nu_{\text{l}} = \text{k}_{\text{B}}T/(\eta l_{\text{p}} 2\pi R^2)$.

Rupture behaviour: In Fig. 5.6 (b) we qualitatively analyse the rupture behaviour of both the linear spring and the WLC where the rupture angle is defined as $\theta_{\text{r}} = \arccos(1 - F_{\text{r}}/F_z)$, using the parameter values shown in Table 5.3, if not varied. The plot on the left shows the rupture angle as a function of the particle radius for a fixed rupture force in blue (red) for the linear spring (WLC). The plot on the right shows the force which the tension sensor exerts on the particle as a function of uptake height for a fixed rupture force. Given the same rupture force F_{r}, the linear spring and the WLC rupture at different extensions z or different rupture angles θ_{r} as the spring constant of the spring as well as the persistence length and total length of the WLC are fixed. In addition, the force builds up linearly for the spring and non-linearly for the WLC. As a consequence, we expect that the spring stronger affects the uptake behaviour compared to the WLC although the assumed rupture force is equal.

5.4.2 Stochastic approach

In chapter 3 and 4 we found that the discrete and stochastic nature of ligand-receptor binding strongly affects the system's uptake behaviour. Therefore, we now consider a stochastic model for substrate-attached particle uptake. Using the same framework as in chapter 3 and 4 we deduce the rates of the ME from the deterministic model. The forward rate does not change and equals $g_N = \nu_{\text{w}} N_{\mathcal{E}}(N)$ and $g_1 = \nu_{\text{w}}\sqrt{N_{\text{max}}}$.

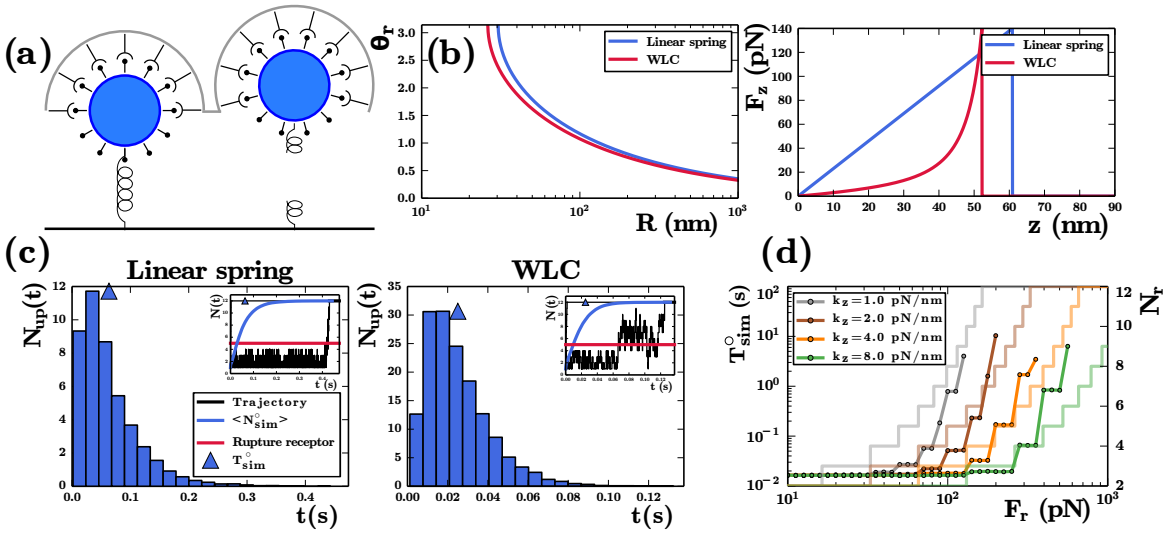

Figure 5.6 | Substrate-attached particle uptake. **(a)** Uptake schematics. The substrate-attached particle is pulled by the cell against a molecular tension sensor. Due to uptake and particle motion in z-direction the tension sensor acts a force F_z on the particle. Beyond the rupture force F_r the tension sensor breaks. **(b)** The rupture angle as a function of the particle radius (left). The force which the tension sensor exerts on the particle as a function of uptake height (right). In both plots the linear spring is shown in blue and the WLC in red. **(c)** Distribution of uptake times for 10^4 trajectories for spring (left) and WLC (right) and mean uptake time (blue triangle). (Inset) Typical trajectories (black) and rupture receptor (red line). **(d)** The mean uptake time T°_sim as a function of the rupture force F_r for different linear springs constants (data points and opaque lines) averaged over 10^4 trajectories per data point with a maximal trajectory length of 10^5 steps. On the right y-axis the rupture receptor N_r is shown (transparent lines).

Attachment by a linear spring: To model the linear spring we rewrite the backward rate as

$$r_N = \begin{cases} \nu_\kappa N_\mathcal{E} + 2\left(\nu_\sigma + \nu_z\right) N_\mathcal{E} \frac{N-1}{N_\mathrm{max}-1} & \text{for} \quad F_z < F_\mathrm{r}, \\ \nu_\kappa N_\mathcal{E} + 2\nu_\sigma N_\mathcal{E} \frac{N-1}{N_\mathrm{max}-1} & \text{for} \quad F_z \geq F_\mathrm{r}\,. \end{cases} \tag{5.9}$$

Attachment by a worm-like chain: Similarly, we rewrite the backward rate of the WLC

$$r_N = \begin{cases} \nu_\mathrm{l} \left(\frac{2\frac{R}{L}(N-1)}{(N_\mathrm{max}-1)} + \frac{1}{4\left(1-\frac{2\frac{R}{L}(N-1)}{(N_\mathrm{max}-1)}\right)^2} - \frac{1}{4} \right) N_\mathcal{E} + \left(\nu_\kappa + \nu_\sigma \frac{N-1}{N_\mathrm{max}-1}\right) N_\mathcal{E} & \text{for} \quad F_z < F_\mathrm{r} \\ \nu_\kappa + \nu_\sigma \left(1 - \cos(\theta)\right) & \text{for} \quad F_z \geq F_\mathrm{r}\,. \end{cases} \tag{5.10}$$

Table 5.3 | Parameters for the uptake of substrate-attached particles.

Parameter	Used value	Ref.
Adhesion energy density	$W = 4.4 \cdot 10^{-2}\,\mathrm{mJ/m^2}$	Estimated, see chapter 3
Bending rigidity	$\kappa = 25\,\mathrm{k_B T}$	[120, 34]
Membrane tension	$\sigma = 0.9 \cdot 10^{-5}\,\mathrm{N/m}$	[87]
Spring constant	$k_\mathrm{z} = 2.3\,\mathrm{pN/nm}$	[171]
Persistence length	$l_\mathrm{p} = 0.38\,\mathrm{nm}$	[171]
Rupture force	$F_\mathrm{r} = 140\,\mathrm{pN}$	Estimated
Tension sensor length	$L = 60.1\,\mathrm{nm}$	Computed
Effective membrane microviscosity	$\eta = 1\,\mathrm{Pa\ s}$	[85]
Particle radius	$R = 90\,\mathrm{nm}$	
Receptor number	$N_\mathrm{max} = 12$	
Thermal energy	$k_\mathrm{B}T = 4.1\,\mathrm{pN\,nm}$	

5.4.3 Results

Fig. 5.6 (c) shows the results of the stochastic simulations using the Gillespie algorithm [121] (compare Appendix A.2) and the parameters listed in Table 5.3. The uptake distribution of 10^4 trajectories for the spring (left) and WLC (right) shows, as expected, that the uptake against the spring consumes more time compared to the uptake against the WLC. The reason is that the substrate-attachment in the spring model affects the particle already when binding to the first receptors, whereas for the WLC the uptake dynamics is affected only later. Considering the mean uptake time (blue triangle) we therefore observe a larger value for the spring compared to the WLC. The inset shows typical trajectories (black) for which we can identify two distinct uptake regimes. First, it takes comparably long for the force sensor to rupture (red line) and secondly, we have free uptake until the particle is fully taken up, which occurs on another timescale. To be precise, the rupture of the tension sensor corresponds in our discrete approach to the binding of the rupture receptor $N_\mathrm{r} = \lceil F_\mathrm{r}(N_\mathrm{max} - 1)/(2Rk_\mathrm{z}) + 1 \rceil$ (where $\lceil\cdot\rceil$ is the ceiling function).
In Fig. 5.6 (d) we consider the mean uptake time as a function of the rupture force for different spring constants k_z. The simulated uptake times (data points and opaque lines) increase with increasing rupture force. Due to the discrete nature of the system the increase occurs step-wise, as an increasing rupture force only results in an increase of uptake time if the spring ruptures later, i.e. while binding an additional receptor upon the rupture force is reached. Thus, we plot the rupture receptor N_r as a function of rupture force (transparent lines) on the right y-axis. The step-wise increase of the uptake time nicely agrees with the step-wise increase of the rupture receptor.

5.5 Conclusion

In the first part of this chapter we discussed experiments that quantified the forces, exerted on virus and nanoparticles at the ventral side of cells during uptake by means of tension sensors. The reported results are in the order of several tens of pN, in agreement with a recent study [140] and our theoretical prediction in chapter 3. By investigating the uptake of nanoparticles with various surface coatings, i.e. adhesion energies, it was demonstrated that an increased adhesion strength leads to reduced uptake times.

In the second part we used the deterministic model of chapter 3 to compute the adhesion energy of nanoparticles during uptake from measured forces and estimated the corresponding number of ligand-receptor bonds. We find qualitative good agreement between the prediction of the adhesion energy of our model and literature values [85]. However, we have to note that our model cannot explain the time scales on which uptake is observed in the experiments, which is not surprising as we neglect several features within our model. First, we do not consider that in the experiment cells are dynamic as they spread and migrate. Thus, it is not clear how the cell membrane makes exactly contact to virus and nanoparticles, how the number of surface receptor varies locally and how the membrane tension is influenced. Secondly, we neglect the role of the actin cytoskeleton and thirdly, we do not consider the formation of the membrane neck. To conclude, we think that the studied experiments are rather complex and many parameters cannot inferred directly (membrane tension, number of involved surface receptors, role of CME). Hence, we suggest to simplify the experimental approach in the future e.g. by using synthetic vesicles which would represent a minimal cell without cytoskeleton. In such experiments one could e.g. study the uptake and forces of substrate-attached synthetic nanoparticles of various shapes. In addition, one could think of using surface attached nanoparticles of various sizes as tension probes [84].

In the last part of this chapter, we then developed a stochastic model for substrate-attached particle uptake similar to chapter 3 and 4. We modelled the tension probes either by a linear spring or a WLC. We showed that the linear spring has the effect of membrane tension stiffening and found that substrate-attachment leads to increased uptake times both for attachment by a linear spring and a WLC. In addition, our results show that the linear spring stronger affects the uptake compared to the WLC. In the future, it would be interesting to investigate the effect of substrate-attachment by several tension probes, which might be relevant from an experimental point of view. In particular, it is not clear how the uptake time would be affected in such a situation.

6 Flat-to-curved-transition during clathrin-mediated endocytosis

This chapter is based on a published manuscript that originates from a collaboration with several experimental groups, at Heidelberg and in the US [172]. More details on the experiments can be found in the publication.

6.1 Introduction

Clathrin-mediated endocytosis (CME) is an essential uptake pathway that relocates membrane or extracellular cargo into the cell to regulate multiple cellular functions and cell homeostasis [173]. During CME, the clathrin coat is assembled to form a clathrin-coated pit (CCP) that after dynamin-mediated scission from the plasma membrane (PM) leads to the formation of a clathrin-coated vesicle (CCV) [174]. This process is coordinated by numerous adaptor and accessory proteins [173, 175]. Electron microscopy (EM) of clathrin-coated structures (CCSs) has shown the architectural complexity of the clathrin meshwork organised into hexagons and pentagons [23, 176]. From this EM analysis, it was proposed that a CCV initiates as a flat clathrin lattice that is then rearranged to form a curved CCP [23, 177, 178]. However, for topological reasons this requires a major ultrastructural rearrangement of the clathrin lattice which appeared to be dynamically difficult and energetically costly [179, 76, 180, 37, 34]. For these reasons, this notion was replaced by a general belief that CCSs grow with a constant curvature (constant curvature model, Fig. 6.1 (a)) [179, 76, 27] and that flat CCSs are distinct from CCPs and serve different purposes [181, 40, 182]. This model was supported by the finding that purified clathrin triskelia self-assemble into curved clathrin baskets in vitro [183, 184]. Recently, correlative light and electron microscopy (CLEM) analyses provided experimental evidence that CCSs first grow flat to their final size and then acquire curvature (constant area model, Fig. 6.1 (a)) [38]. However, this study did not measure the dynamics of CCP formation directly, and it did not identify the cellular factors that might determine when the flat-to-curved transition occurs. Thus, a comprehensive understanding of the dynamic process of coat rearrangement, of the temporal aspects of flat-to-curved transition and of what governs this ultrastructural rearrangement during CME is still missing. In this chapter we combine simple mathematical growth laws and CLEM analysis to provide a comprehensive description of the dynamic ultrastructural rearrangement of

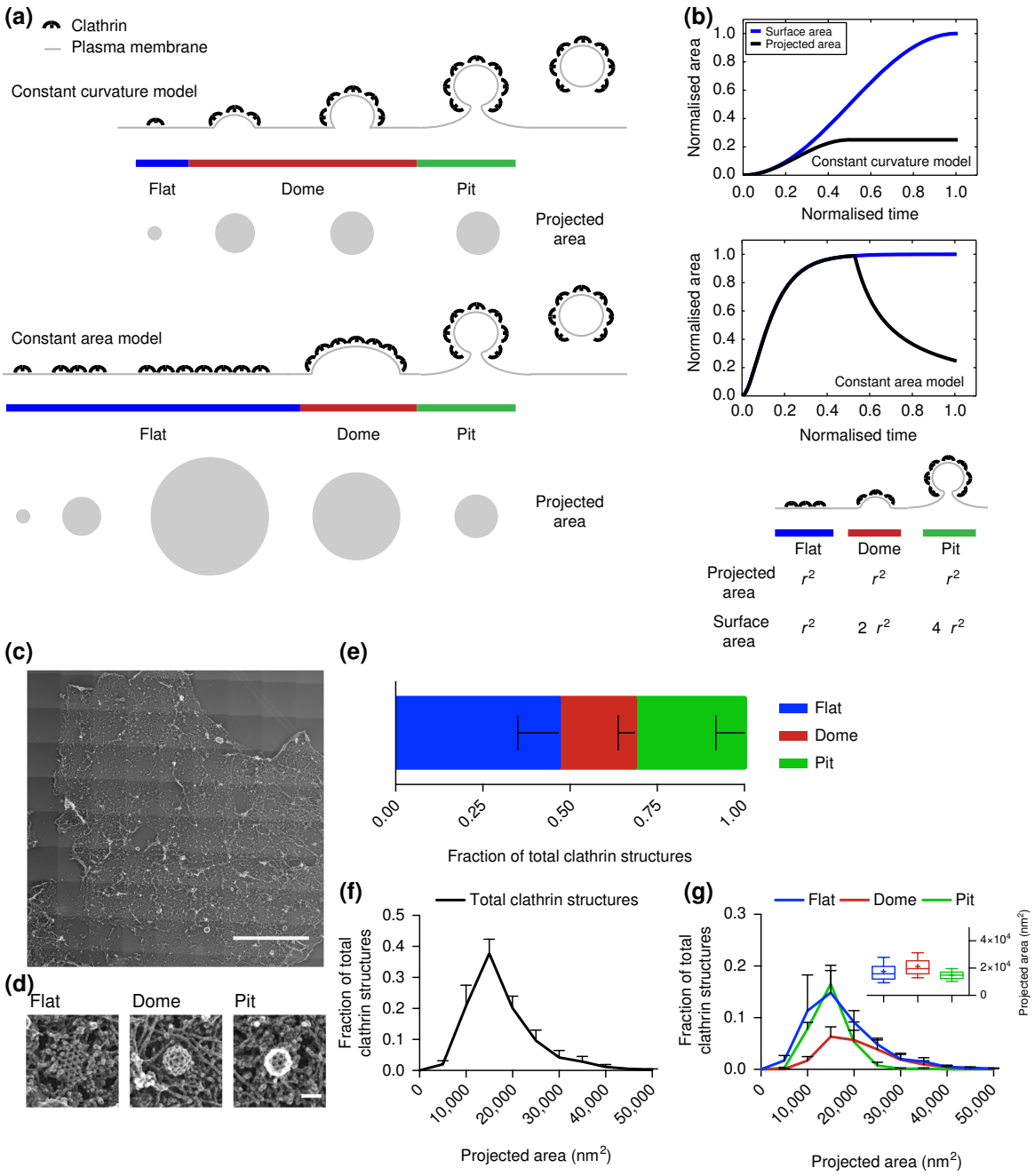

Figure 6.1 | Comprehensive ultrastructural characterisation of CCS in BSC-1 cells by TEM. **(a)** Schematic of the constant curvature and constant area models. The stages of different curvature (flat (blue), dome (red), pit (green)) and the variation of projected area, which can be assessed during TEM imaging, is depicted for both growth models. **(b)** Difference between projected area (black) and surface area (blue) during the course of CCP formation according to the two models. The schematic illustrates the relationship between projected area and surface area for flat, dome (approximately a hemisphere) and pit (approximately a complete sphere) CCSs. **(c)** TEM of metal replica from unroofed PM, overview of whole membrane, scale bar: 10 μm. **(d)** Examples of flat, dome and pit structures, scale bar: 100 nm. **(e)** Fraction of flat (blue), dome (red) and pit (green) CCSs in whole PM of BSC-1 cell. **(f)** Projected area distribution of all CCSs (black) measured by TEM. Continued on the following page.

Figure 6.1 | (g) Projected area distribution of the different clathrin morphologies (flat, dome, pit). A box/whisker plot of the projected area is shown in the inset. Mid-line represents median, cross represents the mean and the whiskers represent the 10 and 90 percentiles. Results are calculated from three different membranes (number of CCSs per membrane: 746, 869 and 739); means with SD are shown. Figure taken and adapted from [172].

the clathrin coat during CME. We demonstrate that CCPs indeed initially grow as flat arrays, but that their reorganisation into curved structures occurs before reaching their full clathrin content. Towards the end of this chapter we correlate this flat-to-curved transition with a change in the AP2/clathrin ratio and show that it is governed by biophysical properties of the PM.

6.2 EM and CLEM analyses of clathrin coats

6.2.1 EM analysis

To address whether CCP formation follows the constant curvature model or the constant area model (Fig. 6.1 (a)) [27], we chose BSC-1 cells, a widely used cellular model to study CME [180, 181, 185]. BSC-1 cells present homogenous CME events in regard to both lifetime and intensity profiles and lack the long-lived flat clathrin-coated plaques [180, 40]. Both models predict different growth profiles for the surface and projected area during CCP formation. The constant curvature model implies that the projected area will quickly be smaller than the surface area. In contrast, the constant area model implies that both projected and surface areas initially show similar growth but then the projected area should drop significantly as bending starts (Fig. 6.1 (b)). To comprehensively characterise the ultrastructural organisation of CCSs in BSC-1 cells, we performed transmission electron microscopy (TEM) of metal replicas from unroofed PMs [23, 186] (Fig. 6.1 (c)). We confirmed that CCSs are not altered by the unroofing procedure using stimulated emission depletion (STED) super-resolution microscopy of intact and unroofed cells. The number and size distribution of CCSs were indeed similar between intact and unroofed cells. CCSs in TEM images of whole PM sheets were counted, categorised as flat, dome or pit structures (Fig. 6.1 (d), (e)) and their size was measured as projected area (Fig. 6.1 (a), (f), (g)). For the constant curvature model, we would expect no flat structures at all and no dome structures that exceed the projected area of pits (Fig. 6.1 (a), (b)). In contrast, our EM data reveal that around 50% of the CCSs in BSC-1 correspond to flat CCSs (Fig. 6.1 (e)) and that a large fraction of the flat and dome structures has a projected area larger than the projected area of the pits (Fig. 6.1 (g)). Since BSC-1 cells do not have clathrin-coated plaques [180, 40], these results demonstrate that the constant curvature model cannot explain the CCS size distribution, in agreement with the recent results by Avinoam

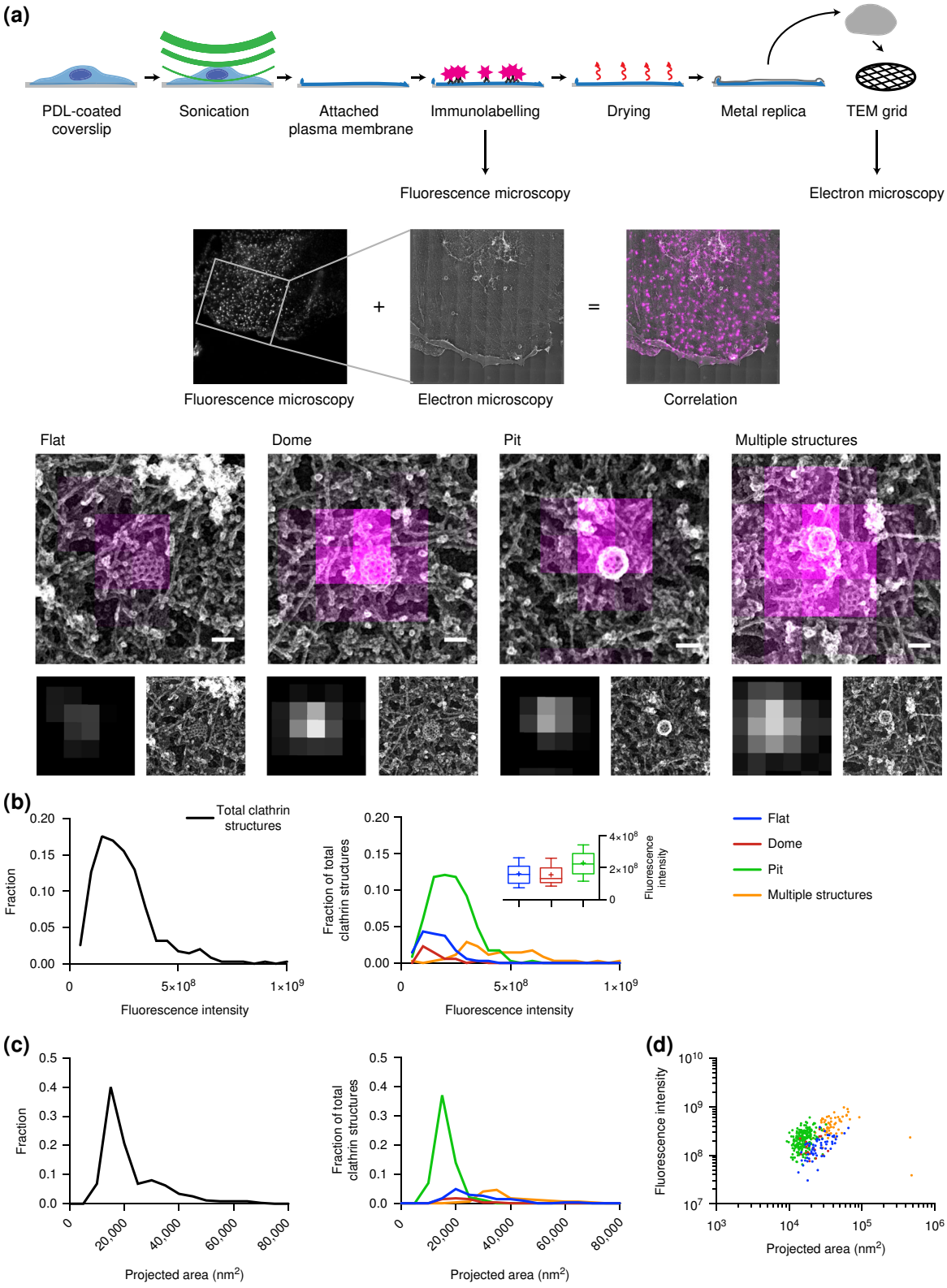

Figure 6.2 | CLEM of CCSs. **(a)** Schematic representation of the CLEM approach. (Upper part) Cells growing on poly-D-lysine (PDL)-coated coverslips were unroofed by sonication. Attached PMs were immunostained and imaged using FM. Samples were then critical-point dried and a metal replica was created and lifted from the sample onto a TEM grid for imaging in TEM. Continued on the following page.

Figure 6.2 | (Middle part) The FM and EM pictures were then correlated to combine their information. Unroofed PMs were immunostained using an anti-clathrin heavy chains antibody. The white inset box represents the area observed by TEM. (Lower part) Examples of flat, dome, pit and multiple structures; top panel: CLEM, lower left: FM lower right: TEM; scale bar: 100 nm. **(b)** Fluorescence intensity distribution (clathrin heavy chain antibody, X22) of all CCSs (black line, left panel) and of flat (blue), dome (red), pit (green) CCSs and multiple structures which cannot be distinguished by fluorescence microscopy (orange) (right panel). A box/whisker plot of the fluorescence intensity is shown in the inset. Mid-line represents median, cross represents the mean and the whiskers represent the 10 and 90 percentiles. **(c)** Projected area distribution of all CCSs (black line, left panel) and of the different clathrin morphologies (right panel). **(d)** Correlation of size and fluorescence intensity of all CCSs sorted by their different morphologies. Graphs show one representative CLEM result with a total of 347 CCSs from one PM. Figure taken and adapted from [172].

et al. [38]. Since the existence of flat CCSs seems to argue in favour of the constant area model, we would expect that some flat structures have the same projected area as the surface area of fully formed pits (Fig. 6.1 (a), (b)). Since the surface area of a spherical pit ($4\pi r^2$, Fig. 6.1 (b)) is four times larger than its projected area (πr^2, Fig. 6.1 (b)), we would expect the mature flat structures to have around four times the projected area of pits (Fig. 6.1 (b)). Instead, we found no flat structures at all with a projected area four times larger than the mean projected area of CCP (Fig. 6.1 (g)). Additionally, the constant area model would imply that the projected area of a dome structure (which resembles a hemisphere) is reduced by a factor of two when converting to a CCP. Instead, we found only a slight increase of the mean projected area of domes compared to pits (Fig. 6.1 (g)), distribution and inset box/whiskers). Together, these observations argue against the constant area model.

6.2.2 CLEM analysis

To further challenge the two growth models, we used a CLEM approach [186, 187] (Fig. 6.2 (a)). BSC-1 cells were immunostained with a clathrin heavy chain antibody and the fluorescence intensity of CCSs (Fig. 6.2 (b)) was correlated to their size and ultrastructural organisation measured using TEM of metal replicas (Fig. 6.2 (c), (d)). CCSs were classified according to their ultrastructural organisation observed by TEM as flat, dome and pit structures. Some of the CCSs could be separated and identified by TEM but not by fluorescence microscopy (FM) due to its lower resolution (i.e., multiple CCSs appearing as one fluorescent object). We classified them as 'multiple structures' (Fig. 6.2 (a), lower panel) and excluded them from further analysis. For the constant curvature model, we would expect the intensity to increase with increasing contact angle (Fig. 6.1 (a), (b)). In case of the constant area model, we would expect equal intensity for the largest flat, dome as well as all pit structures (Fig. 6.1 (a),

(b)). However, our CLEM analysis clearly revealed that flat and dome structures have similar fluorescence intensities while pits tend to display higher fluorescence intensities (Fig. 6.2 (b), (d)). These flat CCSs had a mean fluorescence intensity of around 70% of the pits (Fig. 6.2 (b) box/whiskers; mean fluorescence intensity for flat CCSs: 1.6 × 108; pits: 2.3 × 108). In conclusion, our TEM and CLEM analyses argue that neither of the proposed growth models fully explain the observed ultrastructural distribution and corresponding fluorescence intensities of CCSs in BSC-1 cells.

6.3 Growth laws for clathrin-coated structures

Although EM of metal replicas is a high-resolution microscopy technique revealing detailed information about the size and ultrastructure of CCSs, it only provides snapshots of the dynamic process of CCP assembly [188]. In contrast, live FM of CME mostly allows the characterisation of the dynamics of different proteins during the formation of CCSs but does not provide ultrastructural information [76]. To obtain a more comprehensive dynamical picture, we used mathematical modelling of clathrin growth behaviour to combine the ultrastructural information from EM with the dynamic information obtained from total internal reflection fluorescence (TIRF) microscopy of fluorescently tagged clathrin light chain (CLC). Our approach is to estimate the morphology distribution of CCSs by fitting growth curves to individual CME fluorescence profiles. As the formation of CCS is a complex process with numerous yet unknown variables, here the modelling approach is used only to combine and compare the different data sets (FM, TEM and CLEM), with minimal assumptions on the underlying mechanisms. To correlate the temporal information of CCS dynamics obtained by live FM to the size information of these CCSs obtained by TEM, we used CLEM to convert the fluorescence signal into an estimate for the surface area (see Appendix A.6). Since we found a substantial number (around 50%) of flat CCSs with projected areas similar to pits (Fig. 6.1 (e), (g)), we rule out the possibility that the constant curvature model might be the dominant growth behaviour in BSC-1 cells. We therefore start by describing the growth of CCSs according to the constant area model.

6.3.1 Constant area model

As the fluorescence intensity of labelled clathrin triskelia is proportional to the number of incorporated clathrin triskelia or equivalently to the size of clathrin covered membrane area, we model the assembly of CCV as surface growth. In the constant area model, CCSs first initiate as flat circular planar discs that grow to a finite size before bending (Fig. 6.3 (a)). We assume growth of a CCS to be possible only at its

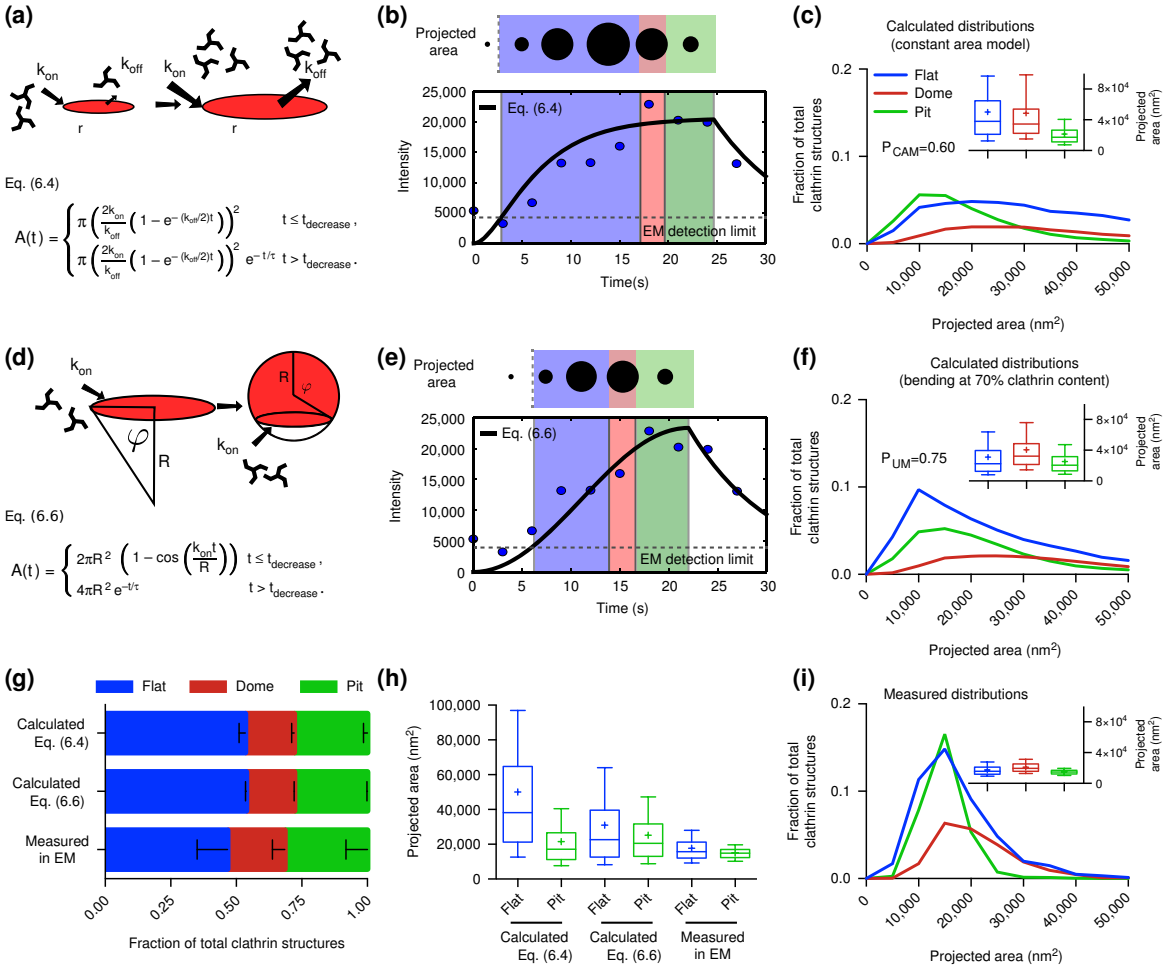

Figure 6.3 | Mathematical modelling of CCS growth from intensity profiles of individual CME events. **(a)** Mathematical representation of the constant area model, flat-to-curved transition happens at the time when clathrin reaches its final content. **(b)** Example of a clathrin intensity track fitted by the constant area model. Blue dots represent measured intensity of a single CME event; black line represents the fit with Eq. (6.4), dashed grey line marks the EM detection limit. The schematic on the top illustrates the calculated projected area and assigned curvature, flat (blue), dome (red) and pit (green). **(c)** Calculated projected area and curvature distributions of the CCSs according to the constant area model for 4927 FM tracks of 4 different cells. P-value of Welch's t-test to compare the predicted to the measured distribution in **(i)**. A box/whisker plot of the projected area is shown in the inset. Mid-line represents median, cross represents the mean and the whiskers represent the 10 and 90 percentiles. **(d)** Mathematical representation of the curvature acquisition during growth model where a flat clathrin patch grows and the flat-to-curved transition happens before reaching the final clathrin content. **(e)**, **(f)** Same as **(b)**, **(c)** but using Eq. (6.6). **(g)** Comparison of the predicted ratio of flat, dome and pit structures from both growth model (Eq. (6.4) and Eq. (6.6)) and the distribution obtained from TEM imaging. Results are calculated for 4927 FM tracks of 4 different cells; means with SD are shown. **(h)** Direct comparison of the projected area distribution of flat and pit structures calculated by Eq. (6.4) and Eq. (6.6) as well as measured in EM, box/whisker plot. **(i)** Measured projected area and curvature distributions of the CCSs from TEM data as shown in Fig. 6.1. Figure taken and adapted from [172].

edge L with rate k_{on}, because incorporation of new triskelia in the area A with radius r is expected to be energetically and topologically unfavourable. To avoid explosive growth, however, this process has to be balanced by another process. Geometrically the simplest possible model is that growth is limited by a process coupled to the area of the planar disc. Dissociation over the area would be such a process, but alternatively one could think of negative biochemical feedback increasing in proportion to the area (see Fig. 6.3 (a)). Effectively we model this as dissociation over the area of the patch with rate k_{off}, which can be expressed by

$$\dot{A} = k_{\text{on}} L - k_{\text{off}} A \,. \tag{6.1}$$

The growth equation can be simplified by plugging in the surface of a circular patch $A = \pi r^2$. It follows

$$\dot{r} = k_{\text{on}} - \frac{k_{\text{off}}}{2} r \,, \tag{6.2}$$

with steady state radius $r_{\text{ss}} = 2k_{\text{on}}/k_{\text{off}}$. By integrating this equation, we find the patch area as a function of time

$$A(t) = \pi \left(\frac{2k_{\text{on}}}{k_{\text{off}}} \left(1 - \mathrm{e}^{-(k_{\text{off}}/2)t} \right) \right)^2 . \tag{6.3}$$

In the observed fluorescence intensity tracks the intensity decreases after some time until the intensity vanishes completely. Biologically, this indicates that the clathrin coated vesicle pinches off the cell membrane and therefore, moves out of the focus of the microscope. We model this by assuming an exponential decay of the area with time constant τ, starting at time t_{decrease}

$$A(t) = \begin{cases} \pi \left(\frac{2k_{\text{on}}}{k_{\text{off}}} \left(1 - \mathrm{e}^{-(\mathrm{k_{off}}/2)t} \right) \right)^2 & t \leq \ t_{\text{decrease}}, \\ \pi \left(\frac{2k_{\text{on}}}{k_{\text{off}}} \left(1 - \mathrm{e}^{-(\mathrm{k_{off}}/2)t} \right) \right)^2 \mathrm{e}^{-t/\tau} & t > t_{\text{decrease}}. \end{cases} \tag{6.4}$$

We note that modelling the pinching as an exponential decay only serves as a measure to robustly define the end-point of a fluorescence track. No further information is extracted from this. As the steady state is only reached approximately we define an area plateau at 95% of the steady state area and the corresponding time t_{plateau}. The constant area model assumes that a flat patch transforms into a spherical pit as soon as the patch reaches the area plateau. Here, we neglect the exact details of the transformation process but classify the CCS as flat, dome (less than a half sphere) or pit according to time. Before reaching the plateau, the area is considered flat. After reaching the plateau we classify CCS in the first 40% of the remaining time until t_{decrease} to be domes and in the last 60% of time to be pits. For the exact choice we use our EM data and the data set of Avinoam et al. [38] and calculate the histogram $p(\varphi)$ of the growth angle φ (compare Fig. 6.4 (a)). The number of structures which

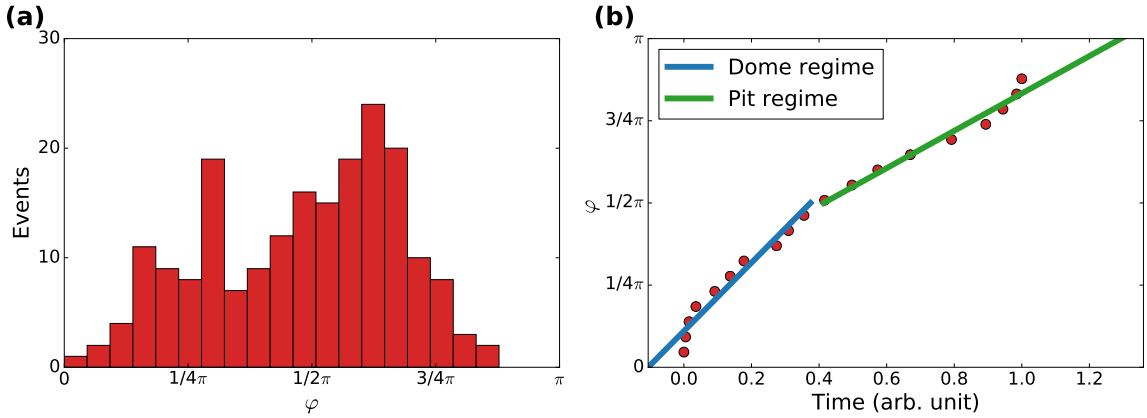

Figure 6.4 | Dome and pit transformation time deduced from Avinoam et al. [38]. **(a)** Histogram of the growth angle (red). **(b)** The growth angle as a function of the normalised sum of all structures with growth angle smaller or equal to φ (red) which is proportional to a time assuming a linear time relationship between φ and time. From the linear fit to the data with φ smaller than $\pi/2$ for domes (blue) and with φ larger than $\pi/2$ for pits (green) we compute the ratio of transformation times for domes and pits and obtain roughly 2:3.

one finds between φ and $\varphi + \mathrm{d}\varphi$ should be proportional to the time it takes for a structure to evolve from φ to $\varphi + \mathrm{d}\varphi$, assuming a linear time course. Therefore, φ as a function of the integral should give a measure of the time course. Since we are mostly interested in the number of domes and pits, we approximate the time course of φ for domes and pits by assuming a different linear relationship between φ and time. By dividing the time which it takes to form a half sphere by the time it takes to from a full sphere we end up with a forming ratio time of domes and pits of roughly 2:3 (compare Fig. 6.4 (b)).

Calculation of the size and morphology histogram

By fitting Eq. (6.4) and assigning the three different morphologies to the individual intensity profiles obtained by TIRF microscopy (Fig. 6.3 (b)), we could calculate the size and morphology distribution of CCSs as predicted by the constant area model (Fig. 6.3 (c)). For details on the fitting procedure as e.g. how to relate different data sets, data filtering or parameter choice see Appendix A.6 and Appendix A.7.

We proceeded as follows:

1. From each of the fitted growth curves we uniformly drew a number of time points, proportional to the time until the structure pinches off the cell membrane, that is given by t_{decrease} (Fig. 6.3 (a) and (b)). We used 4927 FM tracks of 4 different cells giving us 4 million time points, which we used to calculate the size histogram.

2. We classified the chosen times and corresponding areas into three categories. If $t < t_{\text{plateau}}$ the structure is flat (blue region in Fig. 6.3 (b)). We assume that the transformation process from flat to dome takes 40% of the plateau time whereas from dome to pit it takes 60% (see before). Therefore, if $t_{\text{plateau}} < t < t_{\text{plateau}} + \frac{2}{5}(t_{\text{decrease}} - t_{\text{plateau}})$ the structure is a dome (red region in Fig. 6.3 (b)) and otherwise it is classified as a pit (green region in Fig. 6.3 (b)).

3. We computed the projected area by assuming that the transformation within the dome and pit phase is a linear function of time. Therefore, we divided the area by $1 + \frac{5}{2}\frac{t - t_{\text{plateau}}}{t_{\text{decrease}} - t_{\text{plateau}}}$ for domes and $2 + \frac{5}{3}\frac{t - t_{\text{plateau}} - \frac{2}{5}(t_{\text{decrease}} - t_{\text{plateau}})}{t_{\text{decrease}} - t_{\text{plateau}}}2$ for pits. This factor equals 1 for a flat patch, 2 for a completed dome (half sphere) and 4 for a completed pit (full sphere).

4. We excluded times for which the corresponding area is below the area threshold, since the corresponding structures fall under the detection limit of TEM determined as being the smallest object that can be confidently identified as clathrin coat by TEM (Fig. 6.3 (b), white region and dashed line) or where the area already decreases (Fig. 6.3 (b), white region). This ensures that both the calculated and measured data sets are similarly restricted.

5. From the calculated projected areas, we then determined the size histogram (Fig. 6.3 (c)), which we compare to the EM data (Fig. 6.3 (h)).

Comparison of the calculated distribution to the acquired EM data reveals that the ratio between the flat, dome and pit structures is biased toward flat structures compared to the EM data (Fig. 6.3 (g)). Additionally, the means of the predicted size distributions of flat and pit structures are clearly separated with a shift of the flat projected area towards bigger sizes (Fig. 6.3 (c), (i), box/whiskers and Fig. 6.3 (h)). In agreement with our TEM and CLEM results, our mathematical modelling approach thus demonstrates that the constant area model does not correctly describe the assembly process of CCPs in BSC-1 cells.

6.3.2 Curvature acquisition during growth

Given the high proportion of flat structures (Fig. 6.1 (e)), we reasoned that CCSs start as flat structures and then acquire curvature before reaching the full clathrin content (Fig. 6.3 (d)). In contrast to the constant area model (Fig. 6.3 (a)), now the system has an intrinsic mechanism to stop growth, namely formation of a sphere, and therefore needs no balancing mechanism (no regulation by the area) besides the regulation by curvature in a minimal model. As we previously observed that the clathrin content of flat structures represents 70% of the clathrin content of CCPs

(Fig. 6.2 (b), box/whiskers), we reasoned that transition from flat to dome occurs at 70% of their final clathrin content (Fig. 6.3 (e), blue area), which we determine by taking the inverse of the intensity ratio of pit and flat structures in clathrin CLEM, which is 1.44. As before we model the assembly of clathrin coated vesicles as surface growth. Our mathematical description of the 'curvature acquisition during growth model' considers a spherical cap with area $A = 2\pi R^2(1 - \cos\varphi)$ and radius R that grows again only at its edge L with rate k_{on} which can be expressed by

$$\dot{A} = k_{\text{on}} L \,. \tag{6.5}$$

In (Fig. 6.3 (d)) a sketch of the growth schematics is shown. In the limit of a small growth angle $\varphi = k_{\text{on}}t/R < 1$ we recover the growth equation of a flat patch $A(t) = \pi(k_{\text{on}}t)^2$. For an almost complete pit the growth equation also holds perfectly. However, the mathematical description of the growth model approximates the flat patch by a spherical cap for intermediate flat patch sizes. In this case, the error is negligible as the model interpolates between the correctly addressed limiting cases and is not used to assign the shape of the CCS.

In contrast to the constant area model now no dissociation mechanism is included in the growth equation because of two reasons. First, the system has an intrinsic mechanism to stop growth and second, any area-related dissociation mechanism would imply that one could never close the sphere completely. Therefore, to obtain a simple growth law such a mechanism is neglected. We note that this choice does still allow for turnover of the clathrin coat which does not imply a net area loss. To define the ultrastructural organisation of the clathrin lattice, we neglect, as before, the exact details of the transformation process but classify the CCS as flat, dome (less than a half sphere) or pit according to time relative to the time when reaching the maximal area. Before reaching 70% of the maximal area the coat is flat. After reaching 70% of the maximal area we classify CCS in the first 40% of the remaining time to be domes and pits otherwise (similar to the constant area model).

As before we model that vesicles pinch off the membrane by an exponential decay of the area with time constant τ, starting at time $t_{\text{decrease}} = \pi R/k_{\text{on}}$. We note that t_{decrease} carries the unit of a time since the rate k_{on} carries the unit of a velocity. The full growth equation for the area as a function of time $A(t)$ reads

$$A(t) = \begin{cases} 2\pi R^2 \left(1 - \cos\left(\frac{k_{\text{on}}}{R}t\right)\right) & t \leq t_{\text{decrease}} \\ 4\pi R^2 \mathrm{e}^{-\mathrm{t}/\tau} & t > t_{\text{decrease}} \,. \end{cases} \tag{6.6}$$

As before we note that modelling the pinching as an exponential decay only serves as a measure to robustly define the end-point of a fluorescence track. Similar to the constant area model we defined conversion to domes (red area) and pits (green area)

according to their relative ratio observed in TEM. The resulting growth equation was again fitted to the individual intensity profiles of CME events (Fig. 6.3 (e)). For details on the fitting procedure see Appendix A.8.

Calculation of the size and morphology histogram

From the growth curves we calculated a histogram (Fig. 6.3 (f)) to compare 'the curvature acquisition during growth model' to the measured projected size EM histogram (Fig. 6.3 (h)). We proceeded in principle as before and only mention changes:

1. We classified the chosen times (around 4 million time points) and corresponding areas into three categories. If $A(t) < 0.7A_{\max}$ the structure is flat (blue region in Fig. 3e) and we call this time $t_{\text{trans.}}$. We assume that the transformation process from flat to dome takes the first 40% of the remaining time until the maximal area is reached whereas from dome to pit it takes the rest of the time (as before).

2. We computed the projected area by assuming that the transformation within the dome and pit phase is a linear function of time. Therefore, we divided the area by $1 + \frac{5}{2}\frac{t-t_{\text{trans.}}}{t_{\text{decrease}}-t_{\text{trans.}}}$ for domes and $2 + \frac{5}{3}\frac{t-t_{\text{trans.}}-\frac{2}{5}(t_{\text{decrease}}-t_{\text{trans.}})}{t_{\text{decrease}}-t_{\text{trans.}}}2$ for pits. This factor equals 1 for a flat patch, 2 for a completed dome (half sphere) and 4 for a completed pit (full sphere).

6.3.3 Comparison of growth models and data

To test the different models we compare them on the level of size and morphology distributions (instead of single trajectories). Our approach therefore represents the typical statistics of the system and is not meant to describe single trajectories that are prone to depend strongly on molecular details. As a matter of fact, the calculated ratio between the flat, dome and pit structures is similar as before and biased towards flat structures (Fig. 6.3 (g)), but in contrast now the calculated size and morphology distribution fit the EM data better than the distribution according to the constant area model. The means of the predicted projected area of both the flat and pit structures have similar sizes (Fig. 6.3 (f), (h), box/whiskers). These findings strongly support a model where assembly of a CCP initiates flat and then acquires curvature at around 70% of its final clathrin content.

6.4 CLEM analysis of clathrin-coated structures

The flat-to-curved transition of a CCS requires major ultrastructural reorganisation of the coat [37]. To acquire curvature, according to Euler's theorem the hexagonal organisation of the clathrin triskelia needs to reorganise into a polyhedral assembly

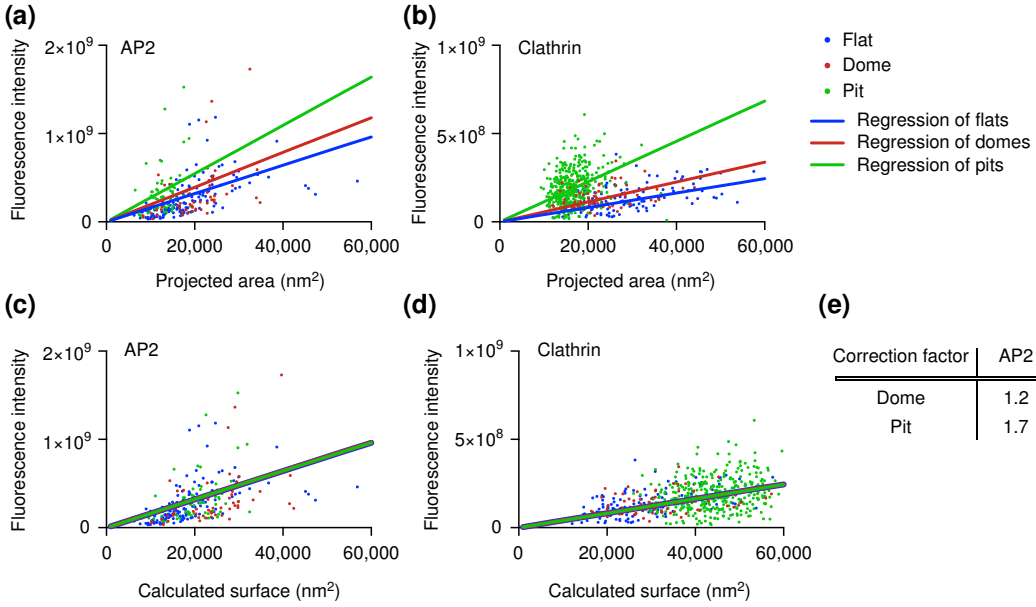

(e)

Correction factor	AP2	Clathrin
Dome	1.2	1.4
Pit	1.7	2.8

Figure 6.5 | The relative amount of AP2 and clathrin molecules per surface unit of a CCS is curvature dependent. CLEM analysis of CCSs labelled with AP2-eGFP **(a)** or clathrin heavy chain antibody **(b)**. Flat (blue), dome (red) and pit (green) CCS. Lines in the corresponding colour show linear regression of the projected area and of the fluorescence intensity. CLEM analysis of CCS corrected according to the regression of flat structures labelled with AP2-eGFP **(c)** or clathrin heavy chain antibody **(d)**. Projected areas of dome and pit structures of the CLEM analysis were multiplied by a correction factor to fit the linear regression of flat CCS. Lines in the corresponding colour show linear regression of the calculated surface and the fluorescence intensity. **(e)** Table shows correction factors for dome and pit structures for AP2-eGFP or clathrin heavy chain labelling used in **(c)** and **(d)**. Figure taken and adapted from [172].

including 12 pentagons [37]. The clathrin lattice in flat structures is mostly composed of hexagons [23, 176]. Although it has been shown using fluorescence recovery after photobleaching (FRAP) that the clathrin coat is highly dynamic, which is a prerequisite for such rearrangement [38, 39, 189], it is still puzzling what regulates the organisation of triskelia in the coat and what coordinates the flat-to-curved transition. It was proposed before that the ratio of the adaptor AP2 to clathrin changes within the growth of CCPs [187, 190, 191]. Therefore, we correlated the relative amount of AP2 and the ultrastructural organisation of CCSs. We performed CLEM analysis using BSC-1 cells expressing AP2 fused to green fluorescent protein (GFP; Fig. 6.5 (a)) and correlated these results to clathrin immunostaining CLEM (Fig. 6.5 (b)). To find the relationship between fluorescence intensity and the surface of CCSs, the measured projected area needs to be corrected for the curvature to obtain the surface area of the CCS (Fig. 6.1 (b)). For flat CCS, projected area and surface area are identical, and thus we used the linear regression of flat coats as a reference to correct the projected area of both domes and pits. Assuming the geometry of a hemisphere for domes and

an almost complete sphere for pits, we expect a correction factor of ≤ 2 for domes and $2 < x \leq 4$ for pit structures if the relationship between fluorescence intensity and surface area is independent of curvature (Fig. 6.1 (b)).

The correction factors inferred from clathrin CLEM for domes and pits were 1.4 and 2.8, respectively, which are within the expected ranges (Figs. 6.5 (d), (e) and 6.1(b)). Strikingly, the correction factors for AP2 CLEM were smaller than expected, especially for the pit structures (domes: 1.2; pits: 1.7) (Fig. 6.5 (c), (e)). This reveals that the AP2/clathrin ratio in a CCS differs depending on its curvature and that this ratio is reduced within the coat as curvature increases.

6.5 AP2/clathrin ratio change marks the starting point of bending

As the AP2/clathrin ratio depends on the curvature of CCS (Fig. 6.5) and as AP2 partitions at different nanoscale zones in relation to the edge of the clathrin lattice during the different stages of CCS formation [187], we hypothesised that the change in the AP2/clathrin ratio correlates with the stage at which a flat CCS bends to form a CCP. Using cells expressing both AP2 fused to GFP and CLC fused to the fluorescent protein tdtomato, we analysed the intensity profiles of AP2 and CLC during CME. While AP2 profiles often show a distinct plateau phase, the intensity of CLC continues to increase until the end of an endocytic event (Fig. 6.6 (a)). By normalising the fluorescence intensities of AP2 as well as CLC to the time point when the AP2 signal plateaus, we can calculate the time offset between the time AP2 signal reaches its plateau and the time point CLC reaches its maximal intensity (Fig. 6.6 (a), (b)). Similarly, we defined the intensity offset of clathrin over AP2 (Fig. 6.6 (a), (c)). We found that the time offset was around 10 s (Fig. 6.6 (b)) and that the intensity offset of clathrin over AP2 was around 15% (Fig. 6.6 (c)).

We hypothesised that the time point when AP2 reaches its plateau and therefore the AP2/clathrin ratio changes marks the starting point of bending. We performed another round of CCP assembly modelling, this time using both AP2 and CLC intensity profiles and defining the time point of flat-to-curved transition when AP2 reaches its plateau phase (Fig. 6.6 (e). At this precise time, the mean clathrin content reached around 70% of its maximal value (Fig. 6.6 (d)). In principle, the only thing that changes in the fitting procedure compared to the curvature acquisition during growth model is that the transition time $t_{\text{trans.}}$ is now given by the time when the AP2 intensity plateaus, which we calculated by fitting Eq. (6.4) to the AP2 FM intensity tracks. We use Eq. (6.4) for the AP2 tracks as they show a clear plateau phase which is reached prior to the onset of coat curvature. Therefore, the growth of the AP2 patch is limited and Eq. (6.4) is a simple representation of such a situation. This assumption is supported

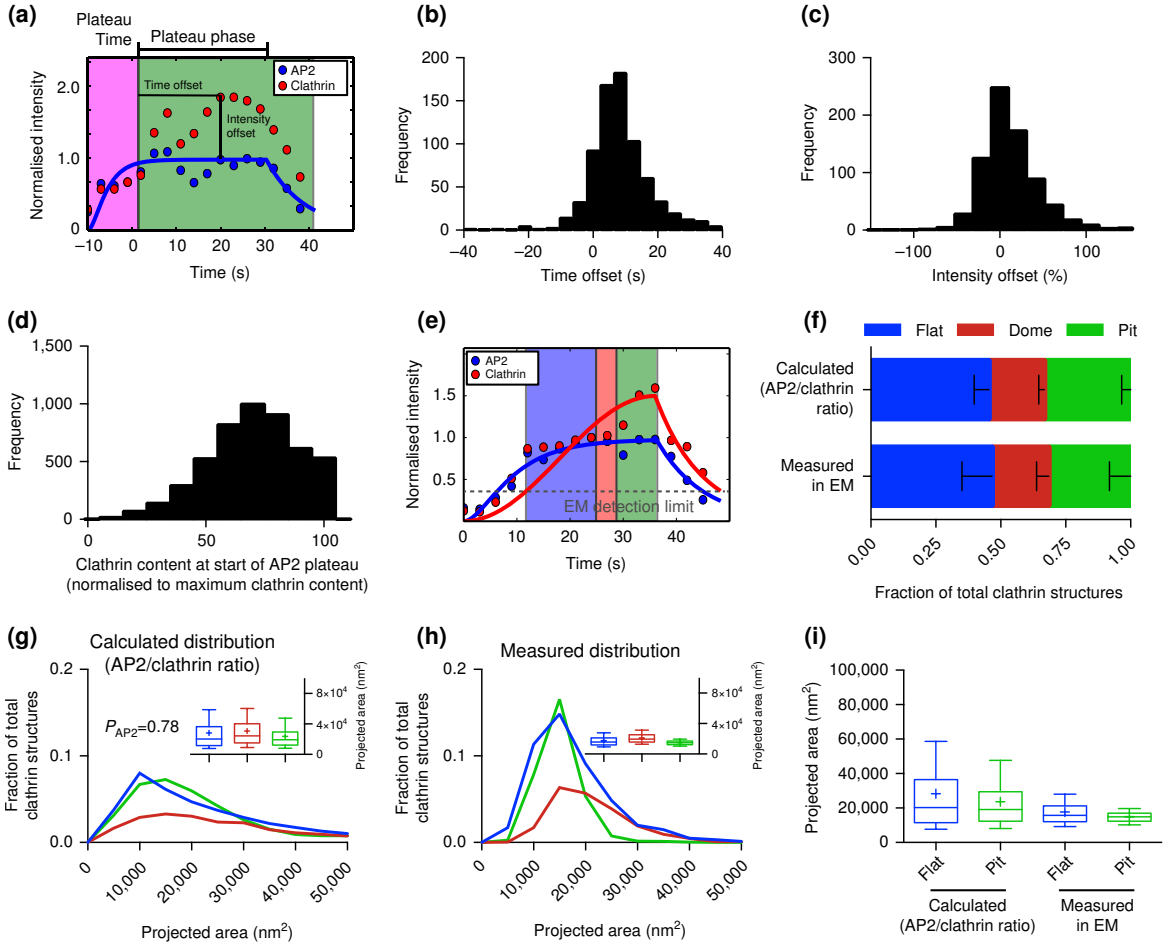

Figure 6.6 | Change in the AP2/clathrin ratio is associated with flat-to-curved transition. **(a)** Example of an AP2 (blue) and clathrin (red) intensity profile from an individual CME event. The AP2 profile was fitted to Eq. (6.4) to find the time when AP2 signal plateaus. The fluorescence intensity of AP2 and clathrin was normalised to the fluorescence intensity of the time when the fitted AP2 profile reaches its plateau. Time offset (difference between the time AP2 plateaus and clathrin reaches its maximum intensity) and intensity offset (excess of maximal clathrin signal over AP2 maximum intensity) are indicated in the profiles. Quantification of the time offset **(b)** and the intensity offset **(c)** for 754 tracks of one single cell. **(d)** Quantification of the clathrin content at the time when AP2 reaches its plateau from 4927 FM tracks. The clathrin signal was normalised to the maximal clathrin signal in each track. **(e)** Example of an AP2 (blue) and clathrin (red) profile fitted to Eq. (6.4) and Eq. (6.6), respectively. These fits were used to calculate the size and morphology distributions of the CCS in **(f)**, **(g)**. **(f)** Comparison of the calculated ratio of flat, dome and pit structures to the measured ratio in TEM. Results calculated from 4927 FM tracks from 4 different cells; means with SD are shown. **(g)** Calculated projected area of the CCSs using a growth model where the flat-to-curved transition corroborates with the change of clathrin/AP2 ratio (when AP2 signal reaches its plateau phase) for 4927 FM tracks of 4 different cells. P-value of Welch's t-test to compare the predicted to the measured distribution in **(h)**. A box/whisker plot of the projected area is shown in the inset. **(h)** Measured projected area and curvature distributions of the CCSs from TEM data as shown in Fig. 6.1. A box/whisker plot of the projected area is shown in the inset. **(i)** Direct comparison of the projected area distribution of flat and pit structures calculated according to the AP2/clathrin ratio as well as measured in EM, box/whisker plot. Figure taken and adapted from [172].

by the experimental finding that AP2 is highly dynamic throughout the coat. Indeed FRAP experiments have demonstrated the high recovery rate of AP2 with CCS [189]. For details on the fitting procedure, see appendix A.9. Using these new parameters, the predicted ratio of flat, dome and pit structures matched the EM data (Fig. 6.6 (f)) and the means of the predicted projected area of both the flat and pit CCSs have similar sizes (Fig. 6.6 (g)-(h), box/whiskers and 6.6 (i)).

Quantification of agreement between measured and predicted size histograms

To determine the level of agreement between measured (Fig. 6.3 (h)) and predicted size histograms (Fig. 6.3 (c), Fig. 6.3 (f) and Fig. 6.6 (e)) we calculated chi-squared

$$\chi_j^2 = \sum_{i=1}^{k} \frac{(N_{ij} - np_{ij})^2}{np_{ij}}\,, \tag{6.7}$$

where we summed over all bins k the occurrences N_i of measured CCS and compared it to the number of expected occurrences np_i, where p_i is the predicted normalised frequency per bin, which we deduced from our models (CAM=constant area model, UM=curvature acquisition during growth model and AP2=transition flat/dome determined by the time when the AP2 intensity plateaus) and $n = \sum N_i$. We repeated this for all CCS such that we found three values for χ_j^2 for each model ($j \in \{\mathrm{CAM}, \mathrm{UM}, \mathrm{AP2}\}$) and cell. We averaged these values for all CCS and four cells and found: $\chi^2_{\mathrm{CAM}} = 1018$, $\chi^2_{\mathrm{UM}} = 649$ and $\chi^2_{\mathrm{AP2}} = 632$ which shows that the model plotted in Fig. 6.6 (e) describes the data best. Additionally, we performed a Welch's t-test to calculate p-values for the null hypothesis that the measured and predicted size distributions of a CCS have identical mean values. We averaged over all CCS and four cells and found $p_{\mathrm{CAM}} = 0.60$, $p_{\mathrm{UM}} = 0.75$ and $p_{\mathrm{AP2}} = 0.78$.
To conclude, this AP2/clathrin ratio model better resembles the parameters measured in EM compared to both the constant curvature and constant area models (Figs. 6.3 (h) and 6.6 (i)). These findings strongly support a model where flat-to-curved transition correlates with the concomitant change in the AP2/clathrin ratio.

6.6 Membrane tension and flat-to-curved transition

By inducing curvature to the PM, the CCS needs to act against the plasma membrane tension (PMT). Higher PMT has been shown to increase the lifetime of clathrin events at the PM [42, 192] and modelling of the energetic cost of membrane bending suggests that it affects the morphology of the CCSs [31, 119]. However, the effects of increasing PMT on the ultrastructural organisation of CCSs have not been investigated in living cells. We monitored the dynamics of clathrin and AP2 during osmotic shock in which the PMT was increased by applying hypotonic medium inducing osmotic swelling

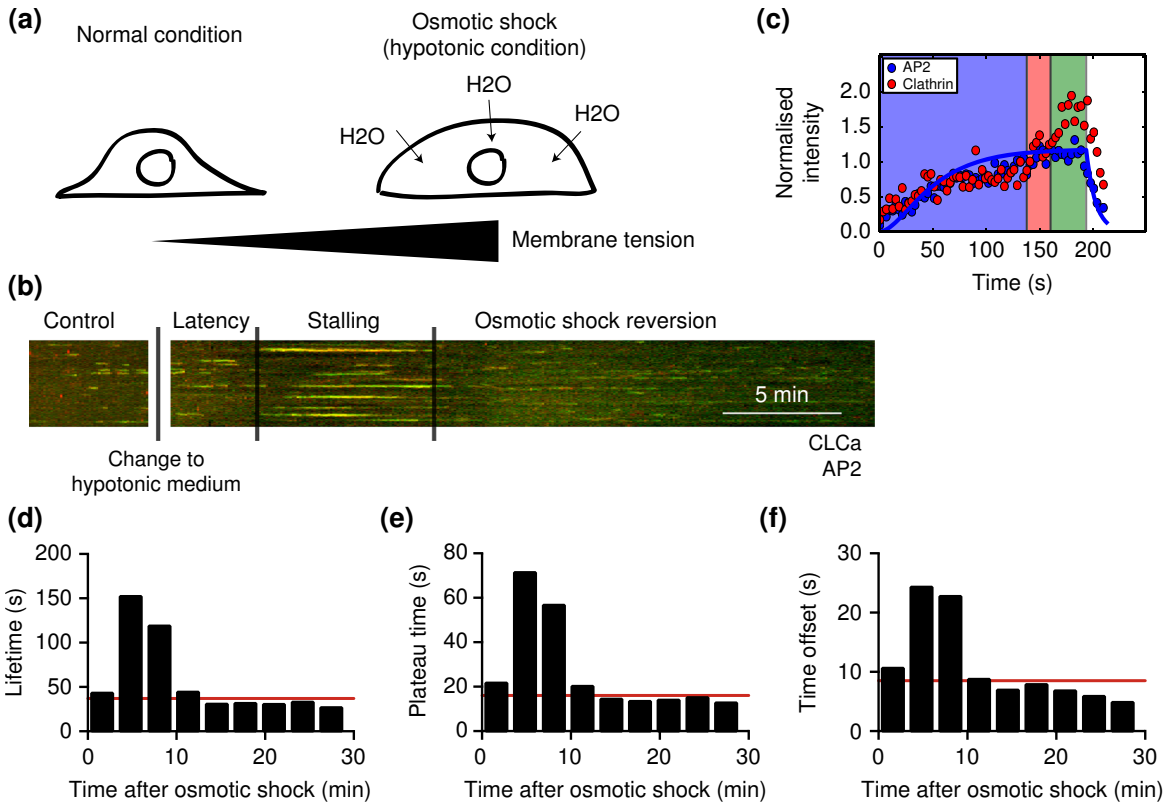

Figure 6.7 | Osmotic shock induces stalling of CCSs. **(a)** Illustration of the effect of osmotic shock on BSC-1 cells. Hypotonic medium was applied to BSC-1 cells, inducing osmotic swelling that results in an increase in PMT. The same BSC-1-expressing fluorescently tagged clathrin light chain and AP2 proteins were followed from 5 min prior (internal control) until 30 min post hypotonic medium application using spinning disc confocal microscopy. **(b)** Kymograph of AP2- eGFP (green) and clathrin light chain a-tdtomato (red)-expressing BSC-1 cells. The dynamics of CCSs was recorded during 5 min prior to osmotic shock until 30 min post osmotic shock. The time after applying the hypotonic medium can be divided into latency, stalling and osmotic shock reversion time depending on the effect on CME dynamics. Scale bar: 5 min. **(c)** Representative AP2 (blue) and clathrin (red) intensity profile from an individual CME event during the time of stalling fitted to Eq. (6.4) to quantify the plateau time. **(d)** Quantification of the lifetime of CME events during osmotic shock experiments for 1607 tracks of one single cell. CME events were binned in 3 min intervals in respect to the onset of osmotic shock. Red line indicates lifetime of CME prior to osmotic shock. **(e)** Quantification of the plateau time of AP2 of individual CME events during osmotic shock experiments (as defined in Fig. 6.6 **(a)**) for 1607 tracks of one single cell. CME events were binned in 3 min intervals in respect to the onset of osmotic shock. Red line indicates plateau time of CME prior to osmotic shock. **(f)** Quantification of the time offset between AP2 plateau and clathrin maximum of individual CME events during osmotic shock experiments (as defined in Fig. 6.6 **(a)**) for 1607 tracks of one single cell. CME events were binned in 3 min intervals in respect to the onset of osmotic shock. Red line indicates time offset of CME prior to osmotic shock. Figure taken and adapted from [172].

of the cells [42] (Fig. 6.7 (a)). Following a short latency period, we observed that CCSs stalled at the PM. This effect was transient and cells quickly reverted to normal clathrin dynamics (Fig. 6.7 (b), (d)). Since the growth dynamics of clathrin is stalled under osmotic conditions, we now determined the flat-to-curved transition time not by determining the time when AP2 reaches is plateau, but by calculating when CLC intensity exceeds the AP2 intensity by 5%, which we controlled to yield similar results under unperturbed isoosmotic conditions.

Calculation of the ratio histogram during the osmotic shock

To determine the ratio histogram of flat, dome and pit CCSs during the osmotic shock (Fig. 6.8 (a) and Fig. 6.8 (c)), we first defined a transition time $t_{\text{transition}}$, when flat CCSs start to invaginate, where the normalised clathrin intensity exceeds the normalised AP2 intensity by 5% (blue region in Fig. 6.7 (c)). We assumed that the transformation process from flat to dome takes the first 40% of the remaining time until the vesicle pinches of the PM, given by t_{decrease} (red region in Fig. 6.7 (c)) whereas from dome to pit it takes the remaining 60% of time (green region in Fig. 6.7 (c)). Next, we started 50 s after the osmotic shock and determined the morphology of all tracks present at that time depending on the description before. We repeated this procedure in steps of 5 s and averaged the number of structures over time intervals of 100 s. In total we used 1356 FM tracks of one cell. The found ratios of flat, dome and pit CCSs were then plotted as a function of the time after the osmotic shock (Fig. 6.8 (a)). To test the consistency of this approach we used it to calculate the ratios for flat, dome and pit structures on the data without osmotic shock consisting of 4927 FM tracks of 4 different cells. Averaging over all tracks and considering only tracks with lifetimes shorter than 90 s and with AP2/clathrin discrepancy we obtained 47.8% flat CCSs, 18.0% dome CCSs and 34.2% pit CCSs which is very similar to the determined ratios in (Fig. 6.6 (g)).

Enhanced membrane tension suppresses flat-to-curved transition

Using fitted AP2 and unfitted CLC intensity profiles under osmotic shock, we showed that the CCSs display a longer AP2 plateau phase (Fig. 6.7 (c), (e)) and that the time offset was increased compared to mock treated cells (Figs. 6.7 (f) and 6.6 (b)). According to our findings that the change in AP2/clathrin ratio coordinates the flat-to-curved transition of CCSs, the delayed offset in the AP2/clathrin ratio under higher PMT suggests that the flat-to-curved transition is suppressed and that the coats are flat under this condition. By looking at the AP2/clathrin ratio during osmotic shock, we predicted that during the stalling phase, 70% of the CCSs would be flat (Fig. 6.8 (a)).

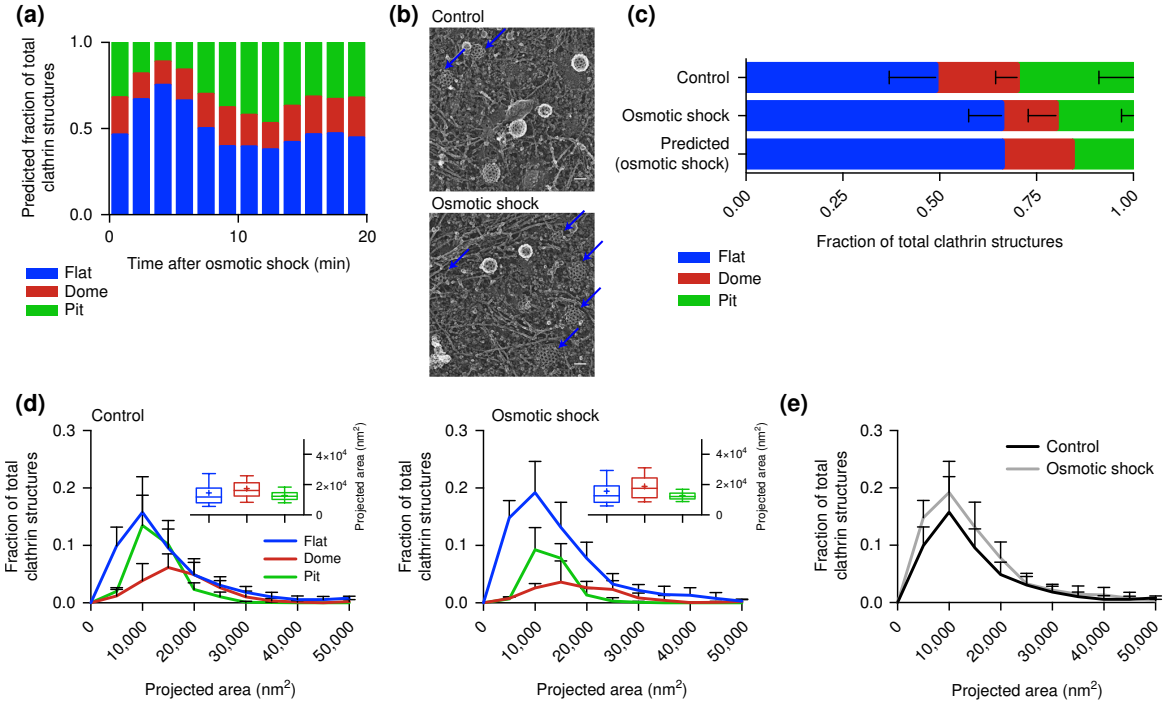

Figure 6.8 | Osmotic shock blocks flat-to-curved transition of CCSs. **(a)** Predicted ratio of flat (blue), dome (red) and pit (green) structures calculated from the binned AP2 and clathrin profiles of CME events (Fig. 6.7 (c)) during osmotic shock for 1357 tracks. **(b)** Examples of CCSs under normal and osmotic shock conditions. Blue arrows point to flat structures. **(c)** Comparison of measured and predicted frequency of flat, dome and pit structures under normal and osmotic shock conditions. **(d)** Projected area distribution of the different clathrin morphologies under normal and osmotic shock conditions. A box/whisker plot of the projected area is shown in the inset. Mid-line represents median, cross represents the mean and the whiskers represent the 10 and 90 percentiles. **(e)** Comparison of projected area distributions of flat CCSs under normal and osmotic shock conditions. Results are calculated from four different membranes (number of CCSs per membrane: normal conditions 267, 308, 229 and 323; osmotic shock: 395, 99, 351 and 201); means with SD are shown. Figure taken and adapted from [172].

To test this notion, we performed EM of metal replica of CCSs under osmotic shock (Fig. 6.8 (b)). We found an accumulation of flat CCSs under osmotic shock compared to normal conditions and the frequency was comparable to our predictions from the AP2 and CLC profiles (Fig. 6.8 (c)). These flat structures, as well as the dome and pit structures, have the same size distribution as under normal conditions (Fig. 6.8 (d) box/whiskers and 6.8 (e)). The EM data confirm that under higher PMT the flat-to-curved transition of CCSs is inhibited. Using our data analysis pipeline from before and individual clathrin and AP2 intensity profiles acquired under osmotic shock, we could predict the morphology of the stalled CCSs. These findings are in agreement with our conclusion from before that the change in clathrin/AP2 ratio represents the precise moment at which the flat-to-curved transition occurs.

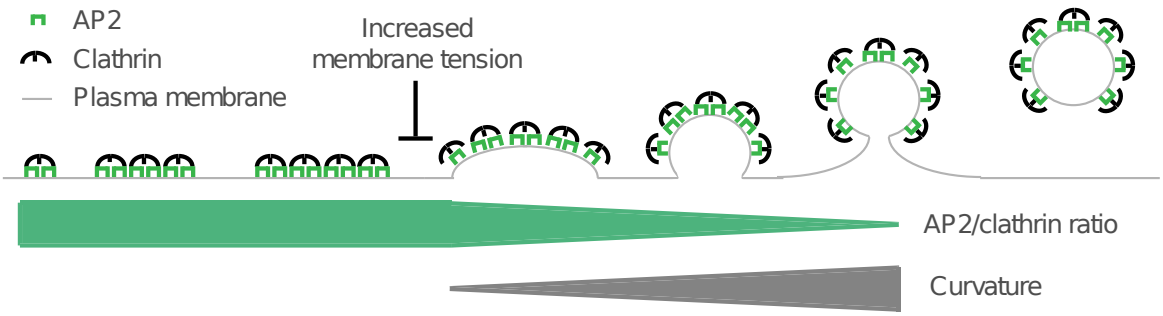

Figure 6.9 | Model of CCP assembly. Schematic representation of the growth model of CCSs. CCSs initiate as flat clathrin array. They first grow in size in a flat morphology with a constant AP2/clathrin ratio. When they reach around 70% of their full clathrin content, the AP2/clathrin ratio starts to decrease and the CCSs start acquiring their curvature. CCPs keep growing by adding additional clathrin molecules until formation and release of CCVs into the cytoplasm. The flat-to-curved transition of CCSs can be inhibited by increasing PMT, resulting in an accumulation of flat structures. We propose that flat- to-curved transition is concomitant with by passing the energy barrier necessary to curve the PM and that this critical step in CME is coordinated by the uncoupling of clathrin and AP2 characterised by their abrupt ratio decrease. Figure taken and adapted from [172].

6.7 Conclusion

The complex coordination of CCS formation during CME has been investigated for decades [193, 194] and the field has been driven by the competition between the constant curvature versus the constant area models [27]. Recent technological advances, in particular in CLEM, favoured the constant area model [38]. In this chapter, we implemented a multidisciplinary approach to combine information from EM, fluorescence intensity profiles of individual endocytic events and mathematical modelling of CCS growth to integrate different data sets into one common framework for the analysis of the ultrastructural rearrangement of CCSs during CME. By modelling the growth behaviour according to the two proposed growth models, we could calculate the expected size and morphology distribution of CCSs (Fig. 6.1 and Fig. 6.3). We could clearly demonstrate that neither of the proposed models explain the ultrastructural organisation and size distribution of CCSs present in BSC-1 cells. Instead, our data support a model in which CCSs first grow flat and then the flat-to-curved transition occurs at around 70% clathrin content (Fig. 6.9). Importantly, we demonstrated that this transition is directly linked to PMT and correlates with a change of the AP2/clathrin ratio within the coat.

Increasing PMT results in inhibition of the change in AP2/clathrin ratio and the subsequent stalling of the ultrastructural rearrangement. Our conclusion that a change in AP2/clathrin ratio drives the flat-to-curved transition is consistent with the recent observation that AP2 (and other adaptor/accessory proteins) partitions in different nanoscale areas of the clathrin coat and that the concentration of AP2 varies within

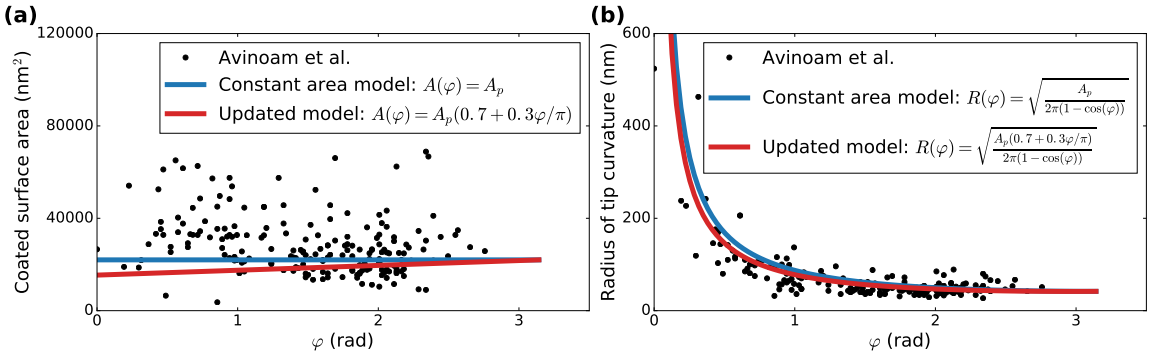

Figure 6.10 | Updated growth model explains the CLEM data from Avinoam et al. [38]. **(a)** Clathrin coated surface area as a function of the growth angle φ. The constant area model where we assume $A = 22000\,\mathrm{nm}^2$, corresponding to the most probable surface area [34] is plotted in blue. Our updated model is plotted in red, where we assume that the surface starts to bend when 70% of the final clathrin content is reached and grows the last 30% linear with φ. The data (black dots) were extracted from Avinoam et al. [38]. **(b)** Radius of tip curvature as a function of the growth angle φ. Again, the constant area model (blue) and our updated model (red) are plotted. The radius of the tip curvature is given assuming that the clathrin structure exhibits the shape of a spherical cap. Then the tip curvature reads $R = \sqrt{A(\varphi)/(2\pi(1-\cos\varphi))}$. The data (black dots) were extracted from Avinoam et al. [38].

these zones at various stages of CCS assembly [187]. Our conclusions on CCP assembly, determined here in BSC-1 cells, may also apply for other cell types. Because our model assumptions are minimal, we expect them to describe the most generic aspects of CME. To test whether our growth model could explain the ultrastructural distribution of CCSs described in previous studies, we extended our mathematical model and calculated the predicted contact angle between the clathrin cage and the PM, the coated surface area and the radius of tip curvature of the CCS (Fig. (6.10)). By comparing the model to the Avinoam et al. data set describing the distribution and ultrastructural organisation of CCSs in SK-MEL-2 cells [38], we could demonstrate that our growth model could also explain their observed distribution. It was proposed earlier that the physical properties of the PM are influencing the morphology of CCSs because PMT energetically acts against curvature acquisition of the clathrin array [42, 31, 119].

We demonstrated the effect of increased PMT on CCS assembly in cells. Under high PMT, the accumulation of stalled flat CCSs at a stage prior to the change in AP2/clathrin ratio reveals an important step of CCP formation to overcome the PMT to acquire curvature. It is tempting to speculate that this change of AP2/clathrin ratio is a key event mandatory for curvature acquisition. The demonstrated interplay between AP2 and PMT shows that both biochemical and physical factors regulate CME. Surprisingly, the increase in PMT only changes the ratio between the differ-

ent morphologies of CCSs in favour of flat structures but does not affect their size (Fig. 6.8 (d), (e)). One could assume that a higher energy barrier of the PM might be counteracted by the clathrin system by the formation of larger flat CCSs, which could accumulate more energy for the bending process by molecular crowding of clathrin itself as well as BAR proteins incorporated in the coat [31, 195, 196, 197]. Since under high PMT the flat CCSs still have the same size as under normal PMT, we suggest that there is an internal limitation of the coat size that might be regulated by certain components of the coat. Proteins that regulate the size of CCV have been reported [198, 199] and it might be possible that the size of a flat clathrin lattice is controlled in a similar way. The fact that other cell types show much larger flat CCSs under normal conditions, commonly referred to as clathrin-coated plaques [180, 40], illustrates that the clathrin machinery is capable of forming large flat structures under certain conditions. However, the factors necessary for clathrin-coated plaque formation have not been described so far. These clathrin-coated plaques might contribute to CME. Live-cell FM [200, 201] and EM [24] of such structures support budding of CCV from such plaques most probably from the edge, again illustrating the ability of a flat CCS to rearrange into a CCP, further supporting that our observed flat-to-curved transition is indeed possible. We could show that during coat assembly the AP2/clathrin ratio changes. This finding is in agreement with other FM [190, 191, 192] and CLEM [187] studies.

Combining mathematical growth laws and CLEM demonstrated the correlation between the change in the AP2/clathrin ratio and the time of coat bending. We found that the biggest flat structures contain the same amount of AP2 compared to fully formed CCPs, while the clathrin content still increases an additional 30% as the coat rearranges from flat to CCPs. This suggests that acquisition of curvature is not linked to addition of additional AP2 in the coat and strongly suggests that other proteins, in conjunction with clathrin, might be involved in driving the ultrastructural rearrangement of the coat. Several other adaptor and accessory proteins have been proposed to influence the ultrastructure of the CCS. Depletion of FCHO 1 and 2 has been reported to alter the ordered hexagonal organisation of the flat clathrin lattices [202]. Other proteins like CALM and NECAP have been proposed to regulate the final size of a CCV [198, 199]. Our approach provides a unifying view on the process of CCP assembly where we demonstrate that CCPs initially grow as flat lattices and that change in clathrin/adaptor ratio correlates with the onset of coat curvature acquisition prior to the completion of coat polymerisation. We propose that the proportion of different coat proteins could ultimately define the morphology of a clathrin structure and temporal changes of this proportion might initiate bending of the coat, allowing for dynamical regulation by the cell.

7 Spatial heterogeneity in flat clathrin lattices

This chapter is a theory study using experimental data and has already been submitted for publication [203].

7.1 Introduction

Clathrin-mediated endocytosis (CME) is one of the major pathways by which cells internalise cargo molecules [14]. In CME clathrin triskelia assemble together with a layer of adaptor and accessory proteins in order to invaginate a patch of the cell membrane of several tens of nanometer radius [204]. The standard sequence of events are nucleation, growth and fission of the clathrin-coated structure [70, 205], but it is still unclear when exactly in this process curvature is acquired [27, 206]. Two models have been proposed to explain how the clathrin coat evolves during the uptake process [35] (compare also chapter 6).

In the constant curvature model (CCM), the clathrin coat assembles with constant curvature [179]. As dictated by Euler's theorem, this requires the presence of twelve pentagons in the hexagonal lattice. The CCM implicitly assumes that these pentagons are incorporated in a continuous manner at the edge of the growing pit. In contrast, in the constant area model (CAM) the clathrin coat first assembles flat to finite size before the clathrin coat starts to bend [38]. Here pentagons have to get integrated either directly into the hexagonal lattice or they have to diffuse from the edge into the bulk of the lattice [207]. Both scenarios require major lattice rearrangements with high energetic and topological barriers [37]. First, multiple molecular bonds with binding energies of $\epsilon_{\mathrm{clathrin}} = 23\ \mathrm{k_B}T$ per triskelion [31] would have to open up. Secondly, to add another face to the hexagonal lattice, one had to add exactly two triskelia to the existing lattice, which then would also create both pentagons and heptagons [36]. As the probability of incorporating two triskelia at the same time is low compared to the growth rate such lattice rearrangements seem to be unlikely.

Although the seminal electron microscopy (EM) work by Heuser and coworkers showed the existence of flat clathrin lattices already in the 1980s [23], the CAM has been disfavoured for the above listed energetic and topological reasons. Recent experiments however have changed this picture. First, fluorescence recovery after photobleaching (FRAP) experiments have shown that the clathrin coat is highly

dynamic [39, 40, 38, 41]. Secondly, EM showed that patch size does not change much with the invagination angle, lending strong support for the CAM [38]. This view was further supported by our quantitative study combining correlative light and electron microscopy (CLEM) and mathematical modelling, which suggested that the lattice first grows flat and starts to bend only after on average 70% of the clathrin content has been acquired (see chapter 6 and [172]). Another recent study using polarised total internal reflection fluorescence microscopy has shown that indeed different assembly pathways coexist [208]. Together these recent developments suggest that the assembly pathway is more plastic than formerly appreciated, and that bending can occur even at relatively late stages.

To address the essential question how bending can become possible in a flat clathrin lattice, in this chapter we explore the possibility that even hexagonal lattices might be less homogenous than usually assumed. We first investigate the question how pentagons can be incorporated within a hexagonal lattice. Using simple dynamic equations we argue that pentagons are more likely incorporated in the bulk to reproduce experimental data. Next, we suggest that flat clathrin lattices grow by developing a spatial heterogeneity of the layered clathrin triskelia facilitating the flat-to-curved transition. By combining CLEM data and computer simulations of clathrin coats, we then demonstrate that clathrin lattices might grow sparsely with a relatively large amount of structural gaps. As structural gaps we define vacancies within the clathrin lattice where lattice sites are unoccupied, but which are distributed in the lattice such that binding triskelia to these vacancies would not change the number of occupied lattice edges.

7.2 Clathrin coat remodelling

7.2.1 Dynamic considerations

Constraint by topology we know that for the transformation of a flat hexagonal lattice into a curved clathrin coated structure exactly twelve pentagons have to be created within the clathrin coat [204]. This is true in order to fulfil Euler's polyhedron formula (see chapter 2). There are two models of how pentagons, which are associated with the on-set of curvature relative to the clathrin coat, are created: The edge- and the bulk-acquisition model [207, 118, 37]. In the following we formulate phenomenological kinetic equations for both models.

In the **edge-acquisition model** (EA) pentagons are formed at the edge of the clathrin lattice (see Fig. 7.1 (a)). We approximate the shape of the clathrin lattice by a compact spherical cap of area $A = 2\pi R^2(1 - \cos\theta)$ in a continuum description in the limit of small invagination angle θ and large radius R, i.e. of a nearly flat lattice. We formulate

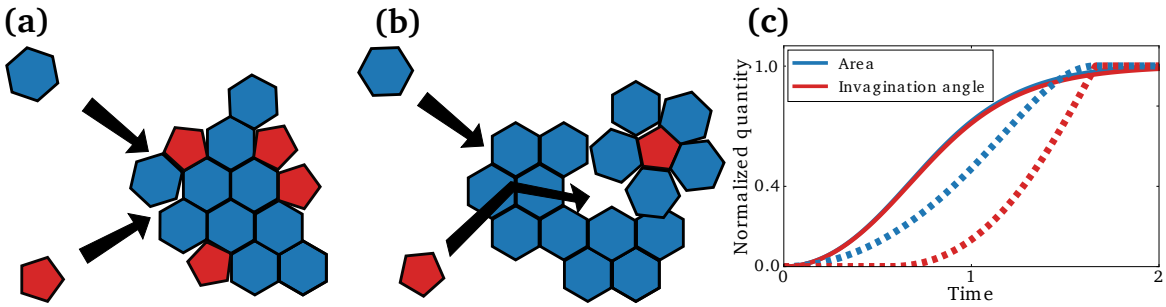

Figure 7.1 | Edge-acquisition and bulk-acquisition model. **(a)** In the edge-acquisition model the lattice incorporates new triskelia, i.e. hexagons (blue) and pentagons (red) over the edge. **(b)** In the bulk-acquisition model the lattice incorporates new triskelia, i.e. hexagons (blue) over the edge. Pentagons (red) are created by lattice rearrangements within the bulk. **(c)** The area (blue) and the invagination angle (red) of the clathrin lattice as a function of time for the edge-acquisition model (solid lines) and bulk-acquisition model (dashed lines).

kinetic equations for this scenario by assuming that both the area and invagination change ($\dot{A}$ and $\dot{\theta}$) are driven by incorporating triskelia and pentagons over the edge of the lattice with length L

$$\begin{aligned} \dot{A} &= k_{\mathrm{on}} L \,, \\ \dot{\theta} &= k_{\mathrm{p}} L \,, \end{aligned} \tag{7.1}$$

where k_{on} and k_{p} are the rates with which new triskelia are incorporated and pentagons are formed. By plugging in the length of the edge $L = 2\pi R \sin\theta$ the second equation implies

$$\dot{\theta} = k_{\mathrm{p}} 2\pi R \sin\theta \sim \theta \,, \tag{7.2}$$

for nearly flat lattices. Consequently, the invagination starts simultaneously to coat growth or in other words we recover a model which could never lead to a flat-to-curved transition. In another variant of the edge-acquisition model pentagons diffuse from the edge of the clathrin lattice toward the bulk [207], implying major coat rearrangements. Given the clathrin binding energy per triskelion of $\epsilon_{\mathrm{clathrin}} = 23\,\mathrm{k_B}T$ [31], however, this seems to be unlikely.

In the **bulk-acquisition model** (BA) pentagons are formed within the bulk of the clathrin coat (see Fig. 7.1 (b)). We formulate kinetic equations for this scenario and assume again that new triskelia are incorporated along the edge of the clathrin lattice. However, different to before, now the invagination angle change $\dot{\theta}$ is driven by incorporating pentagons within the bulk. Due to the geometry of single clathrin triskelia and their arrangement in the lattice where next and next-to-next neighbours are connected, we expect that the transformation only occurs if the lattice reaches a

threshold size A_0. Then the dynamics can be summarised by

$$\begin{aligned} \dot{A} &= k_{\mathrm{on}} L \,, \\ \dot{\theta} &= k_{\mathrm{p}} A H(A - A_0) \,, \end{aligned} \tag{7.3}$$

where $H(x)$ is the Heaviside step function. Such a scenario seems to be in agreement with the experimental finding of a flat-to-curved transition. In Fig. 7.1 (c) the solution to the ODEs for the area (blue) and invagination angle (red) for the EA (solid) and BA (dashed) are shown. Clearly, for the EA no flat lattice growth is possible. In contrast, the clathrin lattice first grows flat for the BA, indicated by a delayed invagination angle increase, before it starts to curve. Microscopically, the BA implies that in the initially hexagonal lattice pentagons are created. Such a transformation implies major coat rearrangements, which, although being not as unlikely as clathrin triskelia diffusion, raises some concerns.

7.2.2 Topological considerations

By using topological arguments Jin and coworkers [36] deduced several relations that are helpful to understand the necessary coat rearrangements for a flat-to-curved transition. We briefly recapitulate them in the following. First Euler's polyhedron formula states

$$F - E + V = 2 \,, \tag{7.4}$$

where F are the faces, E the edges and V the vertices or nodes of a polyhedron or in particular a closed clathrin coat of arbitrary shape (compare chapter 2). For a symmetric hexagonal lattice with k–rings it holds analogously

$$\begin{aligned} 0 &= \Delta F - \Delta E + \Delta V \,, \\ 0 &= 3\Delta F_3 + 2\Delta F_4 + \Delta F_5 + 0\Delta F_6 - \Delta F_7 - 2\Delta F_8 - 3\Delta F_9 + \dots \,, \end{aligned} \tag{7.5}$$

where F_i is the number of facets with i–edges. Eq. (7.5) states that pentagons can only be created by simultaneously creating heptagons or higher order structures. Using this equation and the k-ring structure of the considered lattice one can deduce the following relations

$$\Delta E = \frac{3}{2}\Delta V \,, \qquad \Delta F = \frac{1}{2}\Delta V \,. \tag{7.6}$$

The first relation states that three additional edges are created by incorporating two additional nodes (triskelia) into the clathrin lattice. The second relation implies that one has to add exactly two nodes (triskelia) to create another face. Since the probability of incorporating two triskelia simultaneously is low compared to the growth rate at the edge given by the incorporation of one triskelion, we expect very few of such events. However, we note that the density of clathrin would increase during such

a transformation, which is in agreement with experimental results [187]. In conclusion, kinetic equations and topological arguments show that the flat-to-curved transition could be driven by acquiring pentagons within the lattice bulk. Nevertheless, it seems to be a rare event given the high binding energy of clathrin triskelia and the fact that two triskelia have to be incorporated simultaneously.

Hypothesis: Bulk acquisition by filling up structural gaps

Motivated by the observations of the previous paragraphs we hypothesise whether structural gaps are created during growth of clathrin lattices. Structural gaps would facilitate the rearrangement process of the clathrin lattice as clathrin triskelia have a reduced number of binding partners. As structural gaps we define vacancies within the clathrin lattice where lattice sites are unoccupied, but which are distributed in the lattice such that binding triskelia to these vacancies would not change the number of occupied lattice edges. Hence, due to the geometry of clathrin triskelia a visually fully connected lattice can contain such structural gaps. In contrast to pentagonal or heptagonal defects, which are immediately visible in all standard visualisation methods (light microscopy, metal replica EM, cryoEM, atomic force microscopy), such structural gaps are practically impossible to be seen directly.

7.3 Analysis of size and shape of flat clathrin lattices

To test the hypothesis that flat clathrin lattices might grow with structural gaps, we study a cell line (BSC-1) that is known to not develop large flat lattices (plaques) but rather features many small flat lattices that eventually convert to curved pits [172]. We first analysed the size and shape of these flat clathrin structures on images with ultrastructural resolution. Fig. 7.2 (a) shows an EM image of a subregion of the cell membrane (scale: 1 $pixel = 1.2$ nm) where flat, dome and pit shaped clathrin lattices (stained in brown) can be seen (the image was provided by courtesy of Delia Bucher and Kem A. Sochacki). In Fig. 7.2 (b), a magnification of a typical flat clathrin lattice shows how the size and contour are determined. The red outline, corresponding to the edge length, was determined by marking manually points with ImageJ [209] at the edge of the lattice which confine the lattice. These points are then connected by straight lines. By this choice the contour has the shape of a polygon. We follow this routine as it can be easily extended to computer simulations. We measured the area (A), perimeter or edge length (L) and circularity ($C = 4\pi A/L^2$) of flat clathrin lattices. We use circularity to characterise the roughness of clathrin lattices as it quantifies the deviation from the circle, can be easily compared to simulations and has been previously used to characterise clathrin lattices [40, 41]. While a perfect circle would have $C = 1$, all other structures will have smaller values. Fig. 7.2 finally shows the

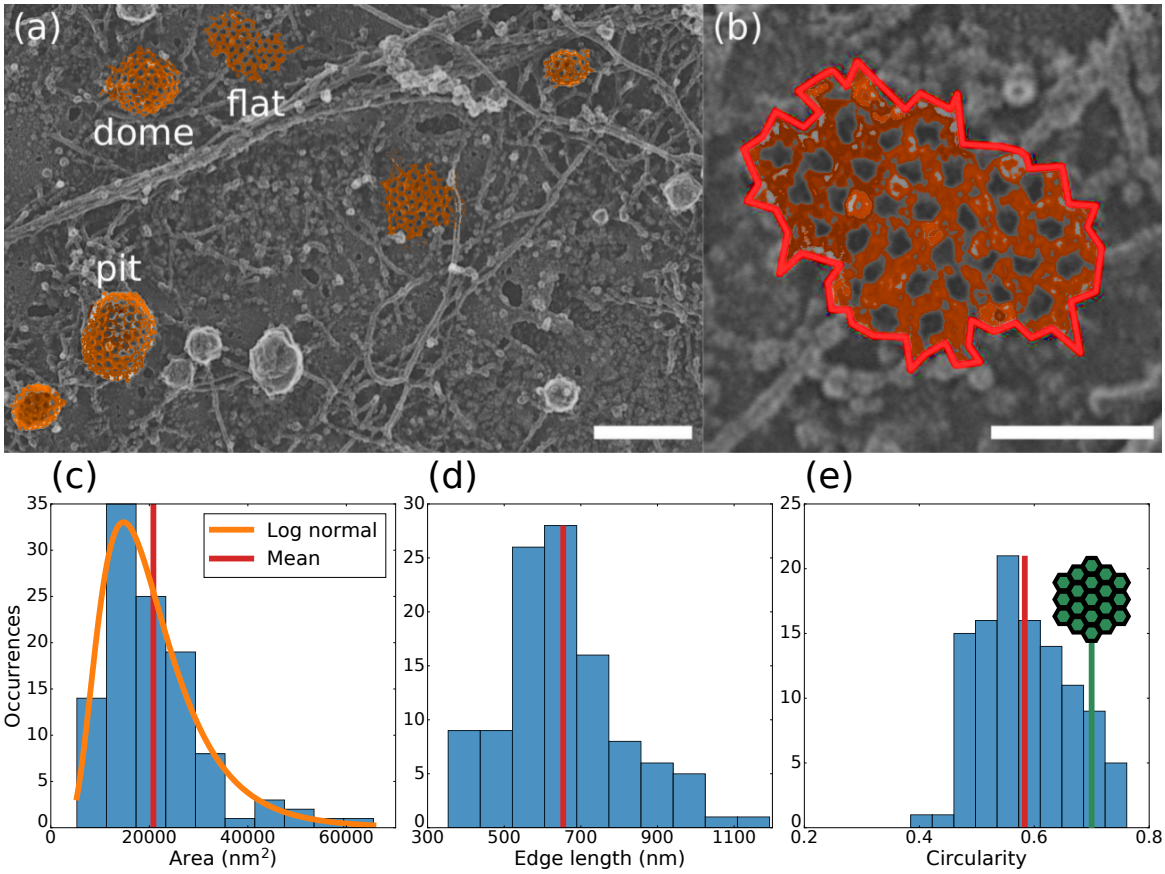

Figure 7.2 | Size and shape of clathrin lattices. **(a)** EM image of a subarea of the cell membrane. Flat, dome and pit shaped clathrin lattices (brown) are shown. Scale bar 200 nm. **(b)** Magnification of a representative flat clathrin lattice. Scale bar 100 nm. The images were provided by courtesy of Delia Bucher and Kem A. Sochacki. The red outline was used to quantify **(c)** area, **(d)** edge length and **(c)** circularity of the lattice in histograms for $N_{\mathrm{EM}} = 109$ flat clathrin lattices. We note that the most circular compact hexagonal shapes of 7, 19 and 37 hexagons have a circularity of around $C = 0.7$ (solid green). Mean values are shown in solid red and the fitted log-normal distribution is shown in solid orange in **(c)**.

measured histograms for area (c), edge length (d) and circularity (e). We note that our results for area of flat lattices agree with those in [172], where similar data sets for BSC-1 cells were evaluated by fitting a smooth contour. We also note that BSC-1 cells have smaller clathrin lattices than other cell lines, e.g. HeLa-cells [40, 41]. Regarding circularity, we note that the most circular compact hexagonal shapes of 7, 19 and 37 hexagons, which represent 13, 30 and 42 edges, respectively, have $C \approx 0.7$ (green in Fig. 7.2 (e)), where the manually measured area of a single hexagon is $A_0 = 796$ nm^2 and the length of a single segment $L_0 = 17.5$ nm. For most lattices the circularity is below this value, suggesting that the main source for the small C-value is not only the rugged rim, but also the elliptical shape.

The results from Fig. 7.2 reveal several important aspects of clathrin lattice growth that are essential for corresponding computer simulations. First, there is a distinct het-

erogeneity between individual lattices, resulting in a broad distribution and suggesting a stochastic model. Secondly, considering the circularity, it is obvious that the clathrin lattices are only in rough approximation circular. The low C-values suggest that this is only partly due to the hexagonal lattice leading to a rough contour, and that the clathrin lattices become anisotropic due to the underlying growth process. Thirdly, the shape of the distributions can be approximated by a log-normal distribution [210] (see fit to the data as solid orange line in Fig. 7.2 (c))

$$f(A) = \frac{1}{\sqrt{2\pi\sigma^2 A}} \exp\left(-\frac{(-\ln(A) - \mu)^2}{2\sigma^2}\right), \tag{7.7}$$

which is typical for growing structures due to the multiplicative rather than additive effect of noise. The fit to the data of the size yields $\mu \approx 9.8$ (corresponding to an area of $A = 18568$ nm^2) and $\sigma = 0.48$. The log-normal distribution can be deduced by assuming that the growth of a flat clathrin lattice with area A and growth rate r can be modelled by Gompertz law [210]

$$\dot{A} = rA\,. \tag{7.8}$$

The equation is motivated by the microscopic picture that new clathrin triskelia can bind to a clathrin triskelion within the bulk. The growth rate is supposed to decrease exponentially

$$\dot{r} = -\alpha r\,, \tag{7.9}$$

as for a larger lattice more and more nodes within the bulk are occupied and at some point the lattice is supposed to invaginate and therefore stops growing flat. We introduce Gaussian white noise $\xi(t)$ with $\langle\xi(t)\rangle = 0$ and $\langle\xi(t)\xi(t')\rangle = \delta(t - t')$ with amplitude σ to the growth process [210] and find a Langevin equation for growing clathrin clusters

$$\dot{A} = \alpha A \ln\frac{A_{\max}}{A} + \sigma A\xi(t)\,. \tag{7.10}$$

The multiplicative character of the noise implies that larger lattices are affected by stronger fluctuations since the number of binding partners increases with the number of triskelia that is proportional to the area. In the steady state, when $A \to A_{\max}$ (corresponding to a snapshot of the cell membrane when assuming that the time average equals the ensemble average), the equation simplifies to

$$\frac{\dot{A}}{A} = \frac{\mathrm{d}\ln A}{\mathrm{d}t} = \sigma\xi(t)\,, \tag{7.11}$$

implying that the stationary distribution of $\ln A$ is distributed normally or equivalently, A is distributed like a log-normal distribution.

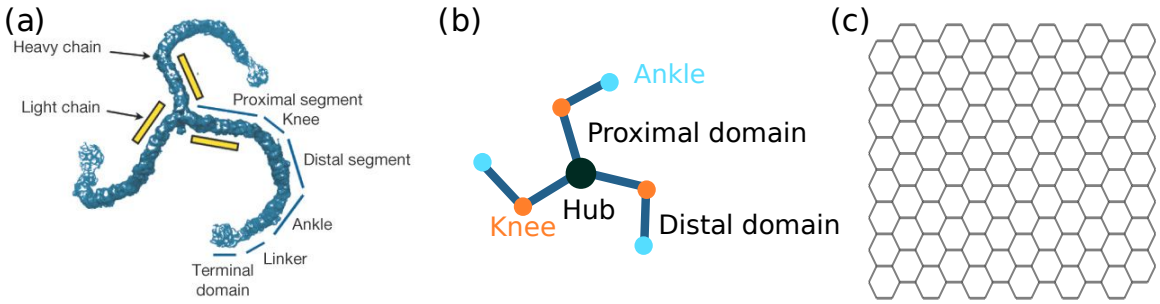

Figure 7.3 | (a) Reconstruction of a clathrin triskelion. Figure taken and adapted from [22]. **(b)** Model representation of a triskelion. **(c)** Model representation of the hexagonal lattice.

7.4 Computer simulations of clathrin lattice growth

To test the hypothesis that clathrin lattices form with structural gaps we use computer simulations of growing clathrin lattices and compare them to EM and CLEM data.

7.4.1 The hexagonal lattice and the clathrin triskelion

The internal structure of a clathrin triskelion is shown in Fig. 7.3 (a), which is an experimentally deduced reconstruction of a clathrin triskelion. From the central hub, three spikes emanate. The proximal and distal domains define the two possible overlap regions in the lattice, with nearest and next-nearest neighbours. The terminal domain is directed towards the membrane and binds adaptor and accessory proteins, so it does not contribute to the flat lattice. In the following, we call the connection between proximal and distal domain the *knee*, and the connection between distal and terminal domain the *ankle*. In Fig. 7.3 (b) the representation of a clathrin triskelion in the simulation and (c) the hexagonal geometry of the clathrin lattice on which we simulate the assembly of clathrin triskelia is shown. Importantly, clathrin triskelia only occur in in the right-handed version of the two possible enantiomers [211] as depicted in 7.3 (a) and (b).

7.4.2 Eden-like model for growing clathrin lattices

Because clathrin lattices grow along the plasma membrane, we require a two-dimensional reaction-diffusion model. Two limiting cases are defined by reaction and diffusion control, respectively (compare chapter 2). The standard reaction-limited model is the Eden model, in which the cluster is growing from inside, without any modelling of the transport required to bring in new components [105]. This model results in compact shapes with limited contour roughness. The complementary model is diffusion-limited aggregation (DLA), which is completely dominated by the transport process and leads to fractal shapes [99]. Given our experimental data as shown in Fig. 7.2, and the

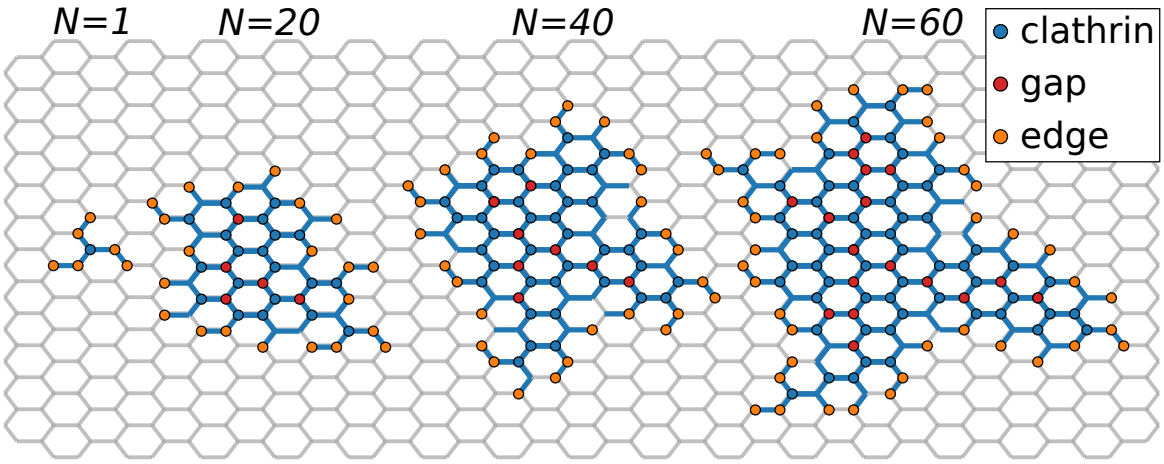

Figure 7.4 | Simulation of clathrin lattice growth. Four snapshots of a growing clathrin lattice of $N = \{1, 20, 40, 60\}$ clathrin triskelia. Lattice nodes (edges) which are occupied by a clathrin triskelion are displayed in blue. Lattice nodes which are part of a triskelion and connected to unoccupied lattice nodes are called edge nodes and are shown in orange. Cluster nodes which are not occupied by a triskelion but which could be occupied by a triskelion without changing the number of cluster nodes are called structural gaps (red circles).

general observation that clathrin structures do not exhibit fractal shapes [23], it is clear that the Eden model is a suitable starting point. In detail, we note that the total binding energy per clathrin triskelia has been estimated to be $\epsilon_{\text{clathrin}} = 23\ \text{k}_\text{B}T$ for clathrin pits [31]. Assuming a similar value for flat lattices and given that a single triskelion has six segments in the lattice (three legs, each with a proximal and a distal domain being part of the lattice), each segment binds with a few units of thermal energy to its environment. This suggests that after binding to the clathrin lattice, the triskelion can still rearrange itself. We also note that the triskelia cannot only attach to the edge of the growing lattice, but also in the bulk, again arguing that transport is not limiting. In order to account for the different degrees of heterogeneity of the growing lattices, we therefore aim at a Eden-type growth model that leads to compact shapes of varying internal density. We note that the clathrin system is especially suited to implement corresponding mechanisms because of the domain substructure of the triskelia.

The growth algorithm

For the simulation of growing clathrin lattices we use the Python software package NetworkX [212]. Fig. 7.4 shows snapshots of a growing lattices of $N = \{1, 20, 40, 60\}$ clathrin triskelia. In the following we explain our growth algorithm:

1. The simulation starts by choosing the initial position of the first clathrin triskelion. The hub or node of the triskelion is shown as a blue circle and the legs of the triskelion as blue edges (compare Fig. 7.4).

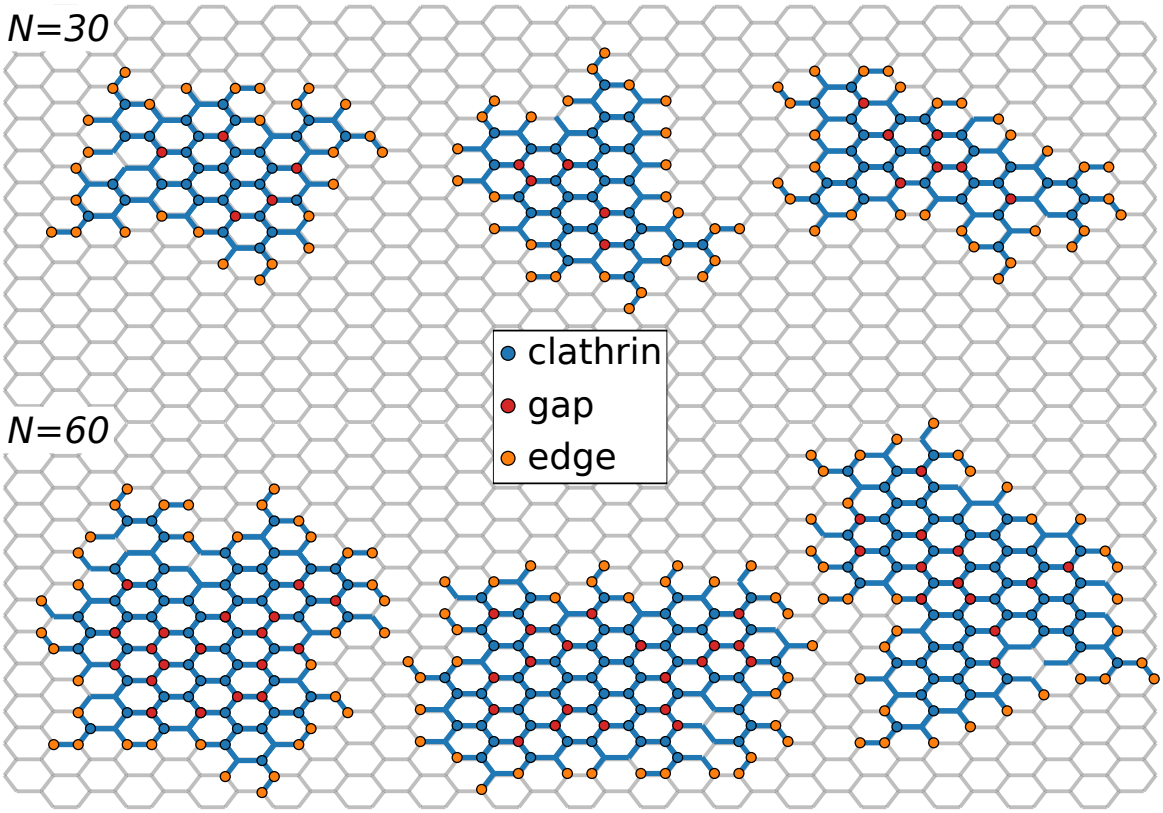

Figure 7.5 | Heterogeneity of simulated clathrin lattices. Three examples of lattices of $N = 30$ and $N = 60$ clathrin triskelia, respectively.

2. Next, a list of potential growth sites is defined by all nodes that are connected to the existing clathrin lattice (in the beginning: a single triskelion) but still unoccupied by a triskelion.

3. From that list of potential growth sites a node is randomly selected where each node has the same weight.

4. After the triskelion is placed into the lattice the algorithm returns to 2.

5. The algorithm stops if the lattice incorporates N triskelia.

In order to compare simulated lattices with each other we define several quantities illustrated in Fig. 7.4. We define *cluster nodes* as all nodes that are either occupied by a clathrin triskelion (illustrated as blue circles) or connected to the hub of a triskelion through a leg (illustrated as blue edges). We define an *edge node* as a cluster node that is connected to an unoccupied node (illustrated as orange circles); this defines the edge of the clathrin cluster. Then, *area* is measured by the number of cluster nodes and *perimeter* by the number of edge nodes. Finally we define a *structural gap* as a node that is not occupied by a triskelion but adding a triskelion to that site would not change the number of cluster nodes (illustrated as red circles). Since the growth

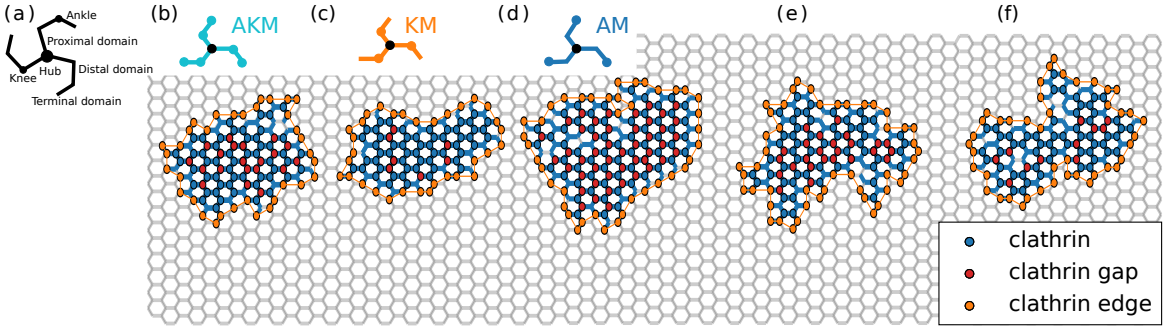

Figure 7.6 | Different models of clathrin growth. **(a)** Schematics of a clathrin triskelion. **(b)** AKM. Cluster nodes that are at the ankle or knee of a triskelion can get populated, i.e. every unoccupied cluster node connected to the lattice can get occupied. **(c)** KM. Only lattice nodes that are at the knee of a triskelion (adjacent to an occupied node) can get populated. **(d)** AM. Only lattice nodes that are at the ankle of a triskelion (next-to-next adjacent to an occupied node) can get populated. **(e)** Strain induced dissociation model. In contrast to **(a)** triskelia that are connected to more than two triskelia can dissociate from the lattice. **(f)** Energy induced dissociation model. In contrast to **(a)** triskelia that are connected to one or two triskelia can dissociate from the lattice.

algorithm is a stochastic process, the formed clathrin lattices differ in size and shape. The heterogeneity is illustrated in Fig. 7.5 for lattices of $N = 30$ and $N = 60$ triskelia, respectively.

7.5 Simulation results

Different models of clathrin lattice growth

We first investigate how different model variants of lattice growth impact the shape and size of clathrin lattices by using the outlined simulation algorithm. In the different model variants clathrin triskelia can differently bind to each other (compare Fig. 7.6 (a)). We consider the ankle-and-knee model (AKM) where triskelia can bind to either the ankle or knee of other triskelia (Fig. 7.6 (b), top), the knee model (KM) where triskelia can only bind to the knee (i.e. next neighbours) of a triskelion (Fig. 7.6 (c), top) and the ankle model (AM), where triskelia can only bind to the ankle (i.e. next-to-next neighbours) of a triskelion (Fig. 7.6 (d), top). These scenarios are motivated by different binding affinities and reflect different transport modes which add new triskelia to the growing cluster. In addition, we consider the impact of dissociation of clathrin triskelia from the clathrin lattice. Dissociation or turnover of clathrin triskelia from flat lattices was observed in several studies by using FRAP experiments [40, 38, 41]. In particular, we consider dissociation of clathrin triskelia from the centre of the lattice (strain induced dissociation) and dissociation of triskelia from the periphery of the lattice (energy induced dissociation).

Fig. 7.6 shows simulated example lattices for the (b) AKM, (c) KM, (d) AM, (e) strain induced dissociation model and (f) energy induced dissociation model. One can already deduce from the visual expression in Fig. 7.6 that model (d) and (e) grow sparsely, whereas model (c) and (f) grow compactly and (b) represents an intermediate case.

For the models shown in (c) - (f) the simulation algorithm is adapted in the following way compared to the outlined algorithm for model (b). In (c) the list of potential growth sites only includes unoccupied cluster nodes that are next neighbours to clathrin triskelia. In (d) the list of potential growth sites only includes unoccupied cluster nodes that are next-to-next neighbours to clathrin triskelia. In (e) instead of a growth step a dissociation step can occur with 20% probability. In a dissociation step a triskelion that is connected to more than two triskelia can dissociate from the lattice. In (f) the situation is similar to (e) but in contrast, now only a triskelion that is connected to one or two triskelia can dissociate from the lattice in a dissociation step.

We compare the mean trajectories of the five models quantitatively in Fig. 7.7 averaged over $N = 1000$ simulation runs. The ankle-and-knee model is shown in cyan, the KM in orange, the AM in blue, the strain induced dissociation model in green and the energy induced dissociation model in red. Comparison of AKM, KM and AM reveals that the AM grows most extended concerning edge length (Fig. 7.7 (a)) and area (Fig. 7.7 (b)) and therefore less circular (Fig. 7.7 (d)), the AKM represents an intermediate case and the KM is the most compact growth model. Considering the density (Fig. 7.7 (c)) and the number of structural gaps (Fig. 7.7 (e)) we find rather dilute growth for the AM and very compact growth for the KM. Again, the ankle-and-knee represents an intermediate case. Especially, the number of gaps per area (here: number of cluster nodes) reaches up to 20% in the AM (Fig. 7.7 (f)). Comparison of AKM, strain induced dissociation model and energy induced dissociation model reveals rather small differences considering shape, i.e. edge length (Fig. 7.7 (a)), area (Fig. 7.7 (b)) and circularity (Fig. 7.7 (d)) as well as content, i.e. density (Fig. 7.7 (c)), gaps (Fig. 7.7 (e)) and gaps per area (Fig. 7.7 (f)). Typically, the strain induced dissociation model grows most extended and dilute, the energy induced dissociation model grows more compact and the AKM represents the intermediate case.

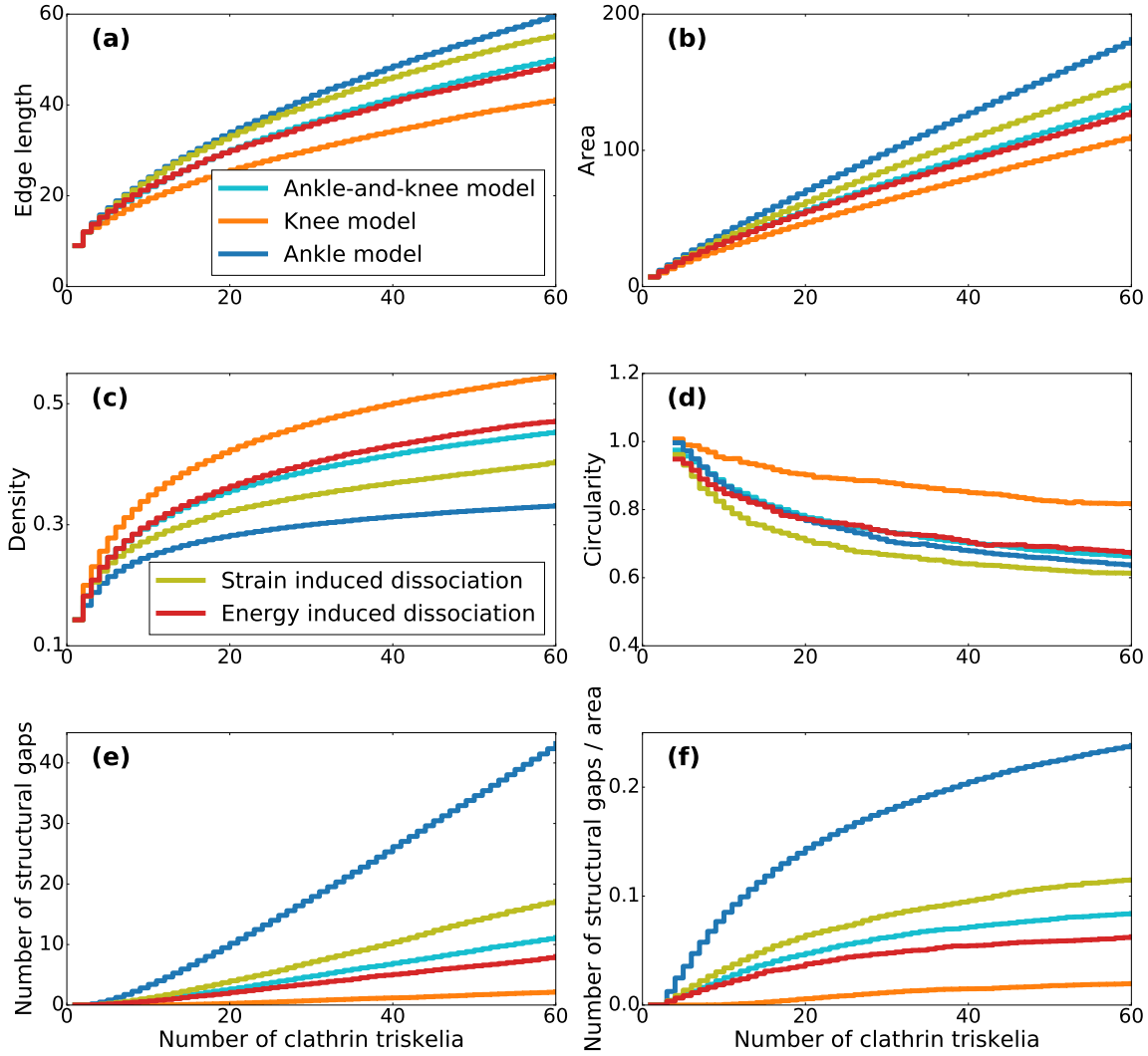

Figure 7.7 | Mean trajectories averaged over $N = 1000$ simulated clathrin lattices for the AKM (cyan), the KM (orange), the AM (blue), the strain induced dissociation model (green) and energy induced dissociation model (red). **(a)** The mean number of edge nodes (here referred to as edge length) as a function of the number clathrin triskelia. **(b)** The mean number of cluster nodes (here referred to as area) as a function of the number of clathrin triskelia. **(c)** The mean density of clathrin lattices, which is the number of triskelia divided by the number of cluster nodes as a function of the number of clathrin triskelia. **(d)** The mean circularity of clathrin lattices as a function of the number of clathrin triskelia. We note that circularity is only reasonably defined for clusters incorporating several triskelia (here at least three). **(e)** The mean number of structural gaps of clathrin lattices as a function of the number of clathrin triskelia. **(f)** The mean number of structural gaps per mean number of cluster nodes of clathrin lattices as a function of the number of clathrin triskelia.

7.6 Comparison of experiment and simulation

To compare simulations and experiments we choose the AKM, the KM and the AM, as they exhibit the largest differences and represent extreme cases. Thus, we address the question of how heterogeneously clathrin lattices grow on the level of different growth modes rather than by introducing different dissociation mechanisms. However, we note that dissociation mechanisms would in addition change the growth behaviour.

Prerequisites to compare simulations to experimental data

To quantitatively compare the size of simulated lattices to experimentally observed ones we have to fix the edge length within the simulation. To measure the edge length of a lattice hexagon in EM we chose randomly lattice hexagons. For $N = 34$ measurements we find a mean edge length of $a = 17.5 \pm 1.7\,\mathrm{nm}$. The area of a hexagon is given by $a^2 3/2\sqrt{3} = 796 \pm 155\,\mathrm{nm}^2$. As a clathrin triskelion consists of 3 legs with 2 segments each, i.e. 6 edges, the area of a triskelion should be similar to the area of a hexagon. In [31] the area of a triskelion was reported to be $800\,\mathrm{nm}^2$ which compares well to our measurement. By scaling the edge length in the simulation by this factor we can quantitatively compare our simulated clathrin lattices to experimental lattices.

In the EM image we observe a snapshot of the cell membrane. Taking the ensemble average as the time average, the distribution of clathrin lattices represents a steady state configuration. To reproduce the experimentally found area distribution of clathrin lattices we stop the growth simulation such that the resulting area distribution matches the experimentally found one. Therefore, we have to convert the fitted value for μ to the corresponding value for the number of triskelia μ'. For this purpose we take the value deduced from the fit ($18568\,\mathrm{nm}^2$), divide it by the measured mean area of a clathrin triskelion ($796\,\mathrm{nm}^2$), take the natural logarithm and get a value of $\mu' = 3.14$. By sampling the size of clathrin lattices from a log-normal distribution with $\mu' = 3.14$ and $\sigma = 0.48$ we get a distribution of cluster sizes that is similar to the one of the experiment. To compare the perimeter of clathrin lattices to experimental results it is not sufficient anymore to take the number of edge nodes. Instead we take the list of edge nodes as and input and solve for the shortest path connecting all edge nodes. As this is in principle a travelling salesman problem, which is NP hard we solve it heuristically [213]. Basically, we use the 2-opt algorithm which reorders a given path to avoid that it crosses over itself by reordering the traversed edge nodes until we find no improvement anymore. An illustration of the calculated lattice edges is shown in Fig. 7.6 (as orange lines). To quantitatively compare the area of clathrin lattices to experimental results we have to calculate the area contained within a given contour.

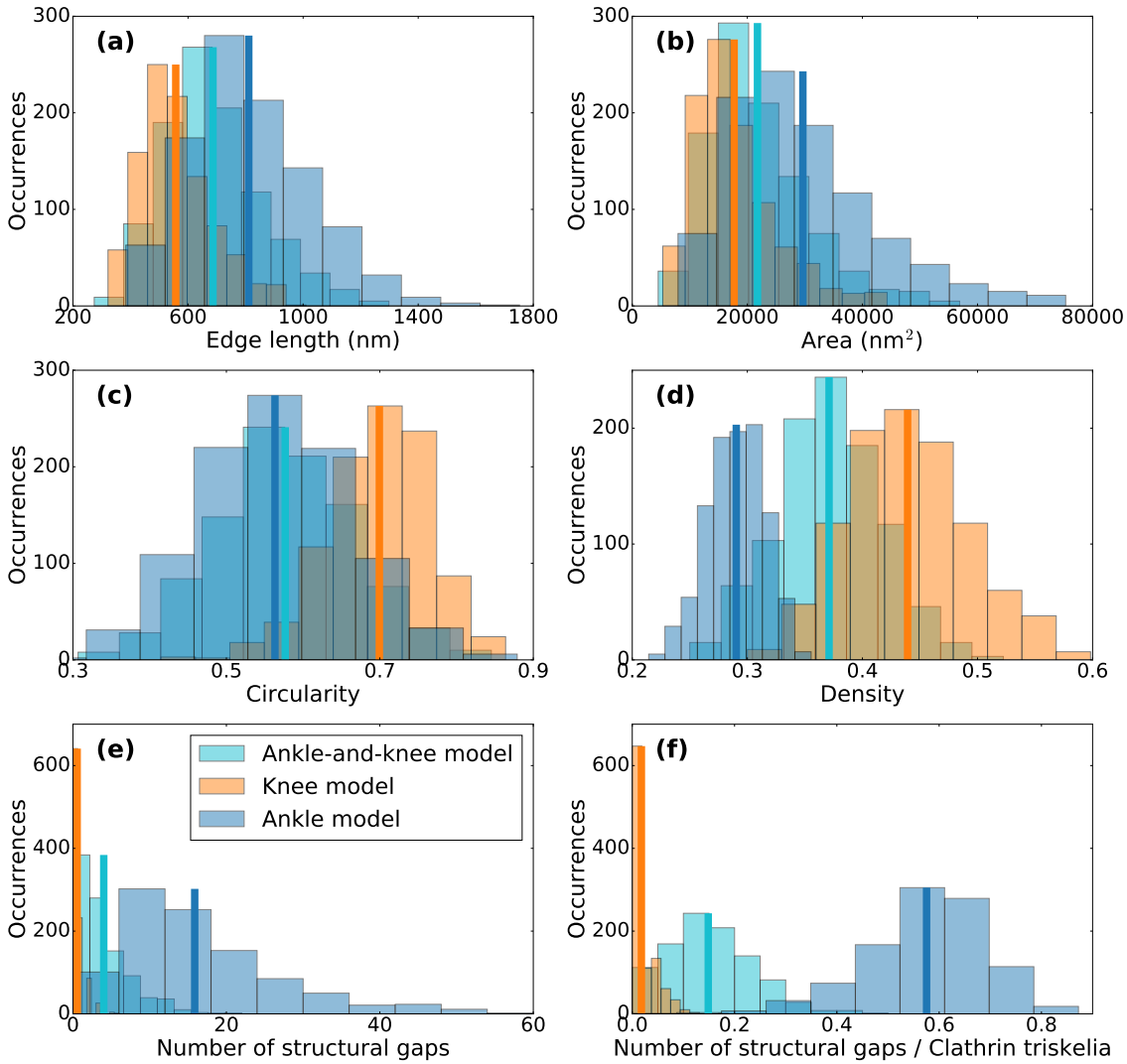

Figure 7.8 | Simulation results of $N = 1000$ simulated clathrin lattices for the AKM (cyan), the KM (orange) and the AM (blue). The corresponding mean values are plotted in the same colour as solid lines. **(a)** Edge length. **(b)** Area. **(c)** Circularity. **(d)** Density. **(e)** Structural gaps. **(f)** Structural gaps relative to the number of clathrin triskelia within the lattice.

For this purpose we use the Sektorformel of Leibniz

$$A_{\text{lattice}} = \frac{1}{2} \sum_{i=1}^{N-1} \left(y_i(x_{i+1} - x_i) - x_i(y_{i+1} - y_i) \right) , \tag{7.12}$$

where the position ξ_i of the edge node i is given by (x_i, y_i) and the edge nodes are ordered such that the closed contour $(\xi_1 = \xi_N)$ has minimal length.

Simulation results

In Fig. 7.8 the simulated histograms are shown for the AKM (cyan), for the KM (orange) and for the AM (blue). In (a) one can see that clathrin lattices have the

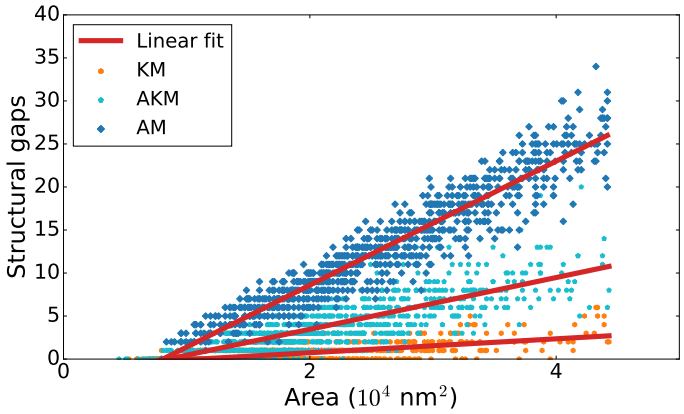

Figure 7.9 | Structural gaps within clathrin lattices. The number of structural gaps against the size of clathrin lattices for $N_{\mathrm{sim}} = 1000$ simulation runs. AKM: The number of structural gaps is proportional to the size of the clathrin lattice. KM: In contrast to the AKM the number of structural gaps is strongly reduced, indicating that lattices grow quasi densely. AM: The lattices exhibit the largest number of structural gaps.

largest edge length in the AM followed by the AKM and the KM. Although, the distribution of clathrin triskelia that underlies the simulations is identical for all three models the covered lattice area differ, as the models differ in the way how densely the assembled structures grow. Thus, the mean area is smallest in the KM followed by the AKM and AM (b). Therefore, the lattices in the KM are most circular, followed by the AKM and the AM (c). In addition, we find that lattices in the KM grow with the highest density (d) and the least number of structural gaps (e). Interestingly, both the AM and the AKM show a considerable amount of structural gaps (e). In particular, the ratio of structural gaps over clathrin triskelia within the lattice is nearly 60% in the AM (f). Comparing these results to the experimental data of Fig. 7.2 we find a first hint that both the AM and the AKM could agree with the experimental data.

Prediction of structural gaps

We now use our simulations to predict the heterogeneity of clathrin lattices. In Fig. 7.9 we show the number of structural gaps as a function of clathrin lattice size for the AKM, the KM and the AM. A linear fit to the data reveals that both quantities are strongly correlated. We determine the Pearson correlation coefficient to be $R_{\mathrm{AKM}} = 0.82$, $R_{\mathrm{KM}} = 0.64$ and $R_{\mathrm{AM}} = 0.95$. As expected, the number of structural gaps is reduced in the KM. In contrast, the AM and AKM predict both a considerable amount of structural gaps in clathrin lattices.

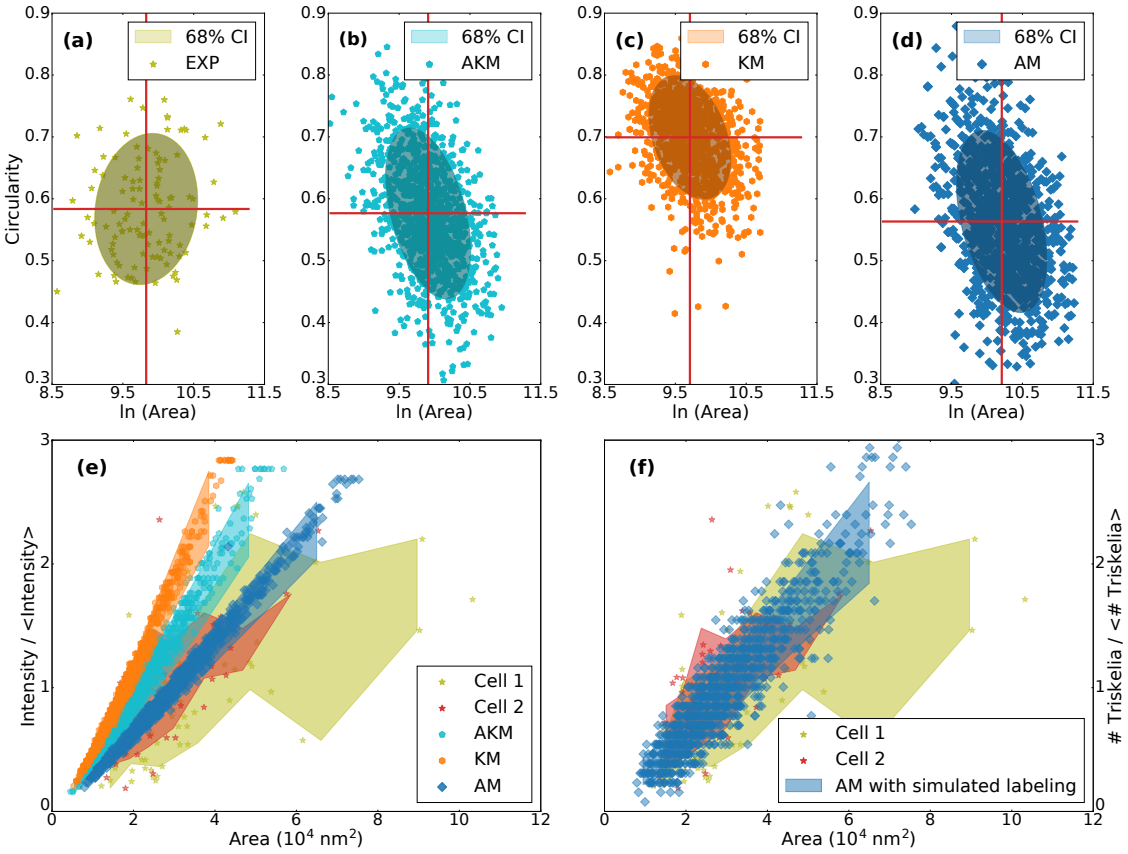

Figure 7.10 | Comparison between EM measurement and lattice growth simulation for $N_{\text{sim}} = 1000$ runs. Scatter plots showing the circularity of lattices as a function of the logarithm of the area. The mean values are shown in red and the 68% confidence interval (CI) as ellipse. **(a)** EM measurement for $N_{\text{EM}} = 109$ lattices. **(b)** AKM. **(c)** KM. **(d)** AM. Comparison between CLEM measurement and lattice growth simulation. **(e)** Scatter plot showing the intensity of flat clathrin lattices immunostained for clathrin heavy chain relative to their mean intensity as a function of the lattice area for the measured CLEM data (green and red stars) with $N_{\text{CLEM}} = 127$ structures from 2 cells. In addition, the number of clathrin triskelia relative to the mean number of clathrin triskelia as a function of the lattice area for the AKM (blue pentagons), KM (purple hexagons) and AM (brown rhombs) is shown. The coloured regions are calculated by binning the data with respect to their area and taking the mean and standard deviation in each bin. **(f)** Same as in **(e)** but only for the AM. In addition, we simulate that on average only half of the clathrin triskelia are immunostained for clathrin heavy chain.

7.6.1 Comparison between simulation and EM measurement

To compare the simulation results to experimental data (see Fig. 7.2), we correlate circularity and the logarithm of the area in Fig. 7.10 (because the logarithm of the area is normally distributed) (a) for the EM measurement, (b) the AKM, (c) the KM, and (d) the AM. Considering the mean values (red) ($C_{\text{Data}} = 0.58 \pm 0.08$, $C_{\text{AKM}} = 0.58 \pm 0.09$, $C_{\text{KM}} = 0.70 \pm 0.07$, and $C_{\text{AM}} = 0.56 \pm 0.10$) we find good agreement between the

experimental data and both the AKM and the AM. In contrast, the KM can be excluded based on these data. Interestingly, the simulated data indicates that larger lattices seem to be less circular. We note that a recent experimental study using electron and super-resolution microscopy found a similar correlation between circularity and area of flat clathrin lattices, albeit for cell types (HEK-293T and HeLa) which have much larger clathrin plaques [40].

7.6.2 Comparison between simulation and CLEM measurement

To compare our simulation results to another experimental data set and in order to discriminate between the AKM and the AM, we use CLEM data which correlate the intensity in FM of flat clathrin lattices immunostained for clathrin heavy chain and their size in EM (same data set as in chapter 6 and [172]). The intensity of the background corrected CLEM data I should be proportional to the number of clathrin triskelia within a clathrin lattice N, both as function of lattice area A. Hence, the intensity relative to the mean intensity equals the number of clathrin triskelia relative to the mean number of clathrin triskelia

$$I(A) = \gamma N(A) \quad \rightarrow \quad \frac{I(A)}{\langle I \rangle} = \frac{N(A)}{\langle N \rangle}\,, \tag{7.13}$$

where γ is a proportionality constant that drops out by normalisation. Hence, it is possible to compare the CLEM data set to the simulation results quantitatively. Fig. 7.10 (e) shows a scatter plot of the intensity relative of the mean intensity as a function of the lattice area for the measured CLEM data (green and red stars). In addition, the number of clathrin triskelia relative of the mean number of clathrin triskelia as a function of the lattice area for the AKM (cyan pentagons), the KM (orange hexagons) and the AM (blue rhombs) is shown. The coloured regions are calculated by binning the data with respect to their area and taking the mean and standard deviation within each bin. Clearly, the AM, which has the largest degree of gaps from all models considered, agrees best with the measured data.

In the CLEM data not every clathrin triskelion is immunostained for clathrin heavy chain. Due to this fact the fluorescence intensity can vary for clathrin lattices spanning across a similar area and containing a similar number of triskelia. To mimic this variation we simulate the number of labeled clathrin triskelia by assuming that each of the triskelia within a lattice of N triskelia in total has the probability $p = 0.5$ to be labeled. Then the probability that n triskelia are labeled is given by a binomial distribution

$$P(n; N) = \binom{N}{n} p^n (1-p)^{N-n}\,. \tag{7.14}$$

By sampling the number of labeled clathrin triskelia we have a quantitative prediction of how strongly the intensity should vary. Fig. 7.10 (f) shows the result. Importantly,

the simulated variation of the AM agrees very well with the measured CLEM data. As in the AM the simulated clathrin lattices agree very well with both the shape (EM) and content (CLEM) of experimentally measured clathrin lattices we conclude that clathrin lattices grow with structural gaps.

7.7 Conclusion

In this chapter we started by investigating both the edge- and bulk-acquisition hypothesis of pentagons and found that plasticity in regard to bending might agree best with the incorporation of pentagons in the bulk. We reasoned that incorporation of clathrin triskelia within the bulk of the clathrin lattice would be facilitated in a clathrin lattice exhibiting spatial heterogeneity. Pentagonal or heptagonal defects and even broken lattices are often found in flat clathrin lattices, but here we addressed another type of potential defect, namely structural gaps that arise because the triskelia might not be close-packed in a flat hexagonal lattice. Such heterogeneity could explain the observed fast exchange dynamics and the plasticity in regard to bending, i.e. in particular the flat-to-curved transition.

The structural gaps addressed here could be related to topological defects and broken lattices, but in principle, they could also occur in hexagonal lattices that upon visual inspection look perfectly regular. In standard light microscopy, they would not be directly detectable due to the resolution limit. Moreover, they are currently almost impossible to see in metal replica EM or even cryoEM. Single molecule fluorescent microscopy or atomic force microscopy (AFM) applied to clathrin lattices [72] might have the required resolution, but have not yet been used to investigate this particular question. We therefore suggest to perform such measurements at flat clathrin lattices. In addition, one could think of synthesising a labeled molecule that preferentially binds to the proximal domain of clathrin triskelia in the absence of another proximal domain to directly visualise structural gaps.

Rather than addressing this important question by microscopic models with many parameters, for example coarse-grained Molecular Dynamics [116] or Brownian Dynamics [37, 117], here we have defined three different models motivated by the Eden model for growth of compact clusters and adapted to the known internal structure of triskelia (three domains connected by two joints, the knee and the ankle, which correspond to potential binding sites of the hubs of other triskelia). We note that the Eden model is especially suited for the simulation of compact clusters, which we have also tested for large lattices of 10^4 triskelia for the AKM (see Appendix A.10). In a two-step procedure, we were able to rule out first the KM and then the AKM. The best agreement with our CLEM data was obtained for the AM, that predicts a surprisingly high degree of heterogeneity. In the AM, new triskelia only bind to binding sites at

the ankle of clathrin legs. This suggests that incoming triskelia are more likely to be bound at the more distal parts, either due to special transport modes or due to increased binding energies. The success of the AM suggests that proximal domains of clathrin triskelia do not bind well to each other in the flat state. We therefore predict that binding of proximal and distal domains is more favourable in the flat state and suggest to test this hypothesis with cryoEM in the future. This agrees with the notion that in assembled hexagonal barrels proximal domains do not align [22].

The structural gaps predicted here could create the necessary space and reduced entanglement that can lead to the observed high degree of clathrin exchange [40, 38, 41] as well as to the lattice rearrangements required for bending [38, 172, 208]. In fact the high degree of clathrin exchange is also another hint for the existence of structural gaps. Taking snapshots of a lattice with clathrin exchange would necessarily reveal a lattice with structural gaps. A lattice that is fully occupied at each point in time cannot exhibit turnover. Importantly, the turnover of flat clathrin lattices is stronger compared to the exchange of curved ones shown using an *in vitro* system [214]. Since new triskelia have to be added for generation of the required pentagons, the density of clathrin triskelia should increase in late stages, which is in agreement with recent observations [187].

Our results agree with the emerging view that clathrin lattices are highly plastic and regulated by cellular factors, such that curvature can be built up once some cellular checkpoint has been cleared [205, 206]. We also note that bending based on structural gaps would first increase density and then stop polymerisation, thus providing a simple physical mechanism to proceed in the standard sequence of CME. Our results also agree with the suggestion that a typical maturation time leads to a typical patch size, around which a statistical distribution exists [34]. We also speculate that gaps in the flat lattice could act as binding sites for signalling molecules. In general, if structural gaps existed in clathrin lattices as predicted here, this would open up many new avenues for controlling their biological function.

8 Modelling the flat-to-curved transition

8.1 Introduction

Clathrin-mediated endocytosis (CME) is one of the most important processes for bringing extracellular material into biological cells. It now becomes increasingly clear that a clathrin-coated structure (CCS) can first assemble flat before it starts to curve the cell membrane [38, 172, 208] (and chapter 6). However, it is still elusive how the exact sequence of lattice rearrangements that are necessary for the flat-to-curved transition might work on a microscopic level of detail. This is even more intriguingly when considering the fact that CCSs are heterogeneous both in their size and shape. Besides flat CCSs and clathrin coated pits with sizes and lifetimes of around $10^4\,\mathrm{nm}^2$ and 30 s also huge clathrin plaques exist with extended sizes and lifetimes of the order of $\mu\mathrm{m}^2$ and several mins [40, 27, 29].

In chapter 7 we showed that flat clathrin lattices assemble and grow spatially more heterogenous than formerly appreciated. In particular, this finding implies that flat clathrin lattices do not show maximal packing density. In addition, there is experimental evidence that the density of clathrin triskelia increases during the flat-to-curved transition [187]. Therefore, we wondered whether an increasing clathrin density might drive the flat-to-curved transition.

In this chapter we theoretically investigate the flat-to-curved transition of clathrin coats based on the assumption that the density of clathrin triskelia within the lattice increases during coat assembly. The assumption is modelled by either an increasing coat rigidity, (see Fig. 8.1 (a)) or line tension (see Fig. 8.1 (b)) and studied by considering the energy of both the membrane and the clathrin coat. Based on this energy model we phenomenologically deduce dynamic equations to investigate the growth and assembly of CCSs. By means of these dynamic equations we study the size and shape of clathrin coats as a function of time and fit our model to experimental data.

8.2 Modelling the geometry and energy of clathrin coats

We first introduce a geometrical model of clathrin coats by spherical caps with varying radius before we develop a model for the energies of the clathrin coat and the cell membrane during CME.

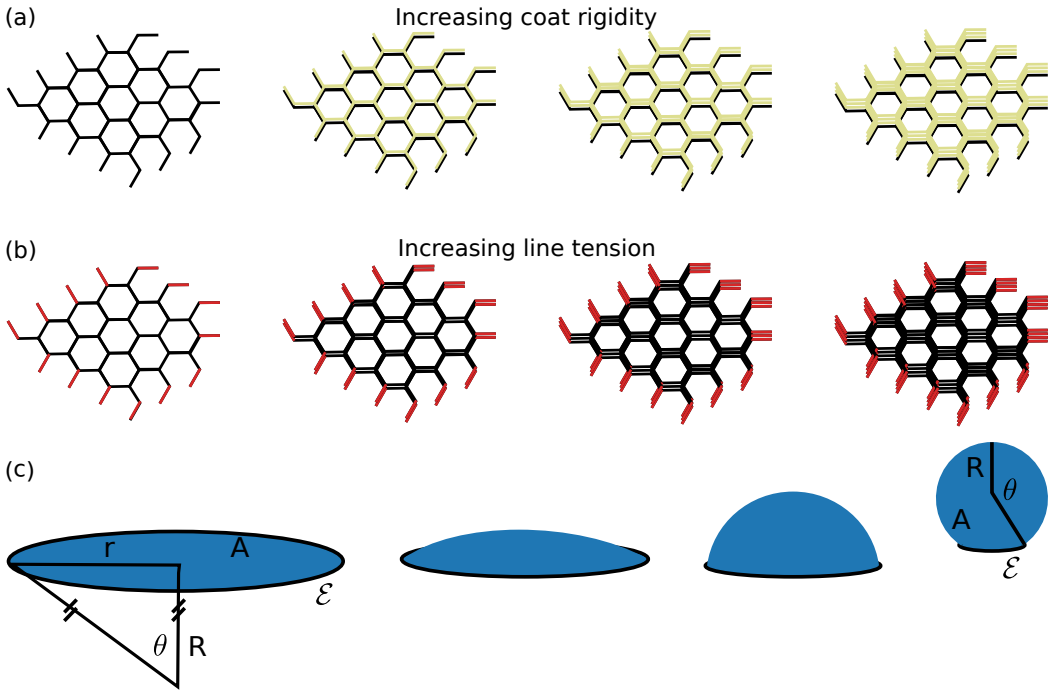

Figure 8.1 | Modelling the flat-to-curved transition of clathrin coats. The effect of an increasing clathrin density is modelled by either **(a)** an increasing coat rigidity or **(b)** an increasing line tension, visualised by an increasing number of clathrin lattice layers from left to right. **(c)** Modelling CCSs with flat, curved and spherical shape by the geometry of a spherical cap. CCSs are characterised by area A, edge length $\mathcal{E}$, radius R and invagination angle θ. Flat CCSs are incorporated in the double limit $R \to \infty$ and $\theta \to 0$ such that $R\theta = r$ (left), and curved CCSs are incorporated for R and θ finite (right).

8.2.1 Geometry of clathrin coats

We model CCSs with flat and curved geometry by a spherical cap with area

$$A(t) = 2\pi R(t)^2 \left(1 - \cos\theta(t)\right) , \tag{8.1}$$

where the radius $R(t)$ of the cap and invagination angle $\theta(t)$ are both functions of time. Then a flat CCS is incorporated in the double limit $\lim_{\theta\to 0}^{R\to\infty} A(t) = \pi(R\theta)^2 = \pi r(t)^2 = A^\diamond$ (note that r is the radius of the flat CCS). In this way, we have a unified description for flat, curved and full spherical shapes. Fig. 8.1 (c) shows the geometry of a flat CCS (left) and the geometry of a spherical CCS (right). From Eq. (8.1) we deduce the radius of the spherical cap

$$R(t) = \sqrt{\frac{A(t)}{2\pi(1 - \cos\theta(t))}} . \tag{8.2}$$

Another important length scale of the spherical cap is its rim or edge length

$$\mathcal{E}(t) = 2\pi R \sin(\theta) = \sqrt{2\pi A(t)\left(1 + \cos(\theta(t))\right)} . \tag{8.3}$$

Next, we calculate the area increase by transforming a flat CCS to a curved state. In this case the area difference between spherical cap area and its projected area is

$$\begin{aligned}\Delta A &= A - \pi R^2 \sin^2(\theta) = A - \frac{\pi A \sin^2\theta}{2\pi\,(1-\cos\theta)} \\ &= A\left(1 - \frac{1-\cos^2\theta}{2\,(1-\cos\theta)}\right) = \frac{A}{2}\,(1-\cos\theta)\ . \end{aligned} \tag{8.4}$$

8.2.2 Energy of clathrin coats

The assembly of clathrin coats is driven by the polymerisation energy of clathrin triskelia and counteracted by the energetic cost of bending the cell membrane and increasing the membrane area. In general, to drive the invagination of the membrane, clathrin coats could either impose their preferred internal geometry (spontaneous curvature) on the membrane (see Fig. 8.1 (a)) or generate curvature due to a line tension (see Fig. 8.1 (b)) [154]. The line tension is created due to open binding sites at the edge of the coat, which reduces the polymerisation energy of clathrin triskelia [31, 120]. The internal geometry of clathrin triskelia would then stabilise the curvature of the membrane and work like a ratchet [215]. Importantly, we here assume that both effects will be proportional to an increasing clathrin density within the coat and therefore increase in time. The total energy can be written by an adapted Helfrich Hamiltonian [86]. In general, to calculate the membrane energy one has to include the contributions both of the clathrin coat and the free membrane parts (as explained in chapter 4). However, as we here focus on a simple description we neglect the contribution of the free membrane parts during the course of this chapter, as it was shown that this energy contribution changes the total energy only modestly [87, 34]. Then, the total energy of a clathrin coat with the shape of a spherical cap reads

$$\begin{aligned}E =& -\mu A + 2\kappa H^2 A + \sigma\Delta A + 2\kappa_{\mathrm{c}}(t)(H-H_0)^2 A + \zeta(t)\mathcal{E} \\ =& -\mu A + 4\pi\kappa(1-\cos\theta) + \frac{\sigma}{2}A\,(1-\cos\theta) \\ &+ 4\pi\kappa_{\mathrm{c}}(t)(1-\cos\theta)\left(1-\frac{R}{R_0}\right)^2 + \zeta(t)\mathcal{E}\,, \end{aligned} \tag{8.5}$$

with the first term representing the polymerisation energy, where μ is the polymerisation energy density of the clathrin coat times coat area A. The second term represents the membrane bending energy, where κ is the bending rigidity and $H = 1/R$ the mean curvature of the spherical cap. The third term represents the energetic cost of increasing the membrane area ΔA where σ is the membrane tension. The fourth term represents the bending rigidity of the coat, where $H_0 = 1/R_0$ is the preferred curvature and $\kappa_{\mathrm{c}}(t)$ the bending rigidity of the coat. The last term is the line tension energy due to unbound clathrin at the edge of the coat, where $\mathcal{E}$ it the edge length and $\zeta(t)$ the

Table 8.1 | Contributions to the total energy of CCSs in the model.

Energy contribution	Motivation	Effect
$-\mu A$	Coat polymerisation energy	Assembly
$2\kappa H^2 A$	Membrane bending resistance	Invagination barrier
$\sigma \Delta A$	Membrane tension	Pit size limitation
$2\kappa_c(t)(H - H_0)^2 A$	Coat bending energy	Invagination transition
$\zeta(t)\mathcal{E}$	Line tension	Invagination transition

effective line tension. Importantly, we here assume that an increasing clathrin density would either increase the coat rigidity or line tension of the coat. The five terms have different effects, which are summarised in Table 8.1. The polymerisation energy drives coat assembly and the bending and tension energy induce flat assembly preferentially. In contrast, the main effect of coat rigidity and line tension is to limit the size of flat CCSs or to drive the invagination process. Both contributions are expected to increase with time as we assume that the clathrin density within the coat increases.

8.3 Energy consideration

The first part of our theoretical analysis of the involved energies during clathrin coat assembly is related to the work of Saleem and coworkers [31] but includes variable coat sizes and the possibility of a flat-to-curved transition. Assuming that the clathrin coat equilibrates fast during coat formation, the system will relax to the state of global minimal energy without any energy barriers. Based on Eq. (8.5) we then predict the shape of assembled clathrin coats. To reduce the complexity of the model and avoid redundancy of mechanisms we consider two cases: First, we investigate the case where the bending rigidity of the coat increases as a function of time and secondly, we assume that the line tension of the coat increases. Importantly, in the first case we neglect the line tension and the second case we neglect the coat rigidity. The parameter values

Table 8.2 | Model parameters.

Parameter	Used value	Reference
Polymer. energy density μ	$0.11\,\mathrm{mJ/m^2}$	[31]
Bending rigidity κ	$25\,\mathrm{k_B T}$	[34]
Membrane tension σ	$10^{-4}\,\mathrm{N/m}$	[34]
Bending rigidity coat $\kappa_c(t)$	$0 - 300\,\mathrm{k_B T}$	[34]
Preferred pit radius R_0	$50\,\mathrm{nm}$	[31, 34]
Line tension $\zeta(t)$	$5.2 \cdot 10^{-2} - 10^{1}\,\mathrm{pN}$	[31]

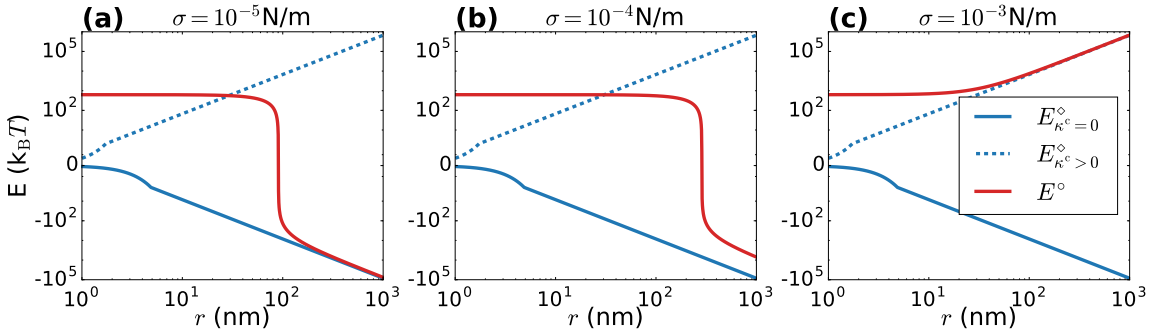

Figure 8.2 | The energy of the flat and spherical state as a function of coat radius for three values of membrane tension σ **(a)** – **(c)**. In solid (dashed) blue the energy of a flat disc for (non-) vanishing coat rigidity $\kappa_c(t) = 0\,k_BT$ ($\kappa_c(t) = 300\,k_BT$), and in solid red for the sphere is plotted. **(a)**, **(b)** For vanishing coat rigidity flat discs are the energy minimum. However, for large coat rigidity and size, spherical structures become energetically favourable. **(c)** For large values of membrane tension the spherical shape is energetically unfavourable.

that are used throughout this chapter are summarised in Table 8.2. We note that for coat rigidity (line tension) the second (first) value in Table 8.2 corresponds to the reported value, whereas the other value is chosen to investigate the effect of the mechanism.

8.3.1 Variable coat rigidity

Minimum energy determines the shape of clathrin coats

We first investigate an increasing clathrin coat rigidity. To simplify the description and investigate the mechanism as transparent as possible we neglect the line tension in this section. We treat the coat rigidity as a dynamic variable which can increase with time. The coat energy is then given by

$$\begin{aligned} E = &- \mu A + 4\pi\kappa(1-\cos\theta) + \frac{\sigma}{2}A\,(1-\cos\theta) \\ &+ 4\pi\kappa_c(t)(1-\cos\theta)\left(1-\frac{R}{R_0}\right)^2 . \end{aligned} \tag{8.6}$$

First, we compare the energy of a flat CCS (flat disc) to a pit (sphere). By going to the double limit of a flat disc $\theta \to 0$ and $R \to \infty$ we find with $A = \pi r^2$

$$E^{\diamond} = -\mu\pi r^2 + \frac{2\kappa_c(t)\pi}{R_0^2} r^2 . \tag{8.7}$$

For the sphere with preferred radius $R = R_0$ and $\theta \to \pi$ the energy equals

$$E^{\circ} = -\mu\pi r^2 + 8\pi\kappa + \sigma\pi r^2 . \tag{8.8}$$

Fig. 8.2 (a) – (c) show the energy of flat and spherical state as a function of coat radius for three different values of membrane tension ($10^{-5} - 10^{-3}$ N/m). For the flat patch we

consider additionally the limit of vanishing (large) coat rigidity $\kappa_c = 0$ ($\kappa_c = 300\,k_BT$). Comparing the flat disc for vanishing coat rigidity (solid blue) with the sphere (solid red) we find that the patch is always energetically favourable. However, by increasing the clathrin density, the coat rigidity is supposed to increase (dashed blue) which would lead to a flat-to-curved transition at some point.

Next, we calculate the transition radius $r_{\diamond\to\circ}$ at which the full sphere is energetically favourable compared to the flat disc

$$\Delta E = E^{\diamond} - E^{\circ} = \left(\frac{2\kappa_c}{R_0^2} - \sigma\right) r^2 - 8\kappa = 0\,, \tag{8.9}$$

which is solve by

$$r_{\diamond\to\circ} = \sqrt{\frac{8\kappa}{\frac{2\kappa_c}{R_0^2} - \sigma}}\,. \tag{8.10}$$

Hence, the sphere wins over the flat disc if the coat rigidity is large i.e. in our model if the coat is dense.

Energy valley separates flat and spherical clathrin coat

We now ask the question whether the spherical state is separated from the flat state by an energy extremum, given that the spherical state is energetically favourable. Therefore, we investigate the energy expression with regard to extrema

$$\frac{\partial E}{\partial \theta} = \sin\theta \left\{\frac{\sigma}{2} A + 4\pi \left(\kappa_c(t)\left(1 - \frac{R}{R_0}\right) + \kappa\right)\right\} \stackrel{!}{=} 0\,. \tag{8.11}$$

Importantly, one can understand the mechanism that will later drive the flat-to-curved transition already at this point. As the coat rigidity drives the system always to a curved state (as the second term is positive) the system assembles never flat. However, we here assume that $\kappa_c(t)$ varies in time, i.e. the flat-to-curved transition might occur when the coat has already grown to some extent. Solving Eq. (8.11) we find

$$\theta^* = 2\arcsin(a)\,, \tag{8.12}$$

with

$$a = \frac{4\kappa_c(t) r}{R_0(\sigma r^2 + 8(\kappa + \kappa_c(t)))}\,. \tag{8.13}$$

The second derivative equals

$$\frac{\partial^2 E}{\partial \theta^2} = \cos\theta \left(\frac{\sigma}{2} A + 4\pi(\kappa + \kappa_c(t))\right) + \frac{\kappa_c(t)}{R_0}\sqrt{2\pi A(1 - \cos\theta)}\,, \tag{8.14}$$

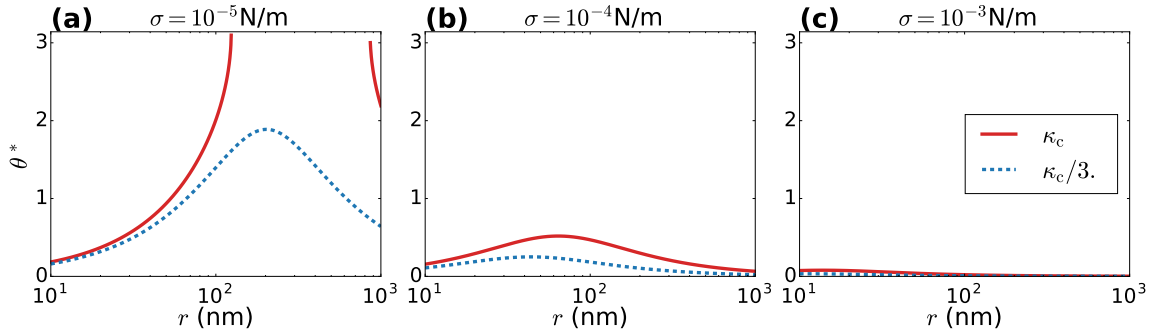

Figure 8.3 | The position of the energy minimum as a function of the coat radius for two different values of coat rigidity and three different values of membrane tension **(a)** $\sigma = 10^{-5}\,\mathrm{N/m}$, **(b)** $\sigma = 10^{-4}\,\mathrm{N/m}$ and **(c)** $\sigma = 10^{-3}\,\mathrm{N/m}$. **(a)** The function diverges at $\theta^* = \pi$ for the larger value of coat rigidity (solid red), indicating that the spherical state is the energy minimum. For the smaller value of coat rigidity (dashed blue) the spherical state never becomes the energy minimum. In **(b)** and **(c)** the energy minimum gets closer to the flat state indicating that the coat will only slightly invaginate.

implying a potential minimum (minimum or maximum) for $\theta^* \leq \pi/2$ ($\theta^* > \pi/2$). We calculate the radius such that the spherical state becomes an **extremum**, $\theta^* = \pi$ i.e. $a(r) = 1$,

$$r^2 - \frac{4\kappa_c(t)}{R_0\sigma} + \frac{8(\kappa + \kappa_c(t))}{\sigma} = 0\,. \tag{8.15}$$

The solution r_{ve} then gives the radius where the boundary extremum vanishes

$$r_{ve} = \frac{2\kappa_c(t)}{R_0\sigma} \pm \sqrt{\left(\frac{2\kappa_c(t)}{R_0\sigma}\right)^2 - \frac{8(\kappa + \kappa_c(t))}{\sigma}}\,. \tag{8.16}$$

In addition, we calculate the radius for which the spherical state becomes a **minimum**

$$\left.\frac{\partial^2 E\,(r)}{\partial\theta^2}\right|_{\theta^*=\pi} \stackrel{!}{=} 0\,, \tag{8.17}$$

which leads to

$$r^2 - \frac{4\kappa_c(t)}{R_0\sigma} + \frac{8(\kappa + \kappa_c(t))}{\sigma} = 0\,. \tag{8.18}$$

Clearly, Eq. (8.15) equals Eq. (8.18). Hence, the radius where the spherical state becomes an extremum is identical to the one where it becomes a minimum. In Fig. 8.3 (a) – (c) the position of the energy minimum θ^* is shown as a function of radius for two different values of coat rigidity and three different values of membrane tension ($10^{-5} - 10^{-3}\,\mathrm{N/m}$). (a) The function diverges at $\theta^* = \pi$ for the larger value of coat rigidity (solid red), indicating that the spherical state is the energy minimum. For the smaller value of coat rigidity (dashed blue) an energy minimum exists in between the flat and the spherical state. In (b) and (c) the energy minimum gets closer to the flat state indicating that the coat will only slightly invaginate.

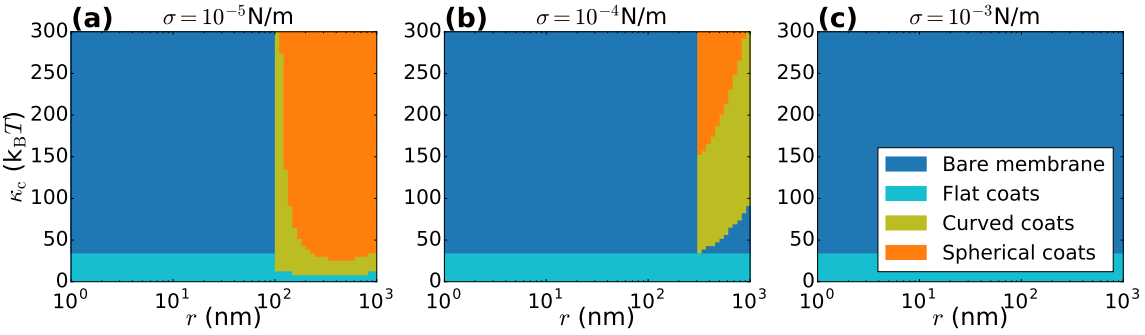

Figure 8.4 | State diagram of clathrin structures as a function of coat radius (size) and coat rigidity for three different values of membrane tension **(a)** $\sigma = 10^{-5}$ N/m, **(b)** $\sigma = 10^{-4}$ N/m and **(c)** $\sigma = 10^{-3}$ N/m. The orange (cyan) region indicates the parameter space where the spherical (flat $\theta < 0.2\pi$) state is energetically favourable. In the yellow region the minimum energy state is curved ($0.2\pi < \theta < \pi$) which is neither flat nor spherical. In the blue region the flat state is energetically unfavourable and the membrane stays bare.

State diagram

The shape of CCSs is strongly determined by size, coat rigidity (clathrin density) and membrane tension. CCSs start as flat coats, which either keep growing flat or transform to spherical pits if a certain patch size is reached. In a certain region in parameter space it is also possible that assembly will not occur at all as the polymerisation energy of the clathrin coat is too small compared to the energetic cost. Fig. 8.4 (a) – (c) shows the state diagram of clathrin structures as a function of coat radius (size) and coat rigidity for three different values of membrane tension ($10^{-5} - 10^{-3}$ N/m). The orange (cyan) region indicates the parameter space where the spherical (flat) state is energetically favourable computed by Eq. (8.16). Importantly, we note that for finite coat rigidity it is always favourable for coats to be slightly curved. Therefore, always an energy valley exists. We define the flat state when the invagination is smaller than $\theta < 0.2\pi$ and calculate this boundary from Eq. (8.13). In the yellow region the minimum energy state is curved ($0.2\pi < \theta < \pi$) which is neither flat nor spherical. In the blue region the flat state is energetic unfavourable such that no assembly occurs and the membrane stays bare, according to Eq. (8.10). Increasing the membrane tension in (b) and (c) constricts the region in which spherical CCSs can form.

In conclusion, a flat-to-curved transition of clathrin coats could only occur if the membrane tension is intermediate. In addition, the coat has to have an intermediate size before the coat rigidity increases. Both coat growth and an increasing coat rigidity are important components to drive the flat-to-curved transition.

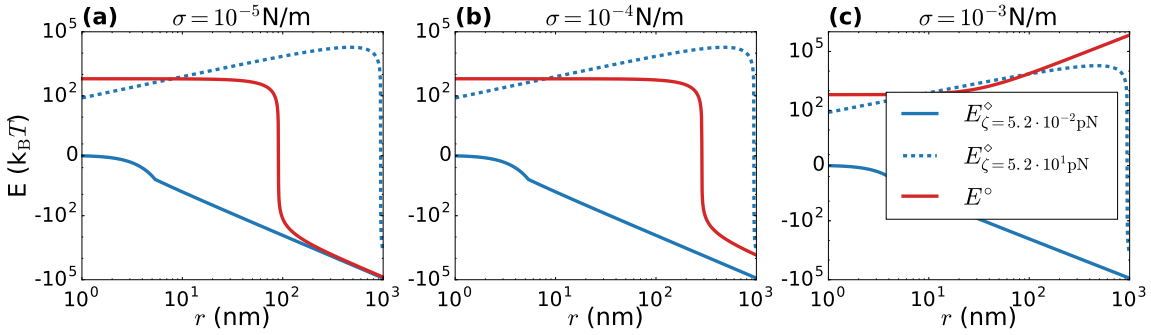

Figure 8.5 | The energy of the flat and spherical state as a function of the coat radius for three different values of membrane tension σ **(a)** – **(c)**. In solid blue the energy of flat structures for low line tension $\zeta = 0.052\,\mathrm{pN}$, in dashed blue for $\zeta = 52\,\mathrm{pN}$ and in solid red for spheres is plotted. The plot indicates that for low line tension flat structures are the energy minimum **(a)** and **(b)**. However, for large line tension and size, spherical coats become energetically favourable. **(c)** For large values of membrane tension spherical structures are not energetically favourable.

8.3.2 Variable line tension

Minimum energy determines the shape of clathrin coats

Next, we investigate an increasing line tension. To simplify the description we neglect the coat rigidity in this section. Therefore, we treat the line tension as a dynamic variable. The coat energy then reads

$$E = -\mu A + 4\pi\kappa(1-\cos\theta) + \frac{\sigma}{2}A\,(1-\cos\theta) + \zeta(t)\mathcal{E}\,. \tag{8.19}$$

As before, we compare the energy of a flat CCS (flat disc) to a coated pit structure (sphere). By going to the double limit of a flat disc $\theta \to 0$ and $R \to \infty$ we find with $A = \pi r^2$

$$E^{\diamond} = -\mu\pi r^2 + \zeta(t)2\pi r\,. \tag{8.20}$$

For the sphere on the other hand, where $\theta \to \pi$ and $R = \text{const.}$ the energy equals

$$E^{\circ} = -\mu\pi r^2 + 8\pi\kappa + \sigma\pi r^2\,. \tag{8.21}$$

Fig. 8.5 (a) – (c) show the energy of flat and spherical state as a function of coat radius for three different values of membrane tension ($10^{-5} - 10^{-3}\,\mathrm{N/m}$). The simple analysis already shows that we expect flat CCSs only for low values of line tension independent of coat size. For intermediate values of line tension flat assembly becomes energetically unfavourable for intermediate patch sizes and we thus expect to get spheres. Only very large flat clathrin coats become again energetically favourable for a large line tension. Next, we calculate the radius r of the flat disc at which the full sphere is energetically favourable compared to the flat disc

$$\Delta E = E^{\diamond} - E^{\circ} = 0, \tag{8.22}$$

and therefore

$$r^2 - \widetilde{2\zeta} + 8\widetilde{\kappa} = 0\,, \tag{8.23}$$

where $\widetilde{\zeta} = \zeta(t)/\sigma$ and $\widetilde{\kappa} = \kappa/\sigma$. Solving this equation for r we get

$$r_{\diamond\to\circ} = \widetilde{\zeta} \pm \sqrt{\widetilde{\zeta}^2 - 8\widetilde{\kappa}}\,. \tag{8.24}$$

In conclusion, the result shows that a flat-to-curved transition can only occur at intermediate clathrin coat size if the line tension is large enough.

Energy barrier separates flat and spherical clathrin coat

As before we investigate the energy with regard to extrema.

$$\frac{\partial E}{\partial \theta} = \frac{\sigma}{2} A \sin\theta + 4\pi\kappa \sin\theta - \zeta(t)\sqrt{\frac{\pi A(1-\cos\theta)}{2}} \stackrel{!}{=} 0\,. \tag{8.25}$$

Solving this equation we find the energy extremum at

$$\theta^* = 2\sec^{-1}\left(\frac{\sqrt{2}}{a}\right)\,, \tag{8.26}$$

with

$$a = \frac{\zeta(t)\sqrt{2\pi A}}{8\kappa\pi + \sigma A}\,. \tag{8.27}$$

The extremum vanishes for $a \geq \sqrt{2}$, i.e. the line tension $\zeta(t)$ and the coat area A determine whether the extremum vanishes or not. Next, we calculate the coat size for which the extremum vanishes

$$r^2 - \widetilde{\zeta} + 8\widetilde{\kappa} = 0\,. \tag{8.28}$$

Solving this equation for r we get

$$r_{\mathrm{ve}} = \frac{\widetilde{\zeta}}{2} \pm \frac{\sqrt{\widetilde{\zeta}^2 - 32\widetilde{\kappa}}}{2}\,. \tag{8.29}$$

Next, we investigate the type of extremum by calculating the second derivative at θ^*

$$\left.\frac{\partial^2 E}{\partial \theta^2}\right|_{\theta=\theta^*} = \frac{1}{2}\left(\frac{\pi A \zeta(t)^2}{A\sigma + 8\pi\kappa} - A\sigma - 8\pi\kappa\right)\,. \tag{8.30}$$

Clearly, this equation becomes negative for small and large values of A, implying a maximum, i.e. an energy barrier. However, for intermediate values of A the equation

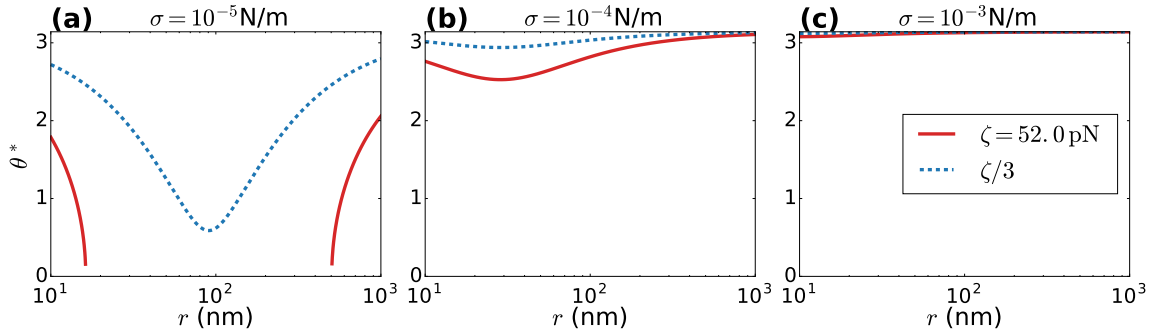

Figure 8.6 | The position of the energy maximum (barrier) as a function of the coat radius for two values of line tension and three values of membrane tension **(a)** $\sigma = 10^{-5}\,\mathrm{N/m}$, **(b)** $\sigma = 10^{-4}\,\mathrm{N/m}$ and **(c)** $\sigma = 10^{-3}\,\mathrm{N/m}$. **(a)** The function vanishes at $\theta^* = 0$ for the larger value of line tension (solid red), indicating that the energy barrier vanishes and hence the spherical state becomes the energy minimum. For the smaller value of line tension (dashed blue) the energy barrier never vanishes. In **(b)** and **(c)** the energy barrier gets closer to the spherical state and does not vanish, indicating that the coat will stay flat.

can be larger than zero, implying a minimum in the energy landscape. We next compute the radius for which the energy maximum could become an energy minimum

$$\left.\frac{\partial^2 E\,(A)}{\partial\theta^2}\right|_{\theta=\theta^*} \stackrel{!}{=} 0\,, \tag{8.31}$$

and hence

$$r_{\mathrm{min}}^2 = \frac{1}{2}\left(\widetilde{\zeta^2} - 8\widetilde{\kappa} \pm \sqrt{\widetilde{\zeta^4} - 32\widetilde{\zeta^2}\widetilde{\kappa}}\right) = \widetilde{\zeta} r_{\mathrm{vb}} - 8\widetilde{\kappa} \equiv r_{\mathrm{ve}}^2\,. \tag{8.32}$$

For $\zeta^2 \geq 32\kappa$ the radius r_{min} where the energy maximum would switch to an energy minimum equals the radius r_{ve} where the energy extremum vanishes completely. Therefore, either the flat state is an energy minimum, or the spherical state is an energy minimum, however, separated by an energy barrier from the flat state, or the spherical state is an energy minimum without energy barrier. In Fig. 8.6 (a) – (c) the position of the energy maximum (barrier) is shown as a function of coat radius for two values of line tension and three values of membrane tension ($10^{-5} - 10^{-3}\,\mathrm{N/m}$). (a) The function vanishes at $\theta^* = 0$ for the larger value of line tension (solid red), indicating that the energy barrier vanishes and hence the spherical state becomes the energy minimum. For the smaller value of line tension (dashed blue) the energy barrier never vanishes. In (b) and (c) the energy barrier gets closer to the spherical state and does not vanish, indicating that the coat stays flat.

In conclusion, this result shows that flat and spherical state are separated by an energy barrier, dependent on line tension. For large line tension the barrier vanishes and the spherical state becomes the energy minimum.

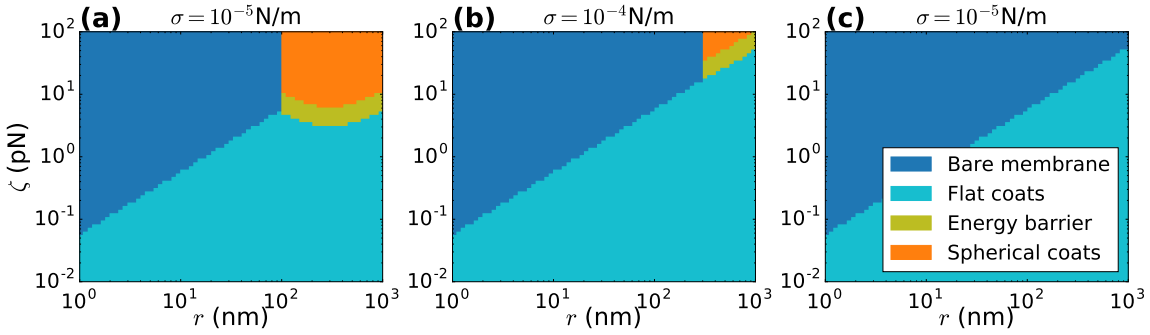

Figure 8.7 | State diagram of clathrin structures as a function of coat radius (size) and line tension for three different values of membrane tension **(a)** $\sigma = 10^{-5}\,\mathrm{N/m}$, **(b)** $\sigma = 10^{-4}\,\mathrm{N/m}$ and **(c)** $\sigma = 10^{-3}\,\mathrm{N/m}$. The orange (cyan) region indicates the parameter space where the spherical (flat) state is energetically favourable. Although in the yellow region the spherical state is energetically favourable, it is separated by an energy barrier from the flat state. Here, the flat state is expected to be occupied. In the blue region the energy gain upon coat assembly is smaller than the cost. Therefore, no assembly at all is expected.

State diagram

In the last paragraph we found that the minimal energy state is determined by both patch size and line tension. Fig. 8.7 (a) – (c) shows the state diagram of CCSs as a function of coat radius (size) and line tension for three values of membrane tension ($10^{-5} - 10^{-3}\,\mathrm{N/m}$). The orange (cyan) region indicates the parameter space where the spherical (flat) state is energetically favourable, determined by Eq. (8.29). Although in the yellow region the sphere wins over the flat CCS from an energetic point of view, the two states are separated by an energy barrier, determined by Eq. (8.24). Here, the flat state is expected to be occupied in the absence of fluctuations that could drive the system to the spherical state. In the blue region the flat state is unfavourable as the energetic gain due to clathrin polymerisation is smaller than the energetic cost determined by Eq. (8.20). Therefore, the membrane is expected to stay bare. Increasing the membrane tension in (b) and (c) decreases the region in which spherical CCSs can form.

In conclusion, the state diagram shows that flat CCSs could transform to curved CCSs if the line tension increases during assembly. Notably, it is not sufficient that the line tension is only high, because in that case flat structures would not assemble and grow at all. Therefore, only the interplay of increasing line tension and growth leads to a flat-to-curved transition.

8.4 Dynamics of clathrin coat assembly

Based on our energy model we now develop a phenomenological model for the dynamics of the assembly of clathrin coats that is driven by an increasing line tension $\dot{\zeta}(t) > 0$.

8.4.1 Phenomenological equations for clathrin coat assembly

To deduce dynamical equations for clathrin coat assembly we use a phenomenological approach that is inspired by Onsager's variational principle [216, 217]. First, we assume that the system's time evolution can be written as

$$\frac{\mathrm{d}\xi_i}{\mathrm{d}t} = -\sum_j L_{ij} \frac{\partial E}{\partial \xi_i}\,, \tag{8.33}$$

where ξ_i are the state variables, L_{ij} are phenomenological coefficients and $-\partial E/\partial \xi_i$ are the generalised forces, which are given by the partial derivative of the energy with respect to the state variable. Onsager's variational principle states that the phenomenological coefficients obey reciprocal relations $L_{ij} = L_{ji}$, assuming time reversal symmetry. Although we break time reversal symmetry in our approach as the clathrin density and therefore the line tension increases as a function of time, we use Eq. (8.33) as a starting point for a phenomenological model.

In our case the energy is given by Eq. (8.19) and the state variables ξ_i are the coat size $A(t)$ and the invagination angle $\theta(t)$. To simplify the description we make two rough approximations. First, we assume that growth and invagination are only weakly coupled and neglect the cross couplings ($L_{A\theta} = L_{\theta A} = 0$). Secondly, for the dynamic equation for A we only consider the dominant contribution of the polymerisation energy to the total energy. A dimensional analysis of the phenomenological coefficient shows that $[L_{AA}] = m^4/(J \cdot s)$. As the clathrin coat bound to the cell membrane grows and the cell membrane invaginates, clathrin triskelia are incorporated and relocated within the coat. Consequently, both the growth and invagination velocity should be proportional to an effective viscosity. Thus, we assume that the phenomenological coefficients have to be proportional to an effective viscosity η. For dimensional reasons, we then find $L_{AA} \sim l/\eta$ where l is a characteristic length of the system which can be a function of the state variables. To make the description of the coat growth consistent, we demand that the change of coat size vanishes for vanishing area ($\dot{A} \to 0$ for $\theta R \to 0$) and closing of the spherical cap ($\dot{A} \to 0$ for $\theta \to \pi$). Therefore, we choose $l = \mathcal{E}$ which is the edge length of the spherical cap. Thus, the growth equation reads

$$\dot{A} = \frac{\mu \mathcal{E}}{\eta}\,. \tag{8.34}$$

This choice implies that flat clathrin coats will grow indefinitely, in contrast to curved coats, which are stopped in growth by geometry as they end up as spherical

coats. We note that this growth equation is identical to Eq. (6.5) of chapter 6. As the assembly of clathrin coats takes $\sim 30-60\,\mathrm{s}$ and coats have a typical size of $\sim 3-6\cdot 10^4\,\mathrm{nm}^2$ [172, 35] corresponding to a flat patch of radius $\sim 50-70\,\mathrm{nm}$, we expect a growth speed of order $\mu/\eta \sim 1-10\,\mathrm{nm\,s^{-1}}$. Therefore, as $\mu = 0.11\,\mathrm{mJ/m^2}$ [31] the effective viscosity should be of order $\eta = 10\,\mathrm{kPa\,s}$. Given this estimated large value, one could think of its physical interpretation and speculate whether it can be understood as the effective viscosity of the clathrin coat. However, for our purposes we treat it as an effective quantity with the physical units of a viscosity.
Next, we consider the invagination equation for the spherical cap

$$\dot{\theta} = -L_{\theta\theta}\left(-\zeta(t)\pi R(1-\cos\theta) + \frac{\sigma}{2}A\sin\theta + 4\pi\kappa\sin\theta\right). \tag{8.35}$$

A dimensional analysis of the phenomenological coefficient shows that $[L_{\theta\theta}] = 1/(J{\cdot}s)$. Following the same argument as above the invagination speed has to be proportional to a viscosity. Thus, we find $L_{\theta\theta} \sim 1/(\eta V)$ where the characteristic volume V is chosen to equal the volume of a spherical CCS, $V = 4/3\pi R_0^3$, where $R_0 = 50\,\mathrm{nm}$ is the radius of a clathrin pit [34]. Furthermore, the change of the invagination angle should vanish in the flat and spherical case, to make the description consistent. Thus, it should hold ($\dot{\theta} \to 0$ for $\theta R \to 0$ and $\theta \to \pi$). Those requirements can be met by choosing

$$L_{\theta\theta} = \frac{1+\cos\theta}{4/3\pi R_0^3\eta}. \tag{8.36}$$

Finally, we assume that the clathrin coat gets denser during coat assembly leading to an increasing line tension as coat density and line tension should be proportional to each other. We expect that the density first increases with a constant rate but as the coat gets denser this rate continuously decreases. A simple way to model such behaviour is

$$\dot{\zeta}(t) = k_{\mathrm{on}} - k_{\mathrm{off}}\zeta(t)\,, \quad \zeta(t=0) = 0\,, \tag{8.37}$$

which can be easily solved by an exponential function. We use $\zeta_0 = k_{\mathrm{on}}/k_{\mathrm{off}} = 52\,\mathrm{pN}$, which is large compared to the value in [31]. However, ζ_0 is here considered as an effective line tension in the sense of [154], also representing adaptor and accessory proteins as part of the clathrin coat that could contribute. We expect that it takes several seconds for the line tension to increase $1/k_{\mathrm{off}} = \tau$, as we expect the density to increase on the same timescale as coat rearrangements are observed experimentally [38]. The system of ODEs, representing our phenomenological model then reads

$$\begin{aligned} \dot{A} &= \frac{\mu\mathcal{E}}{\eta}\,, \qquad \dot{\theta} = \frac{3\sin\theta}{\eta 4R_0^3}\left(\zeta(t)R\sin\theta - (1+\cos\theta)\left(\frac{\sigma A}{2\pi} + 4\kappa\right)\right) \\ \zeta(t) &= \zeta_0\left(1-\mathrm{e}^{-k_{\mathrm{off}}t}\right). \end{aligned} \tag{8.38}$$

By numerically integrating the system of ODEs [218], defined in Eq. (8.38), we can describe the dynamics of the assembly and invagination of CCSs at the cell membrane.

8.4.2 Fitting

Using the same procedure as in [172] and chapter 6 we relate the fluorescence intensity of clathrin tracks with their coat area. For the fit we use the parameters of Table 8.2 and the initial values $(A_0, \theta_0) = (310\,\mathrm{nm}^2\ [120],\ 0.01)$. The fit of Eq. (8.38) to an intensity track is shown in Fig. 8.8 (a) and the deduced fit parameters η and k_{off} are summarised in in Table 8.3. We note that we neglect the scission step of the CCV, related to the intensity decrease at the end of a clathrin intensity track. Importantly, both the data and fitted coat area are normalised to the maximum of the fitted coat area. As expected, $1/k_{\mathrm{off}}$ has the time scale of several seconds. η cannot be directly compared to literature values. Hence, we calculate the growth rate of clathrin coats $\mu/\eta = 9.1\,\mathrm{nm/s}$ as a cross check, which is of the same order of magnitude as the value of Banerjee and coworkers [120] (Table 8.3), implying consistency of our approach.

8.4.3 Results

We now investigate the dynamics of CCS formation. Fig. 8.8 (a) shows the converted data and area fit both normalised to the maximum of the fit, invagination angle, line tension and coat radius as a function of time. As the growth of the area is proportional to the edge length, it first accelerates, then decelerates. We find that θ first stays flat until the line tension is large enough. Then it starts to increase which is associated with the beginning of the invagination. This behaviour agrees well with the notion of a flat-to-curved transition. The line tension grows on a timescale of several seconds. This compares well to the highly dynamic turnover of clathrin coats [38]. Finally the coat radius shows the typical behaviour with 3 phases which one would expect for a flat-to-curved transition. First, it increases, secondly it reaches a maximum when the invagination starts and then thirdly it decreases until it reaches some plateau value. Fig. 8.8 (b) shows the coat radius as a function of the invagination angle retrieved from the work of Avinoam et al. [38] and the prediction of their functional dependence by the constant curvature model (CCM), the constant area model (CAM) (see chapter 6), and the dynamic equations, which we name flat-to-curved model (FCM). Although this data set is retrieved from a different cell line (human SK-MEL-2) we expect that our calculated mean dynamics could qualitatively explain the data.

Table 8.3 | Resulting fit parameters.

Parameter	Fit value	Reference
Timescale of density increase	$\tau = 1/k_{\mathrm{off}} = 2.6\,\mathrm{s}$	$\tau = 2.0\,\mathrm{s}$ [38]
Effective viscosity	$\eta = 1.2\,\mathrm{kPa\,s}$	Unreported
Growth rate	$\mu/\eta = 9.1\,\mathrm{nm/s}$	$1.8\,\mathrm{nm/s}$ [120]

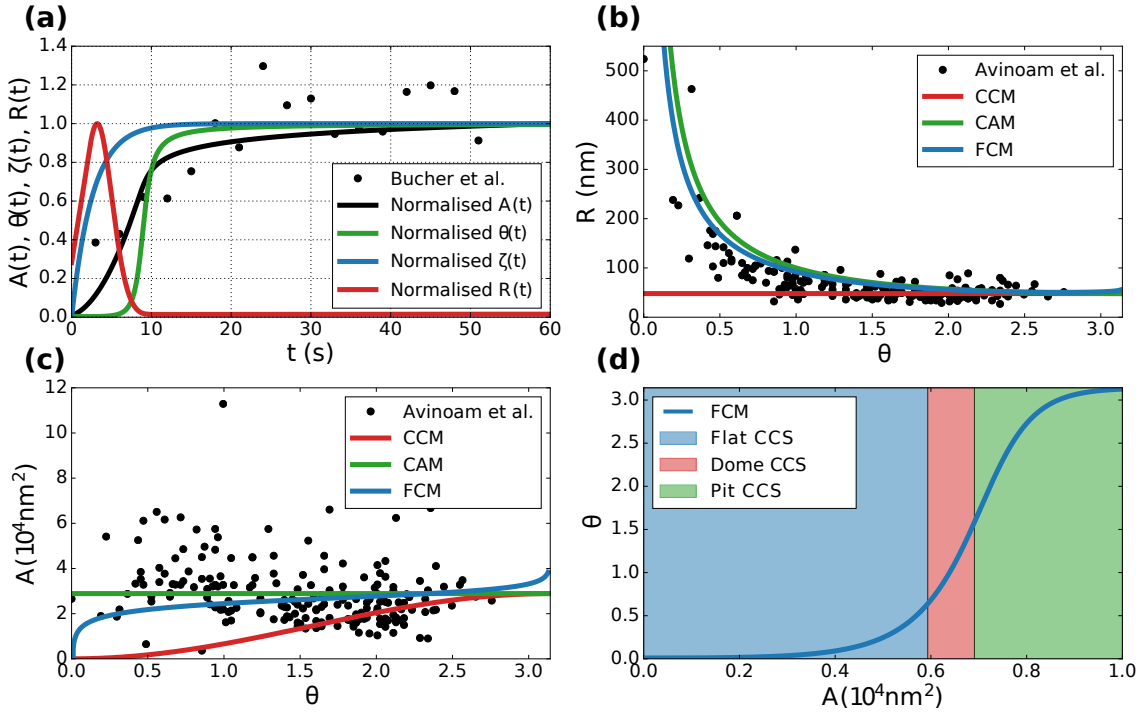

Figure 8.8 | Dynamics of clathrin coat assembly. **(a)** The normalised area (green), invagination angle (black), line tension (blue) and coat radius (red) as a function of time. Fluorescence intensity of a CCS converted to coat size as a function of time (black dots). Fit to the data (solid green) using the dynamical model to get a dynamic description of clathrin coat assembly. **(b)** The coat radius as a function of the invagination angle retrieved from the work of Avinoam et al. [38] (black dots) and computed from the CCM (red), the CAM (green) and the dynamic model (blue). **(c)** The coat size as a function of the invagination angle retrieved from the work of Avinoam et al. [38] (black dots) and computed from the CCM (red), the CAM (green) and the dynamic model (blue). **(d)**The invagination angle as a function of the coat size for the dynamical model (as a solid blue line). We show the different phases as a flat CCS (blue), dome CCS (red) and pit CCS (green). Importantly, the flat-to-curved transition occurs when around 60% of the final coat size is reached.

We find that both CAM and the FCM agree with the data equally well. Only the CCM does not agree with the data. Fig. 8.8 (c) shows the coated area as a function of invagination angle, from the same data set [38] and for the different models. As in (b) the FCM as well as the CAM both agree the data. Fig. 8.8 (d) finally shows the invagination angle as a function of coat size for the FCM. Interestingly, we find that the flat-to-curved transition occurs when around 60% of the final coat size is reached. For this purpose, we have defined that flat CCSs have at most an invagination angle of $\theta < 0.2\pi$ (similar as before). We note that our result of a single fit agrees with our result of chapter 6 and [172], where the transition occurs when around 70% of the final coat content is reached on average. In conclusion, our results show that the flat-to-curved transition can be explained in a model with line tension.

8.5 Conclusion

Although it becomes increasingly clear that clathrin lattices can first assemble flat before they start to curve (compare chapter 6 and [38, 172, 208]), it is still elusive how the flat-to-curved transition might work on a microscopic level. Experimental approaches as light microscopy lack the spatial resolution to elucidate the dynamics of clathrin lattice reorganisation and electron microscopy techniques, although providing ultrastructural information, lack the information on the time domain of clathrin coat rearrangements [70]. Thus in this chapter we applied physical models to indirectly investigate the dynamics of clathrin coat formation and in particular the flat-to-curved transition. The main idea of this chapter is that the flat-to-curved transition is driven by an increasing clathrin density within the clathrin lattice, which we incorporated by either an increasing coat rigidity or an increasing line tension. Our approach is built on the main result of chapter 7, namely that clathrin lattices assemble by incorporating structural gaps, and the observation that the clathrin density increases during the flat-to-curved transition [187]. Rather than providing a complex theoretical description of the flat-to-curved transition by particle based computer simulations [37, 116, 97], our approach takes the first step to explain the mechanisms behind the flat-to-curved transition from the perspective of an increasing clathrin density on a coarse-grained scale.

From a physical point of view the work of this chapter is inspired by the work of Saleem and coworkers [31] who investigated the shape of clathrin coats as a function of coat polymerisation energy and membrane elasticity. However, whereas in their work the shape of clathrin coats is restricted to be curved, we cover the full range of shapes of clathrin coats. Hence, our approach allows to study the flat-to-curved transition during the formation of CCSs. The idea that a flat-to-curved transition can occur as a result of an increasing line tension or preferred curvature of the clathrin coat was already discussed in the work of Lipowsky [154] and Gompper and coworkers [118]. The latter work explains the formation of invaginated clathrin lattices as an example of a two-component fluid in which a crystalline membrane patch, embedded in the plasma membrane, buds. There are two simple models to explain why the plasma membrane can invaginate. In the first model the invagination is driven by a line tension energy (similar to a lipid domain within a fluid membrane) whereas in the second model the invagination is driven by the bending energy of the clathrin patch. In both models the invagination is counteracted by the elasticity of the membrane. Our idea is that the clathrin number density changes during coat formation, rather than the internal structure of the triskelia itself. Therefore, and in contrast to [118], we here considered the case where the bending energy of the coat increases due to an increase of the bending rigidity rather than an increase of spontaneous curvature.

During the course of this chapter we neglected the consideration of the free membrane parts, as the dominant energy contribution comes from the clathrin coated parts [87, 34]. Thus, instead of calculating shapes of clathrin-coated membranes numerically our results were calculated analytically. Importantly, and in agreement with [118], we found that for both an increasing bending energy of the coat and an increasing line tension energy, a flat-to-curved transition occurs that is dependent on the size of flat coats and coat rigidity or line tension, respectively. We note that our results also agree with computer simulations [37] that find a transition of flat clathrin lattices to curved coats. In addition, we studied membrane tension and its effect on the flat-to-curved transition. Our results show that for an increasing membrane tension the bending or line tension energy has to increase to get a flat-to-curved transition. The influence of membrane tension on CME and particular the flat-to-curved transition was already shown in chapter 6 and [172], and previous experimental data [219, 42] and theoretical results [119].

In the second part of this chapter we developed a dynamical model that is based on the energy consideration. Although our phenomenological approach is not rigorous and comes with several rough assumptions it serves as a starting point to deduce dynamical equations that describe the size and morphology of clathrin coats. The equations of the model were fitted with good agreement to fluorescence intensity data of assembling CCSs, validating the idea of our approach. As a result we could predict the size of clathrin coats and their morphology as a function of time, which cannot be inferred from experiments yet. Our model predicts that the flat-to-curved transition occurs when around 60% of the final clathrin content is reached, in agreement with our previous results (see chapter 6 and [172]).

In conclusion, our approach provides a phenomenological description of the shapes and the flat-to-curved transition of clathrin coats, based on the bending and tension energy of the plasma membrane as well as the polymerisation and bending or line tension energy of the clathrin coat. Our results suggest that the flat-to-curved transition is driven by an increasing density of clathrin triskelia at the cell membrane.

9 Conclusion and outlook

Cells constantly relay nutrients and signals across their plasma membranes to bring extracellular material into the cell and to communicate with their surroundings. Thus, cellular uptake is vital. During the course of evolution several uptake mechanisms have evolved. In this thesis, by developing and studying physical models we analysed two of these mechanisms in detail namely receptor-mediated and clathrin-mediated endocytosis (CME). By that we addressed various issues concerning the mechanics and dynamics of cellular uptake which cannot be resolved yet by experimental approaches. Beyond that, by combining our models with existing experimental data we could first validate our models and secondly develop new hypothesises. Together, the presented models help to fill in gaps and to broaden our understanding of a process that is essential for life.

From the viewpoint of physics, cellular uptake is an interesting and rich problem as it relates to membrane biophysics, stochastic dynamics and self-assembly. Hence, this thesis discusses not only one system or process in detail but several, which, however, have to interplay in establishing cellular uptake. In the following we briefly summarise and discuss our results on cellular uptake by ligand-receptor binding of chapter 3-5 and subsequently our results on clathrin-mediated endocytosis of chapter 6-8.

In **chapter 3** we addressed a relatively unexplored aspect of virus and nanoparticle uptake, namely the interplay between stochastic dynamics and particle shape. We first developed a deterministic model for receptor-mediated endocytosis in which uptake is driven by particle adhesion to the plasma membrane and counteracted by the bending and tension energy of the membrane. Using the deterministic model we analysed the uptake dynamics for spherical, normal and parallel oriented cylindrical and spherocylindrical particles. Considering the size of particles we qualitatively found similar behaviour for all particle shapes. As previously shown there is a critical size beyond which particle uptake cannot happen. The reason is that the bending energy is independent of particle size, whereas adhesion energy increases with size. In addition, an optimal particle size exists with minimal uptake time. Quantitatively, spherical particles are taken up slower compared to cylindrical particles at equal volume and radius. Furthermore, we studied the uptake of spherical particles in general and found that uptake is restricted to a certain subregion of the parameter space. In the second part we addressed stochastic effects by deducing a stochastic model that is based on

our deterministic description. Stochasticity is expected to be relevant due to the small system size and the discrete nature of ligand-receptor binding. In our model we solved the underlying stochastic equations either by stochastic simulations or analytically, using several approximations. Surprisingly, and in contrast to the deterministic case, we found that now spherical particles can be taken up faster compared to cylindrical particles. The reason is that spherical particles are affected by multiplicative noise in our model whereas cylindrical particles are subject to additive noise. In our model the timescale for particle uptake is given by the microviscosity of the cell membrane. By incorporating aspects that we have neglected so far (receptor diffusion within the cell membrane, the actin cortex underlying the membrane and the membrane neck formation) one would get additional timescales for the uptake process. To conclude, virus particles come with a huge variety in shape and stochasticity during uptake should be relevant. Thus, we think that although being reductionist, our physical model of uptake contributes to advance our understanding of the important interplay between stochasticity and particle geometry.
In the future it would be interesting to extend the study on the uptake dynamics to differently shaped particles that are biologically relevant. For example, one could investigate bullet-like or conical shapes that should be also affected by multiplicative noise in a stochastic model. In addition, it would be interesting to test our results by coarse-grained molecular dynamics simulations.

In **chapter 4** we extended our study of chapter 3 on the dynamics of particle uptake to incorporate the effect of the free membrane parts. For this purpose we determined the shape of the free membrane that exhibit minimal energy and calculated the corresponding bending and tension energies numerically. However, as we aimed to develop a treatable dynamical model, we decided to represent the energy of the free membrane by either a line tension energy or an extended line tension. Using this phenomenological approach we analysed the deterministic uptake dynamics of spheres and cylinders that are either oriented normal or parallel to the membrane. We calculated the corresponding phase diagrams for uptake and found that short cylinders get taken up faster in normal orientation whereas long cylinders as taken up faster in parallel orientation. For large values of membrane tension only normal cylinders get taken up completely. By calculating dynamic phase portraits for the sphere we could show that either full, partial or no uptake can occur. To conclude, our results show that a line tension counteracts uptake for small uptake angles as it introduces another barrier but also supports uptake once the particle is taken up more than half. Subsequently, we studied stochastic particle uptake dynamics (now incorporating line tension) by computer simulations for the two cylinders and the sphere. We found very similar behaviour compared to chapter 3. Spherical particles can get taken up faster

compared to parallel cylindrical particles due to fluctuations. Finally, we considered the effect of ligand binding on the particle positioning by stochastic simulations. We found similar behaviour for cylindrical and spherical particles. For weak fluctuations and favourable uptake the last bound ligand is located opposed to the first bound ligand whereas for intermediate fluctuations and unfavourable uptake every ligand has equal probability to be the last ligand. Therefore, we concluded that virus particles could wander at the cell membrane, when uptake is unfavourable.
In the future it would be interesting to extend the study of particle wandering with a more detailed approach. It would be intriguing to calculate the phase diagram for a system that can either wander for intermediate noise and a stiff membrane, exhibit partial uptake for weak noise and a stiff membrane, or exhibit full uptake for a soft membrane and either noises. In addition, it would be interesting to compare such a model to mored detailed approaches as particle based simulations.

In **chapter 5** we studied cellular uptake of substrate-attached virus and nanoparticles. We first discussed experiments that quantified uptake forces at the ventral side of cells by means of molecular tension sensors. Next, by using the deterministic model of chapter 3 we could predict the adhesion energy of nanoparticles from measured forces. Several experimental features have been neglected in our model, either to simplify the description (considering cell spreading and migration) or because the parameters cannot be experimentally investigated (the role of CME during uptake). Thus, as expected, the timescale on which uptake is observed in the experiments does not agree with the timescale of uptake in our model. Nevertheless, our model could qualitatively explain the relationship between adhesion strength and uptake time. In addition, we extended our model to study the stochastic dynamics of cellular uptake similar to chapter 3 and 4, but now considering the effect of substrate-attachment. We modelled the tension sensor either by a linear spring or a polymer that behaves like a worm-like chain. We could demonstrate that substrate-attachment significantly increases the uptake time. In the case of substrate-attachment by a linear spring we found that attachment effectively acts as membrane tension stiffening. To conclude, in this chapter we could successfully apply our model to experimental data to get a better understanding of the complex experimental situation.
In the future it would be interesting to compare experimental trajectories of virus particles and stochastic simulations in a quantitative and systematic manner. From the theoretical perspective one could also quantify the time until the force sensor breaks and the time until the uptake is completed, dependent on the different parameters. In addition, it would be interesting to investigate the uptake of particles that are bound to several tension probes (or even clusters) and study whether rupture cascades or oscillations could occur.

In **chapter 6** we investigated the flat-to-curved transition during clathrin-mediated endocytosis (CME). First, we reasoned that the two established assembly models for clathrin, namely the constant curvature model and the constant area model predict different relationships between surface and projected area. We then argued why the EM data is in conflict with the constant curvature model. We developed a simple mathematical growth law to model the self-assembly of clathrin-coated structures in the constant area model. Next, we fitted the growth law to FM data and calculated the corresponding size and morphology histogram. The comparison with the EM data showed that the constant area model is also in conflict with the data. As both, the constant curvature and the constant area model did not agree with the data we tested a hybrid model in which clathrin coats start to bend before they reach their final clathrin content. Repeating the same steps as before we could show that this model better agrees with the data. We then analysed CLEM data both of clathrin and AP2 adaptor molecules and revealed that the AP2/clathrin ratio changes during the invagination of clathrin lattices. Therefore, we tested whether the moment when AP2 content saturates sets the timing for the flat-to-curved transition. Repeating the same steps as before we could show that this model agrees best with the data. In addition, we showed that the ratio of flat, dome and pit clathrin structures changes during an osmotic shock, which increases membrane tension. Finally, we could predict the ratio of flat, dome and pit structures during the osmotic shock by fitting AP2 and clathrin FM intensity curves. In summary, our results show that clathrin-coated structures perform a flat-to-curved transition when around 70% of the final clathrin content is reached on average and that this transition is dependent on membrane tension.
In the future it would be instructive to measure and control membrane tension quantitatively. From a theoretical point of view it would be interesting to repeat the analysis using a model that incorporates a mechanistic description of the flat-to-curved transition. In this way one could gain insight on how the flat-to-curved transition works on a microscopic scale.

In **chapter 7** we investigated the growth of flat clathrin lattices. First, we reasoned that the flat-to-curved transition of clathrin lattices has to be associated with the incorporation of pentagons within the flat hexagonal lattice. Secondly, we argued that the incorporation of pentagons would probably occur along the bulk of the lattice. We then hypothesised that such incorporation would be heavily simplified by a lattice having structural gaps, i.e. which is not fully occupied by clathrin triskelia. Importantly, such structural gaps would go unnoticed in commonly used imaging techniques as EM or FM. We then measured area, perimeter and circularity of flat clathrin lattices in EM. Next, we simulated the growth of flat clathrin lattices by distinct growth models

which follow different growth rules and differ in the resulting clathrin density. By comparing shape and content of simulated clathrin lattices to clathrin lattices that have been observed in EM and CLEM, we found that the ankle-model with many structural gaps agrees best with the data. In conclusion, we studied the growth of flat clathrin lattices by a simple, indirect approach as experimental techniques do not allow to resolve the clathrin lattice growth in the necessary detail and coarse-grained MD or BD simulations would introduce many parameters. Our results suggested that clathrin lattices grow heterogeneously with many structural gaps which would facilitated the rearrangement of the clathrin lattice during the flat-to-curved transition and explain the large degree of clathrin exchange.
In the future it would be interesting to test our hypothesis experimentally. Therefore, we suggest to design labels that especially bind to structural gaps or image clathrin lattices by single molecule resolution either in super-resolution FM or AFM. From the theoretical perspective it would be instructive to study additional models of flat clathrin lattice growth. In addition, one could also extend the model in order to incorporate more physical binding rules, e.g. controlled by Boltzmann factors. Furthermore, the model could be extended to quantitatively describe FRAP data.

In **chapter 8** we investigated mechanisms that could drive the flat-to-curved transition during CME using an indirect approach, as this particular question cannot be experimentally resolved yet. The basic idea is that the flat-to-curved transition of clathrin coats is driven by an increasing clathrin density within the coat. For this purpose, we described the energy of clathrin lattices at the cell membrane by a Helfrich Hamiltonian. Importantly, we added terms that govern the effect of an increasing clathrin density: either by an increasing coat rigidity or by an increasing line tension. Interestingly, we found that a flat-to-curved transition occurs in both models dependent on lattice size and coat density. Based on the static description we deduced dynamic equations that describe both the area and invagination dynamics of clathrin-coated structures. By fitting these equations to a single FM trajectory we showed that this model is in agreement with various data sets and predicts a flat-to-curved transition when around 60% of the final clathrin content is reached, which is in agreement with the results of chapter 6. While our approach represents a transparent way to explain the flat-to-curved transition, several aspects were neglected in this model. First, we neglected the free parts of the membrane in our consideration, secondly, we neither treated the microscopic dynamics of clathrin exchange at the cell membrane nor incorporated adaptor and accessory proteins in our description and last but not least we did not model how the exact rearrangement in the clathrin coat works. In conclusion, our approach presents a first step to a more detailed model to explain the plasticity of clathrin lattices at the cell membrane.

In the future it would be instructive to complement our approach with particle based simulations to carve out the exact details of how the coat rearrangements work on a microscopic level. An interesting question in this context could be why the substructure of the clathrin triskelion is so complex. We speculate that this aims at the adaptability of the clathrin molecule and could hint to more functional diversity of clathrin coats [30]. From the theoretical side it might be desirable to develop a more rigorous framework in order to deduce dynamic equations for coat assembly. We are convinced that especially theoretical input might deepen our current understanding of the clathrin system at this point.

To conclude, this thesis contributes to our understanding of cellular uptake mechanisms by studying two important cellular uptake strategies applying physical methods. Concerning the dynamics of receptor-mediated particle uptake, our results contribute to a better understanding of the interplay between particle shape and uptake dynamics. Concerning clathrin-mediated endocytosis our results contribute to our understanding of the clathrin system as a system that self-assembles with a large degree of variability and plasticity. Both uptake mechanism are paradigms of complex systems, as they relate to problems concerning assembling supramolecular complexes at the cell membrane, incorporate stochasticity and many molecular participants. For this reason, theoretical approaches typically suffer from not knowing all important molecular components and parameters and thus might a priori be insufficient. Despite these shortcomings, we are convinced that our work sheds light on important aspects and predicts missing links, which cannot be filled by experiments yet. Our physical (i.e. reductionist) models are especially well suited to carve out effects that could potentially be obscured by other effects in more detailed theoretical approaches. Beyond the explicit challenges of receptor-mediated and clathrin-mediated uptake, we hope that our work might broaden our understanding of cellular uptake and inspire and stimulate others.

A Appendix

A.1 List of abbreviations

AFM Atomic force microscopy

AKM Ankle-and-knee model

AM Ankle model

ATP Adenosine triphosphate

BA Bulk-acquisition model

BD Brownian dynamics

BFPE Backward Fokker-Planck equation

CCP Clathrin-coated pit

CCS Clathrin-coated structure

CCV Clathrin-coated vesicle

CLC Clathrin light chain

CLEM Correlative light and electron microscopy

CME Clathrin-mediated endocytosis

CSK Cytoskeleton

DLA Diffusion-limited aggregation

DPD Dissipative particle dynamics

EA Edge-acquisition model

ECM Extracellular matrix

EM Electron microscopy

FRAP Fluorescence recovery after photobleaching

FPE Fokker-Planck equation

HPV Human papillomavirus

KM Knee model

KMC Kinetic Monte Carlo

KPZ Kardar-Parisi-Zhang (equation)

MC Monte Carlo

MD Molecular dynamics

ME Master equation

MFPT Mean first passage time

MPCD Multi-particle collision dynamics

NP Nanoparticle

ODE Ordinary differential equation

PDE Partial differential equation

PDF Probability distribution function

PM Plasma membrane

PMT Plasma membrane tension

TIRF Total internal reflection fluorescence

TMV Tobacco mosaic virus

VSV Vesicular stomatitis Indiana virus

WLC Worm-like chain

A.2 Gillespie algorithm

In order to solve the Master equation numerically (ME, cf. Eq. (2.7)) we regularly use the Gillespie algorithm [121, 122] that simulates single trajectories whose distribution function solves the ME. While executing the algorithm we perform the following steps:

1. Two uniformly distributed random numbers ξ_1 and ξ_2 are generated in $(0, 1)$.
2. All transition rates $w_{n'n}$ from the state n to the state n' and the sum of all rates is calculated by $w_0 = \sum_{n'} w_{n'n}$.
3. The transition to the state i is performed if
$$\frac{\sum_{n'}^{i-1} w_{n'n}}{w_0} \leq \xi_1 < \frac{\sum_{n'}^{i} w_{n'n}}{w_0} \,. \tag{A.1}$$
4. The time when the transition takes place is given by
$$\tau = \frac{1}{w_0} \ln\left(\frac{1}{\xi_2}\right) \,. \tag{A.2}$$

A.3 Probability distribution of all states

For a one-step Master equation with vanishing backward rates the probability distribution for all states P_N is known for non-repeating forward rates [141]. Here, we give details on how to calculate P_N for a one-step ME with vanishing backward rates and forward rates that repeat twice, corresponding to the uptake of a spherical particle. We consider the limit where two rates become identical $g_b \to g_a$

$$\lim_{g_b \to g_a} \left\{ \mathrm{e}^{-g_a \tau} \left(\prod_{\substack{k=1 \\ k \neq j}}^{N} \frac{1}{g_k - g_a} \right) + \mathrm{e}^{-g_b \tau} \left(\prod_{\substack{k=1 \\ k \neq j}}^{N} \frac{1}{g_k - g_b} \right) \right\} \tag{A.3}$$

$$= \lim_{g_b \to g_a} \left\{ \mathrm{e}^{-g_a \tau} \left(\prod_{\substack{k=1 \\ k \neq j \\ g_a \neq g_b}}^{N} \frac{1}{g_k - g_a} \right) \frac{1}{g_b - g_a} + \mathrm{e}^{-g_b \tau} \left(\prod_{\substack{k=1 \\ k \neq j \\ g_a \neq g_b}}^{N} \frac{1}{g_k - g_b} \right) \frac{1}{g_a - g_b} \right\} \tag{A.4}$$

$$= \lim_{g_b \to g_a} \mathrm{e}^{-g_a \tau} \left(\prod_{\substack{k=1 \\ k \neq j \\ g_a \neq g_b}}^{N} \frac{1}{g_k - g_a} \right) \frac{1}{g_b - g_a} \left\{ 1 - \mathrm{e}^{-(g_b - g_a)\tau} \left(\prod_{\substack{k=1 \\ k \neq j \\ g_a \neq g_b}}^{N} \frac{g_k - g_a}{g_k - g_b} \right) \right\} . \tag{A.5}$$

with $\mathcal{A} = \mathrm{e}^{-g_a\tau}\left(\prod_{\substack{k=1\\k\neq j\\g_a\neq g_b}}^{N} \frac{1}{g_k-g_a}\right)$ and $\Delta = g_b - g_a$ we find

$$= \lim_{g_b\to g_a} \mathcal{A}\frac{1}{\Delta}\left\{1 - \left(\left(1-\Delta\tau+\mathcal{O}(\Delta^2)\right)\left(\prod_{\substack{k=1\\k\neq j\\g_a\neq g_b}}^{N}\frac{g_k-g_a}{g_k-g_b}\right)\right)\right\} \tag{A.6}$$

$$= \lim_{g_b\to g_a} \mathcal{A}\frac{1}{\Delta}\left\{1 - \left(\left(1-\Delta\tau+\mathcal{O}(\Delta^2)\right)\left(\prod_{\substack{k=1\\k\neq j\\g_a\neq g_b}}^{N}\left(1+\frac{\Delta}{g_k-g_b}\right)\right)\right)\right\} \tag{A.7}$$

$$= \lim_{g_b\to g_a} \mathcal{A}\frac{1}{\Delta}\left\{1 - \left(1-\Delta\tau-\Delta\left(\sum_{\substack{k=1\\k\neq j\\g_a\neq g_b}}^{N}\frac{1}{g_k-g_b}\right)+\mathcal{O}(\Delta^2)\right)\right\} \tag{A.8}$$

$$= \mathcal{A}\left\{\tau - \left(\sum_{\substack{k=1\\k\neq j\\g_a\neq g_b}}^{N}\frac{1}{g_k-g_b}\right)\right\}. \tag{A.9}$$

A.4 Mean uptake time with linear drift

Here, we calculate the mean uptake time T_{up} for a system with linear drift and additive noise

$$\dot{x} = \lambda x + \sqrt{2D}\eta(t). \tag{A.10}$$

The corresponding deterministic equation is solved by $x(t) = x_0\mathrm{e}^{\lambda t}$ such that the time until $x_{\max}$ is reached is given by $t_{\max} = \frac{1}{\lambda}\ln(\frac{x_{\max}}{x_0})$. Following the book of Gardiner [90], the mean uptake time of the stochastic system is given by

$$T_{\mathrm{up}}(x_0) = 2\int_{x_0}^{x_{\max}}\frac{\mathrm{d}y}{\Psi(y)}\int_{x_0}^{y}\mathrm{d}z\frac{\Psi(z)}{2D},$$
$$\text{where}\quad \Psi(y) = \exp\left\{\int_{x_0}^{y}\mathrm{d}x\frac{2\lambda x}{2D}\right\}, \tag{A.11}$$

assuming that x_0 is both reflecting boundary and initial position and $x_{\max}$ is an absorbing boundary. The calculated mean uptake time reads

$$T_{\mathrm{up}}(x_0) = \frac{\pi\,\mathrm{Erfi}(\sqrt{\alpha}x_0)(\mathrm{Erf}(\sqrt{\alpha}x_0)-\mathrm{Erf}(\sqrt{\alpha}x_{\max}))}{4\lambda}$$
$$+\frac{1}{2D}\left(x_{\max 2}^2F_2(\cdot,-\alpha x_{\max}^2)-x_{02}^2F_2(\cdot,-\alpha x_0^2)\right), \tag{A.12}$$

where ${}_2F_2(\cdot, x)$ is the generalised hypergeometric function, $\{\cdot, x\} = \{1, 1; \frac{3}{2}, 2; x\}$ and $\alpha = \frac{\lambda}{D}$. For vanishing noise we get back the deterministic result $T_{\text{up}} \to \frac{1}{\lambda} \ln(\frac{x_{\max}}{x_0}) = t_{\max}$ and for vanishing drift ($\lambda = 0$) we get $T_{\text{up}} \to \frac{1}{2D} (x_0 - x_{\max})^2$.

A.5 Relaxation of the particle position during uptake

Here, we argue why we expect that a particle should symmetrise its position with respect to the cell membrane during uptake as a consequence of membrane tension. First, we consider a parallel cylindrical particle at the cell membrane. We distinguish between a left hand side and a right hand side binding process. Therefore, we model the left and right hand side membrane tension by two elastic springs of spring constant k each. In this case the total tension energy reads

$$E = \frac{k}{2} \left(x_1^2 + x_2^2 \right) , \tag{A.13}$$

where $x = x_1 + x_2$ is the total displacement and x_1 (x_2) is the displacement at the left (right). We assume that due to binding the left spring is extended by x_1, whereas the right spring is not extended, $x_2 = 0$. The relaxation force is given by

$$F_{\text{relax}} = -\frac{\partial E}{\partial x_1} = -k x_1 . \tag{A.14}$$

This force is balanced by a friction force

$$F_{\text{friction}} = \eta L \dot{x_1} , \tag{A.15}$$

affecting the membrane, where L is the length of the membrane displacement, η the microviscosity and $\dot{x}$ the velocity with which the membrane moves. Force balance $F_{\text{relax}} = F_{\text{friction}}$ leads to

$$\dot{x_1} = -\frac{k}{\eta L} x_1 = -\frac{1}{\tau} x_1 , \tag{A.16}$$

solved by a simple exponential decay

$$x_1(t) = x_1^0 \mathrm{e}^{-t/\tau} , \tag{A.17}$$

with $\tau = \eta L / k$ and x_1^0 the displacement upon receptor binding. The spring constant is proportional to the membrane tension $k \sim \sigma$, and therefore the characteristic time scale is given by $\tau = \eta L / \sigma$. For the membrane displacement $L \sim R / N_{\max}$, this timescale if of the same order of magnitude as the typical timescale for binding (unbinding) $1/(N_{\max} \nu_{\text{w}}^{\parallel}) \sim 1/(N_{\max} \nu_{\sigma}^{\parallel}) = \eta R / (N_{\max} \sigma) \sim \tau$. Hence, the particle usually relaxes its position at the cell membrane between several binding (unbinding) steps. In the case, where the diffusion of receptors contributes another timescale to particle uptake [133, 134], it might be even true that relaxation occurs much faster compared to receptor binding.

A.6 Combination of experimental datasets

Relate fluorescence intensity and surface area by means of CLEM

To relate the fluorescence intensity of a clathrin FM track to the corresponding clathrin covered membrane area we use our clathrin CLEM data, relating the projected surface size of CCSs to their fluorescence intensity. We analyse flat CCSs for which the projected area directly corresponds to their surface. By fitting a line through the origin to the clathrin CLEM data we get the slope β providing us with a linear relation between size and intensity. As the local intensity background is removed from the CLEM data we find

$$I(A) = \beta A\,, \tag{A.18}$$

where I is the intensity of the FM data, A is the area of the clathrin structure and β is the proportionality constant. Fig. 6.5 (b) shows the intensity of flat structures as a function of their projected area (blue). We find $\beta = 4085\,\mathrm{nm}^{-2}$.

Relate different FM datasets

To calculate a size histogram from fluorescence intensity tracks we analyse live cell FM data, that have a different intensity level than the fluorescence intensity of the CLEM data. Therefore, we need to relate these two different data sets. As the CLEM intensity I and the live cell FM intensity I' are both proportional to the number of labelled clathrin triskelia, both intensities, which are background corrected, can be related only by some factor α, i.e.

$$I' = \alpha I \rightarrow \alpha = \frac{\langle I' \rangle}{\langle I \rangle}\,, \tag{A.19}$$

which can be calculated by dividing the means (indicated by $\langle \cdot \rangle$) of both data sets.

Relate EM and FM datasets

We next restricted the live cell FM data set to ensure that the calculated size histogram is comparable to the EM histogram. In EM we only detect structures that reach a threshold size. However, in the live cell FM data set we register only detectable intensities, which exceed the local background signal. Therefore, we relate the minimal detectable size in CLEM (A_T) to a threshold intensity (I_T), which we relate to a threshold intensity (I'_T) that we use on the live cell FM tracks. As $I' = \alpha I$ we find

$$\frac{I'_\mathrm{T}}{\langle I' \rangle} = \frac{I_\mathrm{T}}{\langle I \rangle}\,. \tag{A.20}$$

As $\langle I' \rangle$ is a function of I'_T we can find the root of

$$0 = I_\mathrm{T} \frac{\langle I' \rangle}{\langle I \rangle} - I'_\mathrm{T}\,, \tag{A.21}$$

by iteratively increasing I'_{T}. In EM we find that the minimal sized clathrin structure has an area of $A_{\mathrm{T}} = 5644\,\mathrm{nm}^2$, corresponding to a calculated intensity of $I_{\mathrm{T}} = 2.305 \cdot 10^7\,\mathrm{arb.\,unit}$. We find the mean intensity in the clathrin CLEM data of all structures $\langle I \rangle = 1.766 \cdot 10^8\,\mathrm{arb.\,unit}$. To measure the mean intensity in the live cell FM data set, we sample from each FM track that has a lifetime of at least 24 seconds a number of intensities proportional to its lifetime. From these sampled intensities, which we restrict to be larger than the threshold value I'_{T}, we then compute the mean intensity. We obtain $I'_{\mathrm{T}} = 5.450 \cdot 10^3\,\mathrm{arb.\,unit.}$ and $\langle I' \rangle = 4.148 \cdot 10^4\,\mathrm{arb.\,unit}$. By combining Eq. (A.18) and Eq. (A.19) we find

$$A'(I') = \frac{I'}{\alpha\beta}\,, \tag{A.22}$$

according to which we compute the surface of a clathrin structure from its intensity in the live cell FM. Furthermore, we filter all FM tracks showing a mean intensity which is smaller than I'_{T}, as those tracks would not be observable in EM.

A.7 Constant area model

Data fits

To test whether the constant area model correctly describes the shape and size of clathrin coated vesicles we fitted Eq. (6.4) to 4927 FM tracks of 4 different cells (Fig. 6.3 (b)). From the fitted surface area growth curves we then calculated histograms which we could compare to EM histograms. Therefore, we related the intensity of an FM track to its corresponding area. Furthermore, the FM dataset was filtered before the fitting. The exact details of our procedure are described in the following.

Data filtering

Many CCSs at the plasma membrane represent abortive structures that will not commit to form a CCP. To ensure that abortive structures are not analysed in our study, dynamic tracks with a lifetime inferior to 24 s were excluded. Of note, we also repeated our analysis using a minimal lifetime of 12 seconds and found very similar results. We filter our data set for FM tracks with multiple structures (defined as a FM track that shows at least two clear intensity maxima) to allow for direct fitting of single tracks. Precisely, we check for each data point of an intensity track if its intensity exceeds 80% of the mean intensity to find a 'first plateau'. If a data point after a 'first plateau' falls below 40% of the mean intensity we find a 'first low'. If a data point after the 'first low' exceeds the mean again by 20% we found a structure with multiple intensity maxima. Such tracks are filtered out. Furthermore, we filter tracks that start already with a mean intensity level.

Parameter choice and data fitting

The parameters for the fit are restricted by assuming that growth curves should at least reach 90% and at most 120% of the maximal area value. Additionally, we assume that pinch off of clathrin-coated vesicles (corresponding to a decrease in the intensity to 10%) takes between 0 s to 20 s. Additionally, we require the fit to reach 99% of the steady state area before the area decrease happens and at least 10% of that time until the 99% area level are reached. We implement the Python module 'lmfit' [220] for fitting the area tracks where we use the method 'nelder' of the minimizer function. In this way we obtain for each track three parameters with mean values ($r_{\mathrm{ss}} = 65\,\mathrm{nm}$ (as sphere), $k_{\mathrm{off}} = 0.5\,1/\mathrm{s}$ and $t_{\mathrm{decrease}} = 46\,\mathrm{s}$) that characterise the growth curve.

A.8 Curvature acquisition during growth model

Data fits, parameter choice and data fitting

To test whether the 'curvature acquisition during growth model' correctly describes the shape and size of clathrin coated vesicles we fitted Eq. (6.6) to 4927 FM tracks of 4 different cells (Fig. 6.3 (e)) and calculated from the fitted surface area growth curves histograms which we could compare to EM histograms. Therefore, we related the intensity of an FM track to its corresponding area. Furthermore, the FM dataset was filtered before the fitting. The exact details of our procedure are the same as before. The parameters for the fit are restricted by assuming that growth curves should at least reach 90% and maximal 120% of the maximal area value and that pinch off of clathrin-coated vesicles (corresponding to a decrease in the intensity to 10%) takes between 0 s to 20 s. We implement the Python module 'lmfit' [220] for fitting the area tracks where we use the method 'nelder' of the minimiser function. In this way we obtain for each track two parameters with mean values ($R = 69\,\mathrm{nm}$ and $t_{\mathrm{decrease}} = 42\,\mathrm{s}$) that characterise the growth curve.

A.9 Curvature acquisition during growth: updated model

Live cell FM analysis resampling

To determine the ratio of clathrin and AP2 during the process of CME, we performed TIRF microscopy of BSC-1 AP2-eGFP cells transiently expressing CLCa-tdtomato. We analysed the excess of clathrin in comparison with AP2 during the formation of clathrin-coated vesicles. Therefore, we calculated the ratio of the maximum clathrin intensity divided by the intensity of clathrin at the time when AP2 shows an intensity

plateau (95% intensity level) and subtract this ratio from the ratio, which we get for AP2. In detail: we set a threshold for the AP2 intensity underneath fluorescence intensity tracks are excluded (as before). We calculate the plateau time, defined as the time when 95% of the AP2 plateau intensity is reached by fitting the constant area model to the AP2 FM data. Additionally, we normalise all intensity values to the intensity value when 95% of the AP2 intensity (clathrin intensity) is reached. For each track (in total 754 tracks of one single cell) we calculate the difference of the time when AP2 plateaus and clathrin reach the maximum intensity and determine the corresponding histogram (cf. Fig. 6.6 (b)). Furthermore, we calculate the intensity offset given by the normalised maximum clathrin intensity divided by the normalised maximum AP2 intensity (cf. Fig. 6.6 (c)).

A.10 Analysis of large clusters

Here, we analyse the growth of flat clathrin lattices from the perspective of physical aggregation and investigate the growth and structure of large clusters of $N = 10^4$ clathrin triskelia. For simplicity, we use the ankle-and-knee model (AKM) for lattice growth simulations in the following. We compute the mean radius and surface roughness of clathrin lattices, which are quantities that are typically used to describe Eden cluster growth [98]. In the following we shorty summarise the most important definitions. The position of the cluster centre $\vec{r}_{\mathrm{cc}}$ is calculated by averaging the positions of all clathrin triskelia

$$\vec{r}_{\mathrm{cc}} = \frac{1}{N}\sum_{i=1}^{N}\vec{v}_i\,, \tag{A.23}$$

where $\vec{v}_i$ are the node positions of clathrin triskelia at the edge of the cluster. The mean radius of the cluster $\langle r\rangle$ is calculated by averaging the distance of each clathrin triskelion at the edge to the cluster centre $r_i = |\vec{v}_i - \vec{r}_{\mathrm{cc}}|$

$$\langle r\rangle = \frac{1}{N}\sum_{i=1}^{N} r_i\,. \tag{A.24}$$

The roughness is calculated by the deviation of the distance at the edge to the mean radius [98, 221]

$$\sigma = \sqrt{\frac{1}{N}\sum_{i=1}^{N}(r_i - \langle r\rangle)^2}\,. \tag{A.25}$$

For Eden clusters in two dimensions one expects the following scaling behaviour [221]

$$\sigma \sim t^{1/3}\,, \tag{A.26}$$

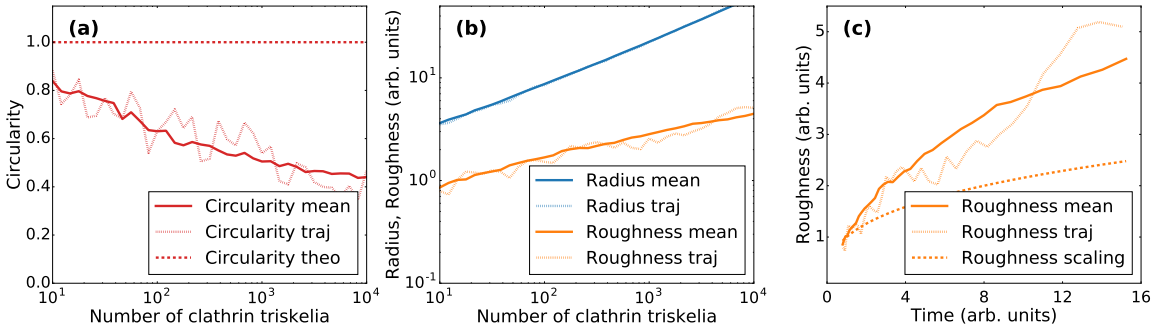

Figure A.1 | Analysis of clusters of $N = 10^4$ clathrin triskelia averaged over 300 simulation runs. **(a)** Mean circularity (solid red), a single trajectory (dotted red) and circularity for a circle (dashed red) as a function of the number of clathrin triskelia. **(b)** Mean radius (roughness) in solid blue (solid orange) and a single trajectory of radius (roughness) in dotted blue (dotted orange) as a function of the number of clathrin triskelia. **(c)** Mean roughness (solid orange) and a single trajectory (dotted orange) are shown as a function of time. Expected Eden scaling is shown in dashed orange.

where the time step is $\Delta t = 1/N_s$ and N_s are the potential growth sites where additional triskelia can bind to [222]. In Fig. A.1 (a) the mean circularity (solid red), a single circularity trajectory (dotted red) and the circularity of a circle (dashed red) are shown as functions of the number of clathrin triskelia. Importantly, we here quantify edge length and area to calculate circularity by the number of edge and cluster nodes, respectively. Therefore the values of circularity can only be qualitatively compared to experiments. However, although the considered clusters are large, the mean circularity only slowly decreases implying that the simulated clusters are still rather compact and only exhibit a limited level of roughness.

In (b) the mean radius (roughness) in solid blue (solid orange) and a single trajectory of radius (roughness) in dotted blue (dotted orange) are shown as a function of the number clathrin triskelia. As both functions appear as straight lines (on the logarithmic scale) we expect a power law scaling. In (c) now the mean roughness (solid orange) and a single trajectory (dotted orange) are shown as a function of time. The expected Eden scaling is shown in dashed orange. As expected, the mean roughness seems to obey the scaling of Eden clusters for large times (as both functions have a similar slope), although the single constituents of the cluster have the structure of clathrin triskelia. In conclusion, our approach of modelling the growth of clathrin lattices by an Eden model is consistent as even very large simulated lattices have a compact shape.

Bibliography

[1] P. Schwille. "How simple could life be?" In: *Angew. Chem. Int. Ed.* 56.37 (2017), pp. 10998–11002 (Cited on page 1).

[2] U. S. Schwarz. "Physik der Zelladhäsion". In: *Phys. J.* 14.7 (2015), pp. 29–34 (Cited on page 1).

[3] T. Auth et al. "Interaction of Particles and Pathogens with Biological Membranes". In: *Physics of Biological Membranes*. Springer, (2018), pp. 471–498 (Cited on pages 1, 5, 16, 47 and 49).

[4] N. von Moos et al. "Uptake and Effects of Microplastics on Cells and Tissue of the Blue Mussel Mytilus edulis L. after an Experimental Exposure". In: *Environ. Sci. Technol.* 46 (2012), pp. 11327–11335 (Cited on pages 1, 5, 27 and 47).

[5] C. M. Rochman et al. "Ingested plastic transfers hazardous chemicals to fish and induces hepatic stress". In: *Sci. Rep.* 3 (2013), p. 3263 (Cited on page 1).

[6] P. Kumberger et al. "Multiscale modeling of virus replication and spread". In: *FEBS Lett.* 590.13 (2016), pp. 1972–1986 (Cited on pages 1, 12, 13, 27 and 47).

[7] P. Jayanth and L. Vinod. "Biodegradable nanoparticles for drug and gene delivery to cells and tissue". In: *Adv. Drug Deliv. Rev.* 55 (2003), pp. 329–347 (Cited on pages 1, 27 and 47).

[8] P. W. K. Rothemund. "Folding DNA to create nanoscale shapes and patterns". In: *Nature* 440.7082 (2006), p. 297 (Cited on pages 1 and 20).

[9] P. Schwille. "Jump-starting life? Fundamental aspects of synthetic biology". In: *J. Cell Biol.* 210.5 (2015), pp. 687–690 (Cited on page 2).

[10] P. Schwille. "Biology and the art of abstraction". In: *Biophys. Rev.* 9.4 (2017), pp. 273–275 (Cited on page 2).

[11] J. L. Van Hemmen. "Theoretische Membranphysik: vom Formenreichtum der Vesikel". URL: `http://www.t35.physik.tu-muenchen.de/addons/publications/vanHemmen-2001b.pdf` (visited on 03/19/2019) (Cited on pages 5 and 15).

[12] D. M. Engelman. "Membranes are more mosaic than fluid". In: *Nature* 438.7068 (2005), p. 578 (Cited on page 6).

[13] U. Seifert. "Configurations of fluid membranes and vesicles". In: *Adv. Phys.* 46.1 (1997), pp. 13–137 (Cited on page 6).

[14] B. Alberts. *Molecular Biology of the Cell*. Sixth edition. Garland science, (2015) (Cited on pages 5, 7, 9, 27, 47 and 103).

[15] S. J. Singer and G. L. Nicolson. “The fluid mosaic model of the structure of cell membranes”. In: *Science* 175.4023 (1972), pp. 720–731 (Cited on page 6).

[16] F. M. Goñi. “The basic structure and dynamics of cell membranes: An update of the Singer–Nicolson model”. In: *Biochim. Biophys. Acta* 1838.6 (2014), pp. 1467–1476 (Cited on page 6).

[17] G. J. Schütz et al. “Single-molecule microscopy on model membranes reveals anomalous diffusion”. In: *Biophys. J.* 73.2 (1997), pp. 1073–1080 (Cited on page 6).

[18] H. Turlier and T. Betz. “Fluctuations in active membranes”. In: *Physics of Biological Membranes*. Springer, (2018), pp. 581–619 (Cited on page 6).

[19] H. M. Nussenzveig. “Cell membrane biophysics with optical tweezers”. In: *Eur. Biophys. J.* 47.5 (2018), pp. 499–514 (Cited on pages 7 and 15).

[20] S. Zhang et al. “Physical principles of nanoparticle cellular endocytosis”. In: *ACS Nano* 9.9 (2015), pp. 8655–8671 (Cited on pages 7, 8, 27 and 47).

[21] F. M. Brodsky. “Diversity of clathrin function: new tricks for an old protein”. In: *Annu. Rev. Cell Dev. Biol.* 28.1 (2012), p. 309 (Cited on page 9).

[22] A. Fotin et al. “Molecular model for a complete clathrin lattice from electron cryomicroscopy”. In: *Nature* 432.7017 (2004), p. 573 (Cited on pages 10, 110 and 122).

[23] J. E. Heuser. “Three-dimensional visualization of coated vesicle formation in fibroblasts”. In: *J. Cell Biol.* 84.3 (1980), pp. 560–583 (Cited on pages 10, 81, 83, 93, 103 and 111).

[24] J. E. Heuser et al. “Deep-etch visualization of 27S clathrin: a tetrahedral tetramer”. In: *J. Cell Biol.* 105.5 (1987), pp. 1999–2009 (Cited on pages 10 and 102).

[25] P. K. Sorger et al. “Clathrin cubes: an extreme variant of the normal cage”. In: *J. Cell Biol.* 103.4 (1986), pp. 1213–1219 (Cited on page 10).

[26] A. J. Spakowitz. “Complex Biological Systems”. In: *Handbook of Science and Technology Convergence* (2016), pp. 239–251 (Cited on pages 10 and 20).

[27] M. Lampe et al. “Clathrin coated pits, plaques and adhesion”. In: *J. Struct. Biol.* 196.1 (2016), pp. 48–56 (Cited on pages 10, 81, 83, 100, 103 and 123).

[28] N. Elkhatib et al. “Tubular clathrin/AP-2 lattices pinch collagen fibers to support 3D cell migration”. In: *Science* 356.6343 (2017), eaal4713 (Cited on page 10).

[29] D. Leyton-Puig et al. “Flat clathrin lattices are dynamic actin-controlled hubs for clathrin-mediated endocytosis and signalling of specific receptors”. In: *Nat. Commun.* 8 (2017), p. 16068 (Cited on pages 10 and 123).

[30] F. Baschieri et al. “Frustrated endocytosis controls contractility-independent mechanotransduction at clathrin-coated structures”. In: *Nat. Commun.* 9.1 (2018), p. 3825 (Cited on pages 10 and 146).

[31] M. Saleem et al. “A balance between membrane elasticity and polymerization energy sets the shape of spherical clathrin coats”. In: *Nat. Commun.* 6 (2015), p. 6249 (Cited on pages 11, 24, 25, 74, 96, 101, 102, 103, 105, 111, 116, 125, 126, 136 and 139).

[32] R. Nossal. “Energetics of clathrin basket assembly.” In: *Traffic* 2.2 (2001), pp. 138–147 (Cited on page 11).

[33] A. Banerjee et al. “Stochastic model of clathrin-coated pit assembly”. In: *Biophys. J.* 102.12 (2012), pp. 2725–2730 (Cited on page 11).

[34] G. Kumar and A. Sain. “Shape transitions during clathrin-induced endocytosis”. In: *Phys. Rev. E* 94.6 (2016), p. 062404 (Cited on pages 11, 17, 28, 29, 51, 62, 74, 79, 81, 101, 122, 125, 126, 136 and 140).

[35] V. Haucke and M. M. Kozlov. “Membrane remodeling in clathrin-mediated endocytosis”. In: *J. Cell Sci.* 131.17 (2018), jcs216812 (Cited on pages 11, 103 and 136).

[36] A. J. Jin and R. Nossal. “Topological mechanisms involved in the formation of clathrin-coated vesicles”. In: *Biophys. J.* 65.4 (1993), pp. 1523–1537 (Cited on pages 11, 103 and 106).

[37] W. K. den Otter and W. J. Briels. “The generation of curved clathrin coats from flat plaques”. In: *Traffic* 12.10 (2011), pp. 1407–1416 (Cited on pages 11, 25, 81, 92, 93, 103, 104, 121, 139 and 140).

[38] O. Avinoam et al. “Endocytic sites mature by continuous bending and remodeling of the clathrin coat.” In: *Science* 348.6241 (2015), pp. 1369–72 (Cited on pages 11, 15, 81, 85, 88, 89, 93, 100, 101, 103, 104, 113, 122, 123, 136, 137, 138 and 139).

[39] X. Wu et al. “Clathrin exchange during clathrin-mediated endocytosis”. In: *J. Cell Biol.* 155.2 (2001), pp. 291–300 (Cited on pages 11, 93 and 104).

[40] J. Grove et al. “Flat clathrin lattices: stable features of the plasma membrane”. In: *Mol. Biol. Cell* 25.22 (2014), pp. 3581–3594 (Cited on pages 11, 81, 83, 102, 104, 107, 108, 113, 120, 122 and 123).

[41] H. Maib et al. “Cargo regulates clathrin-coated pit invagination via clathrin light chain phosphorylation”. In: *J. Cell Biol.* (2018), jcb–201805005 (Cited on pages 11, 104, 107, 108, 113 and 122).

[42] S. Boulant et al. “Actin dynamics counteract membrane tension during clathrin-mediated endocytosis”. In: *Nat. Cell Biol.* 13.9 (2011), p. 1124 (Cited on pages 11, 15, 96, 98, 101 and 140).

[43] M. Mund et al. “Systematic nanoscale analysis of endocytosis links efficient vesicle formation to patterned actin nucleation”. In: *Cell* 174.4 (2018), pp. 884–896 (Cited on page 11).

[44] M. M. Lacy et al. “Molecular mechanisms of force production in clathrin-mediated endocytosis”. In: *FEBS Lett.* (2018) (Cited on page 11).

[45] C. Hulo et al. “ViralZone: a knowledge resource to understand virus diversity”. In: *Nucleic Acids Res.* 39.suppl_1 (2010), pp. D576–D582 (Cited on pages 12, 27 and 45).

[46] M. Breitbart and F. Rohwer. “Here a virus, there a virus, everywhere the same virus?” In: *Trends Microbiol.* 13.6 (2005), pp. 278–284 (Cited on page 12).

[47] M. Krupovic and E. V. Koonin. “Multiple origins of viral capsid proteins from cellular ancestors”. In: *Proc. Natl. Acad. Sci. U.S.A.* 114.12 (2017), E2401–E2410 (Cited on page 12).

[48] A. E. Smith and A. Helenius. “How viruses enter animal cells”. In: *Science* 304.5668 (2004), pp. 237–242 (Cited on page 12).

[49] J. Abrahão et al. “Tailed giant Tupanvirus possesses the most complete translational apparatus of the known virosphere”. In: *Nat. Commun.* 9.1 (2018), p. 749 (Cited on page 12).

[50] F. H. C. Crick and J. D. Watson. “Structure of small viruses.” In: *Nature* 177 (1956), pp. 473–5 (Cited on pages 12 and 27).

[51] P. T. Ho et al. “VIPERdb: A Tool for Virus Research”. In: *Annu. Rev. Virol.* 5.1 (2018). PMID: 30265627, pp. 477–488. DOI: 10.1146/annurev-virology-092917-043405. URL: https://doi.org/10.1146/annurev-virology-092917-043405 (Cited on page 12).

[52] M. G. Mateu. “Structure and physics of viruses”. In: *Thematic issue of Subcell* (2013) (Cited on page 12).

[53] Wikipedia. *Ebola virus*. URL: https://upload.wikimedia.org/wikipedia/commons/thumb/3/3f/Ebola_virus_em.png/400px-Ebola_virus_em.png (visited on 11/19/2018) (Cited on page 13).

[54] Wikipedia. *Human papillomavirus*. URL: https://upload.wikimedia.org/wikipedia/commons/thumb/c/c4/Papilloma_Virus_%28HPV%29_EM.jpg/400px-Papilloma_Virus_%28HPV%29_EM.jpg (visited on 11/19/2018) (Cited on page 13).

[55] Wikipedia. *Reovirus*. URL: https://upload.wikimedia.org/wikipedia/commons/f/f7/Rotavirus.jpg (visited on 11/19/2018) (Cited on page 13).

[56] Wikipedia. *Tobacco mosaic virus*. URL: https://upload.wikimedia.org/wikipedia/commons/thumb/c/c0/TMV_virus_under_magnification.jpg/400px-TMV_virus_under_magnification.jpg (visited on 11/19/2018) (Cited on page 13).

[57] A. Desfosses et al. “Self-organization of the vesicular stomatitis virus nucleocapsid into a bullet shape”. In: *Nat. Commun.* 4 (2013), p. 1429 (Cited on page 13).

[58] B. K. Ganser-Pornillos et al. “Assembly properties of the human immunodeficiency virus type 1 CA protein”. In: *J. Virol.* 78.5 (2004), pp. 2545–2552 (Cited on page 13).

[59] Wikipedia. *Influenza*. URL: https://upload.wikimedia.org/wikipedia/commons/thumb/a/a4/EM_of_influenza_virus.jpg/600px-EM_of_influenza_virus.jpg (visited on 11/19/2018) (Cited on page 13).

[60] B. Hu et al. "Structural remodeling of bacteriophage T4 and host membranes during infection initiation". In: *Proc. Natl. Acad. Sci. U.S.A.* 112.35 (2015), E4919–E4928 (Cited on page 13).

[61] D. S. Dimitrov. "Virus entry: molecular mechanisms and biomedical applications". In: *Nat. Rev. Microbiol.* 2.2 (2004), p. 109 (Cited on pages 12 and 27).

[62] M. Marsh and A. Helenius. "Virus entry: open sesame". In: *Cell* 124.4 (2006), pp. 729–740 (Cited on page 12).

[63] S. B. Sieczkarski and G. R. Whittaker. "Dissecting virus entry via endocytosis". In: *J. Gen. Virol.* 83.7 (2002), pp. 1535–1545 (Cited on page 13).

[64] M. Kielian and F. A. Rey. "Virus membrane-fusion proteins: more than one way to make a hairpin". In: *Nat. Rev. Microbiol.* 4.1 (2006), p. 67 (Cited on page 13).

[65] B. Sodeik. "Mechanisms of viral transport in the cytoplasm". In: *Trends Microbiol.* 8.10 (2000), pp. 465–472 (Cited on page 13).

[66] P. C. Bressloff and J. M. Newby. "Stochastic models of intracellular transport". In: *Rev. Mod. Phys.* 85.1 (2013), p. 135 (Cited on pages 13 and 17).

[67] Z. Schuss et al. "The narrow escape problem for diffusion in cellular microdomains". In: *Proc. Natl. Acad. Sci. U.S.A.* 104.41 (2007), pp. 16098–16103 (Cited on page 13).

[68] W. H. Roos et al. "Physical virology". In: *Nat. Phys.* 6.10 (2010), p. 733 (Cited on pages 13 and 27).

[69] H. Fraenkel-Conrat and R. C. Williams. "Reconstitution of active tobacco mosaic virus from its inactive protein and nucleic acid components". In: *Proc. Natl. Acad. Sci. U.S.A.* 41.10 (1955), pp. 690–698 (Cited on page 13).

[70] A. Picco and M. Kaksonen. "Quantitative imaging of clathrin-mediated endocytosis". In: *Curr. Opin. Cell Biol.* 53 (2018), pp. 105–110 (Cited on pages 14, 103 and 139).

[71] M. Krieg et al. "Atomic force microscopy-based mechanobiology". In: *Nat. Rev. Phys.* (2018), p. 1 (Cited on page 14).

[72] E. Usukura et al. "An unroofing method to observe the cytoskeleton directly at molecular resolution using atomic force microscopy". In: *Sci. Rep.* 6 (2016), p. 27472 (Cited on pages 14 and 121).

[73] A. Yoshida et al. "Morphological changes of plasma membrane and protein assembly during clathrin-mediated endocytosis". In: *PLOS Biol.* 16.5 (2018), e2004786 (Cited on page 14).

[74] A. Wlodawer et al. “Protein crystallography for non-crystallographers, or how to get the best (but not more) from published macromolecular structures”. In: *FEBS J.* 275.1 (2008), pp. 1–21 (Cited on page 14).

[75] Y. Shi. “A glimpse of structural biology through X-ray crystallography”. In: *Cell* 159.5 (2014), pp. 995–1014 (Cited on page 14).

[76] T. Kirchhausen. “Imaging endocytic clathrin structures in living cells”. In: *Trends Cell Biol.* 19.11 (2009), pp. 596–605 (Cited on pages 14, 81 and 86).

[77] P. De Boer et al. “Correlated light and electron microscopy: ultrastructure lights up!” In: *Nat. Methods* 12.6 (2015), p. 503 (Cited on page 14).

[78] E. A. J. Reits and J. J. Neefjes. “From fixed to FRAP: measuring protein mobility and activity in living cells”. In: *Nat. Cell Biol.* 3.6 (2001), E145 (Cited on page 15).

[79] P. P. Ferguson et al. “Mechanoregulation of clathrin-mediated endocytosis”. In: *J. Cell Sci.* 130.21 (2017), pp. 3631–3636 (Cited on page 15).

[80] S. Boulant. “Assaying the Contribution of Membrane Tension to Clathrin-Mediated Endocytosis”. In: *Clathrin-Mediated Endoytosis*. Springer, (2018), pp. 37–50 (Cited on page 15).

[81] L. Shang et al. “Engineered nanoparticles interacting with cells: size matters”. In: *J. Nanobiotechnol.* 12.5 (2014), b26 (Cited on page 15).

[82] J. Zimmerberg and M. M. Kozlov. “How proteins produce cellular membrane curvature”. In: *Nat. Rev. Mol. Cell Biol.* 7.1 (2006), pp. 9–19 (Cited on page 16).

[83] R. Lipowsky and H.-G. Döbereiner. “Vesicles in contact with nanoparticles and colloids”. In: *Europhys. Lett.* 43 (1998), p. 219 (Cited on pages 16, 17, 28, 31, 47, 49, 50, 51 and 66).

[84] M. Deserno. “Elastic deformation of a fluid membrane upon colloid binding”. In: *Phys. Rev. E* 69 (2004), p. 031903 (Cited on pages 16, 17, 28, 45, 47, 49, 50, 52 and 80).

[85] J. Agudo-Canalejo and R. Lipowsky. “Critical particle sizes for the engulfment of nanoparticles by membranes and vesicles with bilayer asymmetry”. In: *ACS Nano* 9.4 (2015), pp. 3704–3720 (Cited on pages 16, 24, 25, 28, 30, 46, 47, 49, 54, 62, 74, 75, 79 and 80).

[86] W. Helfrich. “Elastic properties of lipid bilayers: theory and possible experiments”. In: *Z. Naturforsch. C* 28.11-12 (1973), pp. 693–703 (Cited on pages 16, 28, 49, 73 and 125).

[87] L. Foret. “Shape and energy of a membrane bud induced by protein coats or viral protein assembly”. In: *Eur. Phys. J. E* 37.5 (2014) (Cited on pages 17, 28, 29, 48, 49, 50, 51, 52, 62, 79, 125 and 140).

[88] L. Foret. “Mechanosensitivity of Membrane Budding and Trafficking”. In: *Physics of Biological Membranes*. Springer, (2018), pp. 385–419 (Cited on pages 17 and 49).

[89] M. Thomas and R. Schwartz. "Quantitative computational models of molecular self-assembly in systems biology". In: *Phys. Biol.* 14.3 (2017), p. 035003 (Cited on pages 17 and 20).

[90] C. W. Gardiner. *Handbook of stochastic methods*. Springer, (1985) (Cited on pages 17, 19, 20, 36, 38, 39, 40, 42, 44 and 149).

[91] S. Iyer-Biswas and A. Zilman. "First Passage processes in cellular biology". In: *arXiv preprint:1503.00291* (2015) (Cited on pages 17 and 37).

[92] N. G. Van Kampen. *Stochastic processes in physics and chemistry*. Vol. 1. Elsevier, (1992) (Cited on pages 17, 33, 35, 36 and 60).

[93] J. Honerkamp. *Stochastic dynamical systems: concepts, numerical methods, data analysis*. John Wiley & Sons, (1993) (Cited on pages 17 and 18).

[94] H. Risken. *The Fokker-Planck Equation*. Springer, (1996) (Cited on page 17).

[95] J. D. Perlmutter and M. F. Hagan. "Mechanisms of virus assembly". In: *Annu. Rev. Phys. Chem.* 66 (2015), pp. 217–239 (Cited on page 21).

[96] C. Conde and A. Cáceres. "Microtubule assembly, organization and dynamics in axons and dendrites". In: *Nat. Rev. Neurosci.* 10.5 (2009), p. 319 (Cited on page 21).

[97] M. Giani et al. "Early stages of clathrin aggregation at a membrane in coarse-grained simulations". In: *J. Chem. Phys.* 146.15 (2017), p. 155102 (Cited on pages 21 and 139).

[98] J.-F. Gouyet. *Physics and fractal structures*. Springer, (1996) (Cited on pages 21, 22, 23 and 154).

[99] T. A. Witten Jr and L. M. Sander. "Diffusion-limited aggregation, a kinetic critical phenomenon". In: *Phys. Rev. Lett.* 47.19 (1981), p. 1400 (Cited on pages 21, 23 and 110).

[100] Milo lab in the Weizmann Institute in Israel. *BioNumbers - The database of useful biological numbers*. URL: `http://bionumbers.hms.harvard.edu` (visited on 03/14/2016) (Cited on page 20).

[101] T. Chou and M. R. D'Orsogna. "First passage problems in biology". In: *First-Passage Phenomena and Their Applications*. World Scientific, (2014), pp. 306–345 (Cited on page 20).

[102] R. H. Baughman et al. "Carbon nanotubes–the route toward applications". In: *Science* 297.5582 (2002), pp. 787–792 (Cited on page 20).

[103] A. P. Gast and W. B. Russel. "Simple ordering in complex fluids". In: *Phys. Today* 51 (1998), pp. 24–31 (Cited on page 22).

[104] J. M. Garcıa-Ruiz. "Nucleation of protein crystals". In: *J. Struct. Biol.* 142.1 (2003), pp. 22–31 (Cited on page 22).

[105] M. Eden. "A two-dimensional growth process". In: *Berkeley Symposium on Mathematical Statistics and Probability* 4 (1961), pp. 223–239 (Cited on pages 22 and 110).

[106] M. Kardar et al. “Dynamic scaling of growing interfaces”. In: *Phys. Rev. Lett.* 56.9 (1986), p. 889 (Cited on page 22).

[107] A. Pimpinelli and J. Villain. *Physics of crystal growth*. Vol. 19. Cambridge University Press, (1998) (Cited on page 22).

[108] J. A. D. Wattis. “An introduction to mathematical models of coagulation–fragmentation processes: a discrete deterministic mean-field approach”. In: *Physica D* 222.1-2 (2006), pp. 1–20 (Cited on page 23).

[109] D. Asnaghi et al. “Coagulation kinetics and aggregate morphology in the intermediate regimes between diffusion-limited and reaction-limited cluster aggregation”. In: *Phys. Rev. A* 45.2 (1992), p. 1018 (Cited on page 23).

[110] S. Angioletti-Uberti. “Theory, simulations and the design of functionalized nanoparticles for biomedical applications: A Soft Matter Perspective”. In: *npj Comput. Mater.* 3.1 (2017), p. 48 (Cited on page 24).

[111] U. D. Schiller et al. “Mesoscopic modelling and simulation of soft matter”. In: *Soft matter* 14.1 (2018), pp. 9–26 (Cited on page 24).

[112] K. A. Brakke. “The surface evolver”. In: *Exp. Math.* 1.2 (1992), pp. 141–165 (Cited on page 24).

[113] S. Dasgupta et al. “Wrapping of ellipsoidal nano-particles by fluid membranes”. In: *Soft Matter* 9.22 (2013), pp. 5473–5482 (Cited on pages 24 and 25).

[114] R. Vácha et al. “Receptor-mediated endocytosis of nanoparticles of various shapes”. In: *Nano Lett.* 11.12 (2011), pp. 5391–5395 (Cited on pages 24, 26, 27, 45, 46, 47 and 63).

[115] H.-M. Ding and Y.-Q. Ma. “Role of physicochemical properties of coating ligands in receptor-mediated endocytosis of nanoparticles”. In: *Biomaterials* 33.23 (2012), pp. 5798–5802 (Cited on pages 24 and 26).

[116] R. Matthews and C. N. Likos. “Structures and pathways for clathrin self-assembly in the bulk and on membranes”. In: *Soft Matter* 9.24 (2013), pp. 5794–5806 (Cited on pages 25, 26, 121 and 139).

[117] S. Mehraeen et al. “Impact of defect creation and motion on the thermodynamics and large-scale reorganization of self-assembled clathrin lattices”. In: *Soft Matter* 7.19 (2011), pp. 8789–8799 (Cited on pages 25, 26 and 121).

[118] T. Kohyama et al. “Budding of crystalline domains in fluid membranes.” In: *Phys. Rev. E* 68.6 Pt 1 (2003), p. 061905 (Cited on pages 25, 104, 139 and 140).

[119] J. E. Hassinger et al. “Design principles for robust vesiculation in clathrin-mediated endocytosis”. In: *Proc. Natl. Acad. Sci. U.S.A.* 114.7 (2017), E1118–E1127 (Cited on pages 25, 96, 101 and 140).

[120] A. Banerjee et al. “Kinetics of cellular uptake of viruses and nanoparticles via clathrin-mediated endocytosis”. In: *Phys. Biol.* 13.1 (2016), p. 016005 (Cited on pages 25, 26, 74, 79, 125 and 137).

[121] D. T. Gillespie. “Exact stochastic simulation of coupled chemical reactions”. In: *J. Phys. Chem.* 81.25 (1977), pp. 2340–2361 (Cited on pages 26, 34, 60, 61, 79 and 148).

[122] R. Erban et al. “A practical guide to stochastic simulations of reaction-diffusion processes”. In: *arXiv preprint arXiv:0704.1908* (2007) (Cited on pages 26 and 148).

[123] H. M. Berman et al. “The protein data bank”. In: *Nucleic Acids Res.* 28.1 (2000), pp. 235–242 (Cited on page 26).

[124] F. Frey et al. “Stochastic Dynamics of Nanoparticle and Virus Uptake”. In: *Phys. Rev. Lett.* 122 (8 2019), p. 088102 (Cited on pages 27, 48, 62 and 65).

[125] R. Zandi et al. “Origin of icosahedral symmetry in viruses”. In: *Proc. Natl. Acad. Sci. U.S.A* 101.44 (2004), pp. 15556–15560 (Cited on pages 27 and 45).

[126] S. X. Sun and D. Wirtz. “Mechanics of enveloped virus entry into host cells”. In: *Biophys. J.* 90.1 (2006), pp. L10–L12 (Cited on pages 27, 28 and 47).

[127] E. S. Barton et al. “Junction adhesion molecule is a receptor for reovirus”. In: *Cell* 104.3 (2001), pp. 441–451 (Cited on pages 27 and 47).

[128] T. Erdmann and U. S. Schwarz. “Stability of adhesion clusters under constant force”. In: *Phys. Rev. Lett.* 92.10 (2004), p. 108102 (Cited on pages 27 and 34).

[129] T. Robin et al. “Life time of catch bond clusters”. In: *Phys. A* 507 (2018), pp. 398–405 (Cited on pages 27 and 34).

[130] C. Huang et al. “Role of nanoparticle geometry in endocytosis: laying down to stand up”. In: *Nano Lett.* 13.9 (2013), pp. 4546–4550 (Cited on pages 27, 28, 29 and 47).

[131] S. Dasgupta et al. “Shape and orientation matter for the cellular uptake of nonspherical particles”. In: *Nano Lett.* 14.2 (2014), pp. 687–693 (Cited on pages 28, 29, 45, 47 and 66).

[132] A. H. Bahrami et al. “Wrapping of nanoparticles by membranes”. In: *Adv. Coll. Interf. Sci.* 208 (2014), p. 214 (Cited on pages 28 and 47).

[133] H. Gao et al. “Mechanics of receptor-mediated endocytosis”. In: *Proc. Natl. Acad. Sci. USA* 102.27 (2005), pp. 9469–9474 (Cited on pages 28, 45, 47 and 150).

[134] P. Decuzzi and M. Ferrari. “The role of specific and non-specific interactions in receptor-mediated endocytosis of nanoparticles”. In: *Biomaterials* 28.18 (2007), pp. 2915–2922 (Cited on pages 28, 47 and 150).

[135] X. Yi et al. “Cellular uptake of elastic nanoparticles”. In: *Phys. Rev. Lett.* 107.9 (2011), p. 098101 (Cited on pages 28 and 47).

[136] C. Zeng et al. “Contact mechanics of a small icosahedral virus”. In: *Phys. Rev. Lett.* 119.3 (2017), p. 038102 (Cited on pages 28 and 47).

[137] Z. A. McDargh et al. “Constriction by dynamin: elasticity versus adhesion”. In: *Biophys. J.* 111.11 (2016), pp. 2470–2480 (Cited on pages 28 and 48).

[138] M. Sadeghi et al. “Particle-based membrane model for mesoscopic simulation of cellular dynamics”. In: *J. Chem. Phys.* 148.4 (2018), p. 044901 (Cited on page 29).

[139] D. Alsteens et al. “Nanomechanical mapping of first binding steps of a virus to animal cells”. In: *Nat. Nanotechnol.* 12.2 (2017), p. 177 (Cited on pages 31, 67 and 69).

[140] Y. Pan et al. “The process of wrapping virus revealed by a force tracing technique and simulations”. In: *Adv. Sci.* 4.9 (2017), p. 1600489 (Cited on pages 31, 67, 69 and 80).

[141] T. Erdmann and U. S. Schwarz. “Stochastic dynamics of adhesion clusters under shared constant force and with rebinding”. In: *J. Chem. Phys.* 121.18 (2004), pp. 8997–9017 (Cited on pages 35 and 148).

[142] S. Redner. *A guide to first-passage processes*. Cambridge University Press, (2001) (Cited on pages 37, 38 and 62).

[143] F. A. Barbuto. *Numerical inversion of Laplace transforms using the FFT algorithm.* `https://github.com/ActiveState/code/tree/master/recipes/Python/128243_Numerical_inversiLaplace_transforms_using_FFT`. 2002. (Visited on 03/19/2019) (Cited on page 38).

[144] S. Tollis et al. “The zipper mechanism in phagocytosis: energetic requirements and variability in phagocytic cup shape”. In: *BMC Sys. Biol.* 4 (2010), p. 149 (Cited on page 46).

[145] O. Sandre et al. “Dynamics of transient pores in stretched vesicles”. In: *Proc. Natl. Acad. Sci. USA* 96.19 (1999), pp. 10591–10596 (Cited on page 46).

[146] V. Nier et al. “Tissue fusion over nonadhering surfaces”. In: *Proc. Natl. Acad. Sci. USA* 112.31 (2015), pp. 9546–9551 (Cited on page 46).

[147] F. Frey et al. “Dynamics of particle uptake at cell membranes”. In: *In preparation* (2019) (Cited on page 47).

[148] H. Feldmann et al. “Ebola virus: from discovery to vaccine”. In: *Nat. Rev. Immunol.* 3.8 (2003), p. 677 (Cited on page 47).

[149] S. Matsumoto. “Electron microscope studies of rabies virus in mouse brain”. In: *J. Cell Biol.* 19.3 (1963), pp. 565–591 (Cited on page 47).

[150] X. Yi and H. Gao. “Kinetics of receptor-mediated endocytosis of elastic nanoparticles”. In: *Nanoscale* 9.1 (2017), pp. 454–463 (Cited on page 48).

[151] U. Seifert et al. “Shape transformations of vesicles: Phase diagram for spontaneous-curvature and bilayer-coupling models”. In: *Phys. Rev. A* 44.2 (1991), p. 1182 (Cited on page 50).

[152] F. Jülicher and U. Seifert. “Shape equations for axisymmetric vesicles: a clarification”. In: *Phys. Rev. E* 49.5 (1994), p. 4728 (Cited on page 50).

[153] E. Jones et al. *Using the function: ‘scipy integrate solve bvp’ from SciPy: Open source scientific tools for Python.* `http://www.scipy.org`. (2001–). (Visited on 03/19/2019) (Cited on page 51).

[154] R. Lipowsky. "Budding of membranes induced by intramembrane domains". In: *J. Phys. II* 2.10 (1992), pp. 1825–1840 (Cited on pages 52, 66, 125, 136 and 139).

[155] D. Lepzelter and M. H. Zaman. "Clustered diffusion of integrins". In: *Biophys. J.* 99.12 (2010), pp. L106–L108 (Cited on page 65).

[156] S. Boulant et al. "Dynamics of virus-receptor interactions in virus binding, signaling, and endocytosis". In: *Viruses* 7.6 (2015), pp. 2794–2815 (Cited on page 66).

[157] P. Kukura et al. "High-speed nanoscopic tracking of the position and orientation of a single virus". In: *Nat. Methods* 6.12 (2009), p. 923 (Cited on page 66).

[158] O. M. Szklarczyk et al. "Receptor concentration and diffusivity control multivalent binding of Sv40 to membrane bilayers". In: *PLOS Comput. Biol.* 9.11 (2013), e1003310 (Cited on page 66).

[159] T. Wiegand et al. "Specific virus and virus-like nanoparticle interactions with the ventral cell side determine forces leading to uptake". In: *Submitted* (2018) (Cited on pages 67, 68, 70, 71 and 74).

[160] T Wiegand. "Receptor-mediated Forces for Cell Sensing of Extracellular Ligands and for Virus Particle Uptake". PhD thesis. 2019 (Cited on page 67).

[161] C. Sieben et al. "Influenza virus binds its host cell using multiple dynamic interactions". In: *Proc. Natl. Acad. Sci. U.S.A.* 109.34 (2012), pp. 13626–13631 (Cited on page 67).

[162] F. C. Schenk et al. "Dual-functionalized nanostructured biointerfaces by click chemistry". In: *Langmuir* 30.23 (2014), pp. 6897–6905 (Cited on page 67).

[163] K. Galior et al. "Titin-based nanoparticle tension sensors map high-magnitude integrin forces within focal adhesions". In: *Nano Lett.* 16.1 (2015), pp. 341–348 (Cited on pages 68 and 69).

[164] M. S. Maginnis et al. "β1 integrin mediates internalization of mammalian reovirus". In: *J. Virol.* 80.6 (2006), pp. 2760–2770 (Cited on page 69).

[165] L. S. Jung et al. "Binding and dissociation kinetics of wild-type and mutant streptavidins on mixed biotin-containing alkylthiolate monolayers". In: *Langmuir* 16.24 (2000), pp. 9421–9432 (Cited on page 70).

[166] S. Zhao and W. M. Reichert. "Influence of biotin lipid surface density and accessibility on avidin binding to the tip of an optical fiber sensor". In: *Langmuir* 8.11 (1992), pp. 2785–2791 (Cited on page 70).

[167] G. I. Bell. "Models for the specific adhesion of cells to cells". In: *Science* 200.4342 (1978), pp. 618–627 (Cited on page 70).

[168] V. Tabard-Cossa et al. "Single-molecule bonds characterized by solid-state nanopore force spectroscopy". In: *ACS Nano* 3.10 (2009), pp. 3009–3014 (Cited on page 70).

[169] M.-J. Dejardin et al. “Lamellipod Reconstruction by Three-Dimensional Reflection Interference Contrast Nanoscopy (3D-RICN)”. In: *Nano Lett.* 18.10 (2018), pp. 6544–6550 (Cited on page 73).

[170] J. F. Marko and E. D. Siggia. “Stretching DNA”. In: *Macromolecules* 28.26 (1995), pp. 8759–8770 (Cited on page 76).

[171] D. R. Stabley et al. “Visualizing mechanical tension across membrane receptors with a fluorescent sensor”. In: *Nat. Methods* 9.1 (2012), pp. 64–67 (Cited on page 79).

[172] D. Bucher et al. “Clathrin-adaptor ratio and membrane tension regulate the flat-to-curved transition of the clathrin coat during endocytosis”. In: *Nat. Commun.* 9.1 (2018), p. 1109 (Cited on pages 81, 83, 85, 87, 93, 95, 97, 99, 100, 104, 107, 108, 120, 122, 123, 136, 137, 138, 139 and 140).

[173] H. T. McMahon and E. Boucrot. “Molecular mechanism and physiological functions of clathrin-mediated endocytosis”. In: *Nat. Rev. Mol. Cell Biol.* 12.8 (2011), p. 517 (Cited on page 81).

[174] S. M. Ferguson and P. De Camilli. “Dynamin, a membrane-remodelling GTPase”. In: *Nat. Rev. Mol. Cell Biol.* 13.2 (2012), p. 75 (Cited on page 81).

[175] M. J. Taylor et al. “A high precision survey of the molecular dynamics of mammalian clathrin-mediated endocytosis”. In: *PLOS Biol.* 9.3 (2011), e1000604 (Cited on page 81).

[176] P. Maupin and T. D. Pollard. “Improved preservation and staining of HeLa cell actin filaments, clathrin-coated membranes, and other cytoplasmic structures by tannic acid-glutaraldehyde-saponin fixation”. In: *J. Cell Biol.* 96.1 (1983), pp. 51–62 (Cited on pages 81 and 93).

[177] J. M. Larkin et al. “Potassium-dependent assembly of coated pits: new coated pits form as planar clathrin lattices”. In: *J. Cell Biol.* 103.6 (1986), pp. 2619–2627 (Cited on page 81).

[178] J. E. Heuser and R. G. Anderson. “Hypertonic media inhibit receptor-mediated endocytosis by blocking clathrin-coated pit formation”. In: *J. Cell Biol.* 108.2 (1989), pp. 389–400 (Cited on page 81).

[179] T. Kirchhausen. “Coated pits and coated vesicles – sorting it all out”. In: *Curr. Opin. Struct. Biol.* 3.2 (1993), pp. 182–188 (Cited on pages 81 and 103).

[180] S. Saffarian et al. “Distinct dynamics of endocytic clathrin-coated pits and coated plaques”. In: *PLOS Biol.* 7.9 (2009), e1000191 (Cited on pages 81, 83 and 102).

[181] E. Boucrot et al. “Role of lipids and actin in the formation of clathrin-coated pits”. In: *Exp. Cell Res.* 312.20 (2006), pp. 4036–4048 (Cited on pages 81 and 83).

[182] S. Vassilopoulos et al. “Actin scaffolding by clathrin heavy chain is required for skeletal muscle sarcomere organization”. In: *J. Cell Biol.* 205.3 (2014), pp. 377–393 (Cited on page 81).

[183] T. Kirchhausen and S. C. Harrison. “Protein organization in clathrin trimers”. In: *Cell* 23.3 (1981), pp. 755–761 (Cited on page 81).

[184] B. M. Pearse and M. S. Robinson. “Purification and properties of 100-kd proteins from coated vesicles and their reconstitution with clathrin”. In: *EMBO J.* 3.9 (1984), pp. 1951–1957 (Cited on page 81).

[185] M. Ehrlich et al. “Endocytosis by random initiation and stabilization of clathrin-coated pits”. In: *Cell* 118.5 (2004), pp. 591–605 (Cited on page 83).

[186] K. A. Sochacki et al. “Correlative super-resolution fluorescence and metal-replica transmission electron microscopy”. In: *Nat. Methods* 11.3 (2014), p. 305 (Cited on pages 83 and 85).

[187] K. A. Sochacki et al. “Endocytic proteins are partitioned at the edge of the clathrin lattice in mammalian cells”. In: *Nat. Cell Biol.* 19.4 (2017), p. 352 (Cited on pages 85, 93, 94, 101, 102, 107, 122, 123 and 139).

[188] M. K. Higgins and H. T. McMahon. “Snap-shots of clathrin-mediated endocytosis”. In: *Trends Biochem. Sci.* 27.5 (2002), pp. 257–263 (Cited on page 86).

[189] X. Wu et al. “Adaptor and clathrin exchange at the plasma membrane and trans-Golgi network”. In: *Mol. Biol. Cell* 14.2 (2003), pp. 516–528 (Cited on pages 93 and 96).

[190] S. Saffarian and T. Kirchhausen. “Differential evanescence nanometry: live-cell fluorescence measurements with 10-nm axial resolution on the plasma membrane”. In: *Biophys. J.* 94.6 (2008), pp. 2333–2342 (Cited on pages 93 and 102).

[191] D. Loerke et al. “Measuring the hierarchy of molecular events during clathrin-mediated endocytosis”. In: *Traffic* 12.7 (2011), pp. 815–825 (Cited on pages 93 and 102).

[192] J. P. Ferguson et al. “Deciphering dynamics of clathrin-mediated endocytosis in a living organism”. In: *J. Cell Biol.* 214.3 (2016), pp. 347–358 (Cited on pages 96 and 102).

[193] M. S. Robinson. “Forty Years of Clathrin-coated Vesicles”. In: *Traffic* 16.12 (2015), pp. 1210–1238 (Cited on page 100).

[194] H. Maib et al. “Forty years on: clathrin-coated pits continue to fascinate”. In: *Mol. Biol. Cell* 28.7 (2017), pp. 843–847 (Cited on page 100).

[195] Y. Rao and V. Haucke. “Membrane shaping by the Bin/amphiphysin/Rvs (BAR) domain protein superfamily”. In: *Cell. Mol. Life Sci.* 68.24 (2011), pp. 3983–3993 (Cited on page 102).

[196] J. C. Stachowiak et al. “Membrane bending by protein–protein crowding”. In: *Nat. Cell Biol.* 14.9 (2012), p. 944 (Cited on page 102).

[197] C. Mim and V. M. Unger. “Membrane curvature and its generation by BAR proteins”. In: *Trends Biochem. Sci.* 37.12 (2012), pp. 526–533 (Cited on page 102).

[198] B. Ritter et al. “NECAP 1 regulates AP-2 interactions to control vesicle size, number, and cargo during clathrin-mediated endocytosis”. In: *PLOS Biol.* 11.10 (2013), e1001670 (Cited on page 102).

[199] S. E. Miller et al. “CALM regulates clathrin-coated vesicle size and maturation by directly sensing and driving membrane curvature”. In: *Dev. Cell* 33.2 (2015), pp. 163–175 (Cited on page 102).

[200] C. J. Merrifield et al. “Coupling between clathrin-coated-pit invagination, cortactin recruitment, and membrane scission observed in live cells”. In: *Cell* 121.4 (2005), pp. 593–606 (Cited on page 102).

[201] D. Li et al. “Extended-resolution structured illumination imaging of endocytic and cytoskeletal dynamics”. In: *Science* 349.6251 (2015), aab3500 (Cited on page 102).

[202] P. K. Umasankar et al. “A clathrin coat assembly role for the muniscin protein central linker revealed by TALEN-mediated gene editing”. In: *eLife* 3 (2014), e04137 (Cited on page 102).

[203] F. Frey et al. “Computational support for spatial heterogeneity in flat clathrin lattices”. In: *Submitted* (2019) (Cited on page 103).

[204] M. Kaksonen and A. Roux. “Mechanisms of clathrin-mediated endocytosis”. In: *Nat. Rev. Mol. Cell Biol.* (2018) (Cited on pages 103 and 104).

[205] M. Mettlen et al. “Regulation of clathrin-mediated endocytosis”. In: *Annu. Rev. Biochem.* 0 (2018) (Cited on pages 103 and 122).

[206] K. A. Sochacki and J. W. Taraska. “From Flat to Curved Clathrin: Controlling a Plastic Ratchet”. In: *Trends Cell Biol.* (2018) (Cited on pages 103 and 122).

[207] B. M. F. Pearse and M. S. Bretscher. “Membrane recycling by coated vesicles”. In: *Annu. Rev. Biochem.* 50.1 (1981), pp. 85–101 (Cited on pages 103, 104 and 105).

[208] B. L. Scott et al. “Membrane bending occurs at all stages of clathrin-coat assembly and defines endocytic dynamics”. In: *Nat. Commun.* 9.1 (2018), p. 419 (Cited on pages 104, 122, 123 and 139).

[209] C. A. Schneider et al. “NIH Image to ImageJ: 25 years of image analysis”. In: *Nat. Methods* 9.7 (2012), p. 671 (Cited on page 107).

[210] Edwin L Crow and Kunio Shimizu. *Lognormal Distributions: Theory and Applications*. Marcel Dekker, (1987) (Cited on page 109).

[211] W. K. den Otter et al. “Asymmetry as the key to clathrin cage assembly”. In: *Biophys. J.* 99.4 (2010), pp. 1231–1238 (Cited on page 110).

[212] A. Hagberg et al. *Exploring network structure, dynamics, and function using NetworkX*. Tech. rep. Los Alamos National Lab.(LANL), Los Alamos, NM (United States), 2008 (Cited on page 111).

[213] D. L. Applegate et al. *The traveling salesman problem: a computational study*. Princeton university press, (2006) (Cited on page 116).

[214] P. N. Dannhauser et al. “Effect of clathrin light chains on the stiffness of clathrin lattices and membrane budding”. In: *Traffic* 16.5 (2015), pp. 519–533 (Cited on page 122).

[215] L. Hinrichsen et al. “Bending a membrane: how clathrin affects budding”. In: *Proc. Natl. Acad. Sci. U.S.A.* 103.23 (2006), pp. 8715–8720 (Cited on page 125).

[216] M. Doi. “Onsager’s variational principle in soft matter”. In: *J. Phys. Condens. Matter* 23.28 (2011), p. 284118 (Cited on page 135).

[217] L. Martínez-Balbuena et al. “Onsager’s irreversible thermodynamics of the dynamics of transient pores in spherical lipid vesicles”. In: *Eur. Biophys. J.* 44.6 (2015), pp. 473–481 (Cited on page 135).

[218] E. Jones et al. *Using the function: ‘scipy integrate odeint’ from SciPy: Open source scientific tools for Python.* `http://www.scipy.org`. (2001–). (Visited on 03/19/2019) (Cited on page 136).

[219] N. M. Willy et al. “Membrane mechanics govern spatiotemporal heterogeneity of endocytic clathrin coat dynamics”. In: *Mol. Biol. Cell* 28.24 (2017), pp. 3480–3488 (Cited on page 140).

[220] M. Newville et al. “LMFIT: non-linear least-square minimization and curve-fitting for Python”. In: *Astrophysics Source Code Library* (2016) (Cited on page 153).

[221] L. R. Paiva and S. C. Ferreira Jr. “Universality class of isotropic on-lattice Eden clusters”. In: *J. Phys. A* 40.1 (2006), F43 (Cited on page 154).

[222] S. G. Alves et al. “Universal fluctuations in radial growth models belonging to the KPZ universality class”. In: *EPL* 96.4 (2011), p. 48003 (Cited on page 155).

List of publications

The listed manuscripts have been prepared, submitted or published during the course of this thesis. The right column indicates the chapter of this thesis on which they are (partially) based.

1.	P. Kumberger, **F. Frey**, U. S. Schwarz, and F. Graw. **Multiscale modeling of virus replication and spread.** *FEBS letters*, 590 (13):1972-86 (2016).	Chapter 2
2.	**F. Frey**, F. Ziebert, and U. S. Schwarz. **Stochastic Dynamics of Nanoparticle and Virus Uptake.** *Physical Review Letters*, 122 (8):088102 (2019).	Chapter 3
3.	**F. Frey**, F. Ziebert, and U. S. Schwarz. **Dynamics of particle uptake at cell membranes.** *Currently in preparation. The manuscript will be submitted to Physical Review E,* (2019).	Chapter 4
4.	T. Wiegand, M. Fratini, **F. Frey**, K. Yserentant, E. Weber, Y. Liu, K. Galior, J. Ohmes, D. P. Herten, S. Boulant, U. S. Schwarz, K. Salaita, E. A. Cavalcanti-Adam, and J. P. Spatz. **Specific virus and virus-like nanoparticle interactions with the ventral cell side determine forces leading to uptake.** *Submitted*, (2018).	Chapter 5
5.	D. Bucher*, **F. Frey***, K. A. Sochacki, S. Kummer, J. P. Bergeest, W. J. Godinez, H. G. Kräusslich, K. Rohr, J. W. Taraska, U. S. Schwarz, and S. Boulant. **Clathrin-adaptor ratio and membrane tension regulate the flat-to-curved transition of the clathrin coat during endocytosis.** *Nature Communications*, 9(1):1109, (2018). *Equally contributed.	Chapter 6
6.	**F. Frey**, D. Bucher, K. A. Sochacki, J. W. Taraska, S. Boulant, and U. S. Schwarz. **Computational support for spatial heterogeneity in flat clathrin lattices.** *Submitted*, (2019).	Chapter 7

Danksagungen

Zuallererst möchte ich mich bei meinem Betreuer Prof. Dr. Ulrich Schwarz für seine Unterstützung und Betreuung, seine Anregungen in Form von Ideen, Fragen und Kritik bedanken. Außerdem bedanke ich mich für Gespräche und Diskussionen in denen ich viel über Physik, wissenschaftliche Forschung und Hochschulpolitik lernen konnte und was es bedeutet ein guter Wissenschaftler zu sein. Weiterhin danke ich ihm für das Ermöglichen der Teilnahme an zahlreichen Konferenzen und die Mitarbeit in internationalen Kollaborationen.
Des Weiteren bedanke ich mich bei Prof. Dr. Heinz Horner für das Interesse und die Begutachtung dieser Arbeit. Ein großer Dank geht an die finanzielle und idelle Förderung dieser Arbeit durch die Heidelberg Graduate School of Fundamental Physics (HGSFP) und das Institut für Theoretische Physik.
Ein besonders herzlicher Dank geht an meine Kollaborationspartner (chronologisch geordnet): Delia Bucher, Steeve Boulant, Tina Wiegand, Ada Cavalcanti-Adam, Falko Ziebert, Kem Sochacki und Justin Taraska. Vielen Dank für die gute Zusammenarbeit.
Ganz herzlich bedanke ich mich bei meinen Kollegen der AG Schwarz am Philosophenweg und Bioquant. Bei Justin Grewe für fortwährenden Austausch, IT Unterstützung und aufmunternde Momente. Bei Falko Ziebert für erfolgreiche Zusammenarbeit, fachliche Unterstüzung und gute Ideen. Bei Julia Jäger für die Organisation des DPG Konferenzbesuchs und IT Unterstützung. Außerdem bedanke ich mich bei Dimitri Probst für zahlreiche gemeinsame Reisen zu Konferenzen, Gespräche von linearen Bewegungen bis zu unendliche Reihen. Auch von meiner Seite: immer wieder gerne.
Ein großer Dank geht auch an Niko Schnellbächer für die Organisation zahlreicher gemeinsam besuchter Konferenzen. Außerdem möchte ich Heinrich Klein für die Unterstützung im Übergang zur Doktorarbeit und Philipp Albert für die Unterützung im Erstellen von Postern danken. Bei Anil Kumar Dasanna bedanke ich mich für Zuspruch und anregende Diskussionen. Den ehemaligen Bachelor- bzw. Master- Studenten der AG Schwarz David Outland, Vanessa Scheller, Markus Miltner und Dennis Wörthmüller danke ich für die erfolgreiche Zusammenarbeit. Schließlich bedanke ich mich bei allen anderen aktiven und ehemaligen Mitgliedern der AG Schwarz für das gute Miteinander.
Ein großer Dank geht auch an Justin Grewe, Falko Ziebert, Christian Mauch und Petra Todorović für das unermüdliche Korrekturlesen dieser Arbeit.
Zu guter Letzt bedanke ich mich bei meinen Brüdern Jörg und Stephan Frey für ihr prägendes Vorbild. Ein besonderer Dank geht an meine lieben Eltern für ihre andauernde Unterstützung in jetzt bald drei Jahrzehnten. Zuallerletzt bedanke ich mich bei Petra Todorović für ihre Geduld, Vertrauen und Zuversicht.